Living Rev. Sol. Phys. (2018) 15:3
https://doi.org/10.1007/s41116-018-0012-6

REVIEW ARTICLE

Prominence oscillations

Iñigo Arregui[1] · **Ramón Oliver**[2] · **José Luis Ballester**[2]

Received: 10 July 2017 / Accepted: 21 February 2018

Abstract Prominences are intriguing, but poorly understood, magnetic structures of the solar corona. The dynamics of solar prominences has been the subject of a large number of studies, and of particular interest is the study of prominence oscillations. Ground- and space-based observations have confirmed the presence of oscillatory motions in prominences and they have been interpreted in terms of magnetohydrodynamic waves. This interpretation opens the door to perform prominence seismology, whose main aim is to determine physical parameters in magnetic and plasma structures (prominences) that are difficult to measure by direct means. Here, we review the

---

This article is a revised version of https://doi.org/10.12942/lrsp-2012-2.
Change summary: Major revision, updated and expanded.
Change details: New section on Bayesian analysis. New observations and theoretical models for small and for large amplitude oscillations. About 50 new references were added.

Electronic supplementary material The online version of this article (https://doi.org/10.1007/s41116-018-0012-6) contains supplementary material, which is available to authorized users.

✉ José Luis Ballester
joseluis.ballester@uib.es
http://solar.uib.es; https://joseluisballester.wixsite.com/pers

Iñigo Arregui
iarregui@iac.es
http://www.iac.es/galeria/iarregui/

Ramón Oliver
ramon.oliver@uib.es
http://solar.uib.es

[1] Instituto de Astrofísica de Canarias, 38205 La Laguna, Spain

[2] Departament de Física and Institut d'Aplicacions Computacionals de Codi Comunitari (IAC3), Universitat de les Illes Balears, 07122 Palma de Mallorca, Spain

observational information gathered about prominence oscillations as well as the theoretical models developed to interpret small and large amplitude oscillations and their temporal and spatial attenuation. Finally, several prominence seismology applications are presented.

Keywords Prominences · Oscillations · Seismology

Contents

1 Prominences

Quiescent solar filaments are clouds of cool and dense plasma suspended against gravity by forces thought to be of magnetic origin. They form along the inversion polarity line in or between the weak remnants of active regions. Early observations already suggested that their fine structure is apparently composed by many horizontal and thin dark threads (Jager 1959; Kuperus and Tandberg-Hanssen 1967). More recent high-resolution H_α observations obtained with the Swedish Solar Telescope (SST) in La Palma (Lin et al. 2005) and the Dutch Open Telescope (DOT) in Tenerife (Heinzel and Anzer 2006) have allowed to observe this fine structure with much greater detail (see Lin 2011, for a review). The measured average width of resolved thin threads is about $0.3''$ ($\sim$210 km), while their length is between 5 and $40''$ ($\sim$3500–28,000 km).

The fine threads of solar filaments seem to be partially filled with cold plasma (Lin et al. 2005), typically two orders of magnitude denser and cooler than the surrounding corona, and it is generally assumed that they outline the magnetic flux tubes in which they reside (Engvold 1998; Lin 2005; Lin et al. 2005; Okamoto et al. 2007; Engvold 2008; Martin et al. 2008; Lin 2008). This idea is strongly supported by observations, which suggest that threads are skewed with respect to the filament long axis in a similar way to what has been found for the magnetic field (Leroy 1980; Bommier et al. 1994; Bommier and Leroy 1998). On the opposite, Heinzel and Anzer (2006) suggest that these dark horizontal filament structures are a projection effect. According to this view, many magnetic field dips of rather small vertical extension, but filled with cool plasma, are aligned in the vertical direction and the projection against the disk produces the impression of a horizontal thread.

Prominences are highly dynamic structures that display flows. These flows have been observed in H_α, UV and EUV lines, and their study and characterisation are of great interest for the understanding of prominence formation and stability, the mass supply and the prominence magnetic field structure. In the H_α line, and in quiescent limb prominences, a complex dynamics with vertical downflows and upflows (Berger et al. 2008) as well as horizontal flows is often observed. The velocities are in the range between 2 and 35 km s^{-1}, while in EUV lines flow velocities seem to be slightly higher. When comparing these values one should be aware that these lines correspond to different temperatures, so probably the reported flow speeds correspond to different parts of the prominence. In active region prominences, flow velocities seem to be higher than in quiescent prominences, even reaching 200 km s^{-1}, and some of these high-speed flows are probably related to the prominence formation itself. In the case of filaments observed on the disk in the H_α line, horizontal flows in the filament spine are often observed, while in barbs flows are vertical. The range of observed velocities of filament flows is between 5 and 20 km s^{-1}. A particular feature in these observations is the presence of counter-streaming flows, i.e., oppositely directed flows (Zirker et al. 1998; Lin et al. 2003). Because of the physical conditions of the filament plasma, all these flows seem to be field-aligned. For a thorough information about flows in prominences see Labrosse et al. (2010) and Mackay et al. (2010).

Solar prominences are subject to various types of oscillatory motions. Some of the first works on this subject were concerned with oscillations of large amplitude induced by disturbances coming from a nearby flare. Later, observations performed with ground-based telescopes pointed out that many quiescent prominences and filaments display small amplitude oscillations (Harvey 1969). These oscillations have been commonly interpreted in terms of standing or propagating magnetohydrodynamic (MHD) waves, for which the relevant velocities are the Alfvén and sound speed; their typical values in quiescent prominences are of the order of 100 and 11 km s^{-1}, respectively. Using this interpretation, a number of theoretical models have been set up in order to try to understand the prominence oscillatory behaviour. Such as we will point out in the following, the study of prominence oscillations can provide with an alternative approach for probing their internal structure. The magnetic field structure and physical plasma properties are often hard to infer directly and wave properties directly depend on these physical conditions. Therefore, prominence seismology seeks to obtain information about prominence physical conditions from a comparison between observations and theoretical models of oscillations.

The layout of the review is the following: first of all, the criteria that are used to classify oscillatory events in prominences are described. Next, observational aspects of large amplitude oscillations, together with theoretical models, are described in Sects. 3 and 4; in Sect. 5, the observational background about small amplitude oscillations is reviewed; in Sect. 6, theoretical models of small amplitude oscillations based on linear ideal MHD waves in different configurations are described; next, in Sect. 7, the damping of small amplitude prominence oscillations produced by different mechanisms is studied from a theoretical point of view; finally, in Sect. 8, prominence seismology using large and small amplitude oscillations is introduced.

2 Classification of prominence oscillations

Prominence oscillations have been classified according to different measurable quantities: period, oscillatory amplitude, polarisation of motions, prominence shape, exciter (e.g., Vršnak 1993). In Oliver (1999) we decided to use the velocity amplitude as the only classification parameter and separated prominence oscillations into small and large amplitude events, with respective amplitudes smaller than 3 km s^{-1} and larger than 20 km s^{-1}. The detection of intermediate values in the last two decades reveals that the velocity amplitude alone is not enough to identify an oscillatory event. In spite of this, we maintain these two categories because they represent truly different phenomena: small amplitude oscillations are, *in general*, not related to flare activity and only affect a small volume of the prominence. In addition, oscillatory amplitudes are *usually* smaller than 10 km s^{-1}. On the other hand, large amplitude oscillations are *often* associated to an energetic event that sets the full prominence (or a large part of it) into an oscillatory state. The velocity amplitude is *usually* larger than 10–20 km s^{-1}. Hence, although one should probably speak of local versus global oscillatory events in prominences, we will refer to them using the original small and large amplitude denominations, respectively.

This review is mainly devoted to small amplitude oscillations, although the next two sections also deal with large amplitude oscillations.

3 Large amplitude oscillations: observational aspects

Oscillations that shake a significant part of a prominence and whose velocity amplitude is usually greater than 20 km s^{-1} have been observed in filaments. It was suggested that their exciter was a wave, caused by a flare, which disturbs the filament and induces damped oscillations. This hypothesis was confirmed by Moreton and Ramsey (1960), who used a refined photographic technique that permitted the observation of the propagating perturbation, with velocities in the range 500–1500 km s^{-1}. In some cases, during the course of the oscillations, the filament becomes visible in the H_α image when the prominence is at rest, but when its line-of-sight velocity is sufficiently large, the emission from the material falls outside the bandpass of the filter and the prominence becomes invisible in H_α. This process is repeated periodically and for this reason this type of event is called a winking filament. Ramsey and Smith (1965, 1966) and Hyder (1966) studied 11 winking filaments and the derived oscillatory velocity was quite large compared with the relevant wave speeds in prominences (namely the sound and Alfvén speeds). For this reason, one usually refers to these events as large amplitude oscillations. Furthermore, they derived oscillatory periods between 6 and 40 min, and damping times between 7 and 120 min, and reported that there seemed to be no correlation between the period and the filament dimensions, the distance to the perturbing flare or its size. In addition, a single filament perturbed by four flares during three consecutive days oscillated with essentially the same frequency and damping time in each event. As a consequence, it was suggested that prominences possess their own frequency of oscillation.

Thanks to space and ground-based instruments, observations of large amplitude oscillations have become common and the exciters seem to be Moreton or EIT waves (Eto et al. 2002; Okamoto et al. 2004; Gilbert et al. 2008; Asai et al. 2012), EUV waves (Liu et al. 2012; Shen et al. 2014a; Xue et al. 2014; Takahashi et al. 2015), shock waves (Shen et al. 2014b), nearby jets, subflares and flares (Jing et al. 2003, 2006; Vršnak et al. 2007; Li and Zhang 2012), while in other cases the oscillations are associated to the eruptive phase of a filament (Isobe and Tripathi 2006; Isobe et al. 2007; Pouget 2007; Chen et al. 2008; Foullon et al. 2009; Bocchialini et al. 2011). Although in most of the observed flare-induced filament oscillations the material undergoes vertical oscillations (Eto et al. 2002; Okamoto et al. 2004; Shen et al. 2014a), other authors (Kleczek and Kuperus 1969; Hershaw et al. 2011; Gosain and Foullon 2012; Liu et al. 2012; Shen et al. 2014b) have also reported horizontal oscillations. Moreover, periodic motions along the longitudinal filament axis (Jing et al. 2003, 2006; Vršnak et al. 2007; Li and Zhang 2012; Zhang et al. 2012; Luna et al. 2014; Shen et al. 2014b) as well as oscillations having a mixed character (Gilbert et al. 2008) have also been observed. Some of the above mentioned observations were already described in the review by Tripathi et al. (2009), therefore, in this section we will only take into account observations not covered in that review. These observations will be split according to features such as the polarisation of the oscillatory motions or whether the events take place during a prominence eruption.

3.1 Vertical oscillations

Vertical oscillations have been usually associated with winking filaments (Ramsey and Smith 1965, 1966; Hyder 1966; Eto et al. 2002; Okamoto et al. 2004). An interesting observation was reported by Shen et al. (2014a) who, using H_α observations from the ground (SMART) and space (AIA/SDO), detected a chain of winking filaments produced by an EUV wave, associated to an X2.1 flare. The EUV wave was composed by an upward dome-like wave together with a lateral surface wave. After an analysis of the spatial and temporal relationship between the oscillating filaments and the EUV waves, they attributed the excitation of the winking filaments to the lateral surface wave. In H_α line-wing observations, four filaments were perturbed and started to oscillate in a sequential way depending on their distance to the flare. The oscillating filaments did not show evidence of horizontal motions suggesting that the direction of

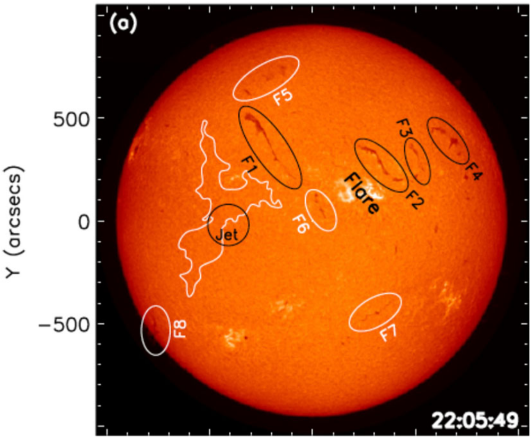

Fig. 1 H_α image with the oscillating filaments, *F1–F4*, highlighted with black ellipses while the white ellipses indicate the nonoscillating ones, *F5–F8*. Image reproduced with permission from Shen et al. (2014a), copyright by AAS

the oscillation was mainly along the line-of-sight, and the oscillations were damped in time. The Doppler velocities at different positions of one filament were fitted with an exponentially decaying sine function and the results showed that the amplitude decreased along the filament while the period remained constant. Therefore, these authors suggested that the filament oscillated as a whole harmonic oscillator. They used the same method with the rest of oscillating filaments, obtaining periods of oscillation and initial amplitudes, and concluded, such as in Ramsey and Smith (1966), that different filaments, excited by a common disturbance, oscillate with their own characteristic frequency. One interesting feature of these observations, shown in Fig. 1, is the lack of oscillations in filaments F5–F8. The reason why the same excitation producing oscillations in a filament is not able to induce oscillations in a neighbour filament remains to be understood.

3.2 Transverse (horizontal) oscillations

Kleczek and Kuperus (1969) proposed an alternative interpretation in terms of transverse, with respect to the longitudinal axis of the filament, horizontal motions, for the winking filaments analysed by Hyder (1966), and further observations of transverse oscillations have been reported during recent years. For instance Hershaw et al. (2011) studied oscillations in an arched prominence observed with SOHO/EIT on 2005 July 30. The perturbations were produced by two consecutive trains of coronal waves coming from two different flares in an active region located far away from the prominence site. Both oscillatory trains had periods of around 100 min and excited prominence oscillations that lasted for about 18 h. During the oscillations, the displacement of the prominence was horizontal with respect to the solar surface. In the case of the first wave train, induced by a more energetic flare than the second one, the displacement in all the considered prominence locations shows a clear time damped oscillatory behaviour (see Fig. 2). The oscillatory period, the damping time and the horizontal velocity at different heights along the two prominence legs were determined (see Table 1 in Hershaw et al. 2011). The prominence oscillatory periods seem to depend on the height

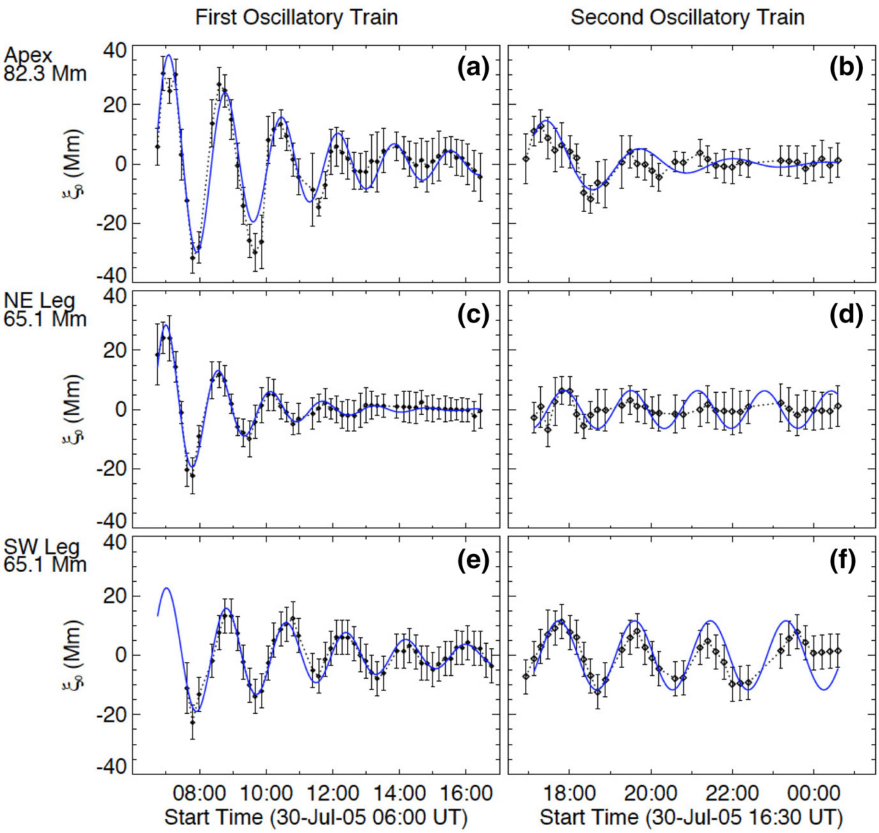

Fig. 2 Displacement versus time produced by two wave trains impacting on a prominence. **a**, **b** In the prominence apex, **c**, **d** in the NE leg, **e**, **f** in the SW leg. Image reproduced with permission from Hershaw et al. (2011), copyright by ESO

at which they were measured and, for each wave train, they show some differences depending on the leg in which they were measured. Focussing on the first wave train, which seems to trigger a clearly damped oscillation, the periods range between 86 and 101 min in one leg, and between 92 and 104 min in the other. Furthermore, the velocity amplitude also changes with height and reaches a maximum value of 50 km s^{-1} in one leg and 33 km s^{-1} in the other. These observational features, differences in the periods measured in both legs, in the velocity amplitudes at both legs, etc., enabled the authors to suggest that the prominence could be composed by separate oscillating filamentary threads. In summary, from the reported observations it seems that one of the wave trains was able to induce large amplitude oscillations in the prominence while the effect of the second wave train was not so strong. The reason for these different behaviours could be attributed to the different energy carried by the wave trains or, in spite of the wave train periods being apparently similar, to a resonance effect between the wave train frequency and the natural oscillatory frequency of the prominence. Also, it is worth to remark that the reported observation was made in EUV while other observations of large amplitude oscillations have been made in H_α. The correspon-

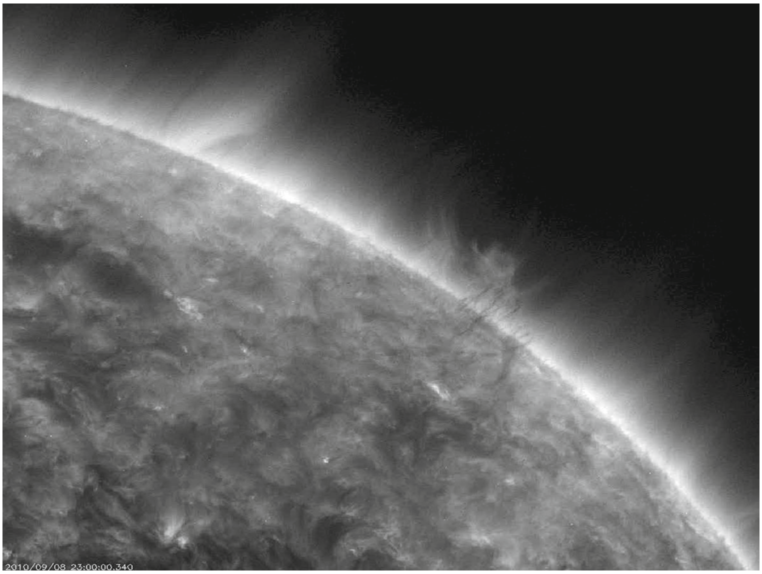

Fig. 3 Still from a movie showing a limb prominence whose global transverse oscillations were analysed by Gosain and Foullon (2012). (To watch the movie, please go to the online version of this review article at doi:10.1007/s41116-018-0012-6)

dence between oscillations observed in EUV and in H_α remains to be ascertained. Probably, only simultaneous observations could cast light on this relationship.

Liu et al. (2012) reported the detection of quasi-periodic wave trains within the broad pulse of a global EUV wave, these wave trains induced transverse oscillations, like fast kink modes, of local structures such as a flux-rope coronal cavity and its embedded filaments. They selected three dark filament threads, embedded in the coronal cavity, as tracers of the oscillations and obtained the space-time position at the centre of each thread which was fitted with an exponentially damped sine function. Although the filaments were located at different positions, the fitted parameters were in a narrow range, suggesting a coherent behaviour consistent with the global oscillations of the full cavity. The found average values were: period 28 min, damping time 120 min, and initial velocity amplitude 9 km s^{-1}. This event was re-analysed by Gosain and Foullon (2012) who focused on transverse large-scale prominence oscillations, investigating also the effect of the two-component EUV coronal wave. Initially, the prominence oscillated in a coherent way but, later on, thread oscillations became out of phase loosing their identity (Fig. 3). The global transverse oscillation suggested the presence of a global kink mode while the non-collective behaviour was probably due to the inhomogeneous prominence structure. After fitting a damped cosine function to a time–distance plot, they obtained a period of about 28 min, a damping time of 44 min and a maximum speed amplitude of 11 km s^{-1}. These authors suggested that prominence oscillations were excited by the arrival of a fast EUV wave. After this excitation, the later arrival of the slow EUV wave to an already oscillating filament acted as a secondary trigger producing a change in the oscillatory phase. It must be noticed that in both studies reported above, the determined velocity amplitudes are small while the oscillations were global (see Sect. 2). Finally, using data from AIA/SDO, Xue et al. (2014) analysed the time behaviour of two filaments located in an active region. After the occurrence of a flare, one filament erupted and, at the same time, an EUV wave started to propagate from the active region. When the EUV wave swept the second filament, transverse oscillations were induced in it although it was difficult to determine if the whole filament was oscillating. With the fit of an exponentially decaying harmonic function, they obtained a period of 1140 s, a damping time of 5920 s and an initial amplitude of 2.17 Mm, and concluded that the oscillations were produced by a fundamental standing kink wave.

3.3 Longitudinal oscillations

Longitudinal oscillations in filaments were first reported by Jing et al. (2003, 2006). Because of the high level of solar activity during recent years, many observations of longitudinal oscillations have been reported. For instance, Zhang et al. (2012) analysed the longitudinal oscillations of an active region prominence observed on 2007 February 6 with Hinode/SOT. The analysis of high resolution Ca II H images suggested that the prominence was made of a bunch of concave-outwards threads indicating the presence of magnetic dips. After a sudden injection of dense plasma in the dip region, this dense material started to oscillate with an initial amplitude of about $30''$ and the oscillation lasted for more than 3.5 h. The amplitude of the oscillations was decreasing with time, but four periods were visible, and the oscillating pattern was fitted with an exponentially decaying sine function. Using this fitting, the period was determined to be 52 min while the damping time was 133 min. On the other hand, before the injection of dense plasma, the more light prominence material was already oscillating with almost the same period as the oscillations described before which suggested that the oscillatory period is mainly determined by the magnetic configuration. Li and Zhang (2012) observed large amplitude longitudinal oscillations in the south and north parts of an active region filament on 2012 April 7. The south part of the filament was observed to be composed by two different regions, 1 and 2, with region 2 located above region 1. A weak flare-brightening close to the south part of the filament activated zone 1 and, after some time, oscillations along zone 1 were initiated followed, with a short delay, by oscillations along zone 2. The oscillatory periods were different for different threads, which suggested that the physical properties of the different threads were different, with periods varying between 44, 54 and 67 min, velocity amplitudes of the order of 40, 60 and 30 km s^{-1}, while the oscillations of the different threads were in phase although they did not show significant damping. These oscillations lasted about 4 h and, later on, this part of the filament erupted. Regarding the activation of the north part of the filament, it was produced by a flare occurring at the middle part of the entire filament and the oscillations, with an initial velocity of 60 km s^{-1}, had a period of 57 min, and lasted for about 3 h before being completely damped out. On 2010 August 20, episodic jets coming from an energetic event triggered large amplitude longitudinal oscillations in a nearby filament which were clearly visible in H_α and three different AIA/SDO filters. Luna et al. (2014)

analysed these oscillations by making time–distance diagrams for 36 positions along the filament. They found that only parts of the filament oscillated while the rest of the filament remained stationary. Then, the time–distance diagrams for the oscillating positions were used to characterise these oscillations in a quantitative way and two different functions such as an exponentially decaying cosine and an exponentially decaying Bessel function were fitted to observational data. Both fits yield similar values, in the range 0.7–0.86 h, for the oscillatory period which is nearly uniform along the filament, however, the oscillations of the different threads were not in phase. The Bessel function fit yields the largest amplitude, being more consistent with the observations during the initial phase and the maximum speeds were in the range 10–47 km s^{-1}. Furthermore, from the time–distance diagrams, it could be seen that the damping of the oscillations followed two different time scales since the oscillations were strongly damped at the beginning (see Fig. 4), with the damping time similar to the period, while the damping became weaker, of the order of a few hours, later on. However, both damping times seemed to be almost uniform along the filament. Bi et al. (2014) analysed longitudinal oscillations, observed with AIA/SDO, associated with a flow of material along the filament axis. Initially, the filament was activated becoming inclined with respect to the solar surface, then, oscillations were observed in the inclined filament. Two oscillating threads were identified which underwent two oscillations before they became undetectable, and the oscillations started with a period of about 67 and 71 min for each thread and, after 2 h the periods increased to 80 and 94 min, respectively. This change in the periods could be attributed to a weakness of the restoring force or to a modification in the magnetic configuration such as the radius of curvature of magnetic field lines (Luna and Karpen 2012). Zhang et al. (2017) reported about longitudinal oscillations observed on 2015 May 3 in a sigmoidal filament located close to an active region. Multiwavelength observations of this filament were obtained with ground-based H_α telescopes from GONG, and with the AIA instrument onboard SDO. Furthermore, photospheric LOS magnetograms were obtained with HMI, also onboard SDO. Evidences of magnetic reconnection, triggering the filament oscillation were observed, and part of the filament oscillated for more than 11 h. Therefore, using H_α images, Zhang et al. (2017) selected ten positions along the oscillating part, made time-slice diagrams and compared the oscillatory patterns, concluding that the oscillation was longitudinal. After a few cycles, the filament suffered mass drainage, a feature also reported by Bi et al. (2014), however, the oscillations did not stop. Using observations made with AIA in 171 Å, time-slice diagrams of the same slices show the oscillations in a more clear way, although they display a very complex behaviour. For instance, in some slices the amplitude grew before the mass drainage, damping later on. However, in other slices the amplitude was damped but increased after mass drainage, and the oscillations did not start simultaneously in all the slices. The oscillatory behaviour observed in each slice was fitted using an appropriate analytical function allowing to obtain numerical values for the period, growing/damping time and the ratio growing/damping time over period, which show a very high dispersion. Furthermore, using the displacement of the filament, velocities were calculated and most of the values were about 20 km s^{-1}. Finally, in order to understand the described complex oscillatory behaviour a tentative explanation based on the numerical simulations by Zhou et al. (2017) (Sect. 4.3) was suggested.

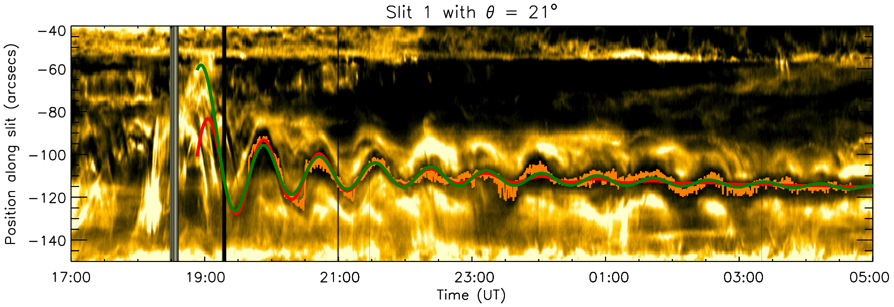

Fig. 4 Time–distance diagram. The fitted functions are plotted as red and green lines corresponding to the exponentially decaying sinusoid and the Bessel function, respectively. Image reproduced with permission from Luna et al. (2014), copyright by AAS

3.4 Simultaneous excitation of transverse and longitudinal oscillations in prominences

Simultaneous excitation of differently polarised oscillations induced by external perturbations have also been described. For instance, Asai et al. (2012) reported the first simultaneous observation of Moreton, fast EUV wave and slow EUV waves, together with oscillations in a limb prominence and in a filament on the disk observed in H_α, with SMART, and in EUV, with AIA/SDO. An X6.9 flare occurred on 2011 August 9 in an active region and, associated with this flare, oscillations of a prominence and a filament were observed. From the SMART H_α wing data, it was observed that the prominence was moving in the line of sight, which suggested longitudinal oscillations. Furthermore, from AIA EUV images the motion in the plane of the sky can also be observed showing that the prominence moved first downward and later upwards, which suggested the presence of transverse oscillations. From SMART H_α images, an oscillatory period of about 15 min and a Doppler velocity of 50 km s^{-1} were determined, while from AIA EUV images a period of 12–16 min and an apparent velocity of 30 km s^{-1} were obtained. Then, in this case simultaneous observations in EUV and in Hα of an oscillating prominence provided with similar results. Regarding the filament, it was observed to be a very weak winking filament.

Shen et al. (2014b) presented interesting observations of simultaneous transverse oscillations of a prominence and a filament together with longitudinal oscillations of another filament detected on 2011 August 9. These oscillations were induced by a single shock wave, associated to an X6.9 flare, which was observed as a Moreton wave in Hα. Transverse oscillations of the prominence were measured at three different heights above the limb and time–distance diagrams, using AIA 193 Å and Hα images, were constructed which allowed to determine the trajectory of the oscillating prominence and the velocity profile. The results showed that the transverse oscillations were initiated once the shock wave reached the prominence, and that the oscillatory amplitude at high altitudes was larger than at low heights. Next, by combining transverse and Doppler velocity components, the full three-dimensional velocity was obtained and the velocity profiles were fitted with an exponentially decaying sine function which

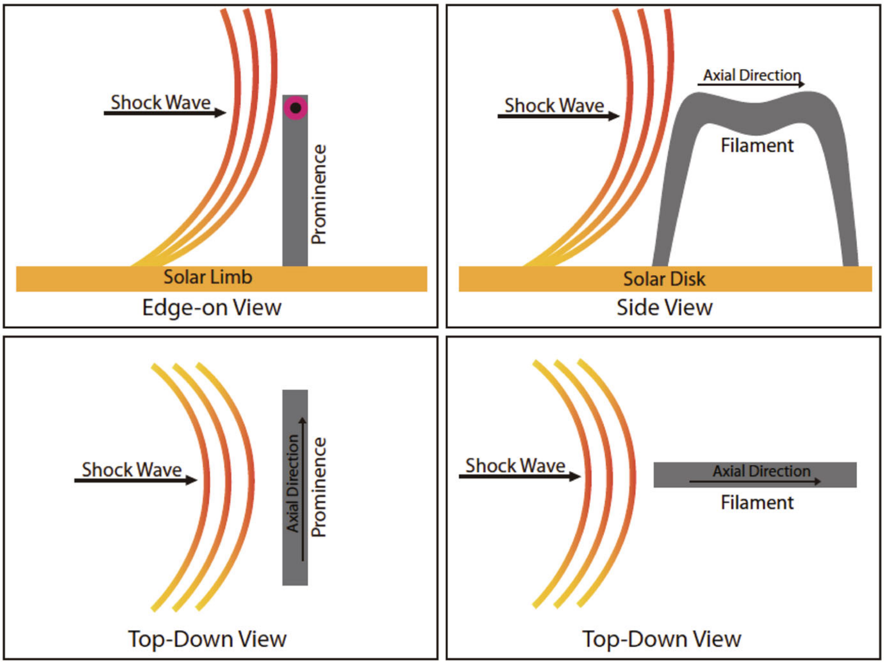

Fig. 5 Cartoon showing the wave-prominence and wave-filament interaction processes triggering transverse and longitudinal oscillations, respectively. Image reproduced with permission from Shen et al. (2014b), copyright by AAS

allowed to obtain periods, damping times and initial amplitudes at different heights. These fittings showed that while the velocity amplitude is larger at high altitude, the oscillatory periods remained the same and equal to 13.5 min, however, the damping time was larger at higher altitude than at lower heights. Regarding the longitudinal oscillations observed in the filament, they were also produced by the passing of the shock wave, and from the STEREO-Ahead observations it could be seen that the wave first interacted with one of the ends of the filament and, then, part of the filament mass started to oscillate along the main axis. A time–distance diagram along the filament axis was generated, and the velocity profile was fitted, again, with an exponentially decaying sine function. The results showed that the filament described four oscillatory cycles with a period of about 80 min and an initial amplitude of 27 km s^{-1}. Weak transverse oscillations of another filament were also observed, however, it seems that in this case the incoming wave suffered reflection processes in open magnetic fields located close to this filament, which reduced the wave speed and, accordingly, the energy of the wave hitting the filament was smaller than in the other studied cases. As an attempt to explain in a qualitative way the observed events, Shen et al. (2014b) illustrated the interaction process between the shock wave and the prominence/filament by means of a cartoon (see Fig. 5) showing how this interaction produced the observed transverse and longitudinal oscillations observed in the prominence and filaments, respectively. In this case, this cartoon points out the importance of the orientation of the prominence/filament with respect to the incoming disturbance. However, this does not seem to be enough since, such as it is shown in Shen et al. (2014a), some filaments remain unperturbed despite being located close to the site where the triggering event takes place. In this sense, one should expect the trapping of a certain amount of energy of the incoming perturbation by the filament. However, what remains to be determined is the efficiency of this trapping by the magnetic configuration of the filament as well as if the injected energy is enough to trigger or not the oscillations.

3.5 Oscillations in erupting filaments

The presence of large amplitude oscillations in erupting filaments has also been reported (Isobe and Tripathi 2006; Isobe et al. 2007; Pouget 2007; Pintér et al. 2008; Chen et al. 2008; Bocchialini et al. 2011). They have been used to perform prominence seismology and as a diagnostic tool for the stability of prominences. Some of these observations together with the conclusions obtained were already summarised in Tripathi et al. (2009), however, it is worth to mention here three further observations about this phenomenon. Using SUMER/SOHO, Chen et al. (2008) observed oscillations in a prominence followed by its eruption. They performed 11 h of spectroscopic observation and the prominence oscillated during 4 h. The analysis of the Doppler velocity time series indicated that two different periods, around 20 and 60 min, were present, while the velocity amplitude was in the range 10–30 km s^{-1}. Later on, the prominence erupted as a blob-like CME. Bocchialini et al. (2011) analysed datasets corresponding to two different filaments observed on 2003 May 30 and 1994 September 18. Two different data sets were used: time series of spectra using He I and Mg X spectral lines measured with CDS/SOHO for the first filament, and time series of intensity and velocity images in H_α line-wings from NSO, for the second filament. In the case of the filament observed in He I and Mg X when the intensity data were considered, two different oscillatory periods appeared in the wavelet analysis for each of the spectral lines, when different time intervals are considered. However, in the Doppler velocity data a common period about 20 min was present, although in the Mg X line another period around 10 min was also found. Regarding the Doppler velocities obtained from the different lines, they were in phase, which seems to indicate that the close overlying corona is affected by filament oscillations and, also, they were quickly damped. A more careful analysis pointed out that the velocity signal in He I could be split in two parts with two very different periods. As a summary, in intensity the periods were in the range 20–30 min although periods longer than 80 min were also detected, while in He I the velocity amplitude was about 12 km s^{-1} with a damping time of 25 min. An increase of the period was also observed by Bi et al. (2014) when longitudinal oscillations and mass drainage were detected during the slow rising motion of a pre-eruptive filament. In the case of the H_α filament (Bocchialini et al. 2011), the results revealed a very complex dynamic behaviour with parts of the filament moving upwards while other parts were moving downwards and no clear oscillatory pattern was observed. Using 171 Å images from SDO/AIA, Joshi et al. (2016) have analysed the activation and eruption of a quiescent filament observed on 2013 August 14. Only the western segment of the filament suffered the activation process in the form of oscillations in thin and long features oriented almost perpendicular to the filament's spine and similar to barbs. Transverse oscillations were observed when the slit was placed along the spine with a period between 60 and 90 min and a velocity amplitude of about 3–5 km s^{-1} in the plane of the sky. These oscillations lasted for about 30 h and, along this time, the filament was slowly rising, which seems to be a common feature of filaments undergoing oscillations before eruption. Finally, only this part of the filament erupted. In the above reported cases, the detected velocity amplitude is smaller than or slightly greater than 20 km s^{-1} but the oscillations affected a substantial part of the filament (see Sect. 2).

4 Large amplitude oscillations: theoretical models

From the theoretical point of view, different models trying to explain the excitation, restoring forces and damping mechanisms of large amplitude oscillations have been put forward. The theoretical complexity of these models has been growing with time from analytical models, based on the harmonic oscillator, up to one dimensional numerical models, whose purpose is to describe longitudinal oscillations. Furthermore, two dimensional numerical models have been also developed which allow to describe in a more complete way the features of the observed oscillations. In the following, we describe, for the different types of large amplitude oscillations, the proposed theoretical models.

4.1 Vertical oscillations

The first attempt to explain vertical oscillations in filaments was made by Anderson (1967) who suggested that the disturbance coming from a flare propagated along the magnetic field and when it arrived to the filament, the material was pushed down. Hyder (1966) proposed a theoretical model based in a Jolly oscillator (mass on a spring, in a viscous fluid and in a uniform gravitational field). Hyder (1966) assumed that the studied winking filaments were located in a depressed magnetic field, like a Kippenhahn–Schlüter model, and interpreted the observations in terms of vertical oscillations damped by the viscosity of the surrounding coronal plasma, with the restoring force being supplied by the magnetic tension. The equation of motion was given by,

$$\ddot{r} + \frac{\mu}{M}\dot{r} + \frac{K}{M}r = 0, \tag{1}$$

with r, the displacement; K, the restoring force per unit displacement written in terms of magnetic tension; M, the mass of the filament, and μ, the effective velocity coefficient of friction in the corona. Using this model, prominence and coronal seismology were performed (see Sect. 8.1). However, vertical oscillations can naturally appear in other situations. For instance, Terradas et al. (2016) have used a magnetic flux rope model developed by Titov and Démoulin (1999) to study numerically the temporal evolution of a prominence, represented by a 3D density enhancement, located inside the flux rope. The flux rope is weakly twisted in order to avoid kink instability and when the prominence is placed within it, a quasi-stationary situation is achieved in some cases after a relaxation phase. This phase is characterised by the excitation of global standing vertical oscillations which are strongly attenuated in time. The damping mechanism is resonant absorption which appears in the inhomogeneous transition (PCTR) between the prominence and solar corona. In this layer, the global oscillation of the whole prominence is transferred to Alfvén continuous modes whose amplitude grows with time until all the energy of the global mode has been transferred and phase mixing develops.

4.2 Transverse (horizontal) oscillations

In order to provide with an explanation for transverse horizontal oscillations, Kleczek and Kuperus (1969) assumed that a line-tied magnetic field was directed along the filament, that the restoring force was supplied by magnetic tension and that the transverse oscillations were damped by wave leakage, i.e., the emission of acoustic waves from the prominence. This emission was assumed to be produced by the motion of the prominence inside the corona which could be considered analogous to emission of acoustic waves from a piston source. The most important effect of this emission was a radiative reaction force producing a radiation damping of the prominence motion. Using the analogy of a circular piston, Kleczek and Kuperus (1969) obtained an expression for the radiative reaction force which, once included in the general equation for a damped harmonic oscillator, gave place to the following equation,

$$m\ddot{\xi} + \rho_c c A \left[1 - \frac{J_1(2ka)}{ka} \right] \dot{\xi} + \frac{dAB^2}{4\pi L^2} \xi = 0, \tag{2}$$

with ξ the displacement, m the total mass of the filament, c the propagation speed of the accoustic waves in the corona, ρ_c the coronal density, d the thickness of the prominence, A the effective surface of the prominence, L the length of the prominence, B the magnetic field strength, J_1 the Bessel function, a the radius of a circular piston, and k the wavenumber. Then, the oscillatory period was given by

$$P = 4\pi L B^{-1} \sqrt{\pi \rho_p}, \tag{3}$$

with ρ_p the prominence density. This model has also been used to explain the transverse oscillation of a pre-erupting filament (Isobe and Tripathi 2006) and to perform prominence seismology (see Sect. 8.1)

4.3 Longitudinal oscillations

In the case of large amplitude longitudinal oscillations observed by Jing et al. (2003, 2006), several possible driving mechanisms, such as gravitational force, pressure imbalance and magnetic tension, were suggested by these authors. Each mechanism was analysed in detail concluding that if gravity was responsible for the oscillations, then, a dipped magnetic configuration was needed. For instance, the depth of the magnetic dips required to explain gravity induced motions was estimated to be 10% of the whole length of the magnetic field lines. Regarding the siphon-like mechanism (pressure-driven motion), it was a possible explanation since the observed motions were along the magnetic field lines and the triggering events were close to the footpoints which could cause a pressure imbalance. However, this mechanism lacks the restoring force needed to explain the large amplitude oscillations. Finally, it is also difficult to attribute the longitudinal oscillations to the magnetic tension since this force produces motions perpendicular to the local magnetic field. As potential damping mechanisms they considered radiative damping and wave leakage (Kleczek and Kuperus 1969).

A more complete theoretical model for these oscillations was proposed by Luna and Karpen (2012) and Luna et al. (2012a). The scenario is the following: when an energetic event (a subflare, for instance) happens close to a filament, the injected energy evaporates plasma at the fluxtube footpoint closest to the energetic event. Then, the flow of hot plasma pushes the cold plasma condensations (threads) located at the dips of the magnetic structure, and the longitudinal oscillations start. After some time, they lose coherence due to period differences. The restoring force is the projected solar gravity directed towards the bottom of the dip and since the magnetic tension in the dip must be larger than the weight of the threads, we have,

$$\frac{B^2}{R} - mng_0 \geq 0,$$

where R is the radius of curvature, m the particle mass, n the particle density, and g_0 the gravitational acceleration. On the other hand, since the oscillation is gravity driven,

$$P = 2\pi\sqrt{\frac{R}{g_0}} \tag{4}$$

and combining the above two expressions, we obtain,

$$B \geq \sqrt{\frac{g_0^2 mn}{4\pi^2}}\,P. \tag{5}$$

Then, knowing the period (P) and assuming a typical density (n), Eq. (5) constrains the minimum field strength (B) as a function of the thread oscillation period. The damping mechanism of the oscillations was attributed to a continuous mass accretion onto the prominence, this mass accretion was already predicted in the thermal non-equilibrium model for filament mass formation and, for standard coronal heating localised at the footpoints, the accretion rate matches the rate of chromospheric evaporation (Luna et al. 2012b). On the other hand, assuming that the oscillations are gravity driven, Eq. (4) allows to obtain the radius of curvature of the magnetic field lines (Luna et al. 2014).

Regarding the damping mechanism, Ruderman and Luna (2016) have studied the damping of longitudinal oscillations of a prominence thread produced by mass accretion. They have considered a simple model in which the prominence thread, made of cold plasma, occupies the central part of a thin curved magnetic flux tube, while the two lateral sides of the tube are filled with hot rarefied plasma. The main assumptions of the model are that there are flows of rarefied plasma, moving towards the cold plasma, which are caused by plasma evaporation at the footpoints of the tube, and that, after its arrival, this hot plasma in instantaneously added to the thread becoming its temperature and density equal to those of the thread. Once the system of differential equations describing the thread dynamics was derived, it was solved for two different geometries of the flux tube. In both cases, the damping time is inversely proportional to the accretion rate which allows to determine the mass accretion rate once the damping time has been determined. From the results, Ruderman and Luna (2016) concluded that mass accretion could be a suitable mechanism to explain the strong damping observed in large amplitude longitudinal oscillations.

Related with longitudinal oscillations, Terradas et al. (2013) made a numerical study of two-dimensional prominence magnetohydrostatic models under the presence of gravity. The initial equilibrium was an isothermal stratified atmosphere permeated by a force-free magnetic field represented by a superposition of arcade solutions. Later, in order to generate the prominence, mass was added at a given location in the preexisting magnetic configuration. Then, once the prominence reached an equilibrium, Terradas et al. (2013) studied its oscillatory behaviour by solving the linearised MHD equations around this final equilibrium. Slow magnetoacoustic-gravity waves were investigated by introducing a horizontal perturbation which excites the whole prominence body, producing motions along the magnetic field lines. From the numerical simulations, they obtained the periods for these field-aligned oscillations which were compared to those obtained using Eq. (4) from Luna and Karpen (2012) and Luna et al. (2012a). The comparison shows a strong disagreement between both periods (see Fig. 19 in Terradas et al. 2013). This lack of agreement could be due to the different physical properties (constant versus non constant radius of curvature, no variation versus variation of magnetic field along the field lines, non isothermal versus isothermal) of the models used by Luna and Karpen (2012), Luna et al. (2012a) and Terradas et al. (2013). As a consequence, these results cast doubts about the role played by gravity as a driver of longitudinal oscillations at least in the configuration studied by Terradas et al. (2013).

To test the validity of the pendulum model, Luna et al. (2016b) performed 2D non-linear time dependent simulations of large amplitude longitudinal oscillations in a dipped magnetic structure. The initial configuration was a force-free magnetic field represented by a symmetric double arcade which had dips close to the surface and in which a prominence mass was loaded. The numerical domain was a box in which open boundary conditions were assumed for the top and the two side boundaries, while at the bottom boundary line-tying was considered. In order to produce longitudinal oscillations, once the full structure, with mass included, is sufficiently relaxed, the configuration was perturbed with a velocity field directed along the magnetic field lines. Figure 6 shows the time behaviour of density and magnetic field and when the system is perturbed, the prominence material starts to move following magnetic field lines until a maximum displacement is attained, then, the motion reverses. However,

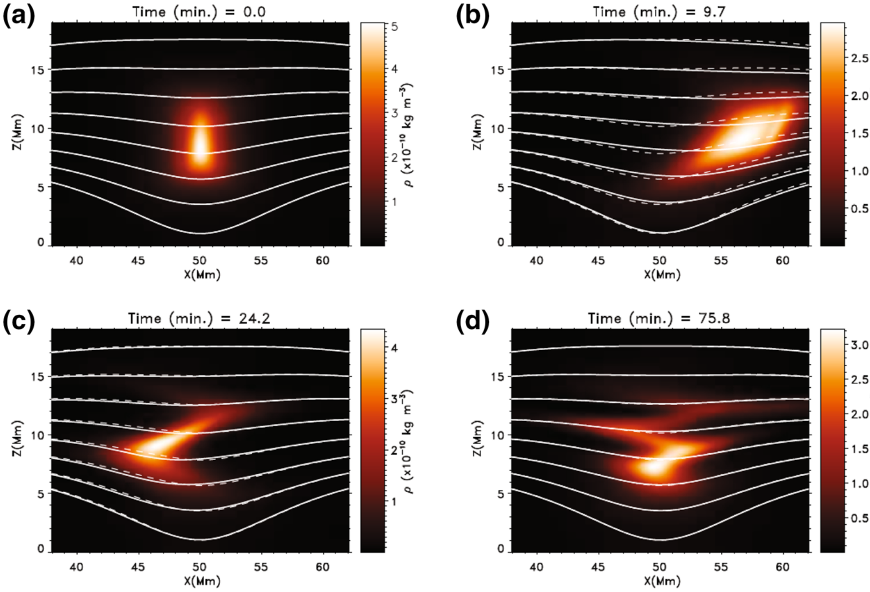

Fig. 6 Time evolution of prominence mass (in colours) and magnetic structure (white lines): **a** for $t = 0$; **b** maximum displacement of prominence mass attained; **c** phase difference between different parts of prominence mass; **d** zig–zag motion of the prominence mass. Time of each frame is shown at its top. Cartoon showing the wave-prominence and wave-filament interaction processes triggering transverse and longitudinal oscillations, respectively. Image reproduced with permission from Luna et al. (2016b), copyright by AAS

this reversal is not in phase for the whole structure and the motions of different parts are out of phase having opposite directions, which suggests that plasma oscillates along the magnetic field with different periods forming a continuous spectrum (Terradas et al. 2013). On the other hand, the magnetic structure does not suffer important changes during the development of the oscillations. The results also show that longitudinal oscillations display a strong damping, whose nature has not been explored, and that the damping times are different for different parts of the structure, being shorter at the bottom part. Regarding the period of the longitudinal oscillations, it increases with height and the obtained values are in agreement with Eq. (4) for heights which include the major part of the prominence mass. However, for greater heights the agreement disappears, which could be due to the role played by the pressure gradient in the restoring force. The agreement found between the numerical results and the Luna and Karpen (2012) theoretical model provides with a tool to determine the curvature radius of the magnetic field lines and, therefore, to perform filament seismology. On the other hand, Luna et al. (2016a) have studied the influence of cross-sectional area variations along a flux tube, which contains a prominence thread and is surrounded by the hot corona, on the longitudinal oscillations. These authors have found that these variations do not affect in a significant way to the oscillations, which validates the pendulum model (Luna and Karpen 2012; Luna et al. 2012a).

Zhang et al. (2012) performed 1D radiative hydrodynamic numerical simulations assuming a dipped magnetic field. In the simulation, a background heating is imposed to maintain the corona-chromosphere structure, and a further localised heating is added at the chromospheric level at the two footpoints of the magnetic field line. Then, chromospheric plasma is heated and evaporated into the corona and once a thermal instability starts in the corona the evaporated mass cools down and condenses forming the prominence. Later, the localised heating is switched off and an oscillation is excited with an initial velocity of 40 km s^{-1}. Zhang et al. (2012) compared the results of the simulations with the oscillations in the active region prominence observed on 2007, February 8 and found that while the oscillatory period was similar, the damping time was 1.5 times greater than the observed one. The restoring forces of the oscillations were assumed to be the field-aligned component of gravity and the gas pressure gradient, however, from the simulations they concluded that the main restoring force is the gravity component. In these simulations, the damping mechanisms were thermal radiation and heat conduction, although they could not fully explain the observed damping.

With the help of radiative hydrodynamic numerical simulations, Zhang et al. (2013) performed a parametric study, which included chromospheric heating duration, initial velocity and field line geometry, of longitudinal oscillations in a filament. The oscillations were excited either by a velocity perturbation or by an impulsive heating near one of the footpoints of the magnetic configuration. The results indicated that the oscillatory period did not strongly depend on the trigger mechanism and only showed a weak dependence on the length and height of the prominence, and on the amplitude of the perturbations. Also, a scaling law for the damping time was obtained which showed a strong dependence on the length, the geometry of the magnetic dip and the width. These results allowed to conclude that the oscillations depend on the prominence itself and the magnetic field configuration, although in the case of the impulsive heating only four percent of the energy is converted into kinetic energy of the prominence. Regarding the restoring force, these authors concluded, again, that the field-aligned component of gravity was dominant over gas pressure gradient, and that only when the prominence is short gas pressure gradient plays a role. Using this conclusion, an expression for the oscillatory period could be computed which gave the same expression obtained by Luna and Karpen (2012), consistent with the linear theory of a pendulum. Finally, from the simulations they concluded that non adiabatic processes, such as radiative losses, were responsible for the observed damping, although mass drainage from the prominence to the chromosphere would also contribute significantly to the damping. The above reported numerical simulations assume that there is only one dip in the magnetic field line in which the filament thread is located. However, some theoretical models have suggested the existence of double dips along a magnetic field line, which would allow the presence of two separate threads interacting with each other through oscillations. Using this magnetic configuration, Zhou et al. (2017) have performed 1D radiative hydrodynamic numerical simulations including optically thin radiation, thermal conduction and a heating term, which decays exponentially with distance, helping to maintain the hot corona. The formation of threads in the magnetic dips is produced by increasing the density and decreasing the temperature along the two dips and, once an equilibrium state is reached, the threads are perturbed by imposing a velocity perturbation on them. For this study, Zhou et al. (2017) considered three different cases: identical dips and initial perturbation imposed in only one thread; two differents dips and initial perturbation imposed in only one thread; and two different dips and perturbations imposed simultaneously in both threads, then, the results allow to extract conclusions about the behaviour of period and damping time of the oscillating threads. For instance, in the first case, energy is pumped from the active (initially excited) to the passive thread, and the oscillation of the passive thread decays very slowly with a damping time much longer than in the case of a single dip, furthermore, after some time, the oscillations of both threads become synchronous. When two threads on non-identical dips are perturbed simultaneously, the oscillation of the thread with shorter period (smaller curvature radius) decays quickly and, after a few periods, keeps almost the same amplitude. This means that energy is initially transferred from the shorter period thread to the longer period thread whose oscillatory behaviour can be fitted with a decaying sine function while its damping time increases because of the thread–thread interaction. However, in order to explain the almost constant amplitude of the shorter period thread it is suggested that, later on, kinetic energy is transferred back from the longer period thread to the shorter period thread. As a consequence, its oscillation becomes almost decayless and can not be fitted either by a decaying sine function or a Bessel function. This would mean that dissipative or radiative losses from the shorter period thread are compensated by this input of energy. In general, although there are some exceptions, while the damping time of each oscillating thread is affected by the thread–thread interaction, the period of the filament longitudinal oscillation is only slightly affected by this interaction. These results point out the need to have a good knowledge of the filament magnetic configuration, since it could be of great importance for the interpretation of the observed oscillatory behaviour and to perform seismological studies.

Another model for longitudinal oscillations, providing with an explanation for the triggering process and the restoring force, was proposed by Vršnak et al. (2007). These authors reported on H_α observations of time damped large amplitude periodical plasma motions along the axis of a filament. The model by Vršnak et al. (2007) was based on the fitting of the oscillation properties to a mechanical analogue model in terms of the classic damped harmonic oscillator equation. This analogue was first used to discard gas pressure as the restoring force, since it leads to sound speed values one order of magnitude larger than those corresponding to the typical temperature of prominence plasmas, and no signature of plasma at those temperatures was observed in TRACE EUV images. In this work, a twisted flux rope model with both axial and azimuthal magnetic field components was considered and an excess azimuthal field at one of the prominence legs was assumed. This gives rise to a magnetic pressure gradient and a torque, which in turn drive a combined axial and rotational motion of the plasma. After linearising the equation of motion, they obtained

$$\ddot{X} = -\frac{2v_{A\varphi}^2}{L^2}X, \tag{6}$$

with X the longitudinal displacement in dimensionless form and $\omega_0^2 = 2v_{A\varphi}^2/L^2$. Then, Eq. (6) provides with an expression for the period, $P = \sqrt{2}\pi L/v_{A\varphi}$, as a function of the Alfvén speed ($v_{A\varphi}$) associated with the poloidal field and the length of the filament (L). However, and such as can be seen from Eq. (6), these authors did not make any assumption for the damping mechanism of the oscillations. On the other hand, and taking into account that the reported oscillations were of large amplitude, Vršnak et al. (2007) considered the case of non-linear oscillations obtaining the following equation of motion,

$$\ddot{X} = -\frac{\omega_0^2 X}{(1 - X^2)^2}, \tag{7}$$

Then, when different initial amplitudes are considered for a fixed period, this quantity decreases when the amplitude increases, and the deviation with respect to the period of an harmonic oscillation becomes larger than 40%. Finally, it is worth to point out that the above described theoretical models (Luna and Karpen 2012; Vršnak et al. 2007) have been used to perform prominence seismology (see Sect. 8.1).

On the other hand, longitudinal oscillations have also been suggested as the origin of counter-streaming flows observed in prominences (Zirker et al. 1998). Thermal non-equilibrium models for filament mass formation (Xia et al. 2011; Luna et al. 2012a; Zhang et al. 2012) predict that after its formation, the cool condensations would oscillate around the magnetic dips. Therefore, counter-streaming might be understood in terms of an ensemble of out of phase oscillating threads.

4.4 Oscillations of line current models

A completely different approach, based on line current models of filaments, was taken by Oord and Kuperus (1992), Schutgens (1997a, b) and Oord et al. (1998) in order to study filament vertical oscillations. They used the model introduced by Kuperus and Raadu (1974), in which the prominence is treated as an infinitely thin and long line, i.e., without internal structure. The interaction of the filament current with the surrounding magnetic arcade and photosphere was taken into account. Furthermore, both normal (NP) and inverse polarity (IP) configurations were considered. When a perturbation displaces the whole line current representing the filament, that remains parallel to the photosphere during its motion, the coronal magnetic field is also disturbed and the photospheric surface current is modified. This restructuring affects the magnetic force acting on the filament current. As a consequence, either this force enhances the initial perturbation and the original equilibrium becomes unstable, or the opposite happens and the system is stable against the initial disturbance. As a further complication, Oord and Kuperus (1992), Schutgens (1997a, b) and Oord et al. (1998) took into account the finite travel time of the perturbations between the line current and the photosphere and investigated the effect of these time delays on the filament dynamics. For both NP and IP configurations, exponentially growing or decaying solutions were found.

Schutgens and Tóth (1999) considered an IP magnetic configuration in which the prominence is not infinitely thin but is represented by a current-carrying cylinder.

They solved numerically the magnetohydrodynamic equations assuming that the temperature has a constant value (10^6 K) everywhere. The inner part of the filament is disturbed by a suitable perturbation that causes the prominence to move like a rigid body in the corona, both vertically and horizontally, undergoing exponentially damped oscillations. Horizontal and vertical motions can be studied separately since they are decoupled. It turns out that the period and damping time of horizontal oscillations are much larger than those of vertical oscillations. Some remarks about the damping mechanism at work in these models are presented in Sect. 7.8.

Kolotkov et al. (2016) considered an equilibrium configuration similar to that in the works described above: the prominence line current is embedded in a coronal magnetic structure created by two photospheric line currents symmetrically placed with respect to the prominence current. Kolotkov et al. (2016) studied the linear oscillations of the system, so that horizontal and vertical motions are decoupled, and found stability conditions and the (stable) periods for the two orientations of motions. Depending on the parameter values of the model (prominence height, intensity of the photospheric and prominence line currents, separation of the photospheric currents) the prominence can be stable or unstable to vertical and/or to horizontal oscillations. It is found that the prominence can be simultaneously stable to oscillations in both directions when its current is larger than that of the photospheric sources and its height is smaller than half the distance between the photospheric currents.

4.5 Final remarks

Theoretical models developed to understand large amplitude oscillations, and to perform prominence seismology, can be classified in two different groups. For transverse (vertical or horizontal) oscillations, Hyder (1966) and Kleczek and Kuperus (1969) models are based on damped harmonic oscillators, with the restoring force supplied by the magnetic tension, and with different damping mechanisms. For longitudinal oscillations, Vršnak et al. (2007) and Luna and Karpen (2012) models have been considered although, taking into account observations and numerical simulations, the Luna and Karpen (2012) pendulum model seems to be the most suitable and, also, it allows to infer filament's geometry. However, oscillations with different polarisation (longitudinal and transverse) of the motions in the same filament have also been observed (Gilbert et al. 2008). An important issue, relevant for this type of oscillations, is to understand how are they generated. Probably, in all the cases, to obtain a full understanding we should resort to numerical simulations by considering that incoming linear or non-linear perturbations (waves) can strongly perturb the prominence global configuration causing the observed oscillations. Then, different situations such as: incidence angles of incoming perturbation; energy budget of the perturbation; distance from the prominence at which the perturbation is generated; background properties of the medium (magnetic field, density, inhomogeneity) in which the perturbation is travelling; amount of perturbation's energy which is trapped by the prominence, etc., could be studied in order to understand the polarisation of the induced oscillations and how are they damped. Finally, MHD models which involve the presence of oscillations have also been proposed. For instance, Sakai et al. (1987) developed a model for the formation of a prominence in a current sheet and one of its features was the presence of non-linear oscillations of the current sheet, while Bakhareva et al. (1992) considered a partially ionised plasma and developed a dynamical model for a solar prominence in which non-linear oscillations were also present; finally, Chin et al. (2010) considered possible oscillatory regimes of non-linear thermal over-stability which can occur in prominences.

5 Small amplitude oscillations: observational aspects

The main purpose of studying prominence oscillations is to obtain insight into their physics via a seismological approach (see Sect. 8). Therefore, the information that observations should provide with are the periods, wavelength, phase and group velocity and damping time of these phenomena. In addition, observations should also determine whether these periodic variations are standing oscillations or propagating waves, whether they affect some prominence threads or larger areas of a prominence, whether threads oscillate independently from their neighbours or which physical variables are disturbed and by which amount.

Attempts to detect prominence oscillations do not always yield positive results. For example, Harvey (1969) noted that in a sample of 68 non-active region prominences, 31% of the objects presented no significant velocity change along the line-of-sight, 28% showed apparently random line-of-sight velocity variations and 41% presented a definite oscillatory behaviour. Analogous results were obtained for a set of 45 active region prominences. Later, Engvold (1981) failed to detect oscillatory motions in the velocity field of a limb prominence, although the observational setup used prevented him from reliably distinguishing velocity amplitudes below 2 km s^{-1}, the range in which many peak values are found. In addition, Malherbe et al. (1981, 1987) recognised no oscillatory pattern in time series of line-of-sight velocities obtained with the MSDP operating on the Meudon solar tower, although positive results were later achieved using the same instrument (Thompson and Schmieder 1991). There are several reasons that may lead to the absence of periodic variations in some prominences when using spectroscopic techniques: the velocity amplitude or its projection along the line-of-sight may be too small to stand above the instrumental noise level; or the prominence material may actually not oscillate at the time the observations are performed; or the light emitted or absorbed by various plasma elements along the line-of-sight and having different oscillatory properties may result in a signal below the detection threshold.

Some authors have expressed concerns about the credibility of detected prominence oscillations with spectrograph slits. This led Balthasar et al. (1993) and Zapiór et al. (2015) to make simultaneous observations with two telescopes to firmly establish the solar origin of the oscillations. In both cases, only a few coinciding oscillatory periods were present in the two data sets, and so this can raise some concerns about the authenticity of prominence oscillations. In the first case, data acquisition in both telescopes (VTT and GCT in Tenerife, Spain) was done with the help of a spectrograph. Hence, it may be argued that the discrepancy of the results could have been caused by guiding errors. Zapiór et al. (2015), however, employed two-dimensional Doppler velocities obtained with the MSDP spectrograph of the Large Coronagraph (Białków Observatory, Poland) together with one-dimensional Doppler data from the HSFA-2 multichannel spectrograph of the Large Horizontal Telescope (Ondřejov Observatory, Czech Republic). Spectra were taken with the latter instrument by placing the spectrograph slit at three positions. After these data had been reduced, they were shifted to a common reference frame with the help of the two-dimensional MSDP data, hence eliminating possible alignment errors between the MSDP and HSFA-2 data sets. It was found that three particular periods (of 26, 31 and 55 min) were present in both data sets and so unquestionably originated in the prominence, but many other periodicities were exclusively present in only one of the two data sets, and for this reason were considered spurious. Hence, the main conclusion reached by Zapiór et al. (2015), beyond the particular periods observed, is that to confirm the solar origin of a periodicity, it must correspond to a coherent signal distributed over a prominence area, such as would be the case of a standing or a propagating wave.

5.1 Detection methods

The investigation of small amplitude prominence oscillations has most often been done by spectroscopic means, but also using images in specific spectral lines (e.g., Yi et al. 1991; Yi and Engvold 1991; Foullon et al. 2004; Lin 2005; Berger et al. 2008; Ning et al. 2009a, b; Hillier et al. 2013). Regarding these studies that make use of a two-dimensional field of view, in some of them the variations along selected straight paths have been analysed (Berger et al. 2008; Ning et al. 2009a, b; Hillier et al. 2013; Schmieder et al. 2013; Ofman et al. 2015). This simplifies the study but also reduces the amount of oscillatory information that can be derived (see Fig. 7).

Regarding spectroscopic observations, different setups have been used to gather the temporal variation of the spectral indicators and more complexity and refinement has been gained over the years. A very widely used method in the investigation of small amplitude prominence oscillations is to place a spectrograph slit on a prominence (a few examples from a very long list are Tsubaki and Takeuchi 1986; Suematsu et al. 1990; Balthasar et al. 1993; Balthasar and Wiehr 1994; Suetterlin et al. 1997). Then, this yields a time series of spectra on each slit position (see for example, Fig. 4 of Tsubaki and Takeuchi 1986), from which the temporal variation of the spectral indicators (Doppler shift, line intensity, integrated line intensity, line width) can be derived. These time series can be later analysed to obtain the period, wavelength, etc. of the oscillations (an example is shown in Fig. 5 of Tsubaki and Takeuchi 1986). Slit observations have also been conducted from space, using SOHO/SUMER (Blanco et al. 1999; Régnier et al. 2001) and SOHO/CDS (Pouget et al. 2006).

A spectroscopic observation using a slit yields restricted information on the spatial distribution of oscillations and, what is even worse, does not ensure that the slit is fixed during the observing time. The first of these concerns also applies to the analysis of images in which only variations in one direction are considered. Observations using a two-dimensional field of view and with high spatial resolution have diminished these worries, while allowing to study how prominence threads participate of the oscillatory motions. These observations have been conducted both with ground-based telescopes

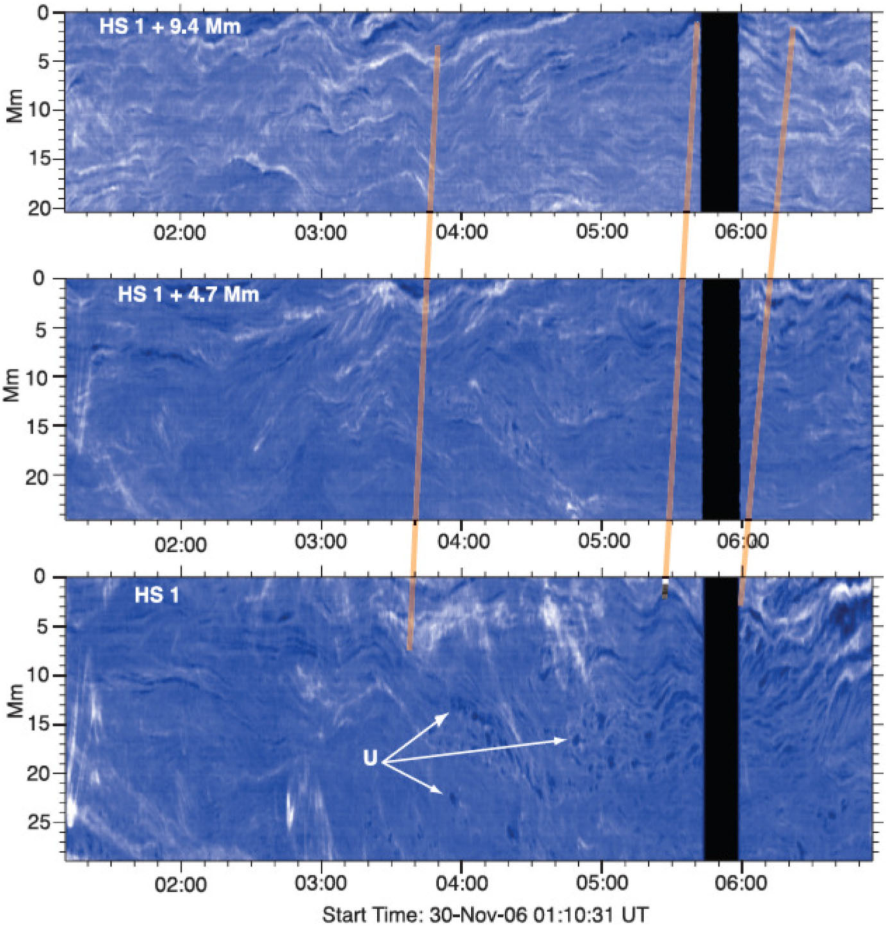

Fig. 7 Time slices taken at three heights in a quiescent prominence. The bright sinusoidal patterns are caused by horizontal oscillations of the plasma with periods between 20 and 40 min. The orange lines denote oscillations with phases that approximately match. The slope of these lines implies an upward propagation speed of about 10 km s^{-1} (projected on the plane of the sky). Image reproduced with permission from Berger et al. (2008), copyright by AAS

(Yi et al. 1991; Yi and Engvold 1991; Lin et al. 2003; Lin 2005; Lin et al. 2005, 2007, 2009) and with space-based telescopes (Okamoto et al. 2007, 2015); the relevant works are presented in Sect. 5.9.4. In addition, two-dimensional Dopplergrams have also been employed (Molowny-Horas et al. 1999; Terradas et al. 2002), although the spatial resolution of this particular observation is not good enough to appreciate the prominence thread structure; see Sect. 5.9.3.

Although most data used in the analysis of small amplitude prominence oscillations come from typical prominence lines, in some cases spectral lines formed at hotter temperatures have also been considered. Examples are the He I line at 584.33 Å, formed at 20,000 K (Régnier et al. 2001; Pouget et al. 2006); the Si IV and O IV lines at 1393.76

Å and around 1401–1405 Å, formed at transition region temperatures (Blanco et al. 1999; Okamoto et al. 2015); and 195 Å images, with a formation temperature of 1.5 MK (Foullon et al. 2004). Cool prominences or filaments can be identified in coronal lines since the line intensity is reduced by means of two different mechanisms: absorption and volume blocking (Anzer and Heinzel 2005). In the first case, coronal radiation coming from behind the cool structure is partially absorbed, while in the second case the volume filled with cool plasma does not contribute to coronal emission and in this region the radiative output is reduced as compared with the surrounding corona. These two mechanisms give place to a brightness reduction of coronal lines and allows us to identify the volume occupied by cool and dark structures like prominences or filaments. Arguably, oscillations in the dense prominence affect their rarer neighbourhood, so a joint investigation of the dynamics of the two media has a very promising seismological potential.

5.2 Spectral indicators

The vast majority of spectroscopic reports of prominence oscillations are based on the analysis of the Doppler velocity. Some other spectral indicators (line intensity and line width) have also been used in the search for periodic variations in prominences and sometimes a periodic signal has been recognised in more than one of these indicators. Landman et al. (1977) observed periodic fluctuations in the integrated line intensity and line width with period around 22 min, but not in the Doppler shift. In addition, Yi et al. (1991) detected periods of 5 and 12 min in the power spectra of the line-of-sight velocity and the line intensity. Also, Suematsu et al. (1990) found signs of a ~ 60 min periodic variation in the Doppler velocity, line intensity and line width. Nevertheless, the Doppler signal also displayed shorter period variations (with periods around 4 and 14 min) which were not present in the other two data sets. We here encounter a common feature of other investigations, namely that the temporal behaviour of various indicators corresponding to the same time series of spectra do not agree, either because they show different periods in their power spectra (as in Tsubaki et al. 1987) or because one indicator presents a clear periodicity while the others do not (Wiehr et al. 1984; Tsubaki and Takeuchi 1986; Balthasar et al. 1986; Tsubaki et al. 1988; Suetterlin et al. 1997). Only rarely have the oscillations been detected in several of these spectral indicators at the same time and with the same period, which constitutes a puzzling feature of prominence oscillations. This can be caused by insufficient instrumental sensitivity or by the effect different waves have on the plasma parameters (pressure, magnetic field, …), which in turn may give rise to perturbations of one spectral indicator alone. This issue has been addressed recently by Heinzel et al. (2014) and Zapiór et al. (2016), who computed synthetic hydrogen spectra of prominence oscillations by means of a combination of MHD and radiative transfer modelling (see Sect. 6.6).

Special mention must be made of the study performed by Balthasar and Wiehr (1994), who simultaneously observed the spectral lines He at 3888 Å, H_8 at 3889 Å and Ca^+IR_3 at 8498 Å. From this information they analysed the temporal variations of the thermal and non-thermal line broadenings, the total H_8 line intensity, the He 3888 Å to H_8 emission ratio and the Doppler shift of the three spectral lines. The power spectra of all these parameters yield a large number of power maxima, but only two of them (with periods of 29 and 78 min) are present in more than one indicator.

5.3 Trigger of small amplitude oscillations

So far it has not been possible to unambiguously identify the trigger of small amplitude oscillations. A popular conjecture about their excitation is that it lies in the periodic motions of magnetic fields caused by photospheric or chromospheric oscillations. The idea is that Alfvén waves ought to propagate upwards and that any prominence material threaded by the field should also be subject to periodic motions if there is enough energy available to overcome the inertia of the dense plasma (Harvey 1969); this idea was later suggested by other authors too (e.g., Yi et al. 1991). Harvey made order-of-magnitude calculations to show that the ratio of prominence to photospheric oscillatory energy is around or smaller than 10^{-4}, which indicates that this excitation mechanism is feasible. Much longer and shorter periods than those present in Harvey's work have been detected afterwards (see Sect. 5.4), so probably this mechanism of energy transfer from the photosphere (or chromosphere), if correct, may not be the only one to cause these prominence oscillations.

Hillier et al. (2013) gave evidence in this direction. In their study of transverse oscillations of vertical prominence threads observed with Hinode/SOT in H_α, they tracked 3436 oscillating features. Each of them was fitted with an attenuated sinusoid with a linearly varying period:

$$A_0 \exp(t/\tau) \sin\left[\frac{2\pi t}{P_0(1+Ct)} + S\right], \tag{8}$$

with A_0, τ, P_0, C and S the initial amplitude, exponential amplification/damping time, initial period, rate of variation of the period and phase. Figure 8 shows the derived velocity power spectrum as a function of frequency (symbols) compared with the power spectrum of horizontal photospheric motions derived from Matsumoto and Kitai (2010) (solid lines) and Chitta et al. (2012) (dashed lines). The agreement between the symbols and the two lines for frequencies ≤ 0.7 mHz led Hillier et al. (2013) to suggest that horizontal photospheric motions are the driver of these particular prominence waves. They added that further information is required to confirm that this agreement actually follows from a causal relationship between the two phenomena. Furthermore, prominence waves possess higher power than photospheric horizontal motions for frequencies ≥ 0.7 mHz. If the interpretation given by Hillier et al. (2013) is correct, then processes other than just horizontal photospheric motions trigger these higher frequency oscillations. It is worth noticing that Fig. 8 does not show enhanced power at either 3 or 5 mHz, which rules out p-modes as the main exciters of oscillations in this prominence.

Further evidence of the photospheric origin of some prominence oscillations was given by Li and Zhang (2013), who used SDO/AIA 171 Å data of a polar crown prominence observed during six consecutive days. In their sample of 58 barbs, all of them featured transverse oscillations, which in some cases were excited by propagating dis-

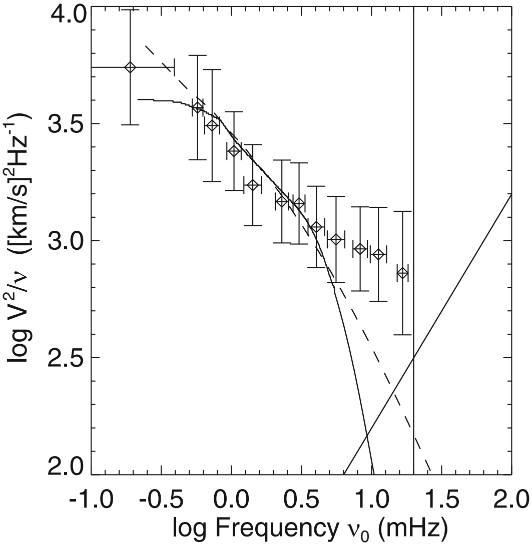

Fig. 8 Hinode/SOT H_α observation of transverse thread oscillations in a quiescent prominence. Velocity power spectrum for the prominence threads (symbols) and for the horizontal photospheric motions: solid line (Matsumoto and Kitai 2010) and dashed line (Chitta et al. 2012). To allow a comparison between the prominence and photospheric spectra, the later have been multiplied by $10^{1.1}$ and $10^{1.4}$, respectively. The two straight solid lines show the observational limits of detection. Image reproduced with permission from Hillier et al. (2013), copyright by AAS

turbances emitted by neighbouring small-scale photospheric brightenings. Moreover, Mashnich et al. (2009b, a) studied the Doppler velocity field in some filaments and the underlying photosphere by means of simultaneous observations of the H_β line and the neighbouring photospheric Fe I line at 4863 Å. They detected a quasi-hourly oscillation in certain areas of the filaments and photosphere and found a good spatial correlation between them. They also reported that the parts of the photosphere displaying this oscillation were often observed below filament barbs. The spatial coincidence of this periodicity and the relation of filament barbs and the photosphere led these authors to suggest that the photosphere was the origin of these particular prominence oscillations. From an observation of a limb prominence with Hinode/SOT, Ning et al. (2009b) reported that the detected oscillatory behaviour only lasted about one period and that new oscillations appeared nearby simultaneously. These authors then concluded that the exciters or drivers of such oscillations are numerous and of small scale.

5.4 Detected periods

Early observational studies of small amplitude prominence oscillations revealed a wide range of characteristic periods, ranging from a few minutes (Harvey 1969; Wiehr et al. 1984; Tsubaki and Takeuchi 1986; Balthasar et al. 1986), to 15–25 min (Harvey 1969; Landman et al. 1977), to 40–90 min (Bashkirtsev et al. 1983; Bashkirtsev and Mashnich 1984; Wiehr et al. 1984; Balthasar et al. 1986). The apparent tendency of periods to group below 10 min or in the range 40–90 min led to the distinction between short- and long-period oscillations to refer to these two period ranges. Later, more reports of periods in the range 10–40 min were published (e.g., Yi et al. 1991; Suetterlin et al. 1997; Blanco et al. 1999; Régnier et al. 2001) and the intermediate-period class emerged. However, this classification (solely based on the period value) is far

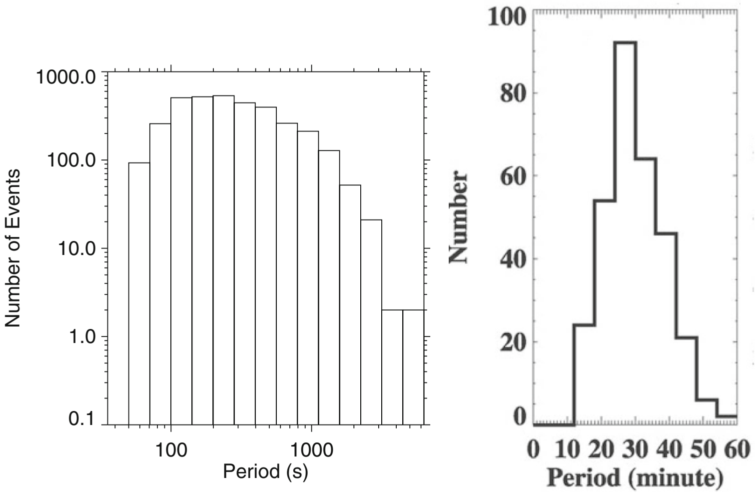

Fig. 9 Left: Hinode/SOT H_α observation of transverse thread oscillations in a quiescent prominence. Histogram of the initial period, P_0 of Eq. (8). Image reproduced with permission from Hillier et al. (2013), copyright by AAS. Right: SDO/AIA 171 Å observation of transverse oscillations of barbs belonging to a polar crown prominence. Histogram of the period. Image reproduced with permission from Li and Zhang (2013), copyright by Springer

from complete: Balthasar et al. (1993) observed a prominence simultaneously with the GCT and VTT telescopes in Tenerife to remove doubts about the instrumental or atmospheric origin of prominence oscillations and obtained strong power in the Doppler shift from both telescopes with period around 30 s; hence, very short-period small amplitude oscillations also exist. Furthermore, a few works in which prominences have been observed from space during extended time intervals show that very long-period oscillations also exist: Pouget et al. (2006) detected periodicities of 5–6 h, while Foullon et al. (2004) and Foullon et al. (2009) have observed variations in EUV filaments with periods around 12 and 10–30 h, respectively. Although the classification in terms of short-period, long-period, etc. oscillations is still in use, it does not cast any light nor gives any help with regard to the nature, origin or exciter of the oscillations (see Sect. 2).

At this point it may seem that a prominence can only sustain a few oscillatory periods, but Hillier et al. (2013) (see Sect. 5.3 for more information on their observation and data analysis) proved that the threads of a single prominence can support a wide range of periods: from 50 s (the minimum value permitted by the analysis method used) to 6000 s, although one may wonder if threads can live long enough to sustain such long period oscillations. The period distribution shows no preference for values around 3 or 5 min: see Fig. 9 (left). More evidence on the ability of prominences to support many periodicities comes from the study of a polar crown prominence in which 58 barbs underwent transverse periodic motions (Li and Zhang 2013). The period distribution, presented in Fig. 9 (right), covers the range 12.6–54.6 min. One can think of several reasons for this variety of periods: it is possible that the detected events are driven by, e.g., photospheric motions. In such a case, the oscillatory period

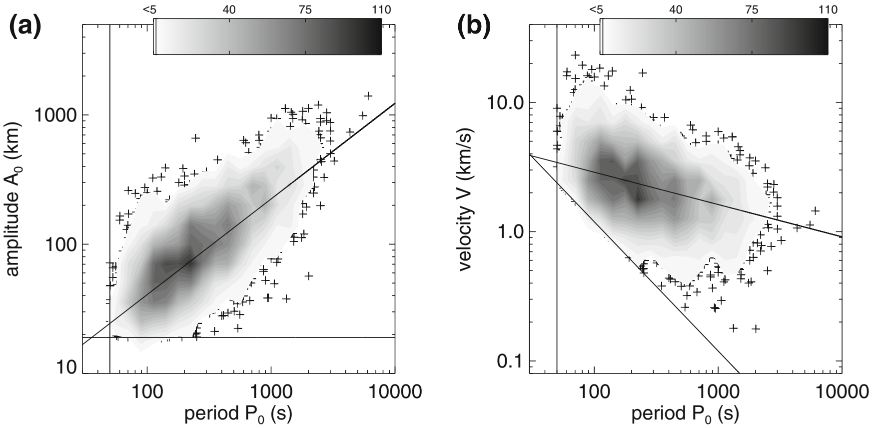

Fig. 10 Hinode/SOT H_α observation of transverse thread oscillations in a quiescent prominence. Correlations between **a** the displacement amplitude and initial period and **b** velocity amplitude and initial period. The density of points is displayed as a contour plot, with plus signs showing the positions of individual points in low density regions. Solid lines through the middle of the contour plots represent the power-laws fitted to the data: **a** $A_0 = 10^{0.13\pm0.02} P_0^{0.74\pm0.04}$ and **b** $V = 10^{0.96\pm0.02} P_0^{-0.25\pm0.04}$. The other two lines show the observational limits of detection. Image reproduced with permission from Hillier et al. (2013), copyright by AAS

revealed by the dense structure is a consequence of the driving period. On the other hand, if oscillations are impulsively triggered then their periods correspond to those of the excited normal modes, which depend on the intrinsic properties of each thread or barb. Furthermore, structural changes can take place that can modify the (normal mode) oscillatory period of a barb or a thread, specially in the very long (6 days) observations of (Li and Zhang 2013). The last hypothesis may not be true in some occasions, in which a given prominence has been observed over a few consecutive days and the outcome is that the same period seems to be recovered (Bashkirtsev and Mashnich 1984; Mashnich and Bashkirtsev 1990; Suetterlin et al. 1997). This seems to indicate that the overall properties of these prominences did not change much over this time interval. Similar studies have not been carried out afterwards.

5.4.1 Correlations between period and other parameters

Some authors have tried to find correlations of the periods of small amplitude oscillations with other parameters. Hillier et al. (2013) found a very clear correlation between the period and amplitude of 3436 transverse thread oscillation events (Fig. 10). In this work evidence is presented in favour of these oscillations being triggered by horizontal photospheric motions (see Sect. 5.3). The correlations of Fig. 10 then would suggest that short (long) period photospheric motions drive transverse thread oscillations of smaller (larger) amplitude.

Harvey (1969) reported a correlation of the period with the unperturbed longitudinal magnetic field, such that long periods are associated with strong field strengths (Fig. 11). This dependence is difficult to understand since, other parameters being

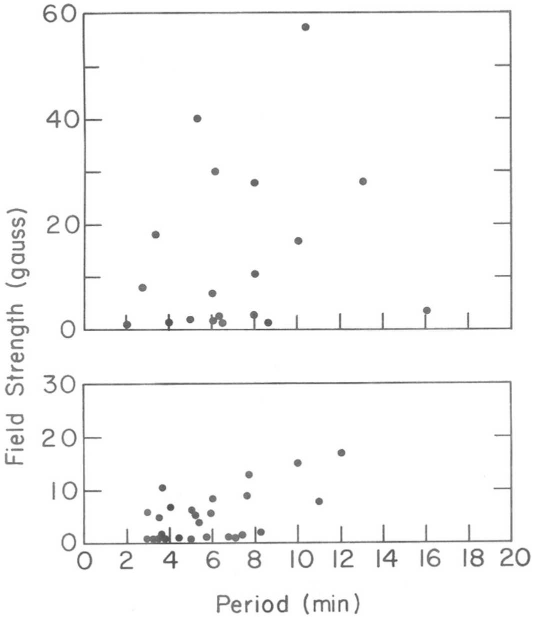

Fig. 11 Period of prominence Doppler velocity oscillations as a function of the line-of-sight magnetic field strength. The top and bottom panels correspond to active region and non-active region prominences, respectively. Image reproduced with permission from Harvey (1969)

equal (density, magnetic field line length, etc.), one expects just the inverse behaviour for fast MHD waves, and no dependence of the period on the magnetic field strength for slow MHD waves.

Bashkirtsev and Mashnich (1993) claimed that the period of oscillation depends on solar latitude. Only periods above 40 min were included in this study and some 40 observations gathered along more than eight years were taken into account. The question then is whether this latitudinal dependence, if real, is related to the solar activity cycle or not. In a subsequent work by Mashnich and Bashkirtsev (1999), a similar latitudinal dependence was obtained for the quasi-hourly oscillations of the photosphere and chromosphere. The implications of these findings are profound and further checks are essential before their reality is firmly demonstrated.

5.5 Oscillatory amplitude

The detected peak Doppler velocity usually ranges from the noise level (down to 0.1 km s^{-1} in some cases) to 2–3 km s^{-1} (e.g., Harvey 1969), although larger values have also been reported (e.g., Bashkirtsev and Mashnich 1984; Molowny-Horas et al. 1999; Ning et al. 2009a).

The statistical study of Hillier et al. (2013), that has already been discussed in Sects. 5.3 and 5.4, provides with valuable information about the distribution of amplitudes in a quiescent prominence. Figure 12 (top) displays histograms of the displacement and velocity amplitudes. They range from 19 to 1400 km and from 0.2 to 23 km s^{-1}, respectively, and have predominant values below 200 km and 5 km s^{-1}.

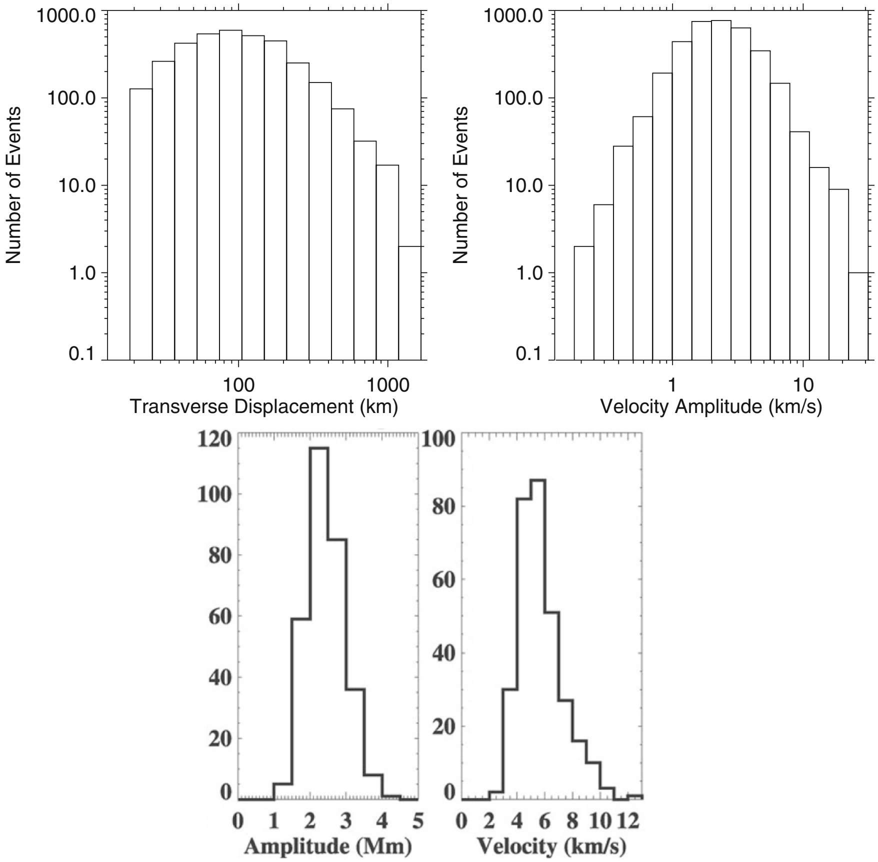

Fig. 12 Top: Hinode/SOT H_α observation of transverse thread oscillations in a quiescent prominence. Image reproduced with permission from Hillier et al. (2013), copyright by AAS. Bottom: SDO/AIA 171 Å observation of transverse oscillations of barb belonging to a polar crown prominence. Image reproduced with permission from Li and Zhang (2013), copyright by Springer. Histograms of (left) displacement amplitude and (right) velocity amplitude

Another statistical study, by Li and Zhang (2013) on transverse oscillations of 58 barbs, also reveals a large spread of displacement and velocity amplitudes; see Fig. 12 (bottom). In particular, these parameters are in the range 1.2–4.2 Mm and 2.9–12.4 km s^{-1}, respectively. Li and Zhang (2013) noted that the oscillatory amplitude was in general considerably larger than the barb width in the 171 Å images. The spatial resolution of these images probably makes it impossible to detect smaller amplitude oscillations, such as those identified by Hillier et al. (2013).

5.6 Spatial distribution of oscillations

It now appears well established that small amplitude, periodic changes in solar prominences do not normally affect the whole object at a time, but are of local nature instead,

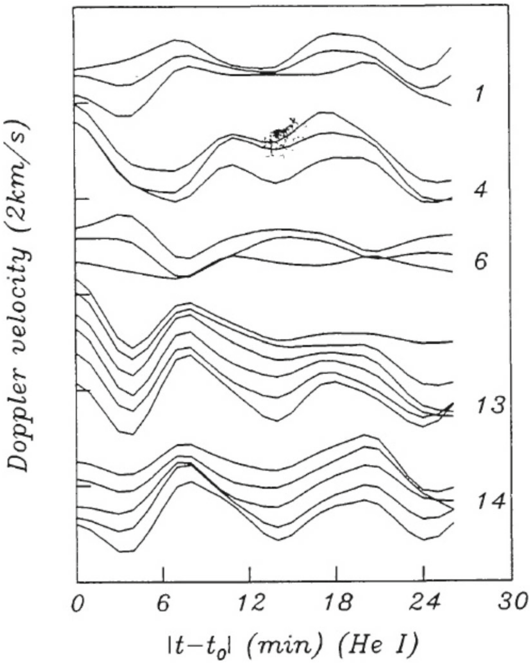

Fig. 13 Temporal variation of the Doppler velocity along threads of a solar filament. Numbers on the right label the various threads. For each thread, the curves correspond to the Doppler velocity measured at different points along the thread. Image reproduced with permission from Yi et al. (1991), copyright by Springer

and that this conclusion is independent of the oscillatory period; see Sect. 2. Hence, it is usually found that only a few consecutive points along the spectrograph slit present time variations with a definite period, while all other points lack any kind of periodicity (e.g., Tsubaki and Takeuchi 1986; Suematsu et al. 1990; Balthasar et al. 1993; Balthasar and Wiehr 1994; Suetterlin et al. 1997; Molowny-Horas et al. 1997).

Obviously, a two-dimensional data set is much more advantageous when it comes to ascertaining which part of a prominence is affected by oscillations. Terradas et al. (2002) reported on the propagation of waves over a large region (some 54,000 km by 40,000 km in size) in a limb prominence and high spatial resolution observations with Hinode/SOT (Berger et al. 2008) also show oscillations that affect a small area of a prominence. See also the discussion in Sect. 5.9.4 of the work by Lin et al. (2007) that gives evidence of coherent Doppler shift oscillations over a rectangular area $3.4'' \times 10''$ in size.

Other observations with high spatial resolution have shown that individual threads or small groups of threads may oscillate independently from the rest of the prominence with their own periods (Thompson and Schmieder 1991; Yi et al. 1991). Figure 13 displays some of the results in Yi et al. (1991). It is clear that thread groups 1, 4, 13 and 14 oscillate in phase with their own period, which ranges from 9 to 14 min. In addition, Tsubaki et al. (1988) obtained successively two time series of spectra by placing the spectrograph slit first at a height of 30,000 km above the solar limb and next 40,000 km above the limb. A group of vertical threads detached from the prominence main body displayed 10.7-min periodic variations at both heights, which was a first indication that threads can oscillate collectively. After these preliminary studies, much attention has been given to the detection of thread oscillations (Lin et al. 2003; Lin 2005; Lin et al. 2005, 2007, 2009; Okamoto et al. 2007; Ning et al. 2009a, b; Okamoto et al. 2015). Apart from reporting on thread oscillations, these works have also given detailed information about wave features such as the period, wavelength and phase speed. Because of the importance of these quantities in the seismology of prominences, these works are discussed in more detail in Sect. 5.9.4.

There is also some evidence that velocity oscillations are more easily detected at the edges of prominences or where the material seems fainter, while they sometimes look harder to detect at the prominence main body (Tsubaki and Takeuchi 1986; Tsubaki et al. 1988; Suematsu et al. 1990; Thompson and Schmieder 1991; Terradas et al. 2002). This result has occasionally been interpreted as the consequence of integrating the velocity signals coming from various moving elements along the line-of-sight. This explanation, however, would imply the presence of broader spectral lines at the positions showing periodic variations, which is not observed, so other explanations are also possible (Suematsu et al. 1990). Mashnich et al. (2009b, a) gave evidence that different parts of filaments may support different periodicities: short-period variations (with periods shorter than 10 min) had coherence scales shorter than $10''$ and were detected near the edges of filaments placed close to the Sun's central meridian. These oscillations, hence, were characterised preferentially by vertical plasma displacements. On the other hand, variations with period around 1 h occured in different positions of the filament and the size of the oscillating area was not larger than 15–$20''$. In addition, these oscillations had an amplitude that increased by an order of magnitude or more in filaments far from the solar centre compared to those near the centre of the Sun's disk. Then, these oscillations showed a mainly horizontal velocity.

More information about the spatial distribution of prominence oscillations comes from Ning et al. (2009b), who detected transverse oscillations of 13 threads in a quiescent prominence observed with Hinode/SOT. These authors found that prominence threads in the upper part of the prominence oscillate independently, whereas oscillations in the lower part of the prominence do not follow this pattern. Furthermore, the oscillatory periods were short (between 210 and 525 s), with the dominant one appearing at 5 min (more information is given in Sect. 5.9.4). In a subsequent work, Ning et al. (2009a) used the same data set to analyse the motions of two spines in the same quiescent prominence. The spine is synonymous with the horizontal fine structure along the filament axis and is the highest part of the prominence. In the observations of Ning et al. (2009a), the spines showed drifting motions that were removed by the subtraction of a linear trend, which allowed the authors to uncover the existence of oscillations with a very similar period (around 98 min) in both structures. Further insight into the behaviour of the spines comes from a fit of a function $A[0]\sin(2\pi t/A[1]+A[2])\exp(A[3]t)$ to the detrended data. Here $A[0]$ is the oscillatory amplitude, $A[1]$ the period, $A[2]$ the oscillatory phase and $-1/A[3]$ the damping time. The detrended signals and the function fits are displayed in Fig. 14, which includes the fitted parameters, that give the following information: from the oscillatory amplitude, the peak velocities of the spines are 1 and 5 km s^{-1}. The periods are almost identical (96.5 and 98.5 min) and the phase difference is 149°, which means that the spines oscillated almost in anti-phase. These results about the period and phase were taken by Ning et al. (2009a) as an indication of a collective behaviour of the two

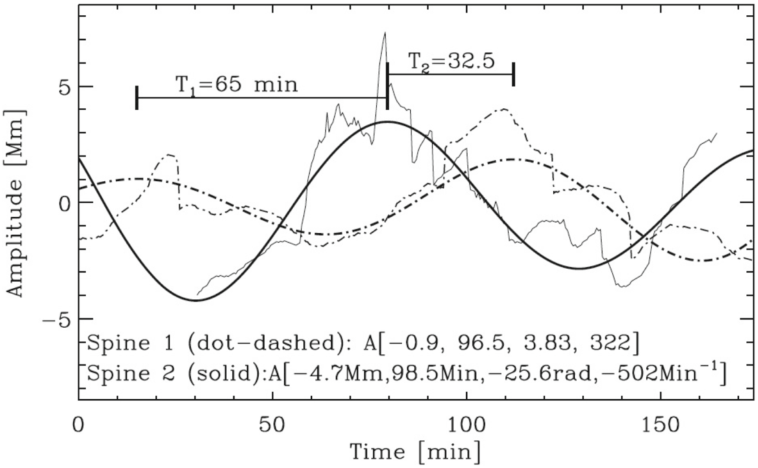

Fig. 14 Displacement of two spines of a quiescent prominence (thin lines) and best fits using the function $A[0]\sin(2\pi t/A[1] + A[2])\exp(A[3]t)$ (thick lines). The fitted values of the parameters $A[0]$ to $A[3]$ are written at the bottom of the figure. Note that the values of $A[3]$ displayed in the figure cannot be correct since they give a very strong amplification/damping that totally disagrees with the almost undamped behaviour of the thick lines. Image reproduced with permission from Ning et al. (2009a), copyright by AAS

structures. These authors considered an analogy with the transverse MHD oscillations of two cylinders (a problem studied by Luna et al. 2008, and discussed in Sect. 6.3) and concluded that a coupling of kink-like modes can give the observed behaviour. In particular, the A_x mode of the system (see Sect. 6.3.2 and Fig. 47) has motions resembling the anti-phase oscillatory behaviour found by Ning et al. (2009a).

5.7 Polarisation of wave motions

The use of spectral techniques alone (as in the vast majority of observational works on small amplitude oscillations) only allows to determine the presence of a velocity component parallel to the line-of-sight. This information can be used to conjecture about the orientation of plasma motions with respect to the prominence sheet (e.g., longitudinal, transverse) or thread (horizontal, vertical or inclined), but no firm conclusion on the three-dimensional direction of motions can be reached.

Using data from the Swedish 1-m Solar Telescope in La Palma, Lin et al. (2009) performed a novel analysis of thread oscillations by combining simultaneous recordings of motions along the line-of-sight and in the plane of the sky, which provides with information about the orientation of the oscillatory velocity vector. From the measurements of swaying motions in the plane of the sky, several threads in this work presented travelling disturbances whose main features were characterised (period, phase velocity and oscillatory amplitude). Moreover, two of the previous threads also showed Doppler velocity oscillations with a period similar to that of the swaying motions, so that the threads had a displacement that was neither in the plane of the sky nor along the line of sight. By combining the observed oscillations in the two orthogonal directions, Lin et al. (2009) derived the full velocity vectors. They suggested that thread oscillations were probably polarised in a fixed plane that may attain various orientations relative to the local reference system (for example, horizontal, vertical or inclined). In the case of the two analysed threads, a combination of the observed velocity components yielded an orientation of the velocity vectors of 42° and 59° with respect to the plane of the sky. Once the heliocentric position of the filament was taken into account, these angles transformed into oscillatory motions which were reasonably close to the vertical direction. Lin et al. (2009) alerted that this conclusion is based on only two cases and that it is not possible to draw any general conclusion about the orientation of the planes of oscillation of filament threads. In fact, Yi and Engvold (1991) found no centre-to-limb variations of the velocity amplitude of threads displaying Doppler velocity oscillations, so they concluded that there did not seem to be a preferred direction of oscillatory motions in their data set.

The work of Okamoto et al. (2015) is analogous to that of Lin et al. (2009) in that an analysis of simultaneous thread oscillations in the plane of the sky and along the line-of-sight was carried out. In the case of Okamoto et al. (2015), however, two instruments were used to acquire the data: plane of the sky displacements were determined from Hinode/SOT Ca II H images while Doppler velocities came from spectra taken with IRIS in the Mg II k line. A novelty of this paper is that these two quantities are plotted together (Fig. 15) so that their relative temporal phase can be examined. Based on the visual inspection of these results (Fig. 15), Okamoto et al. (2015) claim that this phase takes values between 90° and 180° and explain this in terms of resonant absorption (see Sect. 7.3.1).

The work of Mashnich et al. (2012) also gives some insight into the orientation of oscillatory motions. These authors used a combination of plane of the sky position and Doppler velocity to study small amplitude oscillations of two filaments (one of these two data sets had already been analysed by Mashnich et al. 2009b). The position of minimum intensity along the spectrograph slit was taken as a proxy for the filament position. Mashnich et al. (2012) found that the two filaments presented quasi-hourly oscillations (more precisely with 56 and 50 min periods) both in the plane of the sky and in the Doppler velocity. One can then deduce that in these events the velocity vector of the filament oscillations is well determined. Furthermore, Mashnich et al. (2012) noted that the amplitude of these quasi-hourly oscillations of the Doppler velocity can decrease by a factor 2–3 as the filament approaches the central meridian, which would favour the interpretation of these events as horizontal, transverse oscillations of the filaments. The thread oscillations of Lin et al. (2009) and the filament oscillations of Mashnich et al. (2012) would then have completely different polarisations.

5.8 Wave damping and oscillation lifetime

A visual inspection of the data sometimes reveals the existence of outstanding periodic variations and use of the FFT, or even better the periodogram (which yields an increased frequency resolution), is only necessary to derive a precise value of the period. In such cases it usually turns out that the oscillatory amplitude tends to decrease in time in such a way that the periodicity totally disappears after a few periods (e.g., Landman et al.

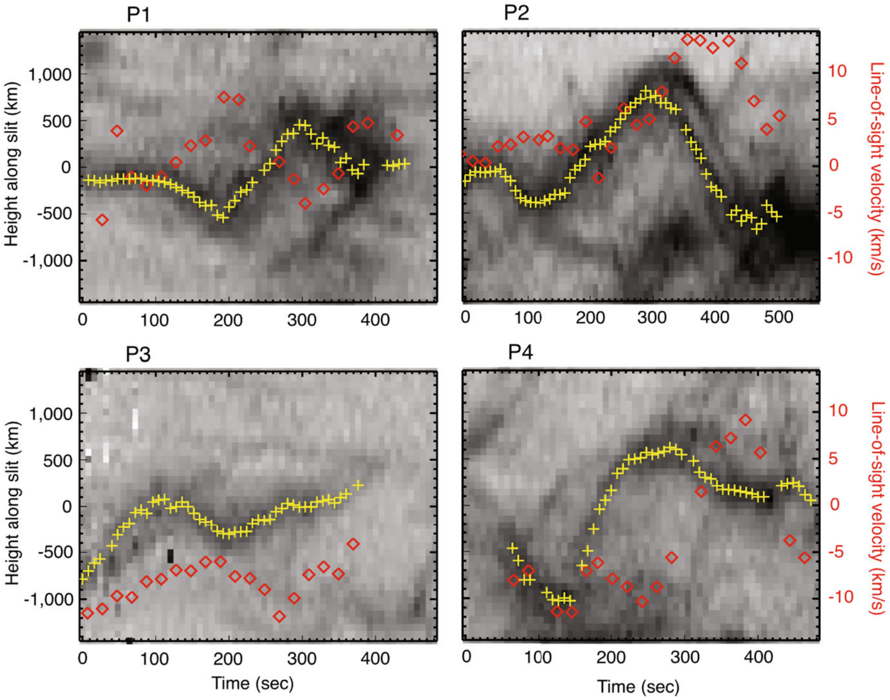

Fig. 15 Thread oscillations simultaneously detected with Hinode and IRIS. Each panel presents a space-time plot (grey scale) at a fixed prominence position from Hinode/SOT Ca II H images. The yellow crosses denote the central position of the threads. Moreover, the red diamonds give the line-of-sight velocity, at the same position, obtained from IRIS spectra in the Mg II k line. Image reproduced with permission from Okamoto et al. (2015), copyright by AAS

1977; Tsubaki and Takeuchi 1986; Wiehr et al. 1989; Molowny-Horas et al. 1999; Terradas et al. 2002; Lin 2005; Berger et al. 2008; Ning et al. 2009a, b), just as found in large amplitude oscillations. This is then interpreted as a sign of wave damping, although the specific mechanism has not been commonly agreed on (see Sect. 7 for a summary of theoretical results on this topic).

Reliable values of the damping time, τ, have been derived by Molowny-Horas et al. (1999) after fitting the function $v_0 \cos(\omega t + \phi) \exp(-t/\tau)$ to Doppler velocity time series recorded simultaneously in different positions of a polar crown prominence (Fig. 16). The values of τ thus obtained are usually between 1 and 4 times the corresponding period, in agreement with previous observational reports. In addition, there is one particular case for which the line-of-sight velocity grows in time, but no interpretation of this result is given by these authors.

Terradas et al. (2002) performed a deeper investigation of the data of Molowny-Horas et al. (1999). After fitting the same sinusoidal function to all points in the two-dimensional field of view, Terradas et al. (2002) generated two-dimensional maps of various oscillatory parameters, such as the period, damping time and velocity amplitude (Fig. 17). Terradas et al. (2002) stressed that there is a region near the prominence edge (54,000 km by 40,000 km in size) in which the correlation coefficient of the fit is

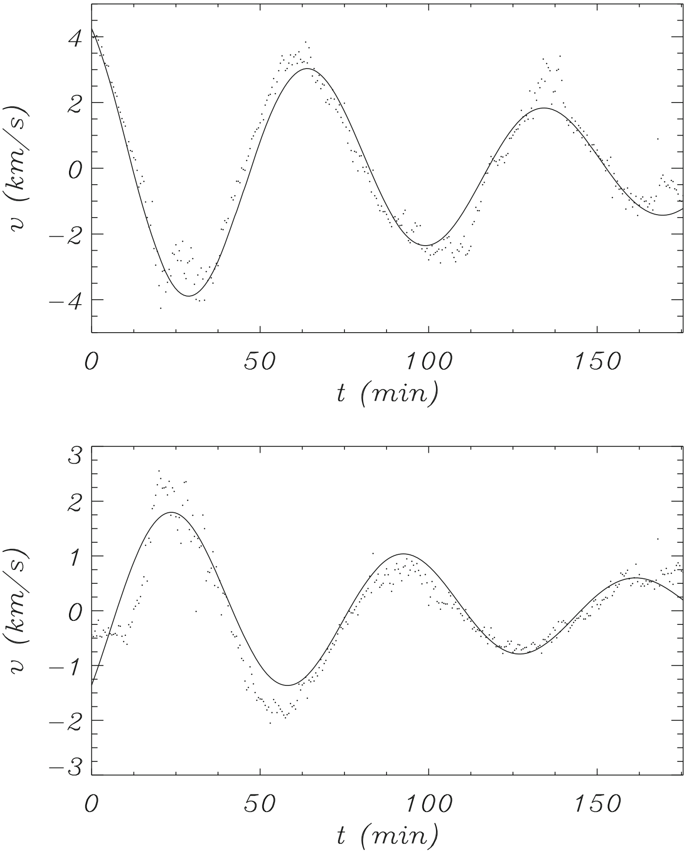

Fig. 16 Observed Doppler velocity (dots) and fitted function (continuous line) versus time at two different points in a quiescent prominence. The period is 70 min in both points and the damping time is 140 and 101 min, respectively. The function fitted to the observational data is of the form $v_0 \cos(\omega t + \phi) \exp(-t/\tau)$. Adapted from Molowny-Horas et al. (1999)

rather large and in which the period and damping time are very uniform. The mentioned region is around position $x = 80$, $y = 50$ of Fig. 17. In Sect. 5.9.3 we discuss other aspects of this work, which is unique since it is one of a few in which coherent wave behaviour has been found in a large area of a prominence and the only one in which the wave parameters in a two-dimensional prominence area have been computed.

Very often the presence of a periodic signal in the data is not obvious under a visual scrutiny and the FFT or periodogram simply give the period of such signal, but not its duration. Dividing the time series into shorter intervals and calculating the Fourier spectrum of each of them allows to narrow down the epoch of occurrence of the oscillation. Wiehr et al. (1984) followed this procedure and determined that a 3-min oscillation found in a 2-h Doppler velocity record only existed in the last 40 min of the sample. The wavelet technique, however, is much better suited for the calculation of lifetimes since it can be used to precisely determine the beginning and end of the time interval in which a periodicity, previously detected in the Fourier spectrum, takes

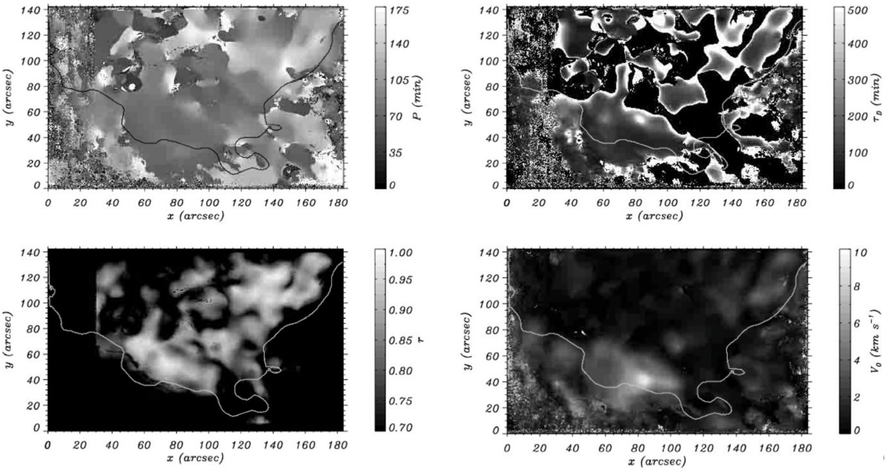

Fig. 17 Results of fitting the function of Fig. 16 to the Doppler velocity in the whole two-dimensional field of view. The spatial distribution of the fitted period and damping time is shown in the top panels, while that of the correlation coefficient and fitted amplitude is displayed in the bottom panels. The continuous white line (black in the top left panel) represents the approximate position of the prominence edge. The photosphere is slightly outside the image top. Image reproduced with permission from Terradas et al. (2002), copyright by ESO

place. This approach was used by Molowny-Horas et al. (1997), who obtained a period around 7.5 min in 16 consecutive points, spanning a distance of 7300 km, along the spectrograph slit. The time/frequency diagram of the corresponding 16 time signals indicates that the periodic perturbation is not present for the whole duration of the data and that it only operates for about 12 min (Fig. 18). Molowny-Horas (1998) performed a similar study by placing the slit on a filament, rather than on a limb prominence, with comparable results. Two oscillations with periods around 2.7 and 12.5 min were present at consecutive points covering some 2000 and 3300 km, respectively. From the wavelet analysis, the lifetimes of these two perturbations are of the order of 10 and 20 min, respectively. These results provide with convincing evidence of the train-like character of some prominence oscillations. Further details of the work by Molowny-Horas et al. (1997) are given in Sect. 5.9.2.

Oscillations of prominence threads also display fast attenuation. For example, Lin (2005) detected several periodicities over large areas of a filament, with maximum power at periods of 26, 42 and 78 min. Pronounced Doppler velocity oscillations with 26 min period could only be observed for 2–3 periods, after which they became strongly damped.

5.9 Wavelength, phase speed and group velocity

To derive the wavelength (λ) and phase speed (c_{ph}) of oscillations, time signals at different locations on the prominence must be acquired. The signature of a propagating wave is a linear variation of the oscillatory phase with distance. Hence, when several

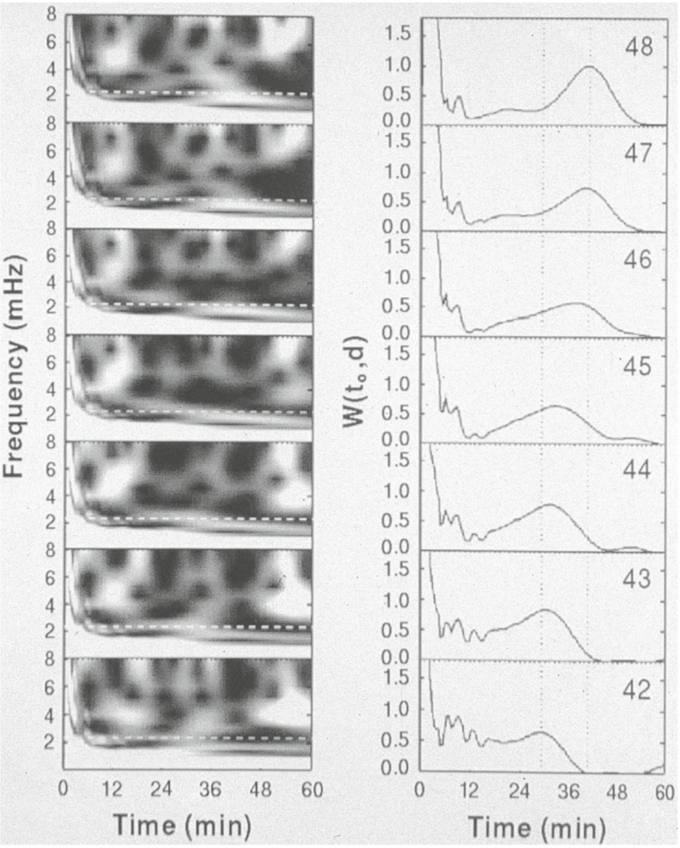

Fig. 18 Left: time–frequency diagrams of the Doppler velocity at several aligned, equispaced points in a quiescent prominence. White/black correspond to large/small wavelet power. Right: time variation of wavelet power from the diagrams on the left column for a period of 7.5 min (i.e., frequency around 2.2 mHz). The presence of power peaks suggests a finite duration of the perturbation, while the linear displacement of these peaks at the seven positions from $t = 28$ min to $t = 42$ min is an indication of a disturbance travelling with a group velocity $v_g \geq 4.4$ km s^{-1}. Image reproduced with permission from Molowny-Horas et al. (1997), copyright by Springer

neighbouring points are found to oscillate with the same frequency, one can compute the Fourier phase of the signal at each of the points and check whether it varies linearly with distance. If it does, this gives place to a wave propagation interpretation and the wavelength can be calculated. This approach has been followed by Thompson and Schmieder (1991), Molowny-Horas et al. (1997) (about which more details are given in Sect. 5.9.2) and Terradas et al. (2002) (see Sect. 5.9.3). On the other hand, Lin (2005) and Lin et al. (2007) (see Sect. 5.9.4) detected wave propagation along threads by studying Doppler velocity variations at fixed times. They observed a sinusoidal variation of the Doppler shift with distance along the thread, which allowed them to compute the wavelength. Moreover, the phase velocity of the oscillations can be derived from the inclination of the coherent features in the Doppler velocity time-slice diagrams. Other authors have followed less strict methods to calculate these wave parameters.

It must be mentioned that observations of wave propagation in slender waveguides or plane wave propagation in a uniform medium do not provide with the actual value of the wavelength (λ), but its projection on the plane of the sky, which is shorter than λ. And if a slit or some points along a straight line are used, then the computed wavelength is the projection of λ on the slit or the line. The observationally measured period and wavelength can in turn be used to calculate the phase speed, but since the observational wavelength is a lower limit to λ, this observational phase speed is also a lower limit to c_{ph} (Oliver and Ballester 2002). Hence, even if it is not explicitly mentioned, the values of λ and c_{ph} quoted here are observationally derived lower bounds to the actual values.

The results presented in this section are grouped in four parts, the first three of them in increasing order of complexity of the data analysis; the fourth one is devoted to thread oscillations. The reported wavelength values cover a range from less than 3000 km (for waves propagating along some threads) to 75,000 km (for waves propagating in a large area of a quiescent prominence). These numbers must be taken into account in the theoretical study of these events.

5.9.1 Simple analyses

Malville and Schindler (1981) observed a loop prominence some 90 min before the onset of a nearby flare and detected periodic changes with a wavelength along the loop of 37,000 km. This value, together with the period of 75 min, results in a phase speed of about 8 km s^{-1}.

Subsequent reports, which we now describe, are based on sheet-like prominences. Thompson and Schmieder (1991) detected periodic variations with periods between 3.5 and 4.5 min in a filament thread. They then computed the Fourier phase of the points along the thread and, after confirming its linearity from a phase versus distance plot, the value $\lambda \simeq 50{,}000$ km was derived, from which the phase speed is $c_{\mathrm{ph}} \simeq 150 - 200$ km s^{-1}. In other works (e.g., Tsubaki and Takeuchi 1986; Tsubaki et al. 1987, 1988; Suematsu et al. 1990) the signal in some consecutive locations along the slit has been found to be in phase. Although this seems to indicate that the wavelength of oscillations is much larger than the distance between the first and last of those points, this may not be necessarily true and a proper determination of the wavelength requires computing the Fourier phase corresponding to the oscillatory period.

Blanco et al. (1999) detected 15–20 min periodic variations corresponding to a pulse travelling with a speed of 170 km s^{-1}. Such a large phase velocity is hard to reconcile with the typical speeds in a prominence, but it must be taken into account that this result has been obtained using Si IV and O IV lines, which are formed at transition region temperatures.

Foullon et al. (2004) analysed the intensity on a set of points along the main axis of a filament in 195 Å images. A time–space plot shows a clear oscillatory pattern at one end of the filament (around position 25 in Fig. 19a). The oscillatory phase, displayed in Fig. 19b, presents oscillatory fronts that are well correlated along the filament, meaning that the oscillations of neighbouring points along the filament are almost in phase. This

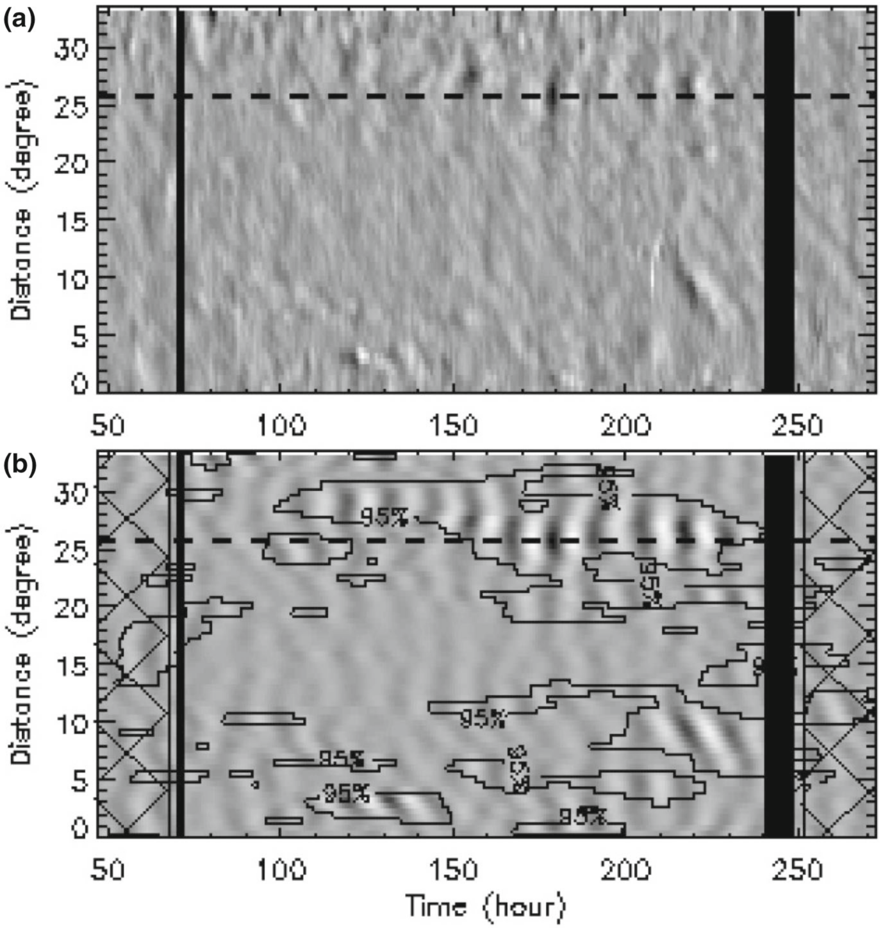

Fig. 19 **a** Time–space diagram of the 195 Å image intensity along the main axis of a filament. The vertical black stripes are caused by the lack of observational data. **b** Spatial distribution of the Fourier phase (gray coloured contours). Image reproduced with permission from Foullon et al. (2004), copyright by ESO

is true in particular for positions around 25, although in positions around 5 and 10 the phase presents a linear trend in neighbouring points, which can be interpreted as wave propagation along the filament axis. Lower bounds to the wavelength and phase speed in this area could be determined as explained above. It is remarkable that the most pronounced periodic intensity variations, those around position 25, were detected during 6 days, which suggests that they suffered very little damping or were excited continuously during this time span.

Berger et al. (2008) used high-resolution observations of limb prominences made by Hinode/SOT and detected oscillations that do not affect the whole prominence body. They considered three horizontal time slices at heights separated by 4.7 Mm and detected the presence of coherent oscillations in the three slices (Fig. 7). A phase matching of the sinusoidal profiles of these oscillations results in a vertical propagation speed (i.e., phase speed) around 10 km s^{-1}. Again, this value comes from a projection on the plane of the sky and is therefore a lower bound of the actual value.

Schmieder et al. (2013) used Hinode/SOT Ca II K data to observe a limb prominence. They detected vertically propagating waves in three vertical pillars contained in a large foot of the prominence. The vertical distance between Ca II K intensity maxima gave values of the wavelength (projected on the plane of the sky) of 2000 km and 900 km for the waves propagating in the first two pillars. As for the period and projected phase speed, the values obtained in the three pillars were 277 ± 50 s, 205 ± 54 s, 314 ± 125 s and 10 ± 4 km s^{-1}, 5 ± 3 km s^{-1}, – 5 ± 2 km s^{-1}, respectively, where the minus sign in the third phase velocity means downward propagation. Simultaneous spectropolarimetric measurements acquired with THEMIS allowed to determine the magnetic field vector, which in one of the pillars was nearly horizontal and mainly in the plane of the sky, and had a strength of 7.5 G. Hence, wave propagation is perpendicular to the local magnetic field. Ofman et al. (2015) subsequently performed a more detailed analysis of the same data set along the first pillar. Using a time–distance diagram, they found that the projected propagation speed takes typical values between 5.9 ± 1.0 and 8.5 ± 1.2 km s^{-1} (which can be compared to the value 10 ± 4 km s^{-1} derived by Schmieder et al. 2013). Furthermore, Ofman et al. (2015) determined the period of propagating disturbances at 6 separate heights along the pillar (ranging from $11.1''$ to $15''$) and derived values between 4.9 ± 0.5 and 11.3 ± 1.2 min; these periods show a decreasing trend above $12.7''$. These numbers must be compared with $P = 277 \pm 50$ s $= 4.6 \pm 0.8$ min obtained by Schmieder et al. (2013) after examining the time variation of the Ca II K intensity on a single point of the pillar. Ofman et al. (2015) also noted that the intensity variations in this event are not small compared with the unperturbed value and that they increase with height. This, together with the presence of sharp fronts in the propagating waves, led these authors to conclude that non-linear effects are important in this wave phenomenon.

5.9.2 An elaborate one-dimensional analysis

Molowny-Horas et al. (1997) took into account the projection effects in their analysis of the Doppler velocity along the spectrograph slit. They detected periodic velocity variations with period of 7.5 min some 7300 km along the slit and found that the Fourier phase of the velocity at this period changes linearly with distance (Fig. 20). The value $\lambda \geq 20{,}000$ km was derived. The corresponding phase speed is $c_{\mathrm{ph}} \geq 44$ km s^{-1}.

To obtain the group velocity of this event, Molowny-Horas et al. (1997) performed a wavelet analysis of the same set of data, which revealed the presence of a train of 7.5-min waves in the slit locations (Fig. 18). Moreover, the time of occurrence of the train of waves increases linearly along the slit, which agrees with the assumption of a propagating disturbance. The velocity of propagation along the slit can then be computed and the value $v_{\parallel} \simeq 4.4$ km s^{-1} is obtained. Taking into account that $v_{\parallel}$ is the projection of the group velocity, v_{g}, on the slit, one concludes that the above value is a lower limit for the group velocity, so $v_{\mathrm{g}} \geq 4.4$ km s^{-1}.

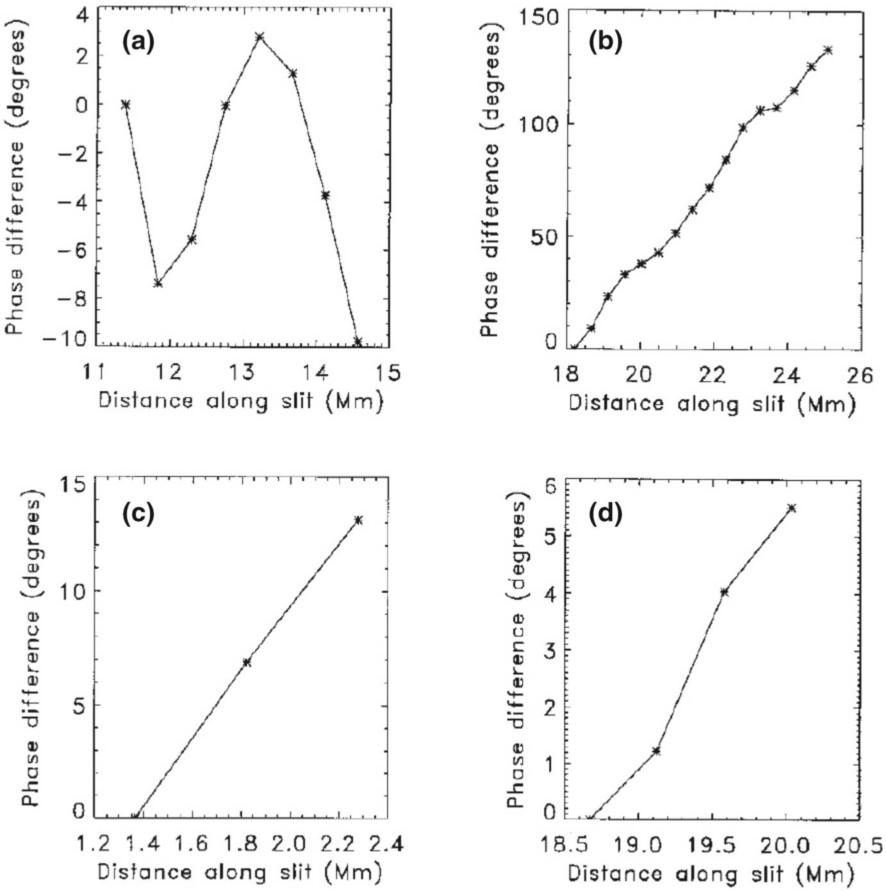

Fig. 20 Relative Fourier phase as a function of position along the slit for several sets of consecutive points with similar oscillatory period: **a** 10.0 min, **b** 7.5 min, **c** 12.0 min and **d** 4.0 min. The variation of the phase in (**a**) is not linear and so this oscillatory feature is not interpreted as a true signal. Regarding **c** and **d**, the phase varies linearly with position, but the number of points involved is too small to make a firm conclusion. Finally, the phase in (**b**) displays a very robust linear dependence with distance, so this is interpreted as a signature of wave propagation. Image reproduced with permission from Molowny-Horas et al. (1997), copyright by Springer

5.9.3 A two-dimensional analysis

This section is devoted to review the work by Terradas et al. (2002), that stands out among all other works in which wave properties have been determined since in this one a fully two-dimensional analysis is carried out. Figure 21 shows a time series of H_β filtergrams of the prominence studied by Terradas et al. (2002). The corresponding time series of the Doppler signal is presented in Fig. 22.

The data used by Molowny-Horas et al. (1999) were re-analysed by Terradas et al. (2002) and clear evidence for propagating and standing waves was uncovered. These authors started from the Doppler velocity, which in many areas of the two-dimensional

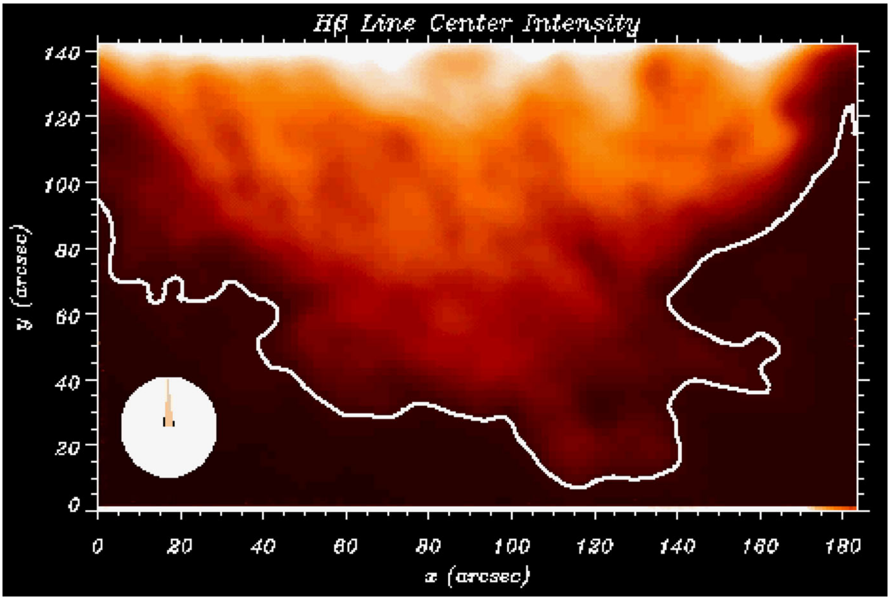

Fig. 21 Still from a movie showing H_β line centre images of a quiescent prominence observed with the VTT of Sacramento Peak Observatory. Images have been coaligned and a persistent drift towards the left has been suppressed. The thick white line displays the prominence edge and the solar photosphere is at the top (from Terradas et al. 2002). (To watch the movie, please go to the online version of this review article at doi:10.1007/s41116-018-0012-6)

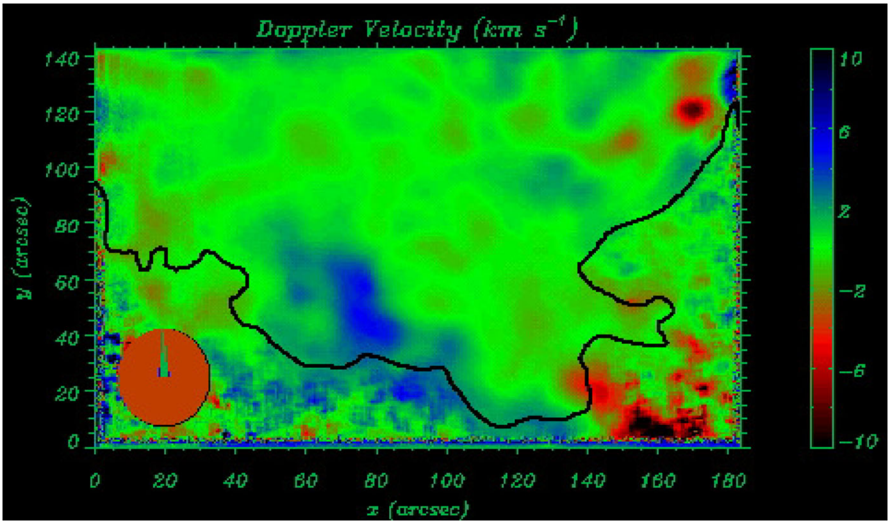

Fig. 22 Still from a movie showing the temporal evolution of the Doppler velocity in all points of the field of view of Fig. 21. (To watch the movie, please go to the online version of this review article at doi:10.1007/s41116-018-0012-6)

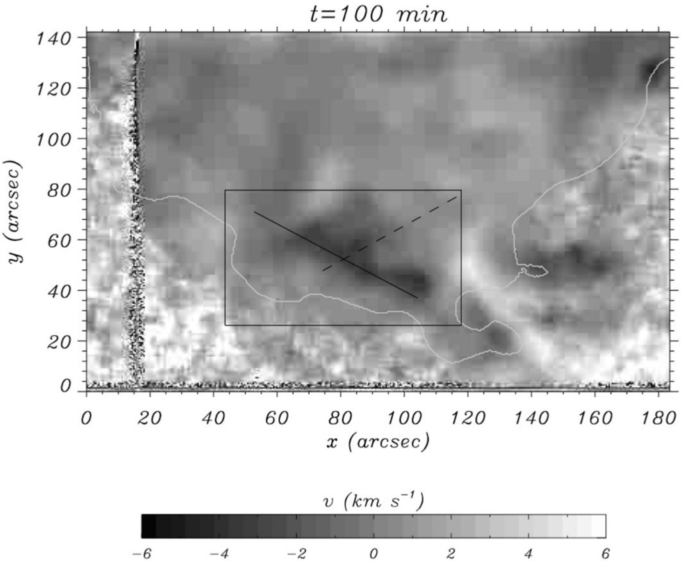

Fig. 23 Two-dimensional Doppler velocity distribution at a given time in a quiescent prominence. The signal in the black rectangle can be fitted by a damped sinusoid with a high correlation coefficient (see Fig. 17). Two paths (straight continuous and dashed lines) were selected. The continuous white line represents the approximate position of the prominence edge. The photosphere is slightly outside the image top. Image reproduced with permission from Terradas et al. (2002), copyright by ESO

field of view can be very well fitted by a damped sinusoid (Figs. 16, 17). The subsequent analysis was performed in a rectangle (black box in Fig. 23) that includes an area in which the correlation coefficient of the fit is large. The period of the oscillations in this rectangle is quite uniform and with a value around 75 min. First, Terradas et al. (2002) conducted an analysis of the phase along two straight lines inside the rectangle. Along the continuous line in Fig. 23, it is found that waves emanate from a point and propagate away from it (Fig. 24). It is clear both from the raw and the fitted signals in Fig. 24 that the slope of wave propagation to the left is larger than that to the right. To derive the wavelength, Terradas et al. (2002) plotted the Fourier phase associated to the most relevant period in the Fourier spectrum (i.e., the one with 75 min period) along the selected path (right panel of Fig. 24). There is an almost linear decrease of the phase between positions 5 and 30, a linear increase between positions 50 and 62 and a region of roughly constant phase in between. The first two patterns correspond to propagation to the left and right along the path, such as was pointed out from the first two panels of Fig. 24, while the third pattern is caused by standing wave motions. The slope of a straight line fitted to the Fourier phase in each of the regions with wave propagation gives the wavelength of oscillation (projected on the selected path) which is around 75,000 and 70,000 km for propagation to the left and right, respectively. The corresponding phase velocities are around 17 and 15 km s^{-1}.

Another interesting feature of this data set can be discerned by considering the dashed path in Fig. 23. A representation of the Doppler velocity versus position and time (Fig. 25) shows that, at least for the first half of the observational time, positive and

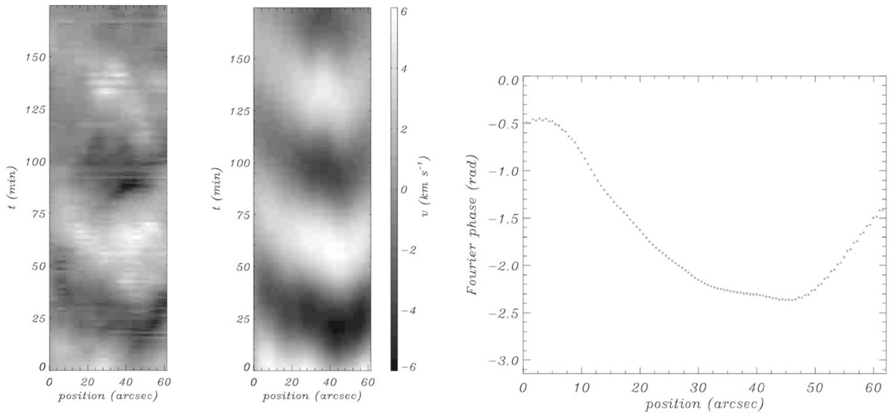

Fig. 24 Doppler velocity versus position and time along the solid path in Fig. 23. Left: Raw Doppler signal. Middle: fitted exponentially damped sinusoid. Right: Fourier phase associated to the 75 min periodicity. Image reproduced with permission from Terradas et al. (2002), copyright by ESO

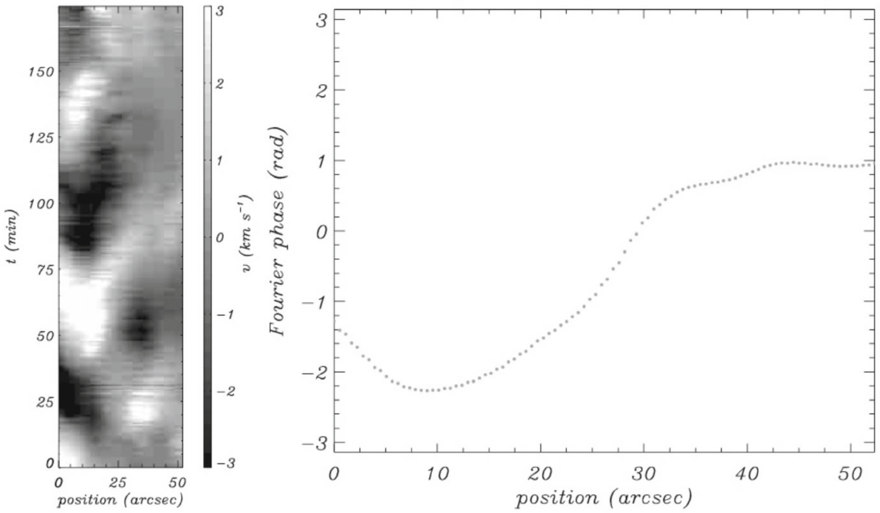

Fig. 25 Doppler velocity versus position and time along the dashed path in Fig. 23. Left: Raw Doppler signal. Right: Fourier phase associated to the 75 min periodicity. Image reproduced with permission from Terradas et al. (2002), copyright by ESO

negative velocities seem to alternate in phase separated by a region, around position 25, with nearly zero amplitude. This pattern suggests that rather than a propagating feature, the signal in this area behaves like a standing wave with two regions completely out of phase. The Fourier phase (right panel of Fig. 25) is practically constant in a small region around position 10 and in a larger region for positions greater than 30, which indicates that there is no signal propagation in these locations. The phase difference between positions 10 and 50 is close to π, which, together with the fact that between these points the amplitude takes low values, is in close agreement with the standing

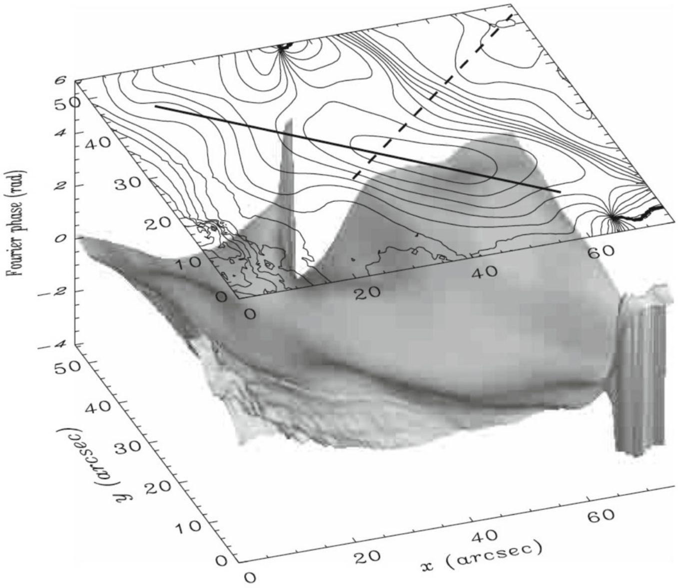

Fig. 26 Fourier phase associated to a period around 75 min (that is, the one corresponding to the largest peak in the Fourier spectrum) for the rectangular region selected in Fig. 23, both as a contour and as a surface plot. The selected paths are also displayed with continuous and dashed straight lines. Note that cuts of the Fourier phase along these two paths give rise to the Fourier phase displayed in Figs. 24 and 25. Image reproduced with permission from Terradas et al. (2002), copyright by ESO

wave picture and so a tentative identification of nodes and antinodes is possible. The estimated distance between the two antinodes visible in the left panel of Fig. 25 is around 22,000 km. This implies that the (projected) wavelength of the standing wave is about 44,000 km and the corresponding phase speed is 10 km s^{-1}. These values are about half those obtained for propagation along the other selected path and are a consequence of the anisotropic propagation of the perturbation.

In addition to the identification of standing and propagating wave features in the prominence, Terradas et al. (2002) went on to perform an investigation of the two-dimensional distribution of the wavelength and phase speed. They started by plotting the Fourier phase for the most relevant period in the Fourier spectrum at each point (Fig. 26), which shows that a deep global minimum is found around the central position of the plot. This particular phase structure is an indication that motions have their origin at the position of the minimum and propagate anisotropically from this point. Terradas et al. (2002) gave a much more clear interpretation of the two-dimensional phase by plotting the wavevector field (Fig. 27), computed as the gradient of the Fourier phase. The arrows in this figure indicate the direction of wave propagation, their length being proportional to the modulus of the wavenumber, k. The projection of the phase velocity on the plane of the sky is also displayed in Fig. 27. The analysis of the wavevector field shown in this figure clearly indicates that motions seem to be generated in a narrow strip close to positions $x = 35 - 50$ and $y = 20 - 30$ and spread out from this region. It is remarkable that the direction of the propagating

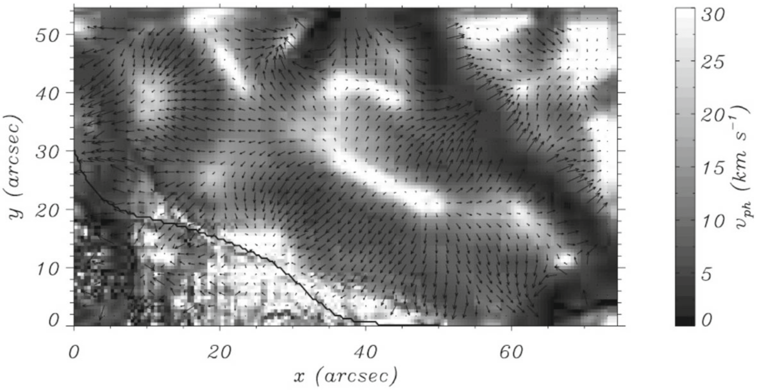

Fig. 27 Arrows represent the wavevector field computed from the gradient of the Fourier phase displayed in Fig. 26, where the length of the arrows is proportional to the modulus of the wavevector. The phase velocity is shown with the help of different levels of grey and black and white colours. Image reproduced with permission from Terradas et al. (2002), copyright by ESO

waves from the source region is essentially parallel to or towards the prominence edge, revealing the anisotropic character of the observed wave propagation. The values of the phase velocity in Fig. 27 are also quite different for both directions, being greater for the direction parallel to the edge, with $c_{\rm ph} \sim 20$ km s^{-1}, than for the direction perpendicular to the edge, with $c_{\rm ph} \sim 10$ km s^{-1}. This is an indication of the possible existence of some wave guiding phenomenon, which shows a preferential direction of propagation. Note the good agreement between the values of the phase velocity in the directions parallel and perpendicular to the edge and those derived from the analysis of the two selected paths based on Figs. 24 and 25.

5.9.4 Thread oscillations

Yi et al. (1991) and Yi and Engvold (1991) used two-dimensional spectral scans and investigated the presence of periodic variations of the Doppler shift and central intensity of the He I 10,830 Å line in two filaments. Yi et al. (1991) performed a first examination of the data and found oscillations with well-defined periods along particular threads in each prominence. For this reason, Yi and Engvold (1991) plotted the Doppler velocity versus position for different times in a given thread, so that a periodic spatial structure would directly yield a measure of the wavelength. Instead of this pattern, an almost linear variation of the velocity along the thread was found and consequently a value of λ much larger than the length of the threads, some 20,000 km in the two cases considered, was reported. Given that the periods are between 9 and 22 min, the corresponding phase speed is $c_{\rm ph} \gg 15$ km s^{-1}. This result suggests that the thread is oscillating in the fundamental kink mode (whose wavelength is of the order of the length of the supporting magnetic tube, that is, around 100,000–200,000 km; see Sect. 6.3.1), rather than being disturbed by a travelling wave. Let us mention that, in general, this analysis may be misleading since the velocity signal does not generally consist of the detected periodic component only, but it is made of this

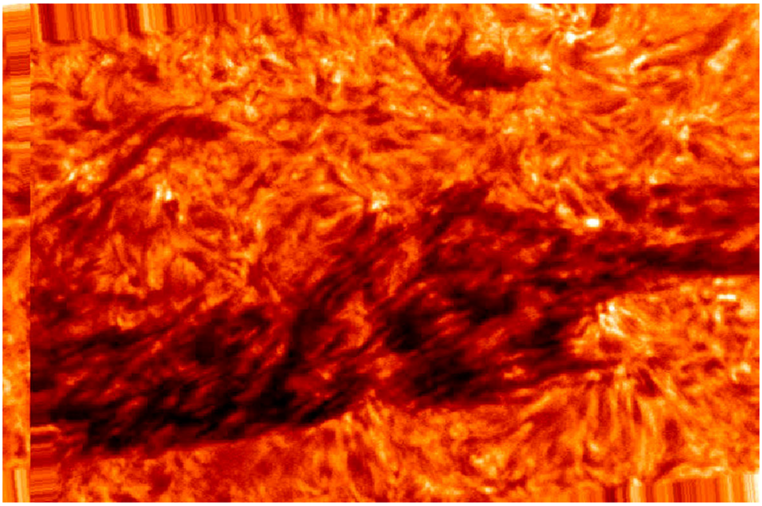

Fig. 28 Still from a movie showing H_α line centre images of a quiescent filament observed with the Swedish Solar Telescope in La Palma. The small-scale structures display the characteristic filament counter-streaming motions and undergo simultaneous transverse oscillations, detected as periodic Doppler variations (from Lin et al. 2003). (To watch the movie, please go to the online version of this review article at doi:10.1007/s41116-018-0012-6)

component mixed with other velocity variations. If the periodic component is weak, then the method used by Yi and Engvold (1991) may fail because the signature of the propagating wave is masked by the rest of the signal.

In the analysis of the Doppler velocity in two threads (denoted as T1 and T2) belonging to the same filament, Lin (2005) found a clear oscillatory pattern in time-slice diagrams along the two thin structures. She determined the following wave properties for thread T1: $c_{\rm ph} = 60$ km s^{-1}, $\lambda = 22, 12, 15''$ and P in the range 2.5–5 min (the 4.4 min period being particularly pronounced). For thread T2, the wave properties are: $c_{\rm ph} = 91$ km s^{-1}, $\lambda = 38, 23, 18''$ and P in the range 2.5–5 min (the 5-min period being particularly pronounced).

A much more profound study was carried out by Lin et al. (2003) by examining the two-dimensional motions and Doppler shifts of 328 features (or absorbing "blobs") of different threads. Forty nine of these features are observed to flow along the filament axis with speeds of 5–20 km s^{-1} while oscillating in the line-of-sight at the same time with periods of 4–20 min (see Fig. 28). To simplify the examination of oscillations, Lin (2005) computed average Doppler signals along each thread and found that groups of adjacent threads oscillate in phase with the same period. This has two consequences: first, since the periodicity is outstanding in the averaged signal for each thread, the wavelength of oscillations is larger than the length of the thread. Again, the interpretation of this result is that the threads oscillate in their fundamental kink mode. Second, in this data set threads have a tendency to vibrate collectively, in groups, rather than independently.

Horizontally flowing threads that undergo simultaneous transverse oscillations have not only been detected by Lin et al. (2003) and Lin (2005), but also by Okamoto et al.

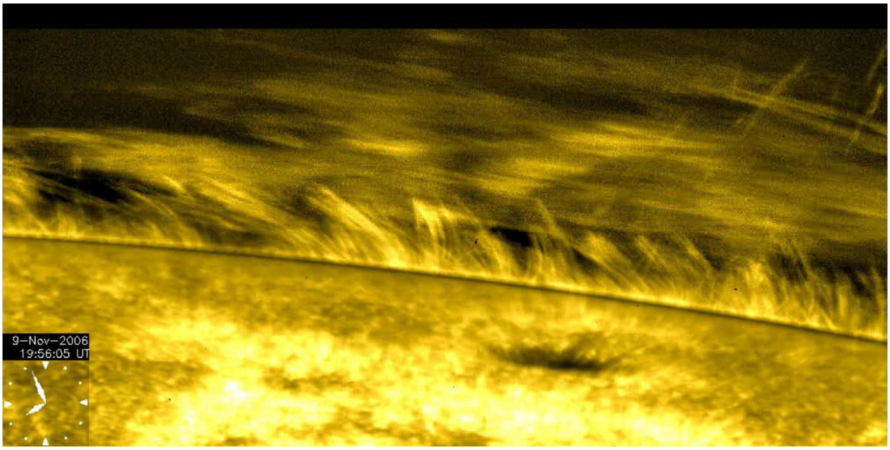

Fig. 29 Still from a movie showing Ca II H line images taken with Hinode/SOT that shows ubiquitous continuous horizontal motions along the prominence threads at the top right of the image. These threads also oscillate up and down as they flow (from Okamoto et al. 2007). (To watch the movie, please go to the online version of this review article at doi:10.1007/s41116-018-0012-6)

(2007) using Hinode/SOT. A Ca II H line movie shows continuous horizontal thread motions along an active region prominence (cf. Fig. 29). This movie also shows that the threads suffer apparently synchronous vertical oscillatory motions. An example of this phenomenon is shown in Fig. 30. Six threads displaying the same behaviour were studied and periods in the range 135–250 s were measured. The thread flow velocities range from 15 to 46 km s^{-1} and the vertical oscillation amplitudes range from 408 to 1771 km. These values are, of course, minimum estimates. A particularly interesting feature of these oscillations is that points along each thread oscillate transversally with the same phase. To reach this conclusion, a given thread is selected and several cuts along its length are considered. A representation of the signal as a function of time reveals that oscillations are synchronous along the entire length of the thread (Fig. 31). Once more this points to the kink mode as the responsible for the oscillations, as first pointed out by Doorsselaere et al. (2008a).

H_α observations conducted with the Swedish 1-m Solar Telescope by Lin et al. (2007) allowed to detect waves propagating in some selected threads. Figure 32 serves to illustrate the data analysis procedure for one thread. Here the line intensity shows no coherent behaviour (Fig. 32a), while the line-of-sight velocity presents some inclined features caused by waves propagating along the thread; two such features are labelled 1 and 2 in Fig. 32b. Figure 32c is another way of presenting Fig. 32b and is useful to illustrate more clearly the wavy character of the line-of-sight velocities along an individual thread. Two shorter time sequencies of Doppler velocity are extracted from Fig. 32c and shown in Figs. 32d and e. It is clear that oscillations are of small amplitude since the Doppler shift has an amplitude of 1–2 km s^{-1}. The power spectra of two of the curves in Fig. 32c (shown in Fig. 32f, g) yield wavelengths of the oscillatory pattern of, respectively, $3.8''$ and $4.7''$. The phase velocity of the oscillations can be derived from the inclination of the features appearing in the Doppler time-slice diagrams of Fig. 32b. The phase velocities thus obtained correspond to, respectively,

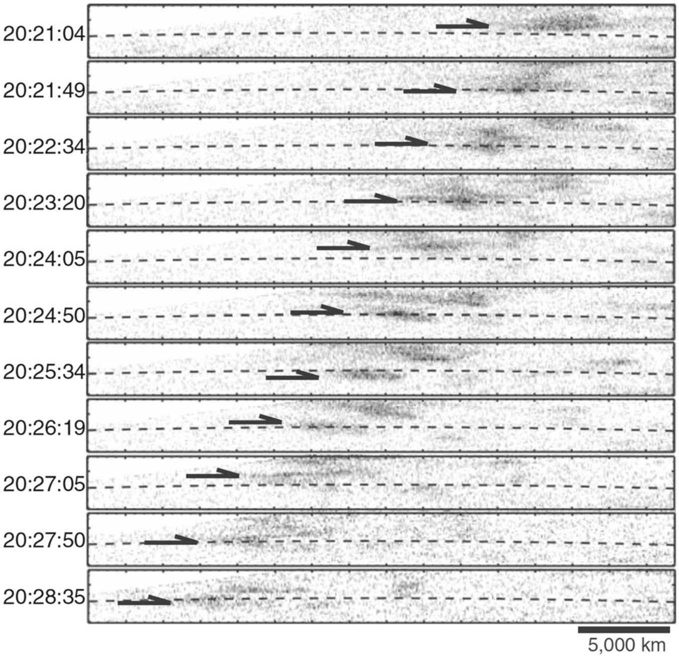

Fig. 30 Close-up view of a flowing thread displaying transverse oscillations. The measured flow speed is 39 km s^{-1}, the amplitude of vertical oscillations is 900 km and the period is 174 s. Image reproduced with permission from Okamoto et al. (2007), copyright by AAAS

8.8 and 10.2 km s^{-1}. Lin et al. (2007) found similar evidence of travelling waves in eight different threads. The mean phase velocity and period (obviously affected by the projection effect) are 12 km s^{-1} and 4.3 min. Periods between 3 and 9 min were found; longer period oscillations could not be detected in the data set used in this work because of its limited duration (18 min).

To test the coherence of oscillations over a larger area, covering several threads, Lin et al. (2007) averaged the line-of-sight velocity in a $3.4'' \times 10''$ rectangle containing closely packed threads. The averaged Doppler signal (left panel of their Fig. 4) displays a very clear oscillation. In addition, the power spectrum of this signal has a significant power peak at 3.6 min. Thus, the conclusion is that neighbouring threads tended to oscillate coherently in this rectangular area, possibly because they were separated by very short distances. This signal averaging could be analogous to acquiring data with poor seeing, such as in Terradas et al. (2002) (see Sect. 5.9.3).

Ning et al. (2009b) analysed the oscillatory behaviour of 13 threads in a quiescent prominence observed with Hinode/SOT. They found that many prominence threads exhibited vertical and horizontal oscillatory motions and that the corresponding periods did not substantially differ for a given thread. In some parts of the prominence, the threads seemed to oscillate independently from one another, and the oscillations were strongly damped. Some of the oscillating threads presented a simultaneous drift in the plane of the sky with velocities from 1.0 to 9.2 km s^{-1}. The reported periods were

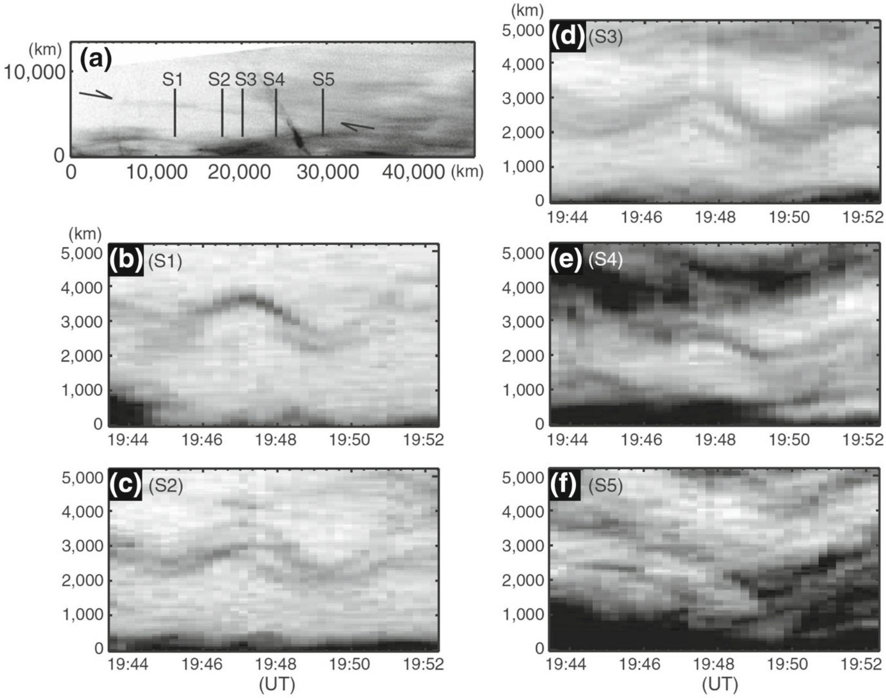

Fig. 31 Example of a prominence thread undergoing synchronous oscillations along its entire length (all images are shown in negative contrast). **a** The ends of the considered thread are marked by the two arrows. *S1–S5* indicate the locations used to make the height versus time plots shown in (**b**)–(**f**). **b**–**f** Height-time plots for the locations indicated in (**a**). Maximum and minimum amplitudes occur at nearly the same time for all locations. Image reproduced with permission from Okamoto et al. (2007), copyright by AAAS

short (between 210 and 525 s), with the dominant one appearing at 5 min. Peak to peak amplitudes were in the range 720–1440 km and the phase velocity varied between 5.0 and 9.1 km s^{-1}.

6 Theoretical aspects of small amplitude oscillations: periods and spatial distribution

The usual interpretation of small amplitude oscillations is that some external agent excites MHD waves in the form of periodic disturbances of the cold plasma. MHD waves can be propagating or standing. In the first case, there is a periodic disturbance of the particles of the prominence plasma that may propagate in the medium. In the second case, the wave is confined to a region with fixed boundaries, thus producing the positive interference of propagating waves. Theoretical models usually consider small amplitude perturbations superimposed on an equilibrium configuration. Then the properties of propagating/standing MHD waves are analysed. In the case of standing waves, we usually refer to the MHD eigenmodes of the system or to the modes for short.

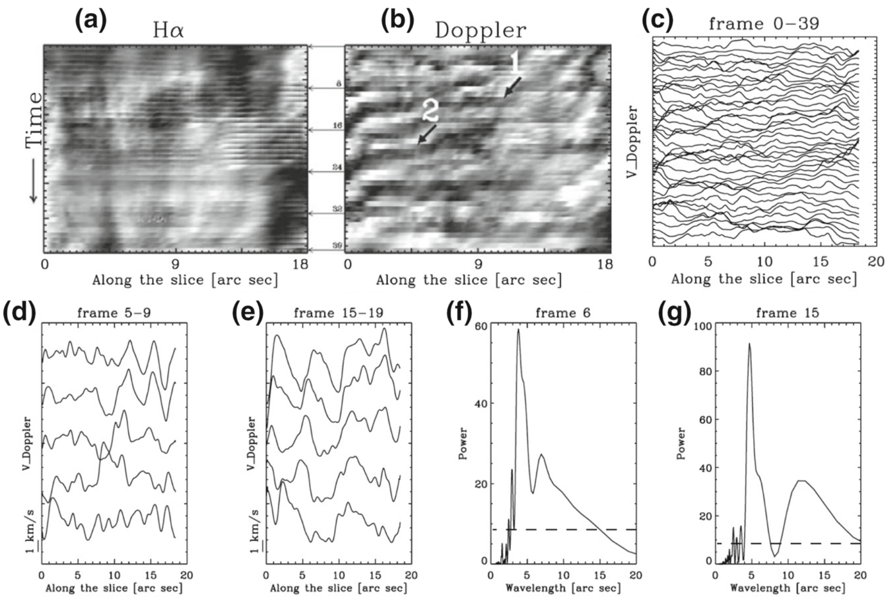

Fig. 32 **a**, **b** Time-slice diagrams of the H_α line intensity and Doppler shift along a filament thread. **c** Data of **b** shown as a set of curves instead of as a contour plot. Each curve represents the Doppler velocity along the thread for a fixed time (frame). **d**, **e** Signals from **c** for some selected times (frames). **f**, **g** Power spectrum of the Doppler shift along the thread for two times. Large peaks help identify the wavelength of propagating oscillations. Image reproduced with permission from Lin et al. (2007), copyright by Springer

Following our previous discussion of observations (Sect. 5.6), oscillations may affect individual threads, groups of threads or even larger areas of a prominence. The wave information (period, wavelength, phase speed, damping time) obtained from the analysis of this kind of events has been presented in Sects. 5.8 and 5.9. Given that the main purpose of studying prominence oscillations is to gain a more profound understanding of their nature via seismological studies, it is necessary to study these oscillations theoretically. The information one expects to derive from these works consists of the main wave properties (period, wavelength, phase speed, damping time, spatial distribution, …). They can then be compared with the observationally determined values. The theory also allows us to determine the temporal variation of the perturbed magnetic field strength and its orientation, the perturbed density, temperature, etc., which means that these variables constitute another source of comparison with observations that will hopefully be exploited in the near future (see Sect. 6.6 for some preliminary attempts in this direction).

The structure of this section is as follows: we start reviewing the theoretical works that deal with the (linear) normal modes of extremely simple prominence models (Sect. 6.1) and of models in which the prominence is represented as a plasma condensation without internal (i.e., thread) structure and surrounded by the solar corona (Sect. 6.2). Next, we describe the (linear) normal modes of prominence threads of either infinite (Sect. 6.3) or finite (Sect. 6.4) length. Sect. 6.5 is devoted to studies in which wave propagation in a prominence is investigated by the numerical solution of the time–dependent MHD equations. Finally, Sect. 6.6 deals with the combination of MHD and radiative transfer calculations.

6.1 Linear oscillations of very simple prominence models

The aim of the works discussed in this section is to follow elementary arguments to derive approximations for the oscillatory period and the polarisation of plasma motions of the main modes of oscillation of a prominence. Some of the obtained results correspond to MHD modes studied in more detail in other works (see Sect. 6.2). One of these works (Joarder and Roberts 1992b) is concerned with a prominence treated as a plasma slab embedded in the solar corona and with a magnetic field perpendicular to the prominence main axis (Fig. 37). Waves are allowed to propagate along the slab. The coordinate system introduced by Joarder and Roberts (1992b) has the x-axis pointing across the prominence (i.e., parallel to the magnetic field), the z-axis in the direction of wave propagation and the y-axis along the prominence. Three MHD modes exist in this configuration: the fast, Alfvén and slow modes, with motions polarised in the z-, y- and x-directions, respectively. Some of the simple analogies discussed next allow us to derive approximations for the period of these modes.

6.1.1 Loaded string: gravity acting as restoring force

A very simplified view of a prominence (Roberts 1991; Joarder and Roberts 1992a) is to consider it as a concentrated mass, M, suspended on an elastic string (representing the sagged magnetic field that supports the prominence; Fig. 33a). Such a model provides us with some insight into the period of the prominence oscillating vertically as a whole under the action of gravity and magnetic tension. The equilibrium state is simply one in which the gravitational force, Mg, is balanced by the upward component of the tension forces, $2T \sin\theta$, where T is the tension in one of the two strings and θ is the angle made by the string and the horizontal. Small amplitude vertical oscillations of the mass about this equilibrium state have a period

$$P = 2\pi \left(\frac{L}{g} \tan\theta \right)^{\frac{1}{2}}, \tag{9}$$

with $2L$ the separation distance between the two anchor points, which is analogous to the distance between the photospheric feet of the magnetic tube supporting the prominence plasma. Roberts (1991) noted that for typical parameter values ($g = 274$ m s^{-2}, $2L = 50{,}000$ km and θ between 3° and 30°), the period of these vertical oscillations is in the range 7–24 min, consistent with observationally reported values.

6.1.2 Loaded string

Roberts (1991) and Joarder and Roberts (1992b) considered a second model of interest (Fig. 33b), that resembles the previous one except that now gravity is ignored. In

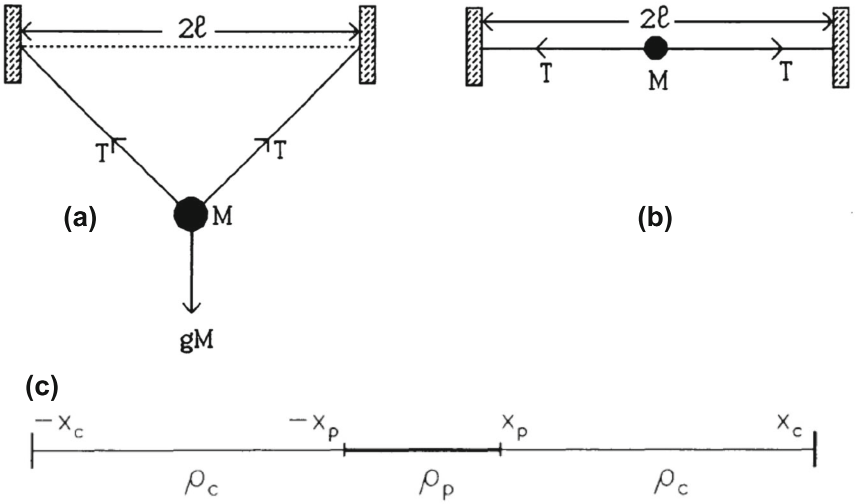

Fig. 33 Simple models of a prominence. **a** Mass suspended from an elastic string under the influence of gravity and the tension force. **b** Mass suspended from a taut string subject solely to the tension force. Bottom: Taut string with density ρ_{c} except for a central part with density ρ_{p}; gravity is also neglected. The size of the system (2ℓ in **a**, **b** and $2x_{\mathrm{c}}$ in **c**) is denoted by $2L$ in the text. Images reproduced with permission from (top) Roberts (1991), copyright by Taylor & Francis; and (bottom) from Oliver et al. (1993) copyright by AAS

this configuration there are two possible types of oscillation: either longitudinal or transversal. The frequencies of oscillation are given by

$$\frac{\omega L}{c_{\mathrm{str}}} \tan\left(\frac{\omega L}{c_{\mathrm{str}}}\right) = \frac{2\rho L}{M}, \tag{10}$$

where again $2L$ is the distance between the anchor points, ρ is the mass density of the string (per unit length) and c_{str} is a natural wave speed of the string. To simplify matters one can assume that the mass of the string ($2\rho L$) is negligible in comparison with M, that is, $M \gg \rho L$. Translating this inequality to prominences, it is equivalent to assuming that the mass of the cold plasma in a magnetic tube is much larger than the coronal mass in the same tube; this assumption seems most reasonable. Then, Eq. (10) reduces to a simple expression for the fundamental mode frequency,

$$\omega = \left(\frac{2T}{ML}\right)^{\frac{1}{2}}, \tag{11}$$

where it has been taken into account that the tension force is $T = \rho c_{\mathrm{str}}^2$. Although M has been considered a point mass, one can assume that it has a short, but finite, width $2x_{\mathrm{p}}$. Then, the previous expression for the tension force applied to the prominence part of the structure is $T = Mc_{\mathrm{pro}}^2/(2x_{\mathrm{p}})$, with c_{pro} a natural prominence wave speed. Now, inserting this expression into Eq. (11) we obtain for the period

$$P = 2\pi \frac{\left(L x_{\mathrm{p}}\right)^{\frac{1}{2}}}{c_{\mathrm{pro}}}. \tag{12}$$

For fast magnetoacoustic waves in a prominence (with transverse polarisation of motions), c_{pro} can be taken as the fast speed,

$$c_{\mathrm{f}} = \left(v_{\mathrm{A}}^2 + c_{\mathrm{s}}^2\right)^{1/2}, \tag{13}$$

with v_{A} and c_{s} the Alfvén and sound speeds, respectively. These quantities are given by

$$c_{\mathrm{s}}^2 = \frac{\gamma R T}{\tilde{\mu}} \tag{14}$$

and

$$v_{\mathrm{A}}^2 = \frac{B^2}{\mu \rho}, \tag{15}$$

with γ the ratio of specific heats, R the gas constant, $\tilde{\mu}$ the mean atomic weight, μ the magnetic permeability of vacuum and T, ρ and B the temperature, density and magnetic field strength. For Alfvén modes (also characterised by transverse displacements in this simplified model) $c_{\mathrm{pro}} = v_{\mathrm{A}}$. The Alfvén velocity is the group velocity but not the phase velocity for Alfvén waves except for parallel propagation. On the other hand, for slow magnetoacoustic waves (with longitudinal polarisation of motions), c_{pro} can be taken to be the cusp speed,

$$c_{\mathrm{T}} = \frac{v_{\mathrm{A}} c_{\mathrm{s}}}{\left(v_{\mathrm{A}}^2 + c_{\mathrm{s}}^2\right)^{1/2}}. \tag{16}$$

The fast speed in Eq. (13) and the cusp speed in Eq. (16) are in general different from the phase speed and the group speed for fast and slow magnetoacoustic waves. Only for very specific directions of propagation are these quantities phase and/or group speeds. Using the same parameters as above together with $v_{\mathrm{A}} = 28$ km s^{-1}, $c_{\mathrm{s}} = 15$ km s^{-1} and a prominence width equal to one tenth the length of magnetic field lines (i.e., $2x_{\mathrm{p}} = 2L/10 = 5000$ km), Eq. (12) yields the periods $P_{\mathrm{fast}} = 26$, $P_{\mathrm{Alfven}} = 30$ and $P_{\mathrm{slow}} = 63$ min, all of them within the range of observed intermediate- to long-period oscillations in prominences.

The reader must be warned that when using the speeds c_{T} and c_{f} for the slow and fast modes, respectively, one is assuming a structuring across the magnetic field that is absent in the models discussed in this section.

6.1.3 Loaded string: finite width prominence

Oliver et al. (1993) (see also Roberts and Joarder 1994) modified the loaded string model of Fig. 33b by replacing the point mass M by a denser central string of width

$2x_\mathrm{p}$ (Fig. 33c). To solve the wave equation it is necessary to impose the continuity of the displacement and its spatial derivative at the joints $x = \pm x_\mathrm{p}$. Here the x-axis is placed along the string with $x = 0$ the string centre. Then, upon imposing that the string is tied at its ends, the dispersion relation for even solutions about the centre of the string can be expressed as

$$\tan \frac{\omega x_\mathrm{p}}{c_\mathrm{pro}} = \left(\frac{\rho_\mathrm{c}}{\rho_\mathrm{p}}\right)^{\frac{1}{2}} \cot \frac{\omega (L - x_\mathrm{p})}{c_\mathrm{cor}}, \tag{17}$$

whereas the dispersion relation for odd solutions can be written as

$$\cot \frac{\omega x_\mathrm{p}}{c_\mathrm{pro}} = -\left(\frac{\rho_\mathrm{c}}{\rho_\mathrm{p}}\right)^{\frac{1}{2}} \cot \frac{\omega (L - x_\mathrm{p})}{c_\mathrm{cor}}. \tag{18}$$

In these formulas c_pro and c_cor represent the natural wave speeds of the prominence and coronal parts of the string and ρ_p and ρ_c their respective densities. These expressions contain a rich array of solutions representing oscillatory modes of the system with different properties. And since there are three characteristic wave modes (fast, Alfvén and slow, with their specific fast, Alfvén and tube speeds in the prominence and corona), each set of modes is repeated three times. For the sake of simplicity, we here keep the parameters c_pro and c_cor in the following expressions, although it must be understood that these two speeds need to be substituted by their corresponding c_f, v_A or c_T to derive the frequencies of the fast, Alfvén and slow solutions.

Equations (17) and (18) can be numerically solved to obtain the frequencies of the various solutions. Nevertheless, some simplifications can be done by taking into account that the prominence width is much smaller than the length of magnetic field lines ($x_\mathrm{p} \ll L$) and that the prominence density is much larger than the coronal one ($\rho_\mathrm{p} \gg \rho_\mathrm{c}$) (Joarder and Roberts 1992b; Roberts and Joarder 1994). Further assuming that $\rho_\mathrm{c}/\rho_\mathrm{p} \ll x_\mathrm{p}/L \ll 1$, the following expression for the frequency of the fundamental mode can be obtained from Eq. (17)

$$\omega = \frac{c_\mathrm{pro}}{\left(L x_\mathrm{p}\right)^{\frac{1}{2}}}. \tag{19}$$

It is not surprising that the period corresponding to this frequency is just the one given by Eq. (12). Other solutions to Eq. (17) can be obtained by simply assuming $\rho_\mathrm{c}/\rho_\mathrm{p} \ll 1$. They come in two sets (Joarder and Roberts 1992b)

$$\omega = n\pi \frac{c_\mathrm{pro}}{x_\mathrm{p}}, \qquad n = 1,2,3,\ldots, \tag{20}$$

and

$$\omega = n\pi \frac{c_\mathrm{cor}}{L - x_\mathrm{p}}, \qquad n = 1,2,3,\ldots \tag{21}$$

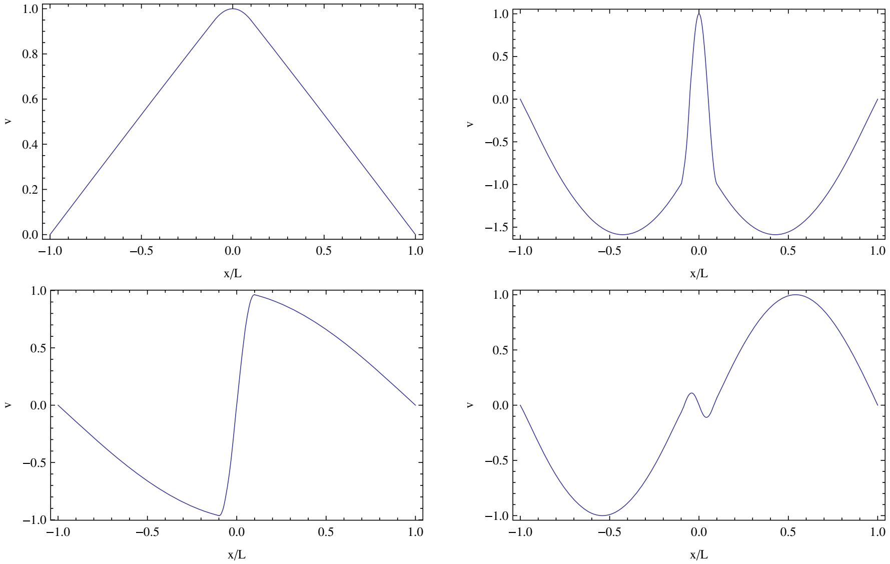

Fig. 34 Spatial distribution of some normal modes of the string shown in Fig. 33c. Top left: hybrid mode. Top right: first internal even overtone. Bottom left: first internal odd overtone. Bottom right: first external odd overtone. The spatial coordinate is given in units of L and the string of density ρ_p is in the range $-0.1 \leq x \leq 0.1$. The wave speeds are $c_\mathrm{pro} = 15$ and $c_\mathrm{cor} = 166$ km s^{-1}, representative of prominence and coronal sound speeds, and the density ratio is $\rho_\mathrm{p}/\rho_\mathrm{c} = 11.25$

On the other hand, Eq. (18) has no low-frequency solution analogous to that of Eq. (19). Instead, it has just two sets of solutions: one of them is identical to Eq. (21) and the other one is similar to that given by Eq. (20), namely

$$\omega = (2n+1)\frac{\pi}{2}\frac{c_\mathrm{pro}}{x_\mathrm{p}}, \qquad n = 0, 1, 2, \ldots \tag{22}$$

To understand the standing solutions supported by the string of Fig. 33c, we now concentrate on their spatial distribution. Figure 34a, b display the two lowest frequency solutions of Eq. (17), while Figs. 34c and d show the two lowest frequency solutions of Eq. (18). Their frequencies are approximately given by Eq. (19), Eq. (20) with $n = 1$, Eq. (22) with $n = 0$ and Eq. (21) with $n = 1$, respectively. Let us refer to the parts of the string with density ρ_c and ρ_p as the external and internal regions. The eigenfunction in Fig. 34d differs from the other three in that the displacement in the external region is an order of magnitude larger than in the internal region. For this reason it is termed an external mode, since its properties are dominated by the nature of the external part of the string (Joarder and Roberts 1992b). One then is tempted to call the other three solutions in Fig. 34 internal modes, but a simple experiment will prove this to be wrong (Oliver et al. 1993). Let us gradually reduce the size of the internal part of the string (by reducing x_p). Then internal mode frequencies (cf. Eqs. 20 and 22) tend to infinity and in the limit $x_\mathrm{p} \to 0$ internal modes disappear and only external modes remain. It turns out that this process of gradually removing the density enhancement in the central part of the string does not eliminate the mode of Fig. 34a, which is transformed into the fundamental mode of the string. Thus, this is not an internal mode. By a similar process (i.e., by letting $x_\mathrm{p} \to L$), the central part of the string can be progressively expanded so that we end up with a uniform density ρ_p. This makes external mode frequencies grow unbounded (cf. Eq. 21) and for $x_\mathrm{p} \to L$ only internal modes remain. In this process the mode of Fig. 34a transforms into the fundamental mode of the string. Hence, this mode is not an external mode, either, and it owes its existence to the concurrent presence of both the internal and external parts of the string. For this reason Oliver et al. (1993) labelled this solution a hybrid mode. The hybrid mode frequency is approximately given by Eq. (19), the internal mode frequencies by Eqs. (20) and (22) and the external mode frequencies by Eq. (21).

This string analogy points out the basic nature of a prominence's modes of oscillation. Because there are in general three MHD modes, there is a fast hybrid mode, an infinite number of internal fast modes and an infinite number of external fast modes (Joarder and Roberts 1992b; Oliver et al. 1993; Roberts and Joarder 1994). Their respective frequencies are given by Eqs. (19), (20), (21) and (22) with c_pro and c_cor substituted by the prominence and coronal fast speeds. Something similar can be said about Alfvén and slow modes.

6.1.4 Loaded string: order of magnitude calculations using the Kippenhahn–Schlüter model

Anzer (2009) performed some simple estimates of the main oscillatory periods of a prominence using the Kippenhahn–Schlüter model (Kippenhahn and Schlüter 1957) modified so as to include the corona in which the prominence is embedded (for a general solution see Poland and Anzer 1971). In this configuration, see Fig. 35, a curved magnetic field gives support of the cold plasma against gravity. Field lines outside the prominence do not bend downwards and so the magnetic field in the coronal environment does not present the desired arcade shape. For this reason, the role of

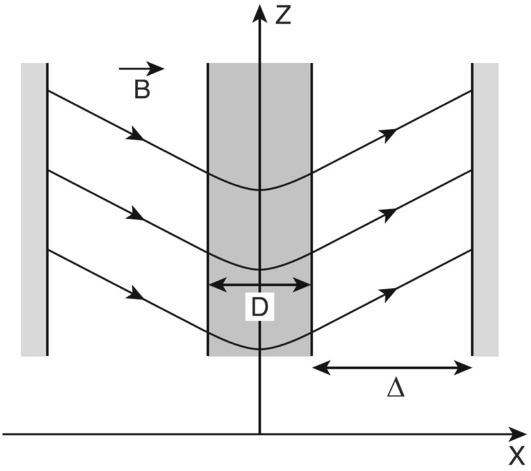

Fig. 35 Sketch of a prominence configuration based on the Kippenhahn and Schlüter (1957) model. In the text the system size (2Δ) and the prominence width (*D*) are denoted by 2*L* and $2x_\mathrm{p}$, respectively. Except for the field line curvature, this configuration is identical to that of Fig. 37. Image reproduced with permission from Anzer (2009), copyright by ESO

the dense photosphere is played by two vertical rigid walls. Note that the configuration used by Anzer (2009) bears some resemblance to that of Fig. 33a: the coronal magnetic field is almost uniform and makes an angle θ with the horizontal direction. Hence, $\tan\theta = B_{z1}/B_x$, with B_{z1} the vertical magnetic field component at the prominence boundary and B_x the uniform horizontal field component. A further similarity between the present model and the previous ones is that the density is analogous to that of Fig. 33c.

Instead of solving the MHD equations, Anzer (2009) took the clever approach of making guesses for the restoring forces acting over the prominence ($F(\xi)$) and then solving the equation

$$M\frac{d^2\xi}{dt^2} = F(\xi), \tag{23}$$

where ξ is the plasma displacement and M is the prominence column mass. For magnetically driven oscillations in the x-direction, caused by the magnetic pressure gradient, it is postulated that

$$F(\xi) = -M\frac{B_{z1}}{B_x}\frac{g}{L}\xi, \tag{24}$$

so that the corresponding oscillatory period is

$$P = 2\pi\left(\frac{B_x}{B_{z1}}\frac{L}{g}\right)^{\frac{1}{2}} = 2\pi\left(\frac{L}{g\tan\theta}\right)^{\frac{1}{2}}. \tag{25}$$

For oscillations in the y- and z-directions the restoring force is the magnetic tension of the stretched field lines. In both cases the restoring force is

$$F(\xi) = -M\frac{B_x}{B_{z1}}\frac{g}{L}\xi, \tag{26}$$

and the oscillatory period is

$$P = 2\pi\left(\frac{B_{z1}}{B_x}\frac{L}{g}\right) = 2\pi\left(\frac{L}{g}\tan\theta\right)^{\frac{1}{2}}. \tag{27}$$

It does not come as a surprise that this formula is identical to Eq. (9).

Anzer (2009) noted that the field line inclination is expected to be very small and therefore $B_{z1}/B_x \ll 1$. As a consequence, the period of x-oscillations will be much larger than that of the other two modes, polarised in the y- and z-directions.

Anzer (2009) also investigated perturbations driven by the gas pressure. He assumed that the coronal magnetic field is so strong that the prominence cannot distort it by a large amount. Further assuming that the magnetic field is horizontal, then the difference in gas pressure on either side of the prominence–corona interface can drive oscillations in the x-direction. The restoring force is approximated by

$$F(\xi) = -M \frac{c_\mathrm{s}^2}{L x_\mathrm{p}} \xi, \tag{28}$$

and consequently the period of this mode is

$$P = 2\pi \frac{\left(L x_\mathrm{p}\right)^{\frac{1}{2}}}{c_\mathrm{s}}. \tag{29}$$

This result coincides with that obtained from the simple string models of Figs. 33b and c; see Eq. (12).

Four oscillatory modes can be identified from these elementary considerations, but the restoring forces in the x-direction act in unison to create a single mode, so we are left with the familiar three MHD modes: fast, Alfvén and slow.

Some values of the periods given by Anzer (2009) are similar to those in previous works: 200 min for the magnetically dominated oscillations in the x-direction, 430 min for the gas pressure driven oscillations and 20 min for the transverse, magnetically driven oscillations.

6.1.5 Loaded string: skewed magnetic field

A further refinement of the string analogy (Joarder and Roberts 1992b; Roberts and Joarder 1994) can be introduced by noting that the magnetic field of a prominence is not at 90° with the prominence axis, contrary to the simple models of Figs. 33 and 35. Instead, the prominence magnetic field makes an angle ϕ, typically around 20°, with the long axis of the slab. This is not too important for the almost isotropic fast modes, but Alfvén and slow modes propagate mainly along field lines, which in a skewed magnetic configuration are longer than $2L$ by a factor $1/\sin\phi \approx 3$. Thus, the periods of these waves become larger by this same factor since the travel time needed for them to travel back and forth between the anchor points increases by $1/\sin\phi$. The result is that the hybrid Alfvén and slow modes can have periods up to 60 min and 5 h, respectively. It has been suggested that the last one may be the cause of the very long-period oscillations observed by Foullon et al. (2004) and Pouget et al. (2006).

6.2 Linear oscillations of prominence models with no internal structure

6.2.1 Slab with longitudinal magnetic field

In a series of three papers, Joarder and Roberts conducted analyses of the modes of oscillation of a magnetised prominence slab embedded in the corona. The influence of gravity was neglected and so the plasma variables (temperature, pressure and density) are uniform both in the prominence and in the coronal region. In the first of these works (Joarder and Roberts 1992a) a purely longitudinal magnetic field was taken (see Fig. 36). The dispersion relation contains a variety of modes, which can be fast or slow, combined with kink or sausage and body or surface. Because of the strong difference of the prominence and coronal physical parameters, some eigensolutions

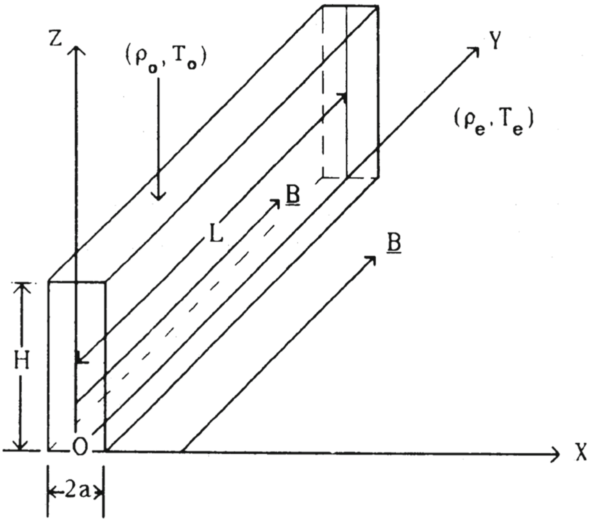

Fig. 36 Sketch of the prominence slab model with longitudinal magnetic field used by Joarder and Roberts (1992a). These authors assumed that the coronal environment in which the prominence is embedded extends infinitely in the x-direction. In this figure, the width of the prominence is denoted by $2a$, whereas in our text $2x_\mathrm{p}$ is used. Image reproduced with permission from Joarder and Roberts (1992a), copyright by ESO

are slow in the external medium and fast in the internal medium. Tabulated periods range from 9 to 5 h to a few minutes. The first values had not been reported at the time this work was published, so emphasis was given by the authors to fast surface modes, with shorter periods around 1 h, and to 5- and 3-min Pekeris and Love modes.

6.2.2 Slab with transverse magnetic field

Joarder and Roberts (1992b) considered the purely transverse magnetic field of Fig. 37. From the characteristic wavenumbers of the solutions in the x-direction, Joarder and Roberts (1992b) created the distinction between internal and external modes (see Sect. 6.1 for a discussion of the features of these solutions). According to these authors, the former group of modes arises principally from the magnetoacoustic properties of the plasma slab, although these modes are somewhat influenced by the external material because of the presence of free interfaces between the prominence and corona. External modes are present, on the other hand, even in the absence of the prominence plasma but are modified because of the introduction of this cool, dense slab. The dispersion diagrams of kink and sausage modes are shown in Fig. 38, where c_sp and v_Ap are the sound and Alfvén speeds in the prominence, while c_sc and v_Ac are their coronal counterparts. Moreover, Joarder and Roberts (1992b) also removed propagation along the prominence by setting $k_z = 0$. The mode frequencies are then those on the vertical axes of Fig. 38. In this case the dispersion relations of kink and sausage modes are those discussed for a string with densities ρ_c and ρ_p (Fig. 33c), namely Eqs. (17) and (18). Joarder and Roberts (1992b) gave the approximate solutions of Eqs. (19)–(22), which are in very good agreement with the results of Fig. 38 for $k_z = 0$.

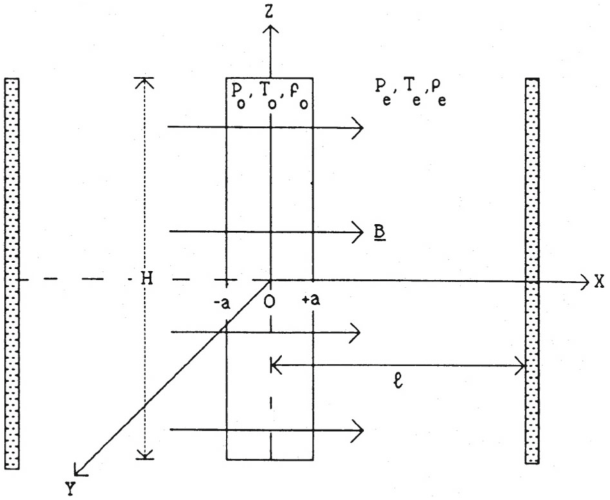

Fig. 37 Schematic diagram of a prominence slab in a coronal environment. The magnetic field is perpendicular to the prominence axis and tied at the photosphere, represented by two rigid conducting walls at $x = \pm \ell$. Note that in the text the position of the photospheric walls is denoted by $x = \pm L$. Image reproduced with permission from Joarder and Roberts (1992b), copyright by ESO

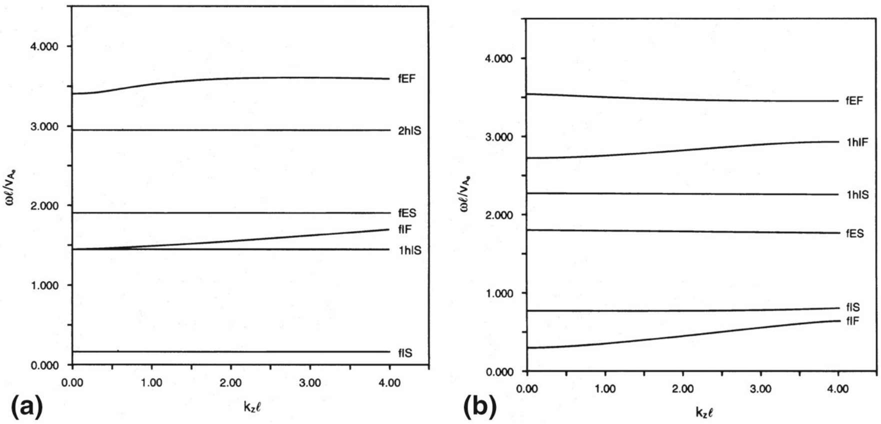

Fig. 38 Dispersion diagram of magnetoacoustic **a** kink modes and **b** sausage modes in the equilibrium model represented in Fig. 37. Meaning of labels at the right of each curve: modes are identified as fundamental (f), first harmonic (1h), second harmonic (2h), …; internal or external (I or E); and fast or slow (F or S). Here ω and k_z are the frequency and the wavenumber along the slab, while v_{Ae} is the coronal Alfvén speed and L (denoted by ℓ in these plots) is half the length of the supporting magnetic field. Parameter values used: $v_{\mathrm{Ap}} = 28$ km s^{-1}, $c_{\mathrm{sp}} = 15$ km s^{-1}, $v_{\mathrm{Ac}} = 315$ km s^{-1}, $c_{\mathrm{sc}} = 166$ km s^{-1}. Image reproduced with permission from Joarder and Roberts (1992b), copyright by ESO

Oliver et al. (1993) presented more insight into the nature of internal and external modes while using the non-isothermal Kippenhahn–Schlüter solution represented in Fig. 35. These authors followed the evolution of fast and slow modes in the dispersion diagram when the prominence is slowly removed by taking $x_{\mathrm{p}} \to 0$. They noted that the frequencies of internal modes, both slow and fast, progressively grow until they exceed the highest ω value of the dispersion diagram and so these modes are no longer present in this plot; therefore, only external modes remain in the dispersion diagram. The presence of the prominence region thus gives physical support for the existence of internal modes. The same is true for external modes when the corona is gradually removed by making $x_\mathrm{p} \to L$. A clear distinction then arises between the two types of modes, although it turns out that the fundamental mode is internal and external at the same time, since it survives both when the prominence and the corona are eliminated. For this reason, this mode with mixed internal and external properties was called hybrid by Oliver et al. (1993) and later string by Joarder and Roberts (1993b) because it arises in the string analogy. Nevertheless, internal and external modes are also present in the string analogy (Sect. 6.1), so perhaps hybrid mode is a better denomination for this solution.

From Oliver et al. (1993) it also appears that the amplitude of perturbations in the prominence is rather small for external modes, a feature that is also present in the string solutions of Fig. 34. For this reason it was postulated that they would probably be difficult to detect in solar prominences and that the reported periodic variations are produced by the hybrid and internal modes. In addition, the frequency of internal modes is shown to depend on prominence properties only, while that of hybrid and external modes depends on other physical variables such as the length of field lines. This is in agreement with the approximate Eqs. (19)–(22).

The essential difference between the equilibrium models in Joarder and Roberts (1992b) and in Oliver et al. (1993) is that gravity is neglected in the former, which results in straight magnetic field lines, while it is a basic ingredient in the later, which results in the curved shape of field lines characteristic of the Kippenhahn–Schlüter equilibrium model. Despite the different shape of field lines, the main features of the oscillatory spectrum are similar and so the influence of gravity and field line shape on the properties of the MHD modes is not too relevant in this kind of configurations.

A study of the oscillatory modes of the Kippenhahn and Schlüter (1957) prominence model was undertaken by Oliver et al. (1992). The equilibrium model is represented in Fig. 35 although the corona is omitted. This implies that this work only gives a restricted account of the MHD modes of a slab prominence since there are no hybrid and external solutions in the absence of the corona. Oliver et al. (1992) noted that the three MHD modes possess different velocity orientations. The fast mode is characterised by vertical motions. The Alfvén mode by motions along the filament long axis, and the slow mode by plasma displacements parallel to the equilibrium magnetic field, which in this configuration is practically horizontal and transverse to the prominence. The immediate consequence of this association between modes and velocity polarisation is that periodic variations in the Doppler shift are more likely to be detected in filaments near the disk centre for fast modes and in limb prominences for Alfvén and slow modes, depending on the orientation of the prominence with respect to the observer. These features of the MHD modes are retained in other models in which the equilibrium magnetic field is assumed perpendicular to the filament axis (Joarder and Roberts 1992b, 1993a; Oliver et al. 1993; Oliver and Ballester 1995, 1996). Nevertheless, the distinction between the three MHD modes is lost when the observed longitudinal magnetic field component is taken into account (Joarder and Roberts 1993b, see Sect. 6.2.3). Probably, there are no characteristic oscillatory directions

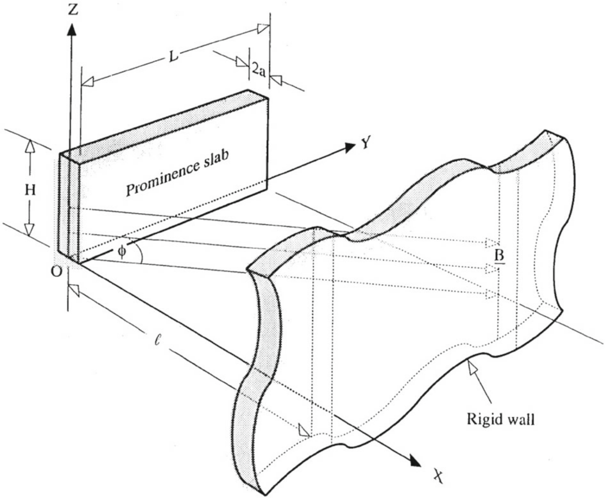

Fig. 39 Schematic diagram of a prominence slab in a coronal environment. The magnetic field makes an angle ϕ with the prominence axis and is tied at the photosphere, represented by two rigid, perfectly conducting walls. Image reproduced with permission from Joarder and Roberts (1993b), copyright by ESO

associated to the various modes (unfortunately, the issue of velocity polarisation in a skewed magnetic equilibrium model has not yet been addressed in the context of prominence oscillations). The actual velocity field in prominences can be substantially more complex than that indicated by investigations based on models with magnetic field purely transverse to the prominence slab.

6.2.3 Slab with skewed magnetic field

It is well known (Leroy 1988, 1989) that magnetic field lines are actually oriented at a rather small angle (around 20°) with the prominence axis. Joarder and Roberts (1993b) took this observational fact into account by adding a longitudinal magnetic field component to the equilibrium model used in Joarder and Roberts (1992b); see Fig. 39. Now, the xy-plane is defined to contain the assumed horizontal magnetic field. Then, it is not possible to place the z-axis parallel to the wavenumber along the prominence axis, so now the k_y and k_z components must be considered. The assumptions of transverse field and propagation of perturbations in the z-direction made in the works discussed above simplify the MHD wave equations since the Alfvén mode is decoupled from the slow and fast modes, which can be studied separately with a subsequent reduction in complexity of the mathematical problem. The problem considered by Joarder and Roberts (1993b), however, contains coupled fast, Alfvén and slow modes. The resulting dispersion diagram (Fig. 40) displays a very rich mode structure with plenty of mode couplings, which anticipates the complex nature of actual prominence MHD modes. Unfortunately, the physical properties of perturbations (velocity polarisation, importance of the various restoring forces, perturbations of the equilibrium variables, …) for the modes in the dispersion diagram have not been examined yet.

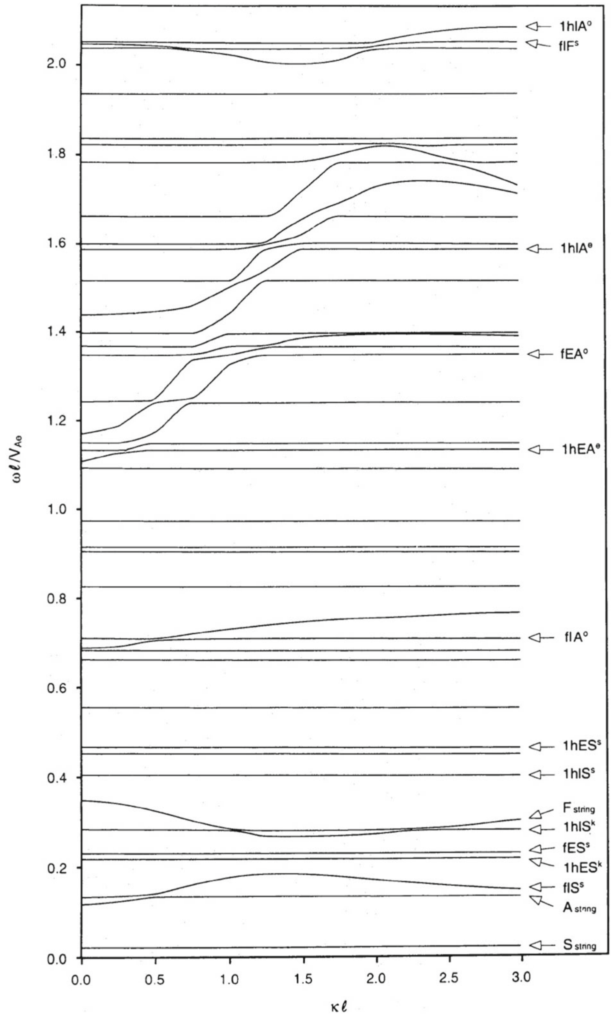

Fig. 40 Dispersion diagram of magnetoacoustic modes in the equilibrium structure of Fig. 39. Meaning of labels at the right of each curve: modes are identified as fundamental (f), first harmonic (1h), second harmonic (2h), …; string, internal or external (I or E); and fast, Alfvén or slow (F, A or S) according to the mode's nature for $\kappa \ll 1$. Here ω and κ are the frequency and the wavenumber modulus, while v_{Ae} is the coronal Alfvén speed and ℓ is half the length of the supporting magnetic field. Parameter values used: $v_{\mathrm{Ap}} = 74$ km s^{-1}, $c_{\mathrm{sp}} = 15$ km s^{-1}, $v_{\mathrm{Ac}} = 828$ km s^{-1}, $c_{\mathrm{sc}} = 166$ km s^{-1}. Image reproduced with permission from Joarder and Roberts (1993b), copyright by ESO

Oscillation periods up to 4 h (for the slow hybrid mode) are present in this configuration.

6.2.4 Slab models with prominence–corona transition region

The previous results rely on models in which the prominence and coronal temperatures are uniform, with a sharp jump of this physical variable from the cool to the hot region at an infinitely thin interface. A smoothed temperature transition between the two domains, representing the prominence–corona transition region (PCTR), was used by Oliver and Ballester (1996) to investigate the MHD modes of a more realistic configuration. Despite the presence of the PCTR in the equilibrium model, internal, external and hybrid modes are still supported, just like in configurations with two uniform temperature regions. Nevertheless, the PCTR results in a slight frequency shift and in the modification of the spatial velocity distribution so as to decrease the oscillatory amplitude of internal modes inside the prominence. Hybrid modes are not so much affected by the presence of the PCTR because their characteristic wavelength is much longer than the width of the PCTR. Then, the conclusion is that the PCTR may influence the detectability of periodic prominence perturbations arising from internal modes.

6.2.5 Stability of two-dimensional prominence models

Some two-dimensional equilibrium models were considered by Galindo Trejo (1987, 1989b, a, 1998, 2006). The focus of these works was in the stability properties of prominence equilibrium configurations (using the MHD energy principle of Bernstein et al. 1958) and for this reason the author concentrated in the lowest eigenvalue squared. This means that information about all other modes of the system is absent; see Figs. 41 and 42.

Galindo Trejo (1987) considered four prominence models, namely those by Kippenhahn and Schlüter (1957), Dungey (1953), Menzel (1951) and Lerche and Low (1980). All these models are isothermal, i.e., they do not incorporate the corona around the prominence plasma. This implies that the important hybrid modes are absent in the analysis. In spite of this, some interesting results were obtained by Galindo Trejo (1987). Here we only mention the most relevant ones. For example, the fundamental mode of the Kippenhahn–Schlüter configuration, whose period is 16 min, has motions polarised mainly across the prominence slab, so it can be associated with the internal slow mode. On the other hand, the fundamental mode of Dungey's model has horizontal motions mostly along the prominence axis (such as corresponds to Alfvén waves) which are more important at the top of the prominence than at the bottom. The oscillatory period ranges from 55 to 80 min. In the case of Menzel's model, the lowest frequency eigenmode has a period of 40 min and motions whose amplitude increases with height and oriented across the prominence. The eigenmode of Lerche and Low's solution presents a greater range of periods (17–50 min) and, once more, with horizontal plasma displacements transverse to the prominence axis. Two improvements of this elaborated work can be done: the inclusion of the coronal plasma and the consideration of the oscillatory properties of other modes.

In two subsequent papers the stability of the prominence model of Low (1981) was investigated. In the first one (Galindo Trejo 1989b) a uniform magnetic field component along the prominence axis was used, whereas in the second one (Galindo Trejo 1989a) this quantity is not uniform. The author concluded that, as long as this magnetic field component is weak, these different choices of the magnetic configuration do not influence much the period of the fundamental mode, which is in the range 3–7 min.

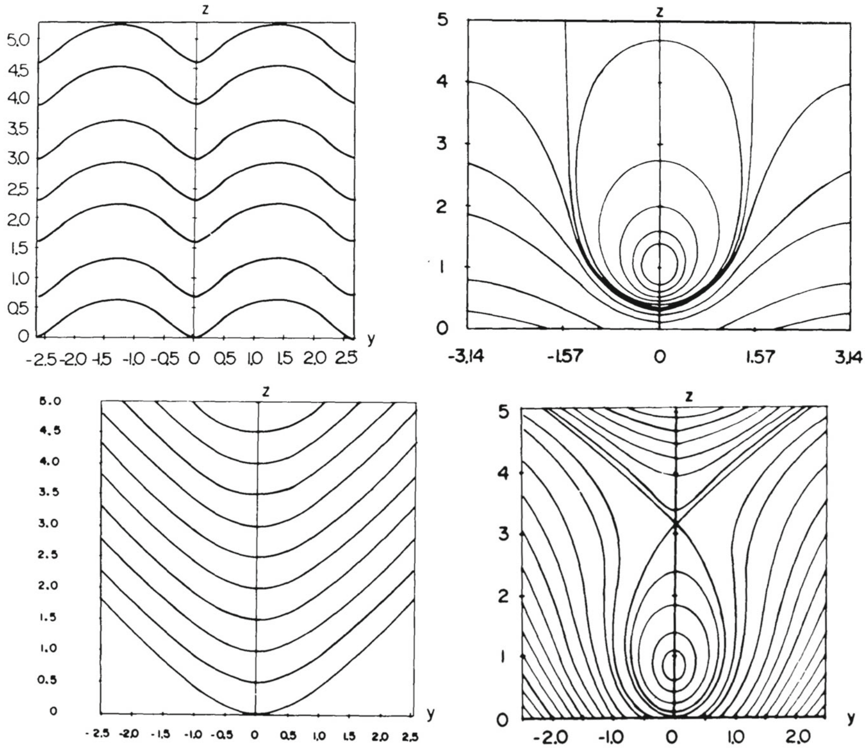

Fig. 41 Magnetic field configuration of the two-dimensional quiescent prominence models whose stability was analysed by Galindo Trejo (1987). Top left: Menzel (1951) model. Top right: Dungey (1953) model. Bottom left: Kippenhahn and Schlüter (1957) model. Bottom right: Lerche and Low (1980) model. These panels do not include all configurations inspected by Galindo Trejo (1987)

The spatial distribution of motions is similar to that found by Galindo Trejo (1987) for Menzel's and Lerche and Low's equilibrium models.

The following paper of this series (Galindo Trejo 1998) is concerned with the prominence model of Osherovich (1985), which is characterised by a surrounding horizontal magnetic field connected with the prominence field. Different values of the equilibrium parameters were used and as a result the fundamental mode has periods that range from 4 to 84 min. Galindo Trejo (1998) found that for small values of the longitudinal magnetic field component large velocity amplitudes predominate in the upper part of the prominence, while the opposite happens for a stronger longitudinal component. The magnetic field shear is also relevant: for a moderate (and hence non-uniform) shear, the fundamental eigenmode is in the intermediate-period range and for a uniform shear long periods are obtained.

Galindo Trejo (2006) investigated the equilibrium solution of Osherovich (1989), that is characterised by an external vertical magnetic field that allows the prominence to be placed on the boundary between two regions of opposite photospheric magnetic polarity. A wide range of periods was obtained in this work (9–73 min). Also, horizontal oscillatory motions either along the prominence or almost across it were

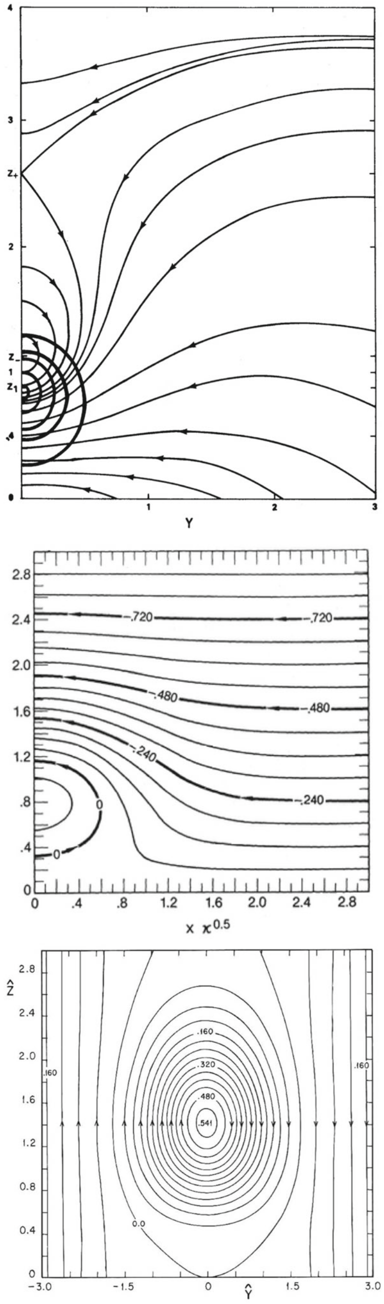

Fig. 42 Magnetic field configuration of the two-dimensional quiescent prominence models whose stability was analysed by Galindo Trejo (1989b, a, 1998, 2006). Top: Low (1981) model, middle: Osherovich (1985) model, bottom: Osherovich (1989) model. These panels do not include all configurations inspected by Galindo Trejo (1989b, a, 1998, 2006). Images reproduced with permission, copyright by AAS

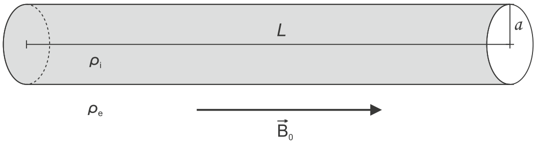

Fig. 43 Sketch of an infinitely long thread immersed in the solar corona. The prominence thread and the coronal density (ρ_i and ρ_e) are denoted as ρ_p and ρ_c in the text. Image reproduced with permission from Lin et al. (2009), copyright by AAS

found. Therefore, it seems that in most configurations studied by Galindo Trejo the fundamental oscillatory mode is a slow mode.

6.3 Fine structure oscillations (propagating waves)

Prominence models considered in Sects. 6.1, 6.2 and 4.4 are very simplified representations of solar prominences. They provide us with information about a prominence global oscillatory behaviour, but high resolution observations (see Sects. 5.6 and 5.9.4) have given us detailed information about the local oscillatory behaviour of the fine, internal structure of filaments. This has prompted the study of thread oscillations. From the existing observational evidence, two situations can be considered: waves propagating along a thread (treated in this section) and standing modes, presumably with a wavelength of the order of the length of the supporting magnetic tube and thus much larger than the thread length (these works are presented in Sect. 6.4.) Other important ingredients uncovered by observations (Sects. 5.6 and 5.9.4) are the collective behaviour and the presence of flows in some oscillating threads. These features have been incorporated into some investigations and will be also discussed here.

6.3.1 Individual thread oscillations

A simple thread model consists of an infinitely long cylinder filled with cold, dense plasma and embedded in the hotter and less dense corona; field line curvature is neglected. The magnetic field is parallel to the cylinder axis and uniform everywhere (Fig. 43).

The MHD modes of this structure have been extensively studied in the context of coronal and photospheric magnetic tube oscillations (Spruit 1982; Edwin and Roberts 1983; Cally 1986). The mode of interest here is the kink mode because it is the only one that produces a significant transverse displacement of the thread, which is the observed behaviour of oscillating threads. In the absence of mass flows and assuming that the thread radius is much smaller than the wavelength, the kink frequency is given by

$$\omega_\mathrm{k} = k_z \sqrt{\frac{\rho_\mathrm{p} v_\mathrm{Ap}^2 + \rho_\mathrm{c} v_\mathrm{Ac}^2}{\rho_\mathrm{p} + \rho_\mathrm{c}}} = k_z v_\mathrm{Ap} \sqrt{\frac{2\zeta}{1+\zeta}}, \tag{30}$$

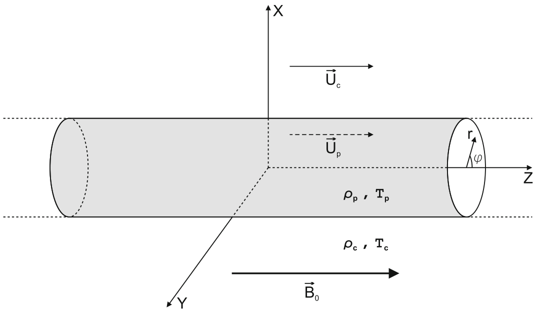

Fig. 44 Sketch of an infinitely long thread immersed in the solar corona. The respective flow speeds in the thread and the corona are denoted by U_p and U_c. Image reproduced with permission from Soler et al. (2008), copyright by AAS

with k_z the axial wavenumber, ρ_p and ρ_c the prominence thread and coronal densities, $\zeta = \rho_\mathrm{p}/\rho_\mathrm{c}$ the density contrast and $v_{\mathrm{Ap,c}} = B/\sqrt{\mu\rho_{\mathrm{p,c}}}$ the prominence thread and coronal Alfvén velocities. In terms of the density contrast, the period of kink oscillations with wavelength $\lambda = 2\pi/k_z$ can then be written as

$$P = \frac{\sqrt{2}}{2}\frac{\lambda}{v_{\mathrm{Ap}}}\left(\frac{1+\zeta}{\zeta}\right)^{1/2}. \tag{31}$$

Note that the factor containing the density contrast varies between $\sqrt{2}$ and 1 when ζ is allowed to vary between a value slightly larger that 1 (extremely tenuous thread) and $\zeta \to \infty$. This defines a narrow range of Alfvén speed values when the inverse problem is solved for plasma diagnostic purposes (see Sect. 8). One can plug typical parameter values into Eq. (31) and periods ranging from 30 s to a few minutes are obtained. This result is in agreement with the observed periods of traveling waves in threads (see Sect. 5.9.4).

This formula for P is based on the assumption that the wavelength is much larger than the thread radius (this approximation is also know as the thin tube limit). Propagating waves in threads have been detected by, e.g., Lin et al. (2007) (see Sect. 5.9.4 and Fig. 32). The reported wavelength is 3.8$''$ and the radius of threads is typically between 0.1 and 0.15$''$, which proves that the assumption made to derive Eq. (31) is satisfied in this event.

Soler et al. (2008) considered non adiabatic waves and included a mass flow parallel to the magnetic field in the thread model of Fig. 44, which is identical to that of Fig. 43 except for the inclusion of plasma flows. Without loss of generality the flow speed in the corona was neglected in this last work, while typical values observed in prominences were taken for the flow speed in the thread (namely $U_\mathrm{p} \leq 30\,\mathrm{km\ s^{-1}}$). In the absence of flow, the complex oscillatory frequencies for a fixed, real and positive wavenumber k_z appear in pairs, $\omega_1 = \omega_\mathrm{R} + i\omega_\mathrm{I}$ and $\omega_2 = -\omega_\mathrm{R} + i\omega_\mathrm{I}$. The solution ω_1 corresponds to a wave propagating towards the positive z-direction (parallel to magnetic field lines). The ω_2 solution corresponds to a wave that propagates toward the negative z-direction (anti-parallel to magnetic field lines). Both solutions have exactly the same physical properties in the absence of flows. In the presence of flow, the frequencies are Doppler shifted. In addition, the symmetry between parallel and anti-parallel propagation is broken. For instance, for strong enough flows, slow waves can only propagate parallel

Fig. 45 Period of the fundamental oscillatory modes of an infinitely long thread versus the mass flow, U_{p}. The top, middle and bottom panels correspond to the slow, kink and thermal modes. Different line styles correspond to waves propagating in the absence of flow (dotted), parallel waves (solid) and anti-parallel waves (dashed). The wavenumber is given by $k_z a = 10^{-2}$, which is consistent with the wavelength of observed propagating waves in prominences (Sect. 5.9); a is the thread radius. Image reproduced with permission from Soler et al. (2008), copyright by AAS

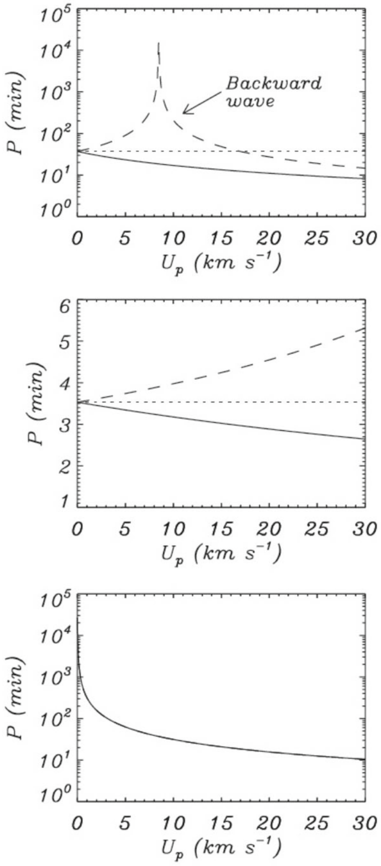

to the flow direction, anti-parallel propagation being forbidden. Figure 45 presents the period of the slow, fast and thermal modes as a function of the flow speed in the thread. For $U_{\mathrm{p}} \neq 0$ the fast and slow waves acquire different periods that diverge as U_{p} is increased. For $U_{\mathrm{p}} \sim 8.5$ km s^{-1} the anti-parallel slow wave becomes a backward wave, which causes its period to grow dramatically near this flow velocity. The influence of the flow on the fast mode is not so severe, while the thermal mode has a finite period that takes very large values.

6.3.2 *Collective thread oscillations*

Some authors have reported that groups of threads oscillate in unison (e.g., Yi et al. 1991) and that large areas of a prominence present in-phase oscillations (e.g., Terradas et al. 2002; Lin et al. 2007), which may be also taken as a sign of collective thread behaviour (see Sects. 5.6, 5.9.3 and 5.9.4). Similar collective oscillations have been observed in coronal loops (Verwichte et al. 2004) and their properties have been studied by, e.g., Murawski (1993), Luna et al. (2008), Doorsselaere et al. (2008b) and

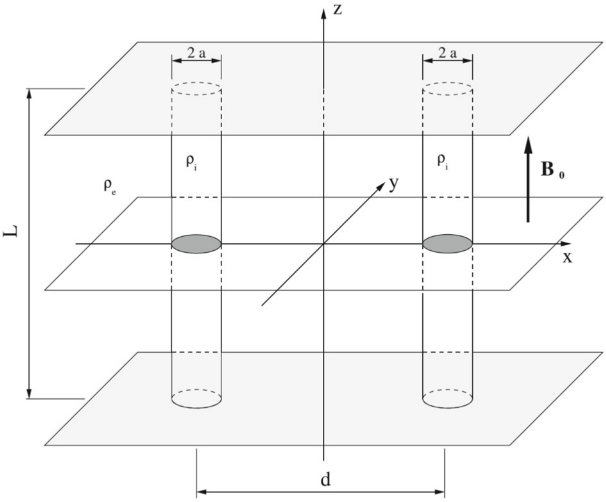

Fig. 46 Sketch of an equilibrium model made of two infinitely long threads embedded in the solar corona. Image reproduced with permission from Luna et al. (2008), copyright by AAS

Robertson and Ruderman (2011). To model this situation, an equilibrium model made of two homogeneous and infinitely long prominence threads embedded in the coronal medium has been considered (see Fig. 46).

When identical threads are considered, the system exhibits four kink-like transverse oscillatory modes (Luna et al. 2008; Soler et al. 2009c). These modes are denoted by S_x, A_x, S_y and A_y. The S and A denote symmetry or antisymmetry of the total pressure perturbation with respect to the yz-plane. The subscript describes the main direction of polarisation of motions, that lie in the xy-plane; the choice of the coordinate axes is shown in Fig. 46 and the spatial distribution of the modes is displayed in Fig. 47. In addition to the kink-like modes, Soler et al. (2009c) studied the collective slow modes and obtained only two fundamental collective solutions, one symmetric and the other antisymmetric with respect to the yz-plane, with motions mainly polarised along the z-direction (Fig. 47).

A measure of the interaction between threads is the frequency of their normal modes. If the modes have frequencies similar to that of the isolated cylinder, then the threads oscillate independently from one another. If the frequencies are significantly different, the threads oscillate in a collective manner. The left panel of Fig. 48 displays the frequency of the four kink-like solutions as a function of the distance between cylinders. For large separations, i.e., for a distance between threads larger than about 6 or 7 radii, the collective kink mode frequencies are almost identical to the individual kink frequency. This is a signature of a weak interaction between threads, which behave as independent structures. On the other hand, for small thread separations, the four frequencies separate in two branches as a consequence of a strong interaction between the cylinders. Therefore, the collective behaviour of oscillations becomes stronger when the threads are closer. In the case of slow modes the interaction between threads is almost negligible and as a result the frequencies of the S_z and A_z modes

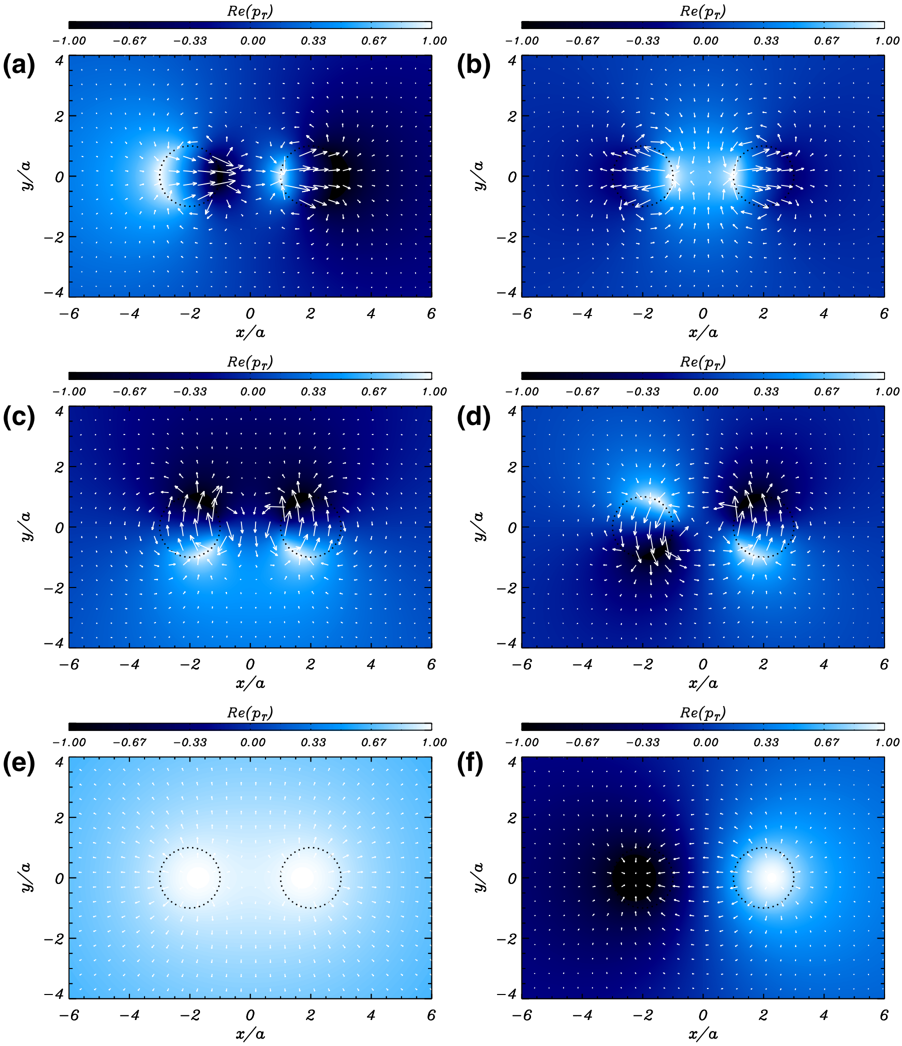

Fig. 47 Fundamental normal modes of two parallel and infinitely long threads (Fig. 46). Total pressure perturbation field (contour plot in arbitrary units) and transverse Lagrangian displacement vector field (arrows) in the xy-plane for the wave modes **a** S_x, **b** A_x, **c** S_y, **d** A_y, **e** S_z and **f** A_z for a separation between threads $d = 4a$ and a longitudinal wavenumber $k_z a = 10^{-2}$, where a is the thread radius. The prominence thread boundaries are denoted by dotted circles. Image reproduced with permission from Soler et al. (2009c), copyright by AAS

are almost identical to the individual slow mode frequency (cf. right panel of Fig. 48) in the whole range of thread separations. This is in agreement with the fact that transverse motions (responsible for the interaction between threads) are not significant for slow modes in comparison with their longitudinal motions. Therefore, the S_z and A_z modes essentially behave as individual slow modes, contrary to kink-like modes, which display a more significant collective behaviour.

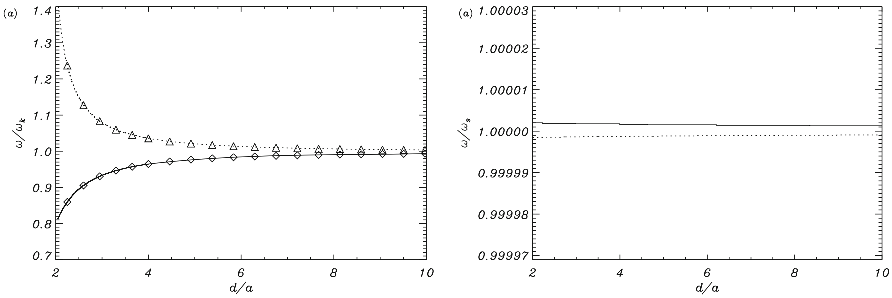

Fig. 48 Fundamental normal modes of two parallel and infinitely long threads (Fig. 46). Left: Ratio of the frequency of the four collective kink-like modes, ω, to the frequency of the individual kink mode, ω_{k}, as a function of the normalised distance between strand axes. Meaning of symbols: S_x (solid line), A_x (dotted line), S_y (triangles) and A_y (diamonds). Right: ratio of the frequency of the two collective slow modes, ω, to the frequency of the individual slow mode, ω_{S}, for the S_z (solid line) and A_z (dotted line). Image reproduced with permission from Soler et al. (2009c), copyright by AAS

Fig. 49 Cross-section of a two-thread model analogous to that of Fig. 46 with the addition of mass flows along the cylinders. Image reproduced with permission from Soler et al. (2009c), copyright by AAS

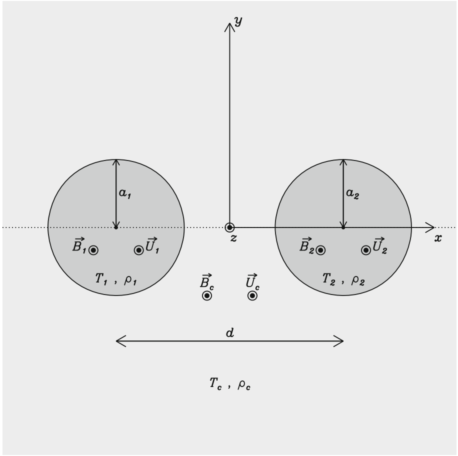

Soler et al. (2009c) assessed the effect of material flows along two threads on the behaviour of collective modes (see Fig. 49 for a sketch of the model). Arbitrary flows U_1 and U_2 were assumed in both cylinders, while coronal flows were neglected. The first main conclusion of this work is that the flows do not eliminate wave modes with collective dynamics (i.e., those that produce significant perturbations in the two threads), even in the case $U_1 \neq U_2$. Nevertheless, the requisite for retaining the collective dynamics is that the Doppler-shifted individual frequencies of the threads must be very similar. In the case of kink-like modes the Doppler-shifted frequencies are given by

$$\Omega_{\mathrm{k}1} = \omega_{\mathrm{k}1} + U_1 k_z, \tag{32}$$

$$\Omega_{\mathrm{k}2} = \omega_{\mathrm{k}2} + U_2 k_z, \tag{33}$$

where $\omega_{\mathrm{k}1}$ and $\omega_{\mathrm{k}2}$ are the kink frequencies of each thread, which are not equal if the thread densities differ. In the limit $\lambda \gg a$, with a the tube radius, these frequencies are given by Eq. (30). Now, the requirement for the two threads to oscillate in phase rather than independently is $\Omega_{\mathrm{k}1} \sim \Omega_{\mathrm{k}2}$. Using Eq. (30) and making the reasonable assumption that the density contrast in both cylinders is much larger than one, Soler et al. (2009c) obtained

$$U_1 - U_2 \approx \pm\sqrt{2}\,(v_{\mathrm{A}2} - v_{\mathrm{A}1})\,, \tag{34}$$

where the + sign is for parallel waves and the − sign is for anti-parallel propagation. A similar analysis can be performed for slow modes to obtain,

$$U_1 - U_2 \approx \pm\,(c_{\mathrm{s}2} - c_{\mathrm{s}1})\,. \tag{35}$$

which points out that the coupling between slow modes occurs at different flow velocities than the coupling between kink modes. Therefore, the simultaneous existence of collective slow and kink-like solutions in systems of non-identical threads is difficult. In the above equations, $v_{\mathrm{A}1,2}$ and $c_{\mathrm{s}1,2}$ correspond to Alfvén and sound speeds in both threads, respectively.

Soler et al. (2009c) extracted another conclusion from Eqs. (34) and (35): the difference between the Alfvén (sound) speed of the threads determines the difference of the flow speeds for the existence of collective behaviour of kink (slow) modes. Therefore, when flows are present in the equilibrium, collective motions can be found even in systems of non-identical threads for very specific combinations of the two flow velocities. These velocities are within the observed values in prominences if threads with not too different temperatures and densities are considered. However, since the flow velocities required for collective oscillations must take very particular values, such a special situation may rarely occur in prominences. This conclusion has important repercussions for future prominence seismological applications, given that if collective oscillations are observed in large areas of a prominence, threads in such regions should possess very particular combinations of temperatures, densities, magnetic field strengths and flows.

6.4 Fine structure oscillations (standing waves)

Filament threads have been modelled as magnetic flux tubes anchored in the solar photosphere which are stacked one on top of one another in the vertical and horizontal directions, giving place to the filament body. In the models presented in this section a thread is envisaged as a cold, dense condensation that fills the central part of a magnetic tube containing hot coronal plasma and anchored in the solar photosphere. Although this structure has been modelled with some complexity (Ballester and Priest 1989; Rempel et al. 1999), only oscillations of much simpler thread configurations have been investigated so far. Because the reported thread oscillations are transverse, we here concentrate on works that investigate this kind of motions.

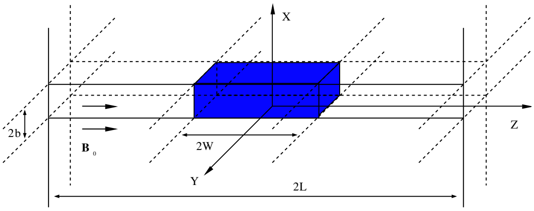

Fig. 50 Sketch of the thread equilibrium model used by Joarder et al. (1997), Díaz et al. (2001, 2003). The blue zone of length $2W$ represents the cold part of the flux tube, i.e., the prominence thread. The length of the magnetic structure is $2L$ and the thread thickness (equivalent to its diameter) is $2b$. The magnetic field is uniform and parallel to the z-axis, and the whole configuration is invariant in the y-direction. Image reproduced with permission from Díaz et al. (2001), copyright by ESO

6.4.1 Cartesian geometry

Joarder et al. (1997) considered a thin thread with finite width and length in Cartesian geometry (Fig. 50). The thread is infinitely deep since the equilibrium configuration is invariant along the y-axis. The influence of the plasma pressure was neglected (i.e., the zero-β limit was taken) and consequently the slow mode is absent from their analysis. Joarder et al. (1997) obtained the dispersion relations for Alfvén and fast modes, and restricted their study to the oscillatory frequencies, omitting other properties that are also relevant for the understanding of oscillations such as the spatial structure and the polarisation of perturbations.

Using the same two-dimensional configuration, Díaz et al. (2001) performed an analytical and numerical study of the behaviour of fast modes when a proper treatment of the boundary conditions at the different interfaces of this thread configuration is included. The main conclusion is that prominence threads can only support a few non-leaky modes of oscillation, those with the lowest frequencies. Also, for reasonable values of the thread length, the spatial structure of the fast fundamental even and odd kink modes is such that the velocity amplitude outside the thread takes large values over long distances (Fig. 51). Fast kink modes are associated to normal motions with respect to the thread length (i.e., in the x-direction; see Fig. 50). The fundamental kink mode (simply referred to as the kink mode) has a velocity maximum at the thread centre, while its first overtone (that is, the fundamental odd kink solution) has a node in the same position.

Later on, Díaz et al. (2003) included wave propagation in the y-direction (see Fig. 50) making the model fully three-dimensional, and two important features appeared. The first is that the cut-off frequency, that separates confined and leaky modes, varies with the longitudinal wavenumber (k_y), which allows the structure to trap more modes. The second one is that a much better confinement of the wave energy is obtained compared to the $k_y = 0$ case (see Fig. 52). An interesting issue concerning these results obtained using Cartesian threads is that large velocity amplitudes are found in the corona, which seems to favour collective thread oscillations over individual oscillations.

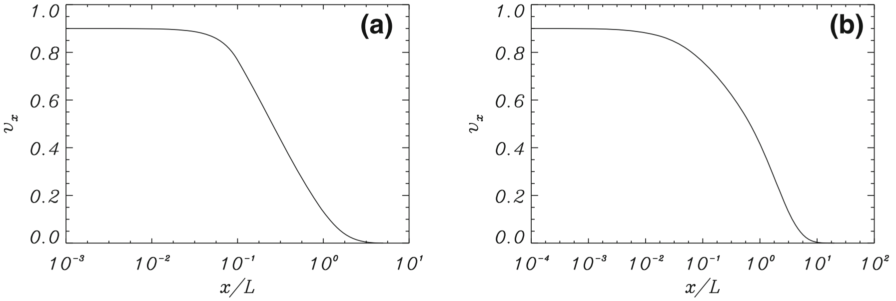

Fig. 51 Kink mode normal velocity component across the axis of the Cartesian prominence thread depicted in Fig. 50. Solutions are symmetric about the thread axis ($x = 0$) and so they are only shown for $x \geq 0$. The length of magnetic field lines is $2L = 200{,}000$ km. **a** In a very thick thread (with a "radius" of 10,000 km) the perturbation is essentially confined to the thread itself, i.e., to $0 \leq x/L \leq 0.1$. **b** In an actual thread (with a "radius" of 100 km) the velocity displays a large amplitude beyond the thread boundary, at $x/L = 0.001$. This means that wave energy spreads into the surrounding coronal medium. Image reproduced with permission from Díaz et al. (2001), copyright by ESO

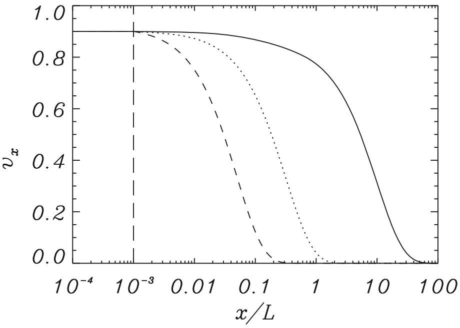

Fig. 52 Normal velocity component (in arbitrary units) of the kink mode in the direction across the thread axis. The ratio of the thread "diameter" to the length of magnetic field lines is 0.001, while the ratio of the thread length to the field lines length is 0.1. The solid, dotted and dashed lines correspond to $k_y L = 0$ (curve of Fig. 51b), $k_y L = 3$ and $k_y L = 20$. All other parameter values are those of Fig. 51. The thread boundary is marked by a vertical dashed line. Image reproduced with permission from Díaz et al. (2003), copyright by ESO

6.4.2 Cartesian geometry: collective thread oscillations

Taking into account observations by, e.g., Lin (2005), which suggest in-phase oscillations of neighbouring threads in a filament, Díaz et al. (2005) studied multi-thread systems in Cartesian geometry. The equilibrium configuration consists of a collection of two-dimensional threads modelled as in Díaz et al. (2001) and separated by an adjustable distance $2c$ (Fig. 53). An inhomogeneous filament composed of five threads was constructed (Fig. 54) with thread density ratios thought to represent the density inhomogeneity of a prominence. The separations between threads were chosen randomly within a realistic range. The thread separations were then changed with respect to the values of Fig. 54 by a certain factor and the kink modes were computed. Their frequencies are displayed in Fig. 55, where c_{ref} is a reference value representative of

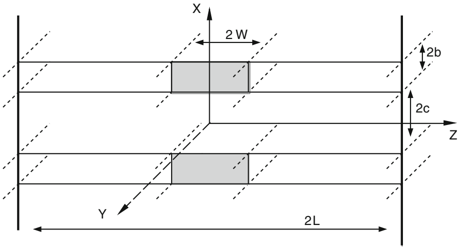

Fig. 53 Sketch of a multi-thread equilibrium configuration. The grey zone represents the cold part of the magnetic tube, i.e., the prominence. The magnetic field is uniform and parallel to the z-axis, and the whole configuration is invariant in the y-direction. Image reproduced with permission from Díaz et al. (2005), copyright by ESO

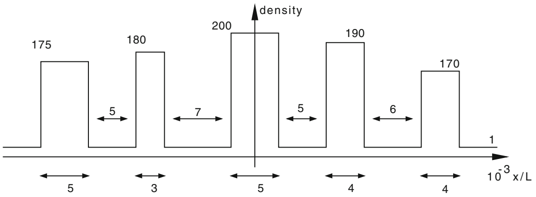

Fig. 54 Sketch of the density profile in the direction $z = 0$ of an inhomogeneous multi-thread system, where the density values are normalised to the coronal value. Between and under the threads the dimensionless separation, $2c/L$, and "diameter", $2b/L$, are given. Image reproduced with permission from Díaz et al. (2005), copyright by ESO

the separations between threads. When the separations are small, i.e., for $c_{\text{ref}}/L \ll 1$, there is a strong interaction between threads since the perturbed velocity in a given thread can easily extend over its neighbours. As a result, there is only one even non-leaky mode: the one producing in-phase oscillations of all threads. The other extreme of Fig. 55, i.e., $c_{\text{ref}}/L \gg 1$, corresponds to very large separations. In this situation, all threads oscillate independently and the individual kink mode frequencies are recovered. Note that realistic thread separations correspond to $c_{\text{ref}}/L \sim 10^{-3} - 10^{-2}$, for which only the kink mode mentioned before is supported by the system. Its frequency is lower than the individual kink mode frequencies. Although these results show some agreement with observations about the collective oscillations of threads, the use of Cartesian geometry favours this kind of combined behaviour and so a similar study based on a cylindrical model is also of interest.

Díaz and Roberts (2006) studied the properties of the fast MHD modes of a periodic, Cartesian thread model (see Fig. 1 of Díaz and Roberts 2006). This configuration represents a bridge between a structure with a limited number of threads (studied by Díaz et al. 2005, see Fig. 53) and a homogeneous prominence with a transverse magnetic field (investigated by Joarder and Roberts 1992b, see Fig. 37). Díaz and Roberts (2006) found that for thread separations of the order of their thickness the only confined modes are those in which large numbers of threads are constrained to oscillate nearly in phase. The spatial structure of these solutions is similar to that of the propagating modes of a homogeneous prominence, with small-scale deviations due to the presence of the dense threads. Their period is equal to $\sqrt{f}P$, with P the

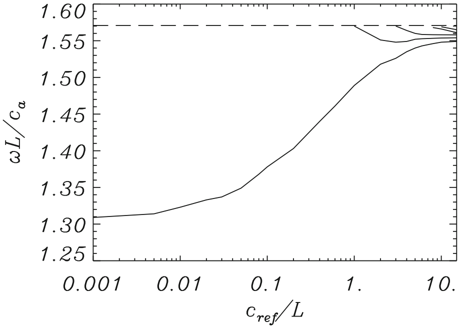

Fig. 55 Dimensionless frequency versus the dimensionless reference separation between threads in a multi-thread system. In this figure c_a is the Alfvén speed in the corona. Image reproduced with permission from Díaz et al. (2005), copyright by ESO

period of the prominence slab and f the filling factor. The system with a limited number of threads has an even shorter period and a comparison between the different configurations considered by Díaz and Roberts (2006) gives periods of 23.6 min for the homogeneous prominence, between 12.1 and 19.3 min for the system of periodic threads and 5.3 for the four-thread configuration studied by Díaz et al. (2005). Hence, the main conclusion of Díaz and Roberts (2006) is that prominence fine structure plays an important role and cannot be neglected.

6.4.3 Cylindrical thread

Since cylindrical geometry is more suitable to model prominence threads, Díaz et al. (2002) considered a straight cylindrical flux tube with a cool region representing the prominence thread, which is confined by two symmetric hot regions (Fig. 56). With this geometry, the fundamental sausage mode ($m = 0$, with m the azimuthal wavenumber) and its overtones are always leaky. However, for all other modes ($m > 0$), at least the fundamental solution lies below the cut-off frequency. Hence, if any of these modes is excited, the oscillatory energy in the prominence plasma does not vary in time after the initial transient has elapsed. Regarding the spatial structure of perturbations, in cylindrical geometry the modes are always confined to the dense part of the flux tube (Fig. 57). Therefore, an oscillating cylindrical thread is less likely to induce oscillations in its neighbouring threads than a Cartesian one.

To study the oscillations of the above mentioned configurations, Díaz et al. (2001, 2002) developed a very general, although cumbersome procedure. However, Dymova and Ruderman (2005) considered the same problem and to simplify its study took advantage of the fact that the observed thickness of oscillating threads is orders of magnitude shorter than their length. Taking this into account, Dymova and Ruderman (2005) used the so-called thin flux tube (TT) approximation, that enables a simpler solution for the MHD oscillations of longitudinally inhomogeneous magnetic tubes. Once the partial differential equation for the total pressure perturbation is obtained, a different scaling (stretching of radial and longitudinal coordinates) of this equation inside the tube and in the corona can be performed. Following this procedure, two

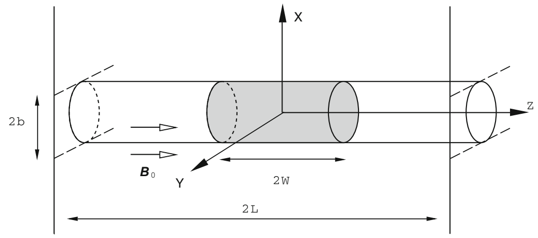

Fig. 56 Sketch of the equilibrium configuration of a thread in a cylindrical coronal magnetic tube. The gray zone of length $2W$ represents the cold part of the flux tube, i.e., the prominence thread. The length of the magnetic structure is $2L$ and the thread radius is b. The magnetic field is uniform and parallel to the z-axis, and the whole configuration is invariant in the φ-direction. Image reproduced with permission from Díaz et al. (2002), copyright by AAS

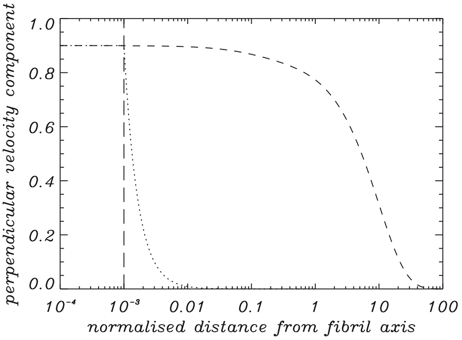

Fig. 57 Cut of the normal velocity component in Cartesian geometry (dashed line, i.e., curve of Fig. 51b) and the radial velocity component in cylindrical geometry (dotted line) in the direction across the thread axis. These solutions correspond to the (fundamental) kink mode in a prominence thread with the parameter values used in Fig. 52. The vertical long dashed line marks the thread boundary. Image reproduced with permission from Díaz et al. (2002), copyright by AAS

different equations for the total pressure perturbation inside and outside the flux tube, with well known solutions, are obtained. After imposing boundary conditions, the analytical dispersion relations for even and odd modes were derived and a parametric study was performed. A comparison between the numerical values of the periods obtained with this approach and that of Díaz et al. (2002) points out differences of the order of 1%. The only drawback of the method of Dymova and Ruderman (2005) is that it can be only applied to the fundamental mode with respect to the radial dependence.

6.4.4 *Flowing cylindrical thread*

Terradas et al. (2008) modelled the transverse oscillations of flowing prominence threads observed by Okamoto et al. (2007) with Hinode/SOT (Sect. 5.9.4). The kink oscillations of a flux tube containing a flowing dense part, which represents the prominence material, were studied from both the analytical and the numerical point of view. In the analytical case, the Dymova and Ruderman (2005) approach with the inclusion of flow was used, while in the numerical calculations the linear ideal MHD equations were solved. The results point out that for the observed flow speeds there is almost no difference between the oscillation periods when static versus flowing threads are considered, and that the oscillatory period matches that of a kink mode. In addition, to obtain information about the Alfvén speed in oscillating threads, a seismological analysis as described in Sect. 8.6 was also performed.

Also motivated by the observations by Okamoto et al. (2007), Soler and Goossens (2011) have further studied the properties of kink MHD waves propagating in flowing threads. In good agreement with Terradas et al. (2008), the period is seen to be slightly affected by mass flows. When the thread is located near the centre of the supporting magnetic tube, and for realistic flow velocities, the effect of the flow on the period is estimated to fall within the error bars from observations. On the other hand, as the thread approaches the footpoint of the magnetic structure, flows introduce differences up to 50% in comparison to the static case. The variation of the amplitude of kink waves due to the flow is additionally analysed by Soler and Goossens (2011). It is found that the flow leads to apparent damping or amplification of the oscillations. During the motion of the prominence thread along the magnetic structure, the amplitude grows as the thread gets closer to the centre of the tube and decreases otherwise. This effect might be important, since it would modify the actual observed attenuation, if any physical damping mechanism is present.

6.4.5 *Some remarks about Cartesian and cylindrical thread models*

Theoretical models described in this section have considered prominence plasmas as either slabs or cylindrical magnetic flux tubes. Slab models were intended to study the global oscillation properties of prominences, while flux tube models seem to be more appropriate for their application to the fine structure of prominences. Nevertheless, the properties of modes of oscillation like the kink mode have often been first studied in Cartesian geometry and then in cylindrical configurations, because the mathematical treatment is simpler in the first geometry. It is worth emphasising that the deformation of a slab or a cylinder boundary looks similar when perturbed by a kink mode: at any time it has a sinusoidal shape, the same of the slab or cylinder axis, with opposite boundary points with respect to the axis having an anti-symmetric displacement. On the other hand, the sausage mode gives rise to a symmetric perturbation of the boundary with respect to its axis, which remains undisturbed. A few differences that arise between Cartesian and cylindrical geometries are relevant when comparing the theoretical results to observations.

The theoretical frequencies for the kink mode in Cartesian geometry are above the value obtained for a cylindrical equivalent with the same physical properties. This has been shown by Arregui et al. (2007), in the context of coronal loop oscillations. By assuming that a kink mode in a cylinder can be modelled in Cartesian geometry by adding a large perpendicular wave number, these authors show that in that limit the cylindrical kink mode frequency is recovered. A similar analogy was used by Hollweg and Yang (1988) who derived an expression for the damping time of a surface wave in Cartesian geometry and applied their result to coronal loops in the limit of large perpendicular wave number.

The spatial distribution of the eigenfunctions also differs when one compares, e.g., the kink mode properties in Cartesian and cylindrical geometry. The drop-off rate of the transverse velocity component is faster in cylindrical flux tubes than in slabs. A cylinder is a much better wave guide. For this reason, an oscillating cylindrical thread is less likely to induce oscillations in its neighbouring threads than a Cartesian thread.

6.5 Numerical magnetohydrodynamic models

The bulk of works in Sects. 6.1, 6.2, 6.3 and 6.4 have several limitations, the most remarkable being the linear approximation assumed (which is valid as long as the velocity amplitude is small) and the simplicity of the equilibrium models (which facilitates the computation of solutions to the MHD equations). Here we summarise works in which the temporal evolution of a prominence model is derived by solving the time–dependent (linear or non-linear) MHD equations. Note that small amplitude oscillations with maximum velocities of the order of the prominence sound speed ($\simeq$ 10 km s^{-1}) have been detected in a few works, e.g., Li and Zhang (2013) and Hillier et al. (2013); see Sect. 5.5. Non-linear effects may be important here.

6.5.1 Impulsive excitation

Terradas et al. (2013) constructed two-dimensional prominence equilibria by loading a coronal arcade by a continuous mass injection. After this process was finished the system was allowed to settle down into an equilibrium that was then perturbed by imposing either a vertical or a horizontal disturbance of the prominence. The time–dependent, linear, ideal MHD equations were solved numerically to study the resulting prominence oscillations.

Vertical oscillations, that are associated with fast MHD waves, are stable for all parameter values considered by Terradas et al. (2013). Their periods were computed for six configurations (corresponding to the combinations of three chosen values of prominence mass and two chosen values of magnetic field strength) and lie in the range 4–10 min. Figure 58 (left) displays the dependence of the period of vertical oscillations with respect to the length of the field line passing through the prominence centre (L_{fl}). One can appreciate that the period only shows some dependence on L_{fl} in the range of small values of this parameter. Furthermore, by comparing each thin line with its thick counterpart one can see that a change of a factor of 2 in the Alfvén speed lowers the periods by the same factor, which hints at a linear relation between the Alfvén speed and the frequency. Finally, the period also becomes larger when the prominence mass is increased.

The periods of horizontal oscillations (transverse to the prominence axis), presented in Fig. 58 (right), range between 15 and 40 min. In this case motions are mostly along the unperturbed magnetic field and so they correspond to slow modes. In the low β regime, considered by Terradas et al. (2013), slow waves have little dependence on the magnetic field strength and for this reason the periods of a pair of thin and thick lines are rather similar. Moreover, the periods of horizontal (slow) oscillations are almost an order of magnitude larger than those of vertical (fast) oscillations, such as

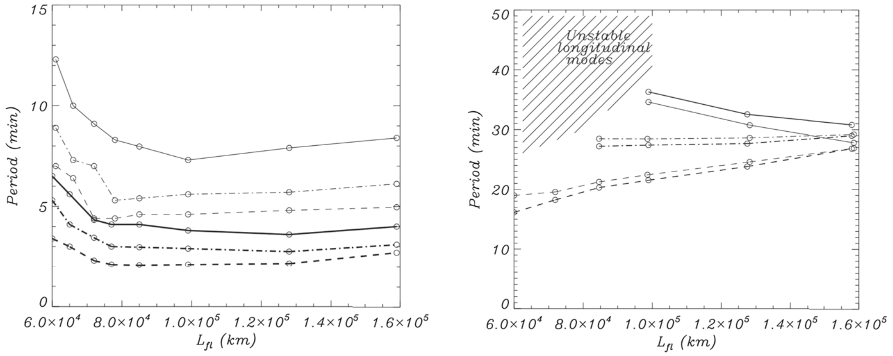

Fig. 58 Period of vertical (left panel) and horizontal (right panel) oscillations of the two-dimensional prominence model of Terradas et al. (2013) versus the length of the field line passing through the prominence centre. Solid, dash-dotted and dashed lines correspond to the prominence mass per unit length (in the ignorable direction) equal to 5.4×10^5, 2.7×10^5 and 1.3×10^5 kg km^{-1}, respectively. Thin/thick curves are associated with $v_{A0} = 10c_{s0}$ and $v_{A0} = 20c_{s0}$, respectively, where v_{A0} and c_{s0} denote the Alfvén and sound speeds at the prominence centre. The hatched area on the right panel shows the instability region of horizontal modes. Image reproduced with permission from Terradas et al. (2013), copyright by AAS

expected from the ratio of slow to Alfvén speed. An outstanding property of horizontal oscillations is that they become unstable for large prominence masses and short field line lengths. Unstable solutions are characterised by an initial oscillatory behaviour followed by an exponential increase of perturbations. The reason for this instability is that short field lines have small dips that can hold up little mass; then, this mass can easily fall down by the effect of gravity when the prominence oscillates sideways. Hence, by reducing both L_{fl} and the prominence mass the instability is favoured.

6.5.2 *Continuous, periodic excitation*

Schmieder et al. (2013) and Ofman et al. (2015) studied vertically propagating waves in a prominence foot (see Sect. 5.9.1) and, in addition, conducted numerical MHD simulations to explain them in terms of propagating fast MHD waves. The main difference between these simulations is that, while Schmieder et al. (2013) restrict themselves to linear perturbations, Ofman et al. (2015) solve the non-linear problem. Both works use the prominence equilibrium represented in Fig. 37, except that the temperature and density in Ofman et al. (2015) have a continuous variation at the interface between the prominence and coronal plasma. The equilibrium is subject to a periodic forcing of the vertical velocity component at the prominence foot. Planar wave fronts resembling the observed ones propagate in the vertical direction, which supports the interpretation of this event as propagating fast MHD waves. Furthermore, Ofman et al. (2015) find a qualitative agreement between the sharp wave fronts in their numerical simulations and the non-sinusoidal shape of the observed waves at various heights in the prominence. This is taken as evidence for the importance of non-linearity in the propagation of these fast MHD waves.

6.6 Radiative magnetohydrodynamic models

Observations in which various spectral indicators are used simultaneously to investigate prominence oscillations are discussed in Sect. 5.2. The interpretation of results is difficult for two reasons: first, oscillations are usually not detected in all available spectral indicators, and second, the outcomes of theory and observations are not directly comparable: whereas the theoretical models can give the temporal behaviour of the plasma velocity, density, pressure and other physical parameters, observations yield information on quantities such as the line intensity, the line width or the Doppler shift. Only this last quantity can be the subject of direct comparison with theoretical results, so that a clear identification of the spectral parameters with physical variables (density, pressure, temperature, magnetic field strength) is required before further progress can be achieved. Then, the presence of a certain period in more than one spectral indicator could be used to infer the properties of the MHD wave involved. Another useful source of information could be the detection of a given period in one indicator but not in the others, such as reported in some works discussed in Sect. 5.2.

Heinzel et al. (2014) and Zapiór et al. (2016) made the first efforts to study the relationship between spectral indicators and the linear MHD waves excited in two simple prominence slab models. Zapiór et al. (2016) considered the configuration of Fig. 59, whereas Heinzel et al. (2014) used the same structure without the corona, i.e., they only included the prominence slab, bounded by rigid walls. Heinzel et al. (2014) analysed linear fast and slow MHD waves, already studied in this configuration by Oliver et al. (1992) (Sect. 6.2.2), and computed the physical variables associated with the fundamental slow mode (fS) and its first overtone (1S), and with the fundamental fast mode (fF) and its first overtone (1F). A velocity amplitude of 2 km s^{-1} was imposed, typical of small amplitude oscillations. The output of the MHD calculation was then used as the input for a one-dimensional radiative transfer code that computes the full spectral profile of the H_α and H_β lines (Heinzel 1995; Labrosse et al. 2010). The line-of-sight was taken perpendicular to the prominence axis and so slow (fast) wave motions were polarised almost parallel (perpendicular) to the line-of-sight. The line profiles were computed for different times and for each of the four waves. We do not review the results of Heinzel et al. (2014) because their prominence model is too simple. Nevertheless, this work is rather relevant because it showed how MHD wave modelling and radiative transfer calculations can be put together to study prominence oscillations and also suggested that MHD perturbations can cause detectable variations in the Doppler velocity, FWHM and/or line intensity.

The work by Zapiór et al. (2016) makes use of the full prominence + corona equilibrium of Fig. 59. These authors followed the same procedure of Heinzel et al. (2014): fast and slow wave perturbations were obtained and synthetic spectral profiles were computed for each of them at different times. The magnetoacoustic waves that propagate in this slab structure were analysed by Joarder and Roberts (1992b) and have been discussed in Sect. 6.2.2. The relevant magnetoacoustic solutions for prominence oscillations are the hybrid and internal ones, and for this reason Zapiór et al. (2016) analysed the hybrid slow and fast waves (denoted as hS and hF, respectively) and their first internal overtones (1iS and 1iF, respectively). The total density, line-of-sight (LOS) velocity and total temperature associated to these modes are shown in Fig. 60

Fig. 59 Sketch of the model used by Zapiór et al. (2016) to compute the H_α and H_β line profiles arising from linear MHD waves propagating in a prominence. The magnetic field threading the prominence is horizontal and tied at its ends to incorporate the effect of the dense photosphere on waves. The line-of-sight (LOS) is perpendicular to the slab. Image reproduced with permission from Zapiór et al. (2016), copyright by AAS

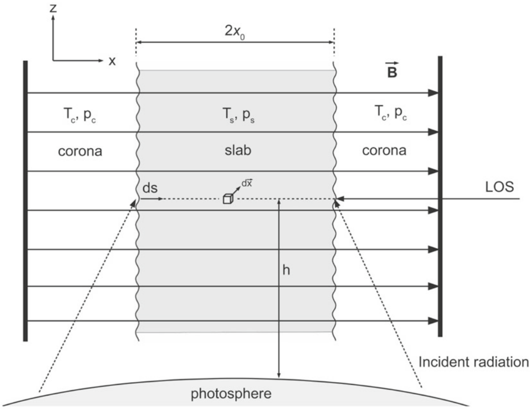

at different phases during a complete oscillatory period. Slow modes have a dominant horizontal polarisation and thus present the largest LOS velocities. The hS mode causes lateral motions of the full prominence with little compression and temperature variations, the hF and 1iS modes give rise to internal compression of the plasma (especially the later) and the 1iF mode is characterised by vertical shearing motions and small internal compression. Figure 61 shows the results for the H_α and H_β lines and different phases during a complete period. These line profiles were then used to extract several spectral line parameters and to plot their time variation: see Fig. 62. It is obvious that different wave modes affect these spectral indicators in different ways, which strongly supports the seismological capabilities of this kind of studies. For example, the hS mode is the only one that produces Doppler velocity variations of the H_β line, whereas only the hF and 1iS modes cause variations of the H_β FWHM and intensity. The 1iF mode, on the other hand, has very little influence on these spectral parameters, its largest effect being $\sim 1\%$ amplitude variations of the H_β line intensity. Furthermore, most parameters in Fig. 62 display a non-sinusoidal time profile.

One of the main purposes of radiative magnetohydrodynamic models of prominence oscillations is to link the detected periodic variations of spectral parameters with a specific MHD wave, with the aim of performing a seismological inversion of the observational data (see Sect. 5.2 for a discussion). To this end, Zapiór et al. (2016) assumed that Doppler velocity oscillations can be detected if their amplitude is larger than 0.25 km s^{-1} and their FWHM and intensity oscillations can be detected if their amplitude is larger than 1%. For example, for the hS mode only the Doppler velocity of both the H_α and H_β lines satisfies these criteria, while the FWHM and intensity of both lines do not. Then, the first two indicators associated with the hS mode are assigned a value of 1 (possible detection), while the other four indicators are assigned a value of 0 (impossible to detect given the assumed thresholds). These six values are presented in the first line of Table 1, which also shows the values associated to the other wave modes considered by Zapiór et al. (2016). The conclusion is that given the very idealised conditions of this work, these six spectral variables would unequivocally lead to the identification of the wave that causes them.

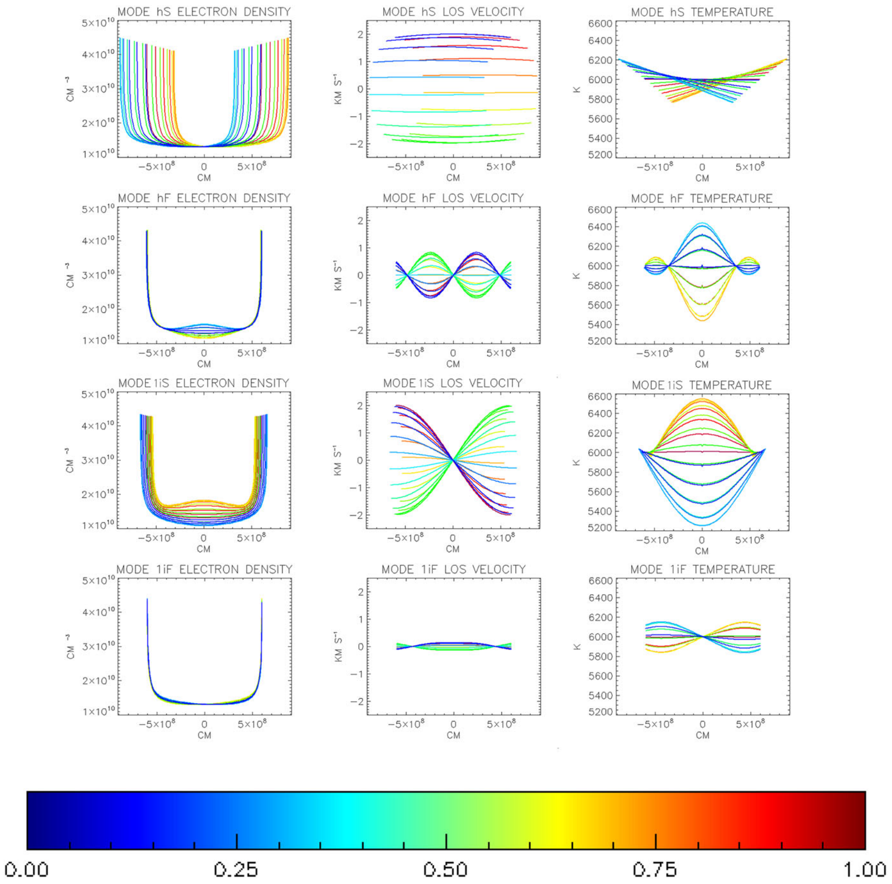

Fig. 60 MHD plus radiative transfer model: spatial and temporal variation of the total density, line-of-sight (LOS) velocity and total temperature associated to four selected magnetoacoustic modes. The horizontal axis gives the transverse position, with the unperturbed prominence plasma in the range -5×10^8 cm $\leq x \leq 5 \times 10^8$ cm. The time of each curve is given by the corresponding oscillatory phase, colour-coded by the bar at the bottom of the plot. Image reproduced with permission from Zapiór et al. (2016), copyright by AAS

Table 1 Possibility of detecting the hS, 1iS, hF and 1iF wave modes using the Doppler velocity (v_D), FWHM and line intensity (I_{max}) of the H_α and H_β spectral lines

Mode	v_D	FWHM H_α	I_{max}	v_D	FWHM H_β	I_{max}
hS	1	0	0	1	0	0
1iS	1	1	1	0	1	1
hF	0	1	1	0	1	1
1iF	0	0	0	0	0	0

The values 0 and 1 respectively indicate that the mode produces an undetectable and a detectable periodic variation. For an oscillation to be deemed detectable its amplitude must be at least 0.25 km s^{-1} (Doppler velocity) or 1% (FWHM or line intensity). Adapted from Zapiór et al. (2016)

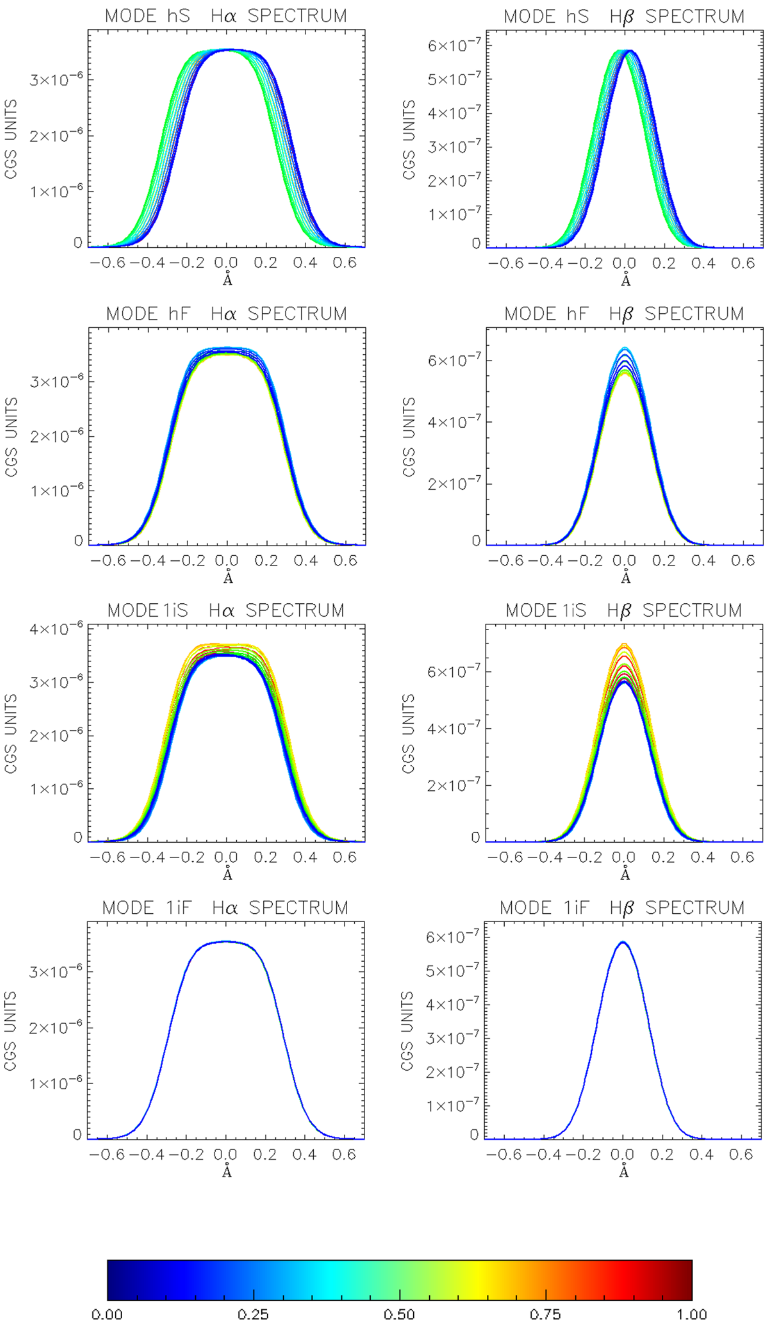

Fig. 61 MHD plus radiative transfer model: temporal variation of the H_α and H_β line profiles for the magnetoacoustic modes whose physical variables are shown in Fig. 60. The time of each curve is given by the corresponding oscillatory phase, colour-coded by the bar at the bottom of the plot. Image reproduced with permission from Zapiór et al. (2016), copyright by AAS

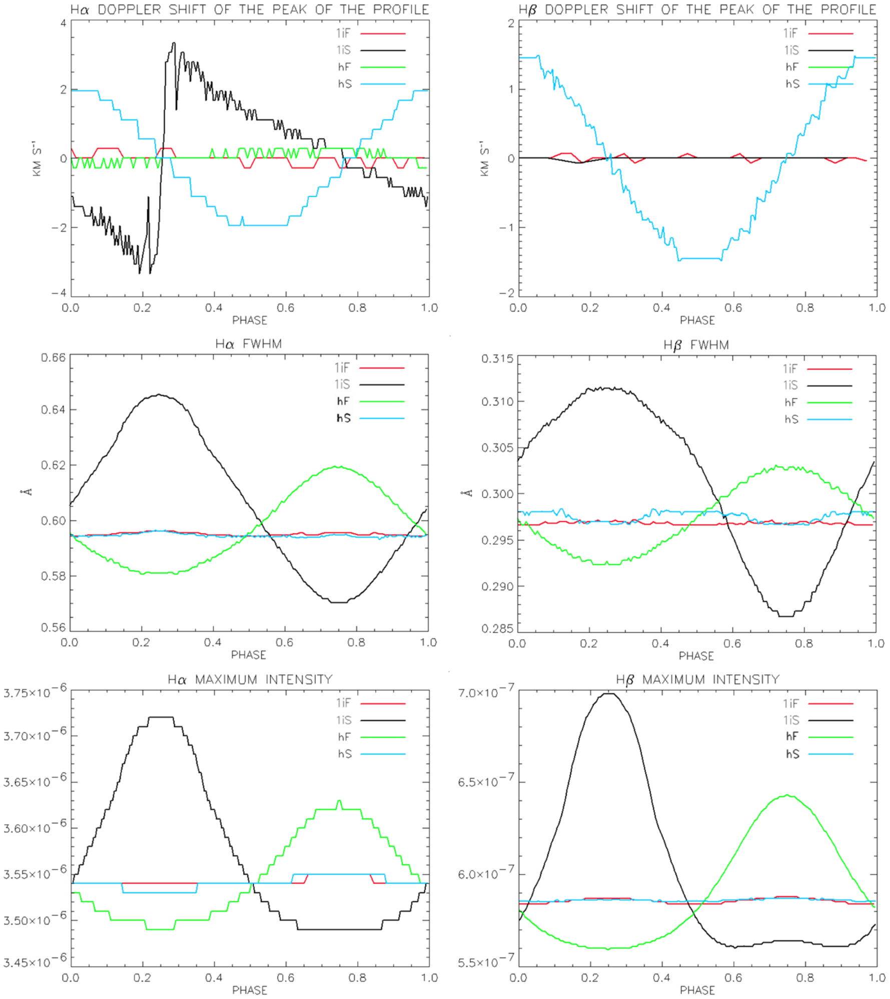

Fig. 62 MHD plus radiative transfer model: temporal variation of the spectral line parameters of the H_α (left) and H_β (right) lines for the magnetoacoustic hS, hF, 1iS and 1iF modes (see text for an explanation of these acronyms). From top to bottom: Doppler velocity, full width at half maximum (FWHM) and line intensity. Image reproduced with permission from Zapiór et al. (2016), copyright by AAS

7 Theoretical aspects of small amplitude oscillations: damping mechanisms

Temporal and spatial damping is a recurrently observed characteristic of prominence oscillations (see Sect. 5.8). Several theoretical mechanisms have been proposed in order to explain the observed damping. Direct dissipation mechanisms seem to be inefficient, as shown by Ballai (2003), who estimated, through order of magnitude calculations, that several isotropic and anisotropic dissipative mechanisms, such as viscosity, magnetic diffusivity, radiative losses and thermal conduction cannot in general explain the observed wave damping. The time and spatial damping of linear non-adiabatic MHD waves has been considered by Carbonell et al. (2004, 2009), Terradas et al. (2001, 2005), Carbonell et al. (2006) and Soler et al. (2007, 2008). The overall conclusion from these studies is that thermal mechanisms can only account for the damping of slow waves in an efficient manner, while fast waves remain almost undamped. Since prominences can be considered as partially ionised plasmas, a possible mechanism to damp fast and Alfvén waves could be ion-neutral collisions (Forteza et al. 2007, 2008), although the ratio of the damping time to the period does not completely match the observations. Besides non-ideal mechanisms, another possibility to attenuate fast waves in thin filament threads comes from resonant wave damping (see, e.g., Goossens et al. 2010), which needs the presence of a smooth variation of the Alfvén speed across the field. This phenomenon is well studied for transverse kink waves in coronal loops (Goossens et al. 2006; Goossens 2008) and provides with a plausible explanation for quickly damped transverse loop oscillations first observed by TRACE (Aschwanden et al. 1999; Nakariakov et al. 1999).

The time scales of damping produced by these different mechanisms should be compared with those obtained from observations, that indicate that the ratio of the damping time to the period, τ_{d}/P, is of the order of 1–4. The theoretical approach of many works about the damping of prominence oscillations has been to first study a given damping mechanism in a uniform and unbounded medium and thereafter to introduce structuring and non-uniformity. This has led to an increasing complexity of theoretical models in such a way that some of them now combine different damping mechanisms. Detailed reports on theoretical studies of small amplitude oscillations in prominences and their damping can be found in Oliver (2009), Ballester (2010) and Arregui and Ballester (2011). Here, we collect the most significant aspects of the theoretical mechanisms that have been proposed to explain the observed time-scales.

7.1 Damping of oscillations by thermal mechanisms

In a seminal paper, Field (1965) studied the thermal instability of a dilute gas in mechanical and thermal equilibrium. Using this approach, the time damping of magnetohydrodynamic waves in bounded Kippenhahn–Schlüter and Menzel prominence models was studied by Terradas et al. (2001). Similar studies using prominence slabs embedded in the solar corona were undertaken by Soler et al. (2007) and Soler et al. (2009a).

7.1.1 Non-adiabatic magnetoacoustic waves in prominence slabs

Terradas et al. (2001) studied the radiative damping of quiescent prominence oscillations. They adopted a relatively simple non-adiabatic damping mechanism, by including a radiative loss term based on Newton's law of cooling with constant relaxation time. The influence of this type of radiative dissipation on the normal modes of Kippenhahn–Schlüter and Menzel quiescent prominence models was analysed. The normal modes of these configurations had previously been investigated by Oliver et al. (1992) and Joarder and Roberts (1993a); cf. Sect. 6.2. In a Kippenhahn–Schlüter prominence model, the fundamental slow mode is unaffected by radiation, but its overtones are strongly damped. On the other hand, in a Menzel prominence configuration all slow modes are characterised by short damping times. The damping time depends on the curvature of field lines, in such a way that more curved models produce larger damping times. In both prominence models, fast modes are practically unaffected by radiative losses and have very long damping times.

A more involved analysis was performed by Soler et al. (2007) by including thermal conduction, optically thin or thick radiation and heating in the energy equation. The prominence was modelled as a plasma slab embedded in an unbounded corona and with a magnetic field oriented along the direction parallel to the slab axis (see Fig. 36); this is the equilibrium configuration of Joarder and Roberts (1992a), whose normal modes have been discussed in Sect. 6.2. Soler et al. (2007) found that radiation losses have a different effect on magnetoacoustic waves depending on their wavenumber. For typical values of observed wavelengths, the internal slow mode is attenuated by radiation from the prominence plasma, the fast mode by the combination of prominence radiation and coronal conduction and the external slow mode by coronal conduction. This study highlights the relevance of the coronal physical properties on the damping properties of fast and external slow modes, whereas this aspect does not affect the internal slow modes at all. For thin slabs, representing a fine thread, Soler et al. (2007) found that the fast mode is less attenuated, whereas both internal and external slow modes are not affected by non-adiabatic damping mechanisms.

Damping of magnetoacoustic waves in slab prominence models with a transverse magnetic field (see Fig. 37 and Sect. 6.2 for a description of the normal modes) were studied by Soler et al. (2009a). The most relevant damping processes are coronal thermal conduction and radiative losses from the prominence plasma. In terms of the spatial distribution of the studied normal modes, it was found that both mechanisms govern together the attenuation of hybrid modes, whereas prominence radiation is responsible for the damping of internal modes and coronal conduction essentially dominates the attenuation of external modes. In terms of the different magnetohydrodynamic wave types, slow modes were found to be efficiently damped, with damping times compatible with observations. On the contrary, fast modes are less attenuated by non-adiabatic effects and their damping times are several orders of magnitude larger than those observed. The inclusion of the coronal medium in the analysis causes a decrease of the damping times compared to those of an isolated prominence slab, but this effect is still insufficient to obtain fast mode damping times compatible with observations.

7.1.2 Non-adiabatic magnetoacoustic waves in a single thread with mass flows

Soler et al. (2008) investigated the effects of both mass flow and non-adiabatic processes on the oscillations of an individual prominence thread modelled as an infinite homogeneous cylinder (Fig. 44). Thermal conduction and radiative losses were taken into account as damping mechanisms. For a discussion of the oscillatory features of this system, see Sect. 6.3.1.

The analysis of the damping time-scales for the different wave types shows that slow and thermal modes are efficiently attenuated by non-adiabatic mechanisms. On

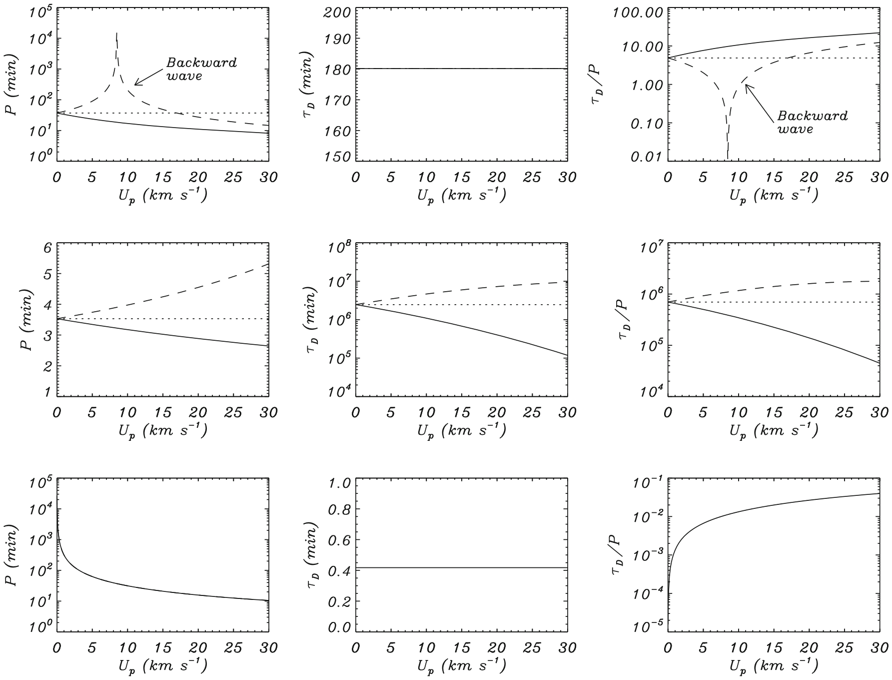

Fig. 63 Wave damping by thermal effects in a uniform, infinitely long thread (Fig. 44). Period (left), damping time (centre) and ratio of the damping time to the period (right) versus the flow velocity for the fundamental oscillatory modes. The upper, middle and lower panels correspond to the slow, fast kink and thermal modes, respectively. Different line styles represent parallel waves (solid line), anti-parallel waves (dashed line) and solutions in the absence of flow (dotted line). Image reproduced with permission from Soler et al. (2008), copyright by AAS

the contrary, fast kink modes are much less affected and their damping times are much larger than those observed. These results are compatible with the known damping properties of these waves in the absence of flows.

In addition, Soler et al. (2008) analysed how mass flows affect these damping properties. Figure 63 shows the dependence of the period, damping time and their ratio as a function of the flow velocity for the slow, fast and thermal modes (for a discussion of the thermal mode, see Carbonell et al. 2009). Note that the left column of this figure has been already presented in Fig. 45, but it is retained here to facilitate our explanation. Flow velocities in the range 0–30 km s^{-1}, that correspond to the observed flow speeds in quiescent prominences, were considered. The damping time of slow and thermal modes is found to be independent of the flow velocity, but the attenuation of the fast kink mode is affected by the flow. The larger the flow velocity, the more attenuated the parallel fast kink wave, whereas the opposite occurs for the anti-parallel solution. This behaviour is due to the weak coupling of the fast modes to external slow modes (Soler et al. 2008).

Although the presence of steady mass flows improves the efficiency of non-adiabatic mechanisms on the attenuation of transverse kink oscillations for propagation parallel

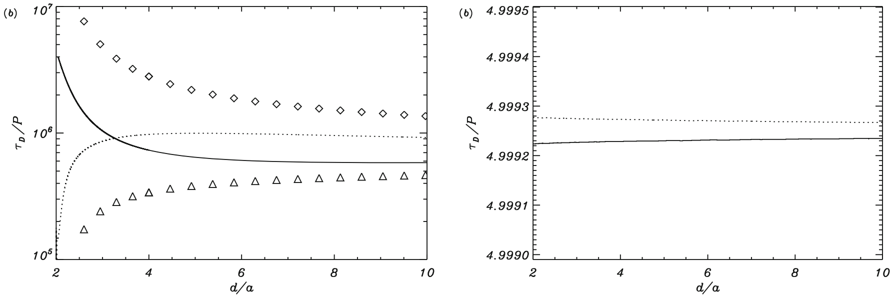

Fig. 64 Wave damping by thermal effects in a two-thread system. Left: ratio of the damping time to the period versus the distance between the thread axes of the S_x (solid line), A_x (dotted line), S_y (triangles) and A_y (diamonds) kink-like modes. Right: the same for the S_z (solid line) and A_z (dotted line) slow wave modes. Image reproduced with permission from Soler et al. (2009c), copyright by AAS

to the flow, its effect is still not enough to obtain damping times compatible with observations.

7.1.3 Non-adiabatic magnetoacoustic waves in a two-thread system with mass flows

The oscillatory properties, namely the frequency and spatial distribution, of fast and slow magnetoacoustic waves in a system made of two infinite threads with mass flows are described in Sect. 6.3.2; see Fig. 49 for a sketch of the equilibrium configuration. Soler et al. (2009c) evaluated the damping time-scales caused by non-adiabatic effects as a function of the distance between the thread axes. The left panel of Fig. 64 shows that the ratio of the damping time to the period of the four kink modes is very large, so that dissipation by non-adiabatic mechanisms is not efficient enough to damp these modes. Hence, the collective nature of the transverse oscillations in a system of two identical threads does not change the conclusion about the irrelevance of thermal mechanisms to account for the damping of fast modes already obtained for one thread.

As concluded in Sect. 7.1.2, slow wave damping can be explained by thermal mechanisms. The right panel of Fig. 64 shows the damping ratios of the S_z and A_z solutions versus the distance between the two threads. Slow modes in a threaded prominence are efficiently attenuated by non-adiabatic mechanisms. Note that τ_d/P is almost independent of the thread separation and the mode because the two threads oscillate independently in the S_z and A_z modes. Time-scales $\tau_\mathrm{d}/P \approx 5$ are obtained, which is in agreement with previous studies (Soler et al. 2007, 2008) and consistent with observations.

Soler et al. (2009c) concluded that collective slow modes are efficiently damped by thermal mechanisms, with damping ratios similar to those reported in observations, while collective fast waves are poorly damped. This is a key point since efficiently damped transverse oscillations have been observed, which could suggest that other attenuation mechanisms could be at work.

7.2 Damping of oscillations by ion-neutral collisions

Since the temperature of prominences is typically of the order of 10^4 K, the prominence plasma is only partially ionised. The exact ionisation degree of prominences is unknown and the reported ratio of electron density to neutral hydrogen density (see, e.g., Patsourakos and Vial 2002) covers about two orders of magnitude (0.1–10). Partial ionisation brings the presence of neutrals in addition to electrons and ions, thus collisions between the different species are possible. Because of the occurrence of collisions between electrons with neutral atoms and ions, and more importantly between ions and neutrals, Joule dissipation is enhanced when compared with the fully ionised case. A partially ionised plasma can be represented as a single-fluid in the strong coupling approximation, which is valid when the ion density in the plasma is low and the collision time between neutrals and ions is short compared with other time-scales of the problem. Using this approximation it is possible to describe the very low frequency and large-scale fluid-like behaviour of plasmas (Goossens 2003).

Partial ionisation affects the induction equation, which contains additional terms due to the presence of neutrals and a non-zero resistivity (Soler et al. 2009d). These terms account for the processes of ohmic diffusion, with coefficient η; ambipolar diffusion, with coefficient η_{A}; and Hall's magnetic diffusion, with coefficient η_{H}. They govern collisions between the different plasma species. Ohmic diffusion is mainly due to electron-ion collisions and produces magnetic diffusion parallel to the magnetic field lines; ambipolar diffusion is mostly caused by ion-neutral collisions and Hall's effect is enhanced by ion-neutral collisions since they tend to decouple ions from the magnetic field, while electrons remain able to drift with the magnetic field (Pandey and Wardle 2008). The ambipolar diffusivity can be expressed in terms of Cowling's coefficient, η_{C}, that accounts for diffusion perpendicular to magnetic field lines, as

$$\eta_{\mathrm{A}} = \frac{\eta_{\mathrm{C}} - \eta}{B^2}, \tag{36}$$

with B the magnetic field strength. For a fully ionised plasma, $\eta_{\mathrm{C}} = \eta$ and there is no ambipolar diffusion, so magnetic diffusion is isotropic. Due to the presence of neutrals, $\eta_{\mathrm{C}} \gg \eta$, which means that perpendicular magnetic diffusion is much more efficient than longitudinal magnetic diffusion in a partially ionised plasma. It is important to note that $\eta_{\mathrm{C}} \gg \eta$ even for a small relative density of neutrals.

7.2.1 Homogeneous and unbounded prominence medium

Several studies have considered the damping of MHD waves in partially ionised plasmas of the solar atmosphere (Pontieu et al. 2001; James et al. 2003; Khodachenko et al. 2004; Leake et al. 2005). In the context of solar prominences, Forteza et al. (2007) derived the full set of MHD equations for a partially ionised, one-fluid hydrogen plasma and applied them to the study of the time damping of linear, adiabatic fast and slow magnetoacoustic waves in an unbounded prominence medium. This study was later extended to the non-adiabatic case by including thermal conduction by neutrals and electrons and radiative losses (Forteza et al. 2008). The main effects of partial ionisation on the properties of MHD waves manifest through a generalised Ohm's law, which adds some extra terms in the resistive magnetic induction equation, in comparison to the fully ionised case. Forteza et al. (2007) considered a uniform and unbounded prominence plasma and found that ion-neutral collisions are more important for fast waves, for which the ratio of the damping time to the period is in the range 1 to 10^5, than for slow waves, for which values between 10^4 and 10^8 are obtained. Fast waves are efficiently damped for moderate values of the ionisation fraction, while in a nearly fully ionised plasma, the small amount of neutrals is insufficient to damp the perturbations.

A hydrogen plasma was considered in the above studies, but 90% of the prominence chemical composition is hydrogen and the remaining 10% is helium. The effect of including helium in the model of Forteza et al. (2008) was assessed by Soler et al. (2010b). The species present in the medium are electrons, protons, neutral hydrogen, neutral helium (He I) and singly ionised helium (He II), while the presence of He III is neglected (Gouttebroze and Labrosse 2009).

The hydrogen ionisation degree is characterised by $\tilde{\mu}_{\mathrm{H}}$, which varies between 0.5 for fully ionised hydrogen and 1 for fully neutral hydrogen. The helium ionisation degree is characterised by $\delta_{\mathrm{He}} = \frac{\xi_{\mathrm{He\,II}}}{\xi_{\mathrm{He\,I}}}$, where $\xi_{\mathrm{He\,II}}$ and $\xi_{\mathrm{He\,I}}$ denote the relative densities of single ionised and neutral helium, respectively. Figure 65 displays τ_{d}/P as a function of the wavenumber, k, for the Alfvén, fast and slow waves, and the results corresponding to several helium abundances are compared for hydrogen and helium ionisation degrees of $\tilde{\mu}_{\mathrm{H}} = 0.8$ and $\delta_{\mathrm{He}} = 0.1$, respectively. We can observe that the presence of helium has a minor effect on the results.

The thermal mode is a purely damped, non-propagating disturbance ($\omega_{\mathrm{R}} = 0$), so only the damping time, τ_{d}, is plotted (Fig. 65d). We observe that the effect of helium is different in two ranges of k. For $k > 10^{-4}\ \mathrm{m}^{-1}$, thermal conduction is the dominant damping mechanism, so the larger the amount of helium, the shorter τ_{d} because of the enhanced thermal conduction by neutral helium atoms. On the other hand, radiative losses are more relevant for $k < 10^{-4}\ \mathrm{m}^{-1}$. In this region, the thermal mode damping time grows as the helium abundance increases. Since these variations in the damping time are very small, we again conclude that the damping time obtained in the absence of helium does not significantly change when helium is taken into account. Therefore, the inclusion of neutral or single ionised helium in partially ionised prominence plasmas does not modify the behaviour of linear, adiabatic or non-adiabatic MHD waves already found by Forteza et al. (2007) and Forteza et al. (2008).

The time damping of non-adiabatic MHD waves in a flowing partially ionised plasma with prominence-like physical conditions was analysed by Barceló et al. (2011). The authors solved the dispersion relation for Alfvén, fast, slow and thermal waves considering non-adiabatic single fluid equations for a partially ionised plasma in the presence of background mass flows. The presence of a background flow in a partially ionised plasma gives rise to the appearance of two critical wavenumbers that constrain the propagation properties of fast and Alfvén waves. The damping of these waves is dominated by resistive effects and leads to damping ratio values well above those observed. On the other hand, slow and thermal damping is dominated by non-adiabatic effects. For slow waves, very long period oscillations (10^3–10^5 min) with very large damping times (10^3–10^6 min) would enable to obtain damping ratio

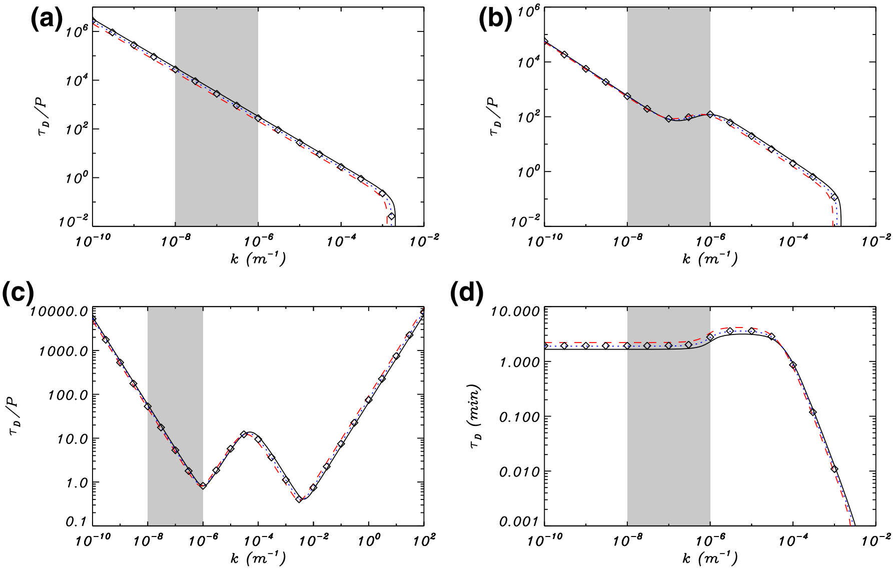

Fig. 65 Wave damping by ion-neutral effects in a uniform medium. **a**–**c** Ratio of the damping time to the period, τ_d/P, versus the wavenumber, k, corresponding to the Alfvén wave, fast wave and slow wave, respectively. **d** Damping time, τ_d, of the thermal wave versus the wavenumber, k. The different linestyles represent the following abundances: $\xi_\mathrm{He\,II} = 0\%$ (solid line), $\xi_\mathrm{He\,II} = 10\%$ (dotted line) and $\xi_\mathrm{He\,II} = 20\%$ (dashed line). In all computations, $\tilde{\mu}_\mathrm{H} = 0.8$ and $\delta_\mathrm{He} = 0.1$. The results for $\xi_\mathrm{He\,II} = 10\%$ and $\delta_\mathrm{He} = 0.5$ are plotted by means of symbols for comparison. The shaded regions correspond to the range of typically observed wavelengths of prominence oscillations. In all the figures the angle between the wavevector and the magnetic field is $\pi/4$. Image reproduced with permission from Soler et al. (2010b), copyright by ESO

values close to those observed. Therefore, except for this unrealistic case, ion-neutral collisions are found to be an inefficient mechanism to explain the observed damping ratio (τ_d/P).

7.2.2 Cylindrical filament thread model

Soler et al. (2009b) applied the equations derived by Forteza et al. (2007) to the study of MHD waves in a partially ionised filament thread modelled as an infinite cylinder with radius a embedded in the solar corona (see Fig. 44). As in Forteza et al. (2007), the one-fluid approximation for a hydrogen plasma was considered. The internal and external media are characterised by their densities, temperatures and their own relative densities of neutrals, ions and electrons. The contribution of the electrons is neglected. The coronal medium is considered as fully ionised, while the ionisation fraction in the prominence plasma, $\tilde{\mu}_\mathrm{p}$, is allowed to vary.

In their analysis, Soler et al. (2009b) neglected Hall's term since it can be ignored when the plasma is magnetised, i.e., when ions and electrons are tightly bound to the magnetic field. The condition to neglect Hall's term can be written in terms of the ion-gyrofrequency (ω_i) and the ion-neutral collision time (τ) as $\omega_i \tau \gg 1$, which once expanded gives,

$$\frac{eB}{m_i}\sqrt{\frac{\pi m_i}{16k_BT}}\frac{1}{n_n\Sigma_{in}} \gg 1,$$

where Σ_{in} is the ion-neutral cross-section and n_n the neutrals number density (Leake et al. 2005; Pandey and Wardle 2008). Using prominence conditions ($\rho = 5 \times 10^{-11}$ kg m^{-3}, $B = 10$ G, $T = 8000$ K, $\tilde{\mu}_{\mathrm{p}} = 0.8$), we obtain the numerical value $\omega_i\tau = 467$, which fully justifies the neglect of Hall's term. Parallel and perpendicular magnetic diffusion can be evaluated by defining the corresponding Reynolds numbers as $R_{\mathrm{m}\|} = c_{\mathrm{sp}}a/\eta$ and $R_{\mathrm{m}\perp} = 4\pi^2 c_{\mathrm{sp}}/\eta_{\mathrm{C}}k_z^2 a$, where the typical velocity scale has been associated to the sound speed in the prominence, c_{sp}. The parallel Reynolds number is independent of the wavenumber, while the relative importance of Cowling's diffusion increases with k_z, the longitudinal wavenumber. In the range of observed wavelengths [$k_z a \sim (10^{-3} - 10^{-1})$] both Cowling's and ohmic diffusion could therefore be important. Soler et al. (2009b) analysed separately the effect(s) of partial ionisation in Alfvén, fast kink and slow waves.

For torsional Alfvén waves, Soler et al. (2009b) found that wave propagation is constrained between two critical wavenumbers (top panels of Fig. 66). These critical wavenumbers are, however, outside the range of the observed wavelengths, in which τ_{d}/P is in the range 10–100 and so is considerably larger than the observed damping rate. Nevertheless, a prominence ionisation fraction larger than the maximum one considered here (namely $\tilde{\mu}_{\mathrm{p}} > 0.95$) can yield $\tau_{\mathrm{d}}/P = 1 - 10$, in agreement with observations. For short wavenumbers, the values of the damping time over the period are independent of the ionisation degree, while for large wavenumbers they become smaller for larger values of $\tilde{\mu}_{\mathrm{p}}$. This behaviour is explained in Soler et al. (2009b) by considering solutions to the dispersion relation in which one of the two possible damping mechanisms, i.e., partial ionisation or ohmic dissipation, is neglected. Soler et al. (2009b) observed that ohmic diffusion dominates for small wavenumbers. Nevertheless, for large wavenumbers Cowling's diffusion dominates over ohmic dissipation and so a larger number of neutrals decreases the damping time: the larger $\tilde{\mu}$ in the thread, the shorter τ_{d} and, consequently, the smaller τ_{d}/P.

The presence of critical wave numbers is also found in the case of transverse kink waves (middle panels of Fig. 66). Within the range of observed wavelengths, the phase speed closely corresponds to its ideal counterpart, $c_{\mathrm{k}} = \omega/k_z$, so non-ideal effects are irrelevant for wave propagation. The behaviour of the damping rate as a function of wavelength and ionisation fraction is seen to closely resemble the result obtained for Alfvén waves, with $\tau_{\mathrm{d}}/P > 10$ in the range of observed wavelengths. Therefore, neither ohmic diffusion nor ion-neutral collisions seem to produce damping times as short as those observed for kink waves in filament threads. Only for an almost neutral plasma, with $\tilde{\mu}_{\mathrm{p}} > 0.95$, the obtained damping rates are compatible with the observed time-scales. Just like for Alfvén waves, ohmic diffusion dominates for small wavenumbers, while ion-neutral collisions are the dominant damping mechanism for large wavenumbers.

Regarding slow waves (bottom panels of Fig. 66), Soler et al. (2009b) concentrated their analysis on the radially fundamental mode with $m = 1$, since the behaviour of the slow mode is weakly affected by the value of the azimuthal wavenumber. Slow wave

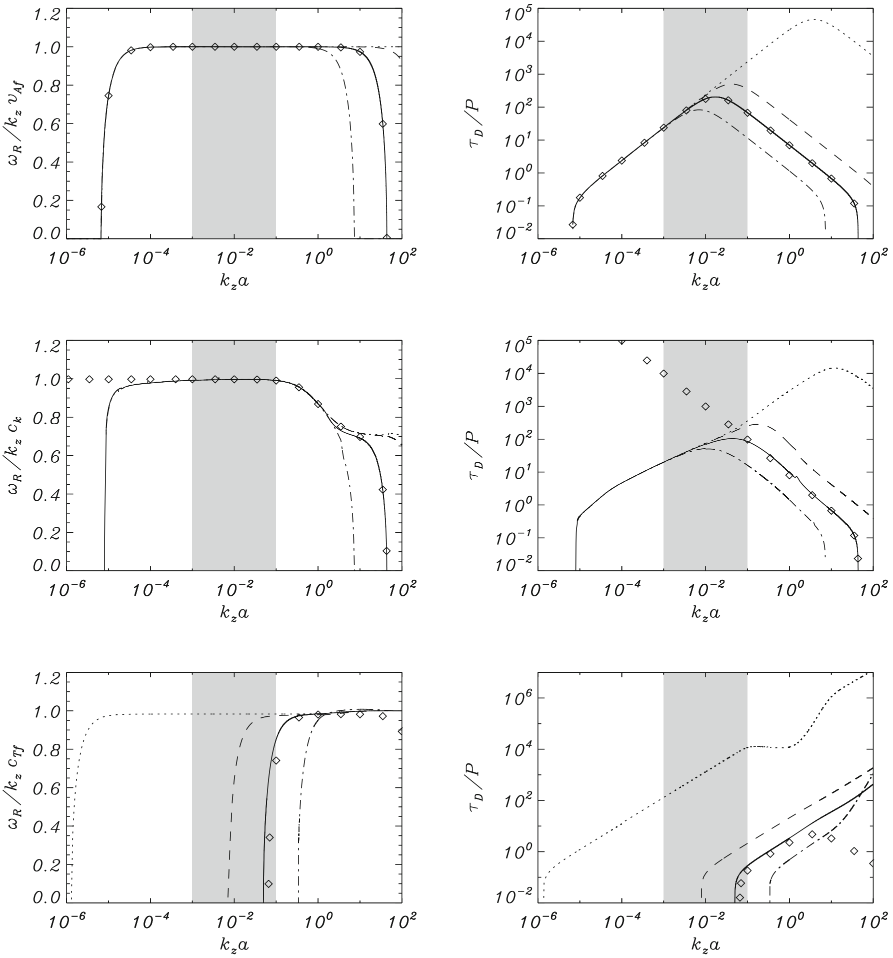

Fig. 66 Wave damping by ion-neutral effects in an infinitely long prominence thread. Dimensionless phase speed (left panels) and ratio of the damping time to the period (right panels) as a function of $k_z a$ for Alfvén waves (top panels), kink waves (middle panels) and slow waves (bottom panels). The different linestyles represent different ionisation degrees: $\tilde{\mu}_{\mathrm{p}} = 0.5$ (dotted), $\tilde{\mu}_{\mathrm{p}} = 0.6$ (dashed), $\tilde{\mu}_{\mathrm{p}} = 0.8$ (solid) and $\tilde{\mu}_{\mathrm{p}} = 0.95$ (dash-dotted). Symbols are the approximate solution given by Equation (36) in Soler et al. (2009b) for $\tilde{\mu}_{\mathrm{p}} = 0.8$. The shaded zones correspond to the range of typically observed wavelengths of prominence oscillations. The Alfvén speed in the thread, v_{Af}, the kink speed, c_{k}, and the cusp speed in the thread, c_{Tp}, have been used to compute the dimensionless phase speed. Image reproduced with permission from Soler et al. (2009b), copyright by AAS

propagation is constrained by only one critical wavenumber, that strongly depends on the ionisation fraction, in such a way that for k_z below this critical wavenumber the wave is totally damped. More importantly, for large enough values of the ionisation fraction, the corresponding critical wavelength lies in the range of observed wavelengths of filament oscillations. As a consequence, the slow wave might not propagate in filament threads under certain circumstances. As for the damping rate, it is found that ion-neutral collisions are a relevant damping mechanism for slow waves, since very short damping times are obtained, especially close to the critical wavenumber. By comparing the particular effects of ohmic diffusion and ion-neutral collisions, the slow mode damping is seen to be completely dominated by ion-neutral collisions. Ohmic diffusion is found to be irrelevant, since the presence of the critical wavenumber prevents slow wave propagation for small wavenumbers, where ohmic diffusion would start to dominate.

7.3 Resonant damping of infinitely long thread oscillations

The phenomenon of resonant wave damping in non-uniform plasmas has been extensively studied in connection to wave-based coronal heating mechanisms (Ionson 1978) and the damping of transverse coronal loop oscillations (Hollweg and Yang 1988; Ruderman and Roberts 2002; Goossens et al. 2002, 2010). The mechanism relies in the energy transfer from the transverse kink mode to small scale Alfvén waves because of the plasma inhomogeneity at the transverse spatial scales of the structures. This idea was put forward by Arregui et al. (2008b), whose analysis is restricted to the damping of kink oscillations due to the resonant coupling to Alfvén waves in a pressureless (zero plasma-β) plasma. It was extended to the case in which both the Alfvén and the slow resonances are present by Soler et al. (2009). Here we discuss the main results from these works, whose aim is to assess the damping properties of resonant absorption. For this reason, the considered configurations are based on the infinitely long thread model of Fig. 43.

7.3.1 Resonant damping in the Alfvén continuum

Arregui et al. (2008b) considered an individual and isolated thread modelled as a cylindrical magnetic flux tube of radius a in a gravity-free environment. The uniform magnetic field points along the axis of the tube (Fig. 67). In the zero plasma-β approximation, the thread is modelled as a density enhancement with a radial variation of density from its internal constant prominence value ρ_p to the coronal constant value ρ_c over a non-uniform layer of thickness l. A typical value of the density contrast between the filament and coronal plasma is $\zeta = \rho_\mathrm{p}/\rho_\mathrm{c} = 200$.

MHD waves of axisymmetric one-dimensional cylindrical flux tubes are characterised by two wave numbers, i.e., the azimuthal wavenumber, m, and the axial wavenumber, k_z. They can have different nodes in the radial direction. Arregui et al. (2008b) concentrated their analysis on the radially and longitudinally fundamental

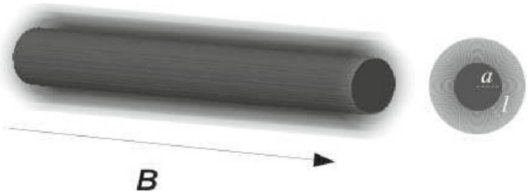

Fig. 67 Model representing a radially non-uniform filament fine structure of mean radius a and transverse inhomogeneity length scale l. Image reproduced with permission from Arregui et al. (2008b), copyright by AAS

transverse wave with azimuthal number $m = 1$, the kink mode. This eigenmode is consistent with the detected Doppler velocity variations (see Sect. 5.9.4) and their associated transverse motions, discussed in Sect. 6.3.1. The frequency of this mode is not influenced by the presence of a layer with small thickness, so the result of Sect. 6.3.1 is approximately correct; see Eq. (30).

When transverse inhomogeneity is considered, the fundamental transverse kink mode resonantly couples to Alfvén waves. The consequence is the transfer of wave energy from the global transverse motion to azimuthal motions of localised nature, and thus the time damping of the kink mode (Goossens et al. 2009). Analytical expressions for the damping time scale can be obtained under the assumption that the transverse inhomogeneity length-scale is small ($l/a \ll 1$). This is the so-called thin boundary approximation. When the long wavelength and the thin boundary approximations are combined, the analytical expression for the damping time over period for the kink mode can be written as (see, e.g., Goossens et al. 1992, 1995, 2002; Ruderman and Roberts 2002)

$$\frac{\tau_{\rm d}}{P} = F \; \frac{a}{l} \; \frac{\zeta + 1}{\zeta - 1}. \tag{37}$$

Here, F is a numerical factor that depends on the particular variation of the density in the non-uniform layer. For a linear variation, $F = 4/\pi^2$ (Hollweg and Yang 1988; Goossens et al. 1992); for a sinusoidal variation, $F = 2/\pi$ (Ruderman and Roberts 2002). Consider for example $\zeta = 200$ as a typical density contrast and $l/a = 0.1$. Then, Eq. (37) predicts a damping time of $\sim$ 6 times the oscillatory period, thus producing a time-scale compatible with observations.

Quantitative parametric results for the damping of resonant kink waves in prominence threads as a function of the relevant parameters are given by Arregui et al. (2008b). The accuracy of the analytical approximations is compared to full numerical results, beyond the long wavelength and thin boundary approximations. These results are shown in Fig. 68. The damping is affected by the density contrast in the low contrast regime and $\tau_{\rm d}/P$ rapidly decreases for increasing thread density (Fig. 68a). Interestingly, $\tau_{\rm d}/P$ stops depending on this parameter in the large contrast regime, typical of filament threads. The damping time over period is independent of the wavelength of perturbations (Fig. 68b), but rapidly decreases with increasing inhomogeneity length-scale (Fig. 68c).

Resonant damping in the Alfvén continuum appears to be a very efficient mechanism for the attenuation of transverse thread oscillations, especially because large density contrasts and transverse plasma inhomogeneities are combined together. The possible role of this mechanism in the heating of prominence plasmas has received strong support by observations and numerical modelling by Okamoto et al. (2015) and Antolin et al. (2015). This was possible because of the combination of simultaneous thread oscillations in the plane of the sky and along the line-of-sight, carried out by Okamoto et al. (2015) and the numerical and forward modelling of observational signatures by Antolin et al. (2015). In particular, the relative temporal phase shift between the plane of the sky displacements determined from Hinode/SOT Ca II H images and the Doppler velocities from spectra taken with IRIS in the Mg II k line take values in

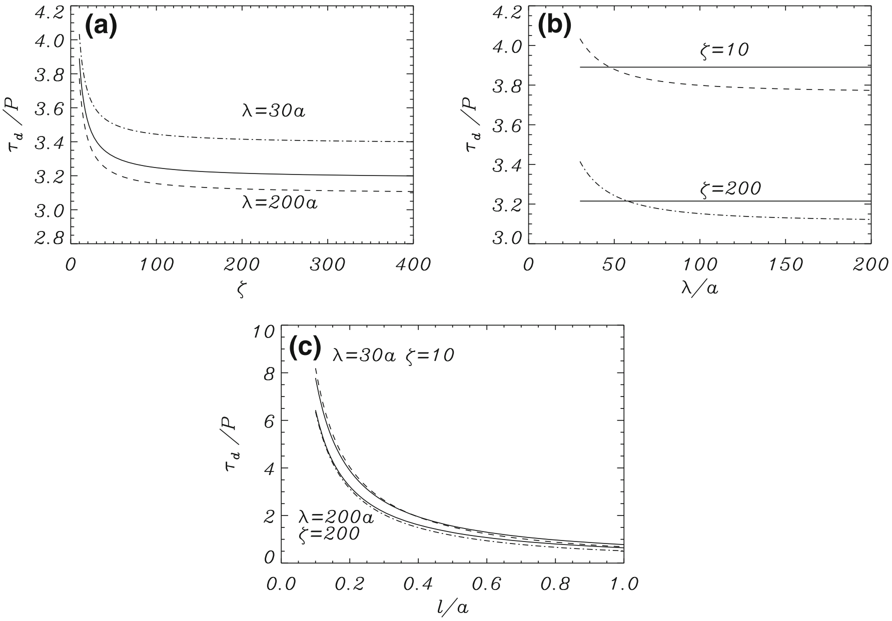

Fig. 68 Wave damping by Alfvén resonant absorption in an infinitely long prominence thread. Damping time over period for fast kink waves in filament threads with radius $a = 100$ km. **a** As a function of the density contrast, with $l/a = 0.2$ and for two wavelengths. **b** As a function of the wavelength, with $l/a = 0.2$, for two density contrasts. **c** As a function of the transverse inhomogeneity length-scale, for two combinations of wavelength and density contrast. In all plots solid lines correspond to analytical solutions given by Eq. (37), with $F = 2/\pi$. Image reproduced with permission from Arregui et al. (2008b), copyright by AAS

between 90 and 180 degree, in accordance with the forward modelling of resonantly damped transverse oscillations in a 3D flux tube model. In addition, signatures of heating from chromospheric to transition region temperatures were found in the form of a fading and thinning of the intensity in chromospheric lines and the corresponding broadening and intensity enhancement in transition region lines, both in the observations (Okamoto et al. 2015) and the numerically forward modelled synthetic data (Antolin et al. 2015).

7.3.2 *Resonant damping in the slow continuum*

Although the plasma-β in solar prominences is probably small, it is definitely non-zero. Soler et al. (2009) showed that, in prominence plasmas, resonant damping of kink waves can additionally be produced due to the coupling to slow continuum waves. In the context of coronal loops, which are presumably hotter and denser than the surrounding corona, the ordering of sound, Alfvén and kink speeds does not allow for the simultaneous matching of the kink frequency with both Alfvén and slow continuum frequencies. Because of their relatively higher density and lower temperature conditions, this becomes possible in the case of prominence threads. Therefore, the kink mode phase speed is also within the slow (or cusp) continuum, which extends between the internal and external sound speeds, in addition to the Alfvén continuum. By considering gas pressure in the cylindrical thread model of Arregui et al. (2008b), Soler et al. (2009) evaluated the contribution of the damping due to the slow continuum to the total resonant damping of the kink mode.

Soler et al. (2009) used the density model of Sect. 7.3.1 and the plasma-$\beta \simeq 0.04$. In order to obtain an analytic expression for the damping rate of the kink mode, first the long wavelength and thin boundary limits were considered. In terms of the physically relevant quantities, the damping time over the period can be cast as

$$\frac{\tau_{\mathrm{d}}}{P} = F \, \frac{a}{l} \left(\frac{\zeta + 1}{\zeta - 1} \right) \left[\frac{m}{\cos \alpha_{\mathrm{A}}} + \frac{(k_z a)^2}{m} \left(\frac{c_{\mathrm{s}}^2}{c_{\mathrm{s}}^2 + v_{\mathrm{A}}^2} \right)^2 \frac{1}{\cos \alpha_{\mathrm{S}}} \right]^{-1} . \tag{38}$$

Here F is the same numerical factor as in Eq. (37), while $\alpha_{\mathrm{A}} = \pi(r_{\mathrm{A}} - a)/l$ and $\alpha_{\mathrm{S}} = \pi(r_{\mathrm{S}} - a)/l$, with r_{A} and r_{S} the Alfvén and slow resonant positions. The term with k_z corresponds to the contribution of the slow resonance. If this term is dropped and $m = 1$ and $\cos \alpha_{\mathrm{A}} = 1$ are taken, Eq. (38) becomes Eq. (37), that only takes into account the Alfvén resonance.

Eq. (38) can now be directly applied to measure the relative contribution of each resonance to the total damping. To do that, Soler et al. (2009) assumed $r_{\mathrm{A}} \simeq r_{\mathrm{S}} \simeq a$, for simplicity, so $\cos \alpha_{\mathrm{A}} \simeq \cos \alpha_{\mathrm{S}} \simeq 1$. The ratio of the two terms in Eq. (38) is then

$$\frac{\tau_{\mathrm{dA}}}{\tau_{\mathrm{dS}}} \simeq \frac{(k_z a)^2}{m^2} \left(\frac{c_{\mathrm{s}}^2}{c_{\mathrm{s}}^2 + v_{\mathrm{A}}^2} \right)^2 , \tag{39}$$

where τ_{dA} and τ_{dS} are the respective contributions of the Alfvén and slow resonances in Eq. (38). A simple calculation shows that, for typical wavelengths of observed thread oscillations, the contribution of the slow resonance is irrelevant in front of that of the Alfvén resonance. Take for instance, $m = 1$ and $k_z a = 10^{-2}$, then Eq. (39) gives $\tau_{\mathrm{dA}}/\tau_{\mathrm{dS}} \simeq 10^{-7}$.

This analytical predictions were further confirmed by Soler et al. (2009) by performing numerical computations outside the thin tube and thin boundary approximations. Figure 69 shows that the slow resonance is much less efficient than the Alfvén resonance. For the wavenumbers relevant to observed prominence oscillations, the value of τ_{d}/P due to the slow resonance is between 4 and 8 orders of magnitude larger than the same ratio obtained for the Alfvén resonance. The overall conclusion by Soler et al. (2009) is that the slow resonance is very inefficient when it comes to damping the kink mode for typical prominence conditions and in the observed wavelength range. The damping times obtained with this mechanism are comparable to those due to the thermal effects discussed in Sect. 7.1. Hence, resonant damping of transverse thread oscillations is governed by the Alfvén resonance.

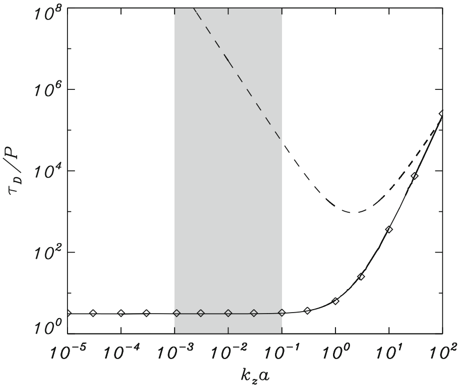

Fig. 69 Wave damping by Alfvén and slow resonances in an infinitely long prominence thread. Kink mode ratio of the damping time to the period, τ_d/P, as a function of the dimensionless wavenumber, $k_z a$, for $l/a = 0.2$. The solid line is the full numerical solution. The symbols and the dashed line are the results of the thin boundary approximation for the Alfvén and slow resonances, i.e., the two terms in Eq. (38). The shaded region represents the range of typically observed values for the wavelengths in prominence oscillations. Image reproduced with permission from Soler et al. (2009), copyright by AAS

7.4 Resonant damping of global prominence oscillations

The results described in Sect. 7.3 consider oversimplified models of transverse prominence thread oscillations and their damping by resonant absorption. The oscillations are monochromatic and, hence, the energy is transferred to a particular location at the flux tube boundary, where the kink mode frequency matches the corresponding Alfvén or slow continuum frequency. In reality, the magnetic and plasma structure of prominences is more complex and only recently numerical models describing the damping of global prominence oscillations and the transfer of energy to small spatial scales by resonant damping were considered.

In view of the need to study prominence dynamics using realistic inhomogeneous models, Terradas et al. (2016) considered the temporal evolution of vertical oscillations in a prominence inserted in a 3D magnetic structure with flux rope properties. The adopted magnetic configuration is the Titov and Démoulin (1999) force-free model and a numerical study of several morphological and dynamical properties was conducted, for different amounts of magnetic twist. After a density enhancement with prominence properties is introduced inside the flux rope, the system, which is out of equilibrium, evolves through a relaxation process in which the morphology of the cold and dense plasma varies from the initial Gaussian shape to a more irregular configuration, with the mass aligned with the flux rope axis. The stage until a quasi-stationary state is reached is found to be quite dynamic. In particular, the analysis of the time evolution of the vertical component of the centre of mass position, taken by Terradas et al. (2016) as a proxy for the vertical motion of the prominence, shows a clear oscillatory behaviour displaying time damping (see Fig. 70). For this particular simulation, a flux rope with weak twist was considered together with a relatively light prominence, with a density enhancement of 5 with respect to the surrounding coronal density. The reason is that under these conditions it is easier to ascertain the physical origin of the

Fig. 70 Temporal evolution of the centre of mass position in a numerical solution for vertical oscillations of a prominence embedded in a magnetic flux rope with a low prominence–corona density contrast in the weak twist regime ($N_t = 2.2$ in the Titov and Démoulin 1999 model), and a spatial resolution of 600 km. Image reproduced with permission from Terradas et al. (2016), copyright by AAS

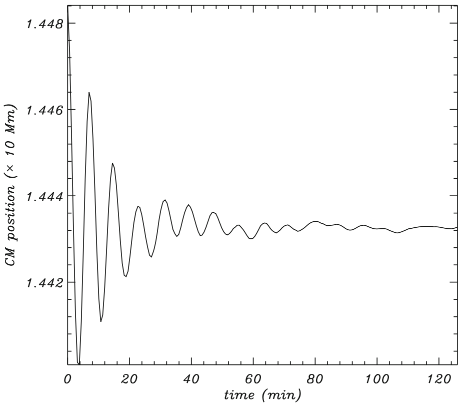

attenuation that is apparent in the oscillation pattern. In general, the oscillation period is rather independent of the amount of twist of the magnetic configuration. For this particular case, the basic vertical oscillation period is around 8 min, although there is evidence for an additional longer 43-min oscillation which corresponds to a global motion along the magnetic field producing contractions and dilatations of the whole prominence.

Terradas et al. (2016) identify three possible sources of attenuation that could explain the damping present in Fig. 70: resonant damping, wave leakage, and numerical diffusion. Numerical diffusion is discarded since convergence tests shows that this effect is irrelevant for the spatial resolution used in their simulation. Wave leakage cannot account for the observed attenuation of the signal neither, because Alfvénic modes in the coronal environment have frequencies that are above the global mode frequency, in the considered system. The resonant or continuum damping remains as the only possible cause and was analysed in more detail.

The study of the spatial distribution of the kinetic energy together with the morphology of the prominence plasma indicates that the reason for the attenuation is due to the conversion of energy of the transverse vertical motion into localised perturbations at the lateral edge of the prominence plasma. Figure 71 shows isocontours of density, representative of the prominence plasma, together with a specific isocontour of kinetic energy. One can see that, as the mode conversion process proceeds, the energy is transferred to small spatial scales and concentrated at a thin region near the edges of the prominence.

Further confirmation of this process taking place comes from the analysis of the power spectrum of the oscillatory signal at two different locations inside the simulation box, one close to the centre of the prominence and another at the transition region between the prominence and the corona (Fig. 72). By computing the power spectrum at these two locations, Terradas et al. (2016) find that the dominant periodicity at the centre of the prominence is the one corresponding to the global mode (8 min), while at the prominence–corona transition region an additional frequency is present, with a period of 5.25 min, which corresponds to a particular Alfvén continuum mode. A similar coexistence of global and local frequencies was reported by Terradas et al.

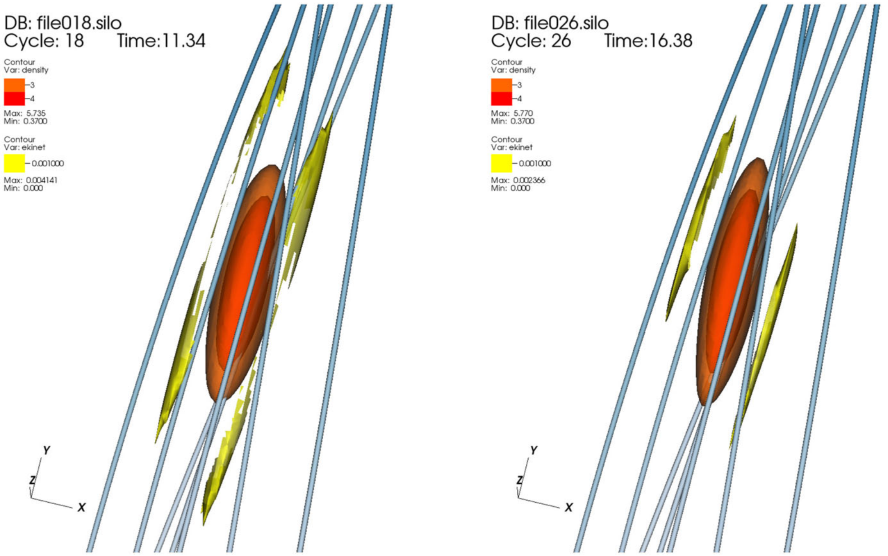

Fig. 71 Detail of the prominence (in red–orange) together with some magnetic field lines and the locations where the kinetic energy increases (in yellow) as a result of resonant damping. The simulation parameters are the same as in Fig. 70. Image reproduced with permission from Terradas et al. (2016), copyright by AAS

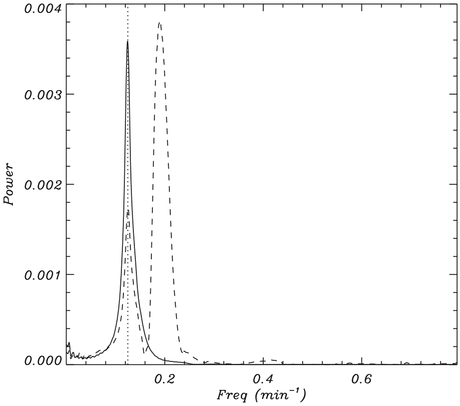

Fig. 72 Power spectrum of the vertical velocity component at two different positions in the prominence. The solid line corresponds to the point close to the centre of the prominence, while the dashed line is in the prominence–corona transition region. The two power spectra show a common peak (plotted with a vertical dotted line), associated with the global motion of the prominence. Image reproduced with permission from Terradas et al. (2016), copyright by AAS

(2008) in a multi-stranded coronal loop model and interpreted as evidence of the physical process of resonant damping of the global mode to Alfvén waves of local character.

The overall conclusion by Terradas et al. (2016), regarding resonant damping processes, is that realistic 3D numerical solutions in complex magnetic flux rope configurations show compelling evidence about the transfer of energy from the initial global oscillation of the whole prominence to Alfvén continuum modes at the edges of the cool and dense plasma structure.

7.5 Resonant damping in partially ionised infinitely long threads

7.5.1 Temporal damping

Damping by resonant absorption in a partially ionised prominence plasma was studied by Soler et al. (2009d), who integrated both mechanisms in a non-uniform cylindrical prominence thread model in order to assess their combined effects. Partial ionisation is relevant for the damping of short wavelength fast waves (Forteza et al. 2007), while resonant damping of kink waves is efficient whenever a transverse density inhomogeneity is present. The question arises on whether partial ionisation affects the mechanism of resonant absorption and viceversa.

The model adopted by Soler et al. (2009d) has the magnetic and density structuring of the models used in Sect. 7.3 (see Fig. 67), but the plasma properties are also characterised by the ionisation fraction, $\tilde{\mu}$. The radial behaviour of the ionisation fraction in threads is unknown, so Soler et al. (2009d) assumed a one-dimensional transverse profile akin to the one employed to model the equilibrium density. The thread ionisation fraction, $\tilde{\mu}_{\mathrm{p}}$, is considered a free parameter and the corona is assumed to be fully ionised, so $\tilde{\mu}_{\mathrm{c}} = 0.5$. The non-uniform transitional layer of thickness l therefore connects two plasmas with densities ρ_{p} and ρ_{c} and ionisation degrees $\tilde{\mu}_{\mathrm{p}}$ and $\tilde{\mu}_{\mathrm{c}}$. Soler et al. (2009d) used the one-fluid approximation and, for simplicity, the $\beta = 0$ limit, which excludes slow waves. The quantities η, η_{C} and η_{H} are here functions of the radial direction.

Soler et al. (2009d) first considered resonant damping in combination with Cowling's diffusion and excluded Hall's dissipation. They derived the following approximate expression for the damping ratio over the period, under the thin boundary approximation,

$$\frac{\tau_{\mathrm{d}}}{P} = \frac{2}{\pi}\left[m\left(\frac{l}{a}\right)\left(\frac{\rho_{\mathrm{p}}-\rho_{\mathrm{c}}}{\rho_{\mathrm{p}}+\rho_{\mathrm{c}}}\right) + \frac{2\left(\rho_{\mathrm{p}}\tilde{\eta}_{\mathrm{Cp}}+\rho_{\mathrm{c}}\tilde{\eta}_{\mathrm{Cc}}\right)k_z a}{\sqrt{2\rho_{\mathrm{p}}\left(\rho_{\mathrm{p}}+\rho_{\mathrm{c}}\right)}}\right]^{-1}, \tag{40}$$

with $\tilde{\eta}_{\mathrm{Cc,p}} = \eta_{\mathrm{C}}/v_{\mathrm{Ac,p}}a$ the coronal and prominence Cowling's diffusivities in dimensionless form. Notice that Eq. (40) reduces to Eq. (37) in a fully ionised plasma, and is in agreement with Eq. (38), in which the slow resonance is additionally included. In this expression, the term due to resonant damping is independent of the value of Cowling's diffusivity and, therefore, of the ionisation degree. The second term, related to the damping by Cowling's diffusion, is proportional to k_z, so its influence in the long-wavelength limit is expected to be small. Soler et al. (2009d) performed a simple calculation by considering $m = 1$, $k_z a = 10^{-2}$ and $l/a = 0.2$. This results in $\tau_{\mathrm{d}}/P \approx 3.18$ for a fully ionised thread ($\tilde{\mu}_{\mathrm{p}} = 0.5$) and $\tau_{\mathrm{d}}/P \approx 3.16$ for an almost neutral thread ($\tilde{\mu}_{\mathrm{p}} = 0.95$). Thus, this approximate expression suggests that the ratio τ_{d}/P depends very slightly on the ionisation degree, suggesting that resonant absorption dominates over Cowling's diffusion.

The analytical estimates described above can be verified and extended by numerically solving the full eigenvalue problem. This approach allowed Soler et al. (2009d) to

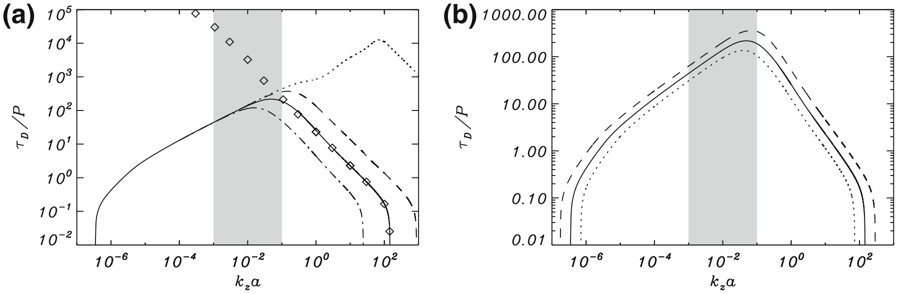

Fig. 73 Wave damping by ion-neutral effects in an infinitely long cylindrical prominence thread. Ratio of the damping time to the period of the kink mode as a function of $k_z a$ for a thread without transitional layer, i.e., $l/a = 0$. **a** Results for $a = 100$ km and different ionisation degrees: $\tilde{\mu}_\mathrm{p} = 0.5$ (dotted line), $\tilde{\mu}_\mathrm{p} = 0.6$ (dashed line), $\tilde{\mu}_\mathrm{p} = 0.8$ (solid line) and $\tilde{\mu}_\mathrm{p} = 0.95$ (dash-dotted line). Symbols are the approximate solution, given by Eq. (40), for $\tilde{\mu}_\mathrm{p} = 0.8$. **b** Results for $\tilde{\mu}_\mathrm{p} = 0.8$ and different thread widths: $a = 100$ km (solid line), $a = 50$ km (dotted line) and $a = 200$ km (dashed line). The shaded zone corresponds to the range of typically observed wavelengths of prominence oscillations. Image reproduced with permission from Soler et al. (2009d), copyright by AAS

additionally include Hall's diffusion in addition to ohmic and Cowling's dissipation. In their study, these authors first considered a configuration with an abrupt density variation across the thread boundary (that is, $l = 0$), which prevents resonant absorption from working. Next, they included the thin transitional layer between the thread and the corona, so that both resonant absorption and ion-neutral effects are at work.

For a homogeneous thread ($l/a = 0$), Soler et al. (2009d) computed the damping rate for different ionisation degrees (see Fig. 73). In agreement with the results displayed for the kink mode in Fig. 66, τ_d/P has a maximum at the transition between the ohmic-dominated regime, which is almost independent of the ionisation degree, to the region where Cowling's diffusion is more relevant and the ionisation degree has a significant influence. The approximate analytical solution for a given value of $\tilde{\mu}_\mathrm{p}$ agrees very well with the numerical solution in the region where Cowling's diffusion dominates, while it significantly diverges from the numerical solution in the region where ohmic diffusion is relevant. Within the range of typically reported wavelengths, τ_d/P is between 1 and 2 orders of magnitude larger than the measured values, so neither ohmic nor Cowling's diffusion can account for the observed damping time.

For the inhomogeneous thread case ($l/a \neq 0$), Fig. 74a displays some relevant differences. First, the damping time is dramatically reduced for intermediate values of $k_z a$, which include the region of typically observed wavelengths. In this region, the ratio τ_d/P becomes smaller as l/a is increased, a behaviour consistent with damping by resonant absorption. The inclusion of the inhomogeneous transitional layer removes the smaller critical wavenumber and consequently the kink mode exists for very small values of $k_z a$. Figure 74a also shows a very good agreement between the numerical and the approximate solutions, this one given by Eq. (40), for wavenumbers above $k_z a \sim 10^{-4}$, and a poor agreement in the range for which ohmic diffusion dominates, below $k_z a \sim 10^{-4}$. To understand this behaviour one has to bear in mind that the analytic approximate solution includes the effects of resonant absorption and Cowling's diffusion, but not the influence of ohmic diffusion. Such as shown in Fig. 74b,

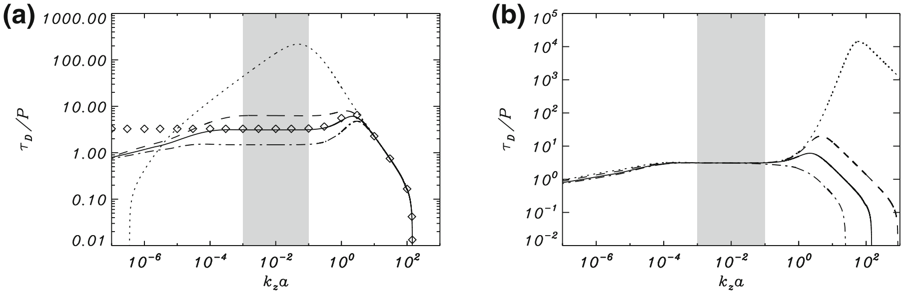

Fig. 74 Wave damping by resonant absorption and ion-neutral effects in an infinitely long cylindrical prominence thread. Ratio of the damping time to the period of the kink mode as a function of $k_z a$ for a thread with an inhomogeneous transitional layer. **a** Results for $\tilde{\mu}_\mathrm{p} = 0.8$ and different transitional layer widths: $l/a = 0$ (dotted line), $l/a = 0.1$ (dashed line), $l/a = 0.2$ (solid line) and $l/a = 0.4$ (dash-dotted line). Symbols are the solution in the thin boundary approximation (Eq. 40) for $l/a = 0.2$. **b** Results for $l/a = 0.2$ and different ionisation degrees: $\tilde{\mu}_\mathrm{p} = 0.5$ (dotted line), $\tilde{\mu}_\mathrm{p} = 0.6$ (dashed line), $\tilde{\mu}_\mathrm{p} = 0.8$ (solid line) and $\tilde{\mu}_\mathrm{p} = 0.95$ (dash-dotted line). In both panels $a = 100$ km. Image reproduced with permission from Soler et al. (2009d), copyright by AAS

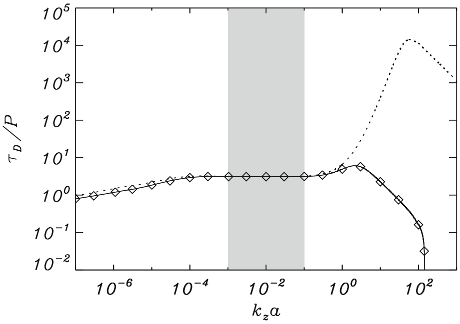

Fig. 75 Ratio of the damping time to the period of the kink mode as a function of $k_z a$ in an infinitely long thread with $a = 100$ km and $l/a = 0.2$. The different line styles represent the results for a partially ionised thread with $\tilde{\mu}_\mathrm{p} = 0.8$ and considering all the terms in the induction equation (solid line), for a partially ionised thread with $\tilde{\mu}_\mathrm{p} = 0.8$ and neglecting Hall's term (symbols) and for a fully ionised thread (dotted line). Image reproduced with permission from Soler et al. (2009d), copyright by AAS

the ionisation degree is only relevant for large wavenumbers, where the damping rate significantly depends on the ionisation fraction through ohmic diffusion.

Figure 75 displays the ranges of $k_z a$ for which Cowling's and Hall's diffusion dominate. Hall's diffusion is irrelevant in the whole range of $k_z a$ studied by Soler et al. (2009d), while Cowling's diffusion dominates the damping for large $k_z a$. In the whole range of relevant wavelengths, resonant absorption is the most efficient damping mechanism and the damping time is independent of the ionisation degree, as predicted by the analytical result (Eq. 40). On the contrary, ohmic diffusion dominates for very small $k_z a$. In this region, the damping time related to Ohm's dissipation becomes even shorter than that due to resonant absorption, which means that the kink wave is mainly damped by Ohmic diffusion.

7.5.2 Spatial damping

Motivated by the spatially damped propagating waves observed by Terradas et al. (2002) (see Sect. 5.9.3), the spatial damping of linear non-adiabatic magnetohydrodynamic waves in a homogenous, unbounded, magnetised and fully ionised plasma was studied by Carbonell et al. (2006). The spatial damping in a flowing partially ionised plasma has been studied by Carbonell et al. (2010). Carbonell et al. (2006) found that the thermal (fast) wave shows the strongest (weakest) spatial damping. For periods longer than 1 s the spatial damping of magnetoacoustic waves is dominated by radiation, while at shorter periods the spatial damping is dominated by thermal conduction. Therefore, radiative effects on linear magnetoacoustic slow waves can be a viable mechanism for the spatial damping of short period prominence oscillations, while thermal conduction does not play any role. On the other hand, Carbonell et al. (2010) found that in the presence of a background flow, new strongly damped fast and Alfvén waves appear whose features depend on the joint action of flow and resistivity. The damping lengths of adiabatic fast and slow waves are strongly affected by partial ionisation, which also modifies the ratio between damping lengths and wavelengths. For non-adiabatic slow waves, the unfolding in both wavelength and damping length induced by the flow allows efficient damping for periods compatible with those observed in prominence oscillations. In the case of non-adiabatic slow waves and within the range of periods of interest for prominence oscillations, the joint effect of both flow and partial ionisation leads to efficient spatial damping of oscillations. For fast and Alfvén waves, the most efficient damping occurs at very short periods not compatible with those observed in prominence oscillations.

Using the same equilibrium model as in Soler et al. (2009d) (see Fig. 67), whose results have been presented in Sect. 7.5.1, Soler et al. (2011) investigated the spatial damping of propagating kink MHD waves in transversely non-uniform and partially ionised prominence threads. The damping mechanisms are resonant absorption and ion-neutral collisions (Cowling's diffusion). In the absence of transitional layer, i.e., when the damping is due to Cowling's diffusion exclusively, the non-dimensional wavelength, the damping length, L_D, and the ratio of the damping length to the wavelength are displayed in Fig. 76. Regarding the wavelength, we see that the effect of Cowling's diffusion is only relevant for periods much shorter than those observed (1–10 min, corresponding to $40 \leq P/\tau_\mathrm{Ap} \leq 400$, with $\tau_\mathrm{Ap} = a/v_\mathrm{Ap}$ the thread Alfvén travel time). On the other hand, an almost neutral plasma, i.e., $\tilde{\mu}_\mathrm{p} \to 1$, has to be considered to obtain an efficient damping and to achieve small values of the damping ratio within the relevant range of periods. Such very large values of $\tilde{\mu}_\mathrm{p}$ are probably unrealistic (Labrosse et al. 2010).

For resonantly damped modes, Fig. 77 shows the results for different values of the thickness of the layer and fixed ionisation degree. Figure 78 displays the results for different values of the ionisation degree and a fixed transverse inhomogeneity length scale. Since the wavelength is not affected by the value of l/a and has the same behaviour as in Fig. 76a, both Figs. 77 and 78 focus on L_D/a and L_D/λ. Depending on the period, two different behaviours of the solutions are obtained. For short periods, the damping length is independent of the layer thickness and is governed by the value of the ionisation degree. On the contrary, for large periods, the damping length

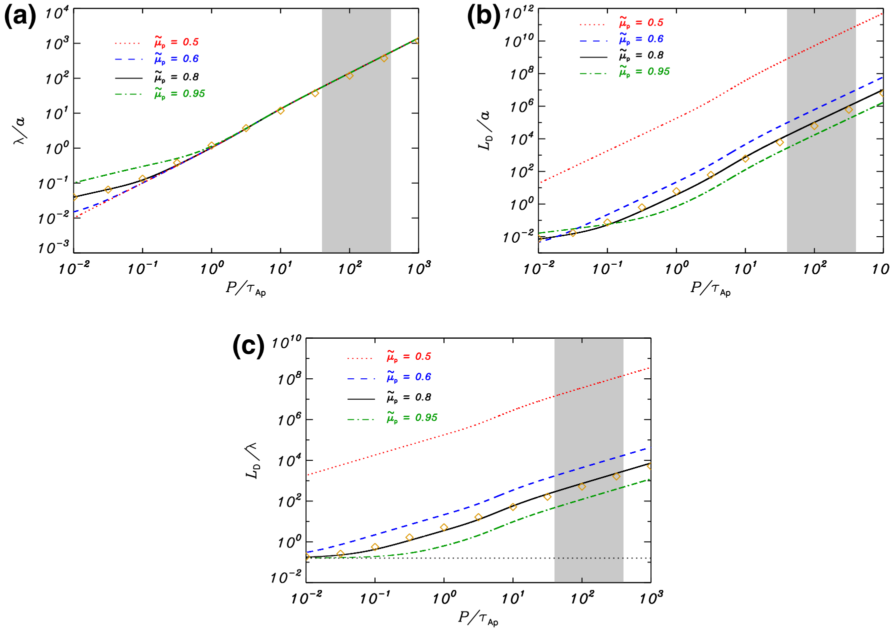

Fig. 76 Spatial damping of kink waves due to ion-neutral effects in an infinitely long prominence thread. Results for the kink mode spatial damping in the case $l/a = 0$: **a** λ/a, **b** L_D/a and **c** L_D/λ versus P/τ_{Ap} for $\tilde{\mu}_p = 0.5$, 0.6, 0.8 and 0.95. Symbols in (**a**), (**b**) and (**c**) correspond to the analytical solution given by Eqs. (12), (13) and (14) in Soler et al. (2011) in the thin tube approximation, while the horizontal dotted line in (**c**) corresponds to the limit of L_D/λ for high frequencies. The shaded area denotes the range of observed periods of thread oscillations. Image reproduced with permission from Soler et al. (2011), copyright by AAS

depends on the value of l/a, but is independent of the ionisation degree. This result indicates that resonant absorption dominates the damping for large periods, whereas Cowling's diffusion is more relevant for short period oscillations. In addition, we can observe that the approximate transitional period for which the damping length by Cowling's diffusion becomes shorter than that due to resonant absorption is much lower than the typically observed periods. This shows that resonant absorption is the dominant damping mechanism in the relevant range. The analytical approximation for the damping ratio obtained by Soler et al. (2011) gives an accurate description of the kink mode spatial damping in the relevant range of periods, such as shown by the diamonds in Figs. 76 and 77.

For typically reported periods of thread oscillations, resonant absorption is an efficient mechanism for the kink mode spatial damping, while ion-neutral collisions have a minor role. Cowling's diffusion dominates both the propagation and damping for periods much shorter than those observed, while resonant absorption could explain the observed spatial damping of kink waves in prominence threads.

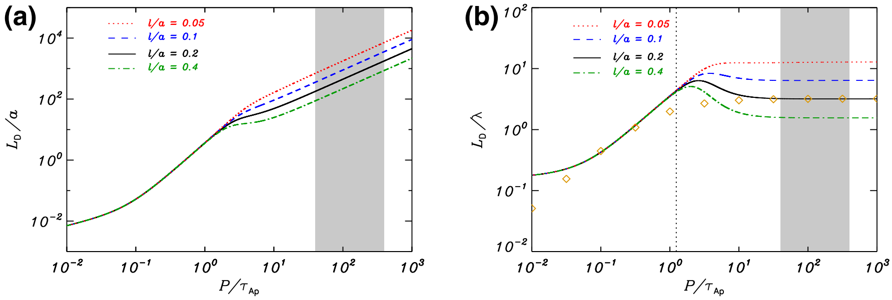

Fig. 77 Results for the kink mode spatial damping in an infinitely long prominence thread, in the case $l/a \neq 0$: **a** L_D/a and **b** L_D/λ versus P/τ_Ap for $l/a = 0.05$, 0.1, 0.2 and 0.4, with $\tilde{\mu}_\mathrm{p} = 0.8$. Symbols in (**b**) correspond to the analytical solution in the thin tube approximation, while the vertical dotted line is the approximate transitional period for $l/a = 0.1$. The shaded area denotes the range of observed periods of thread oscillations. Image reproduced with permission from Soler et al. (2011), copyright by AAS

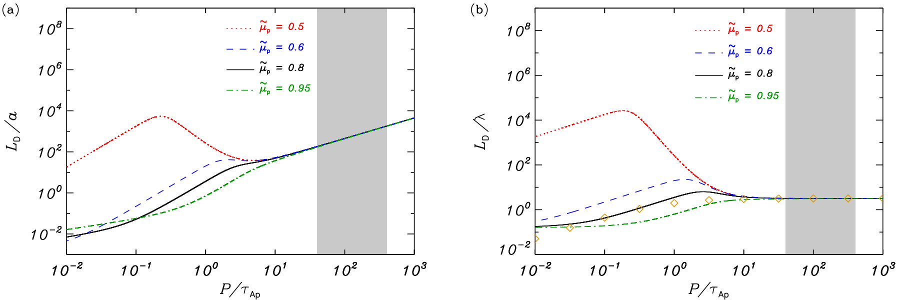

Fig. 78 Results for the kink mode spatial damping in an infinitely long prominence thread, in the case $l/a \neq 0$: **a** L_D/a and **b** L_D/λ versus P/τ_Ap for $\tilde{\mu}_\mathrm{p} = 0.5$, 0.6, 0.8 and 0.95, with $l/a = 0.2$. Symbols in (**b**) correspond to the analytical solution in the thin tube approximation. The shaded area denotes the range of observed periods of thread oscillations. Image reproduced with permission from Soler et al. (2011), copyright by AAS

7.6 Resonant damping in partially ionised finite length threads

The results described in Sects. 7.3, 7.5.1 and 7.5.2 indicate that, because of the coupling of kink waves to Alfvén waves, resonant absorption constitutes a very plausible mechanism for the explanation of the observed spatial and time decay of transverse oscillations. The main limitation of these studies is that they adopt a one-dimensional density model that might not be appropriate in view of the longitudinal structuring of prominence threads. This led Soler et al. (2010a) to investigate the time damping properties of two-dimensional thread models, that is, with density inhomogeneity across the thread and along the magnetic tube in which it is contained. In this study, resonant absorption and damping by partial ionisation effects were considered simultaneously.

Soler et al. (2010a) (see Fig. 79) modelled a prominence fine structure as a straight cylindrical magnetic tube only partially filled with the cold and dense material. The length of the dense part is L_p. The thread may either occupy the centre of the magnetic tube or be displaced, so that the lengths of both evacuated parts of the tube are different.

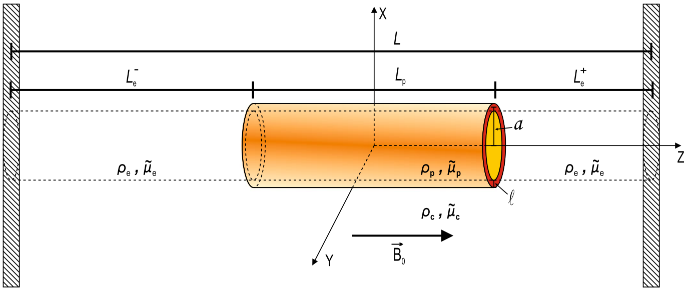

Fig. 79 Model representing a finite length thread. A partially filled magnetic flux tube, with length L and radius a, is considered. The tube ends are fixed by two rigid walls representing the solar photosphere. The tube is composed of a dense region of length L_p surrounded by two much less dense zones corresponding to the evacuated parts of the tube. In the prominence region a transversely inhomogeneous layer of length l is considered. The plasma in the prominence region is assumed to be partially ionised with an arbitrary ionisation degree $\tilde{\mu}_\mathrm{p}$. Both the evacuated part and the corona are taken to be fully ionised. Image reproduced with permission from Soler et al. (2010a), copyright by AAS

By denoting the lengths of the right and left hand-side evacuated regions as L_e^+ and L_e^-, one has $L_\mathrm{e}^+ = L - L_\mathrm{e}^- - L_\mathrm{p}$, with L the full length of the tube. Just like in the works discussed in Sect. 7.5, the prominence plasma is partially ionised and a transverse inhomogeneous transitional layer is included between the prominence thread and the coronal medium. Ion-neutral collisions and resonant absorption are the considered damping mechanisms. The main model improvements in comparison to the thread model by Díaz et al. (2002), discussed in Sect. 6.4 (see Fig. 56), are the ability to model non-centred threads, the inclusion of a non-uniform transverse layer and partial ionisation of the thread plasma.

First, damping by Cowling's diffusion alone is considered by setting $l = 0$. When the thread is located in the centre of the tube the ratio of the damping time to the period is given by the approximate expression

$$\frac{\tau_\mathrm{d}}{P} \approx \frac{1}{2\pi}\left(\frac{\rho_\mathrm{p}+\rho_\mathrm{c}}{\rho_\mathrm{p}}\right)^{1/2}\frac{1}{\tilde{\eta}_\mathrm{Cp}}\sqrt{2\left(1-\frac{L_\mathrm{p}}{L}\right)\frac{L_\mathrm{p}}{L}}, \tag{41}$$

with $\tilde{\eta}_\mathrm{Cp} = \eta_\mathrm{C}/v_\mathrm{Ap}a$ the filament Cowling's diffusivity in dimensionless form. For $\rho_\mathrm{p}/\rho_\mathrm{c} = 200$, $L_\mathrm{p}/L = 0.1$ and $L = 10^5$ km, Eq. (41) gives $\tau_\mathrm{d}/P \approx 5 \times 10^3$ for $\tilde{\mu}_\mathrm{p} = 0.8$ and $\tau_\mathrm{d}/P \approx 150$ for $\tilde{\mu}_\mathrm{p} = 0.99$. Therefore, in a transversally homogeneous thread, an almost neutral prominence plasma is needed, i.e., $\tilde{\mu}_\mathrm{p} \approx 1$, for the damping due to Cowling's diffusion to be efficient. Although the precise ionisation degree is unknown, such large values of $\tilde{\mu}_\mathrm{p}$ are probably unrealistic in the context of prominences.

Next, Soler et al. (2010a) considered $l/a \neq 0$, so that both resonant absorption and Cowling's diffusion can cause wave damping. An approximate expression for the damping ratio for a sinusoidal density variation in the transitional layer is

$$\frac{\tau_{\mathrm{d}}}{P} \approx \frac{2}{\pi}\left[m\left(\frac{l}{a}\right)\left(\frac{\rho_{\mathrm{p}}-\rho_{\mathrm{c}}}{\rho_{\mathrm{p}}+\rho_{\mathrm{c}}}\right)+\tilde{\eta}_{\mathrm{Cp}}\left(\frac{\rho_{\mathrm{p}}}{\rho_{\mathrm{p}}+\rho_{\mathrm{c}}}\right)^{1/2}\frac{4}{\sqrt{2\left(1-\frac{L_{\mathrm{p}}}{L}\right)\frac{L_{\mathrm{p}}}{L}}}\right]^{-1}. \tag{42}$$

As a numerical example, in the case $m = 1, L_{\mathrm{p}}/L = 0.1, L = 10^7$ m and $l/a = 0.2$, the damping ratio is $\tau_{\mathrm{d}}/P \approx 3.18$ for a fully ionised thread ($\tilde{\mu}_{\mathrm{p}} = 0.5$) and $\tau_{\mathrm{d}}/P \approx 3.16$ for an almost neutral thread ($\tilde{\mu}_{\mathrm{p}} = 0.95$). Note that the obtained damping times are consistent with the observations. Moreover, as seen in Sect. 7.5.1, the contribution of resonant absorption to the damping is much more important than that of Cowling's diffusion, so the ratio τ_{d}/P depends only very slightly on the ionisation degree and the second term on the right-hand side of Eq. (42) can in principle be neglected.

When the prominence region is not at the centre of the tube, and assuming $l = 0$, an approximate expression for the damping ratio is

$$\frac{\tau_{\mathrm{d}}}{P} \approx \frac{1}{2\pi}\left(\frac{\rho_{\mathrm{p}}+\rho_{\mathrm{c}}}{\rho_{\mathrm{p}}}\right)^{1/2}\frac{1}{\tilde{\eta}_{\mathrm{Cp}}}\sqrt{2\left[\left(1-\frac{L_{\mathrm{p}}}{L}\right)\frac{L_{\mathrm{p}}}{L}+4\frac{L_{\mathrm{e}}^{-}L_{\mathrm{e}}^{+}}{L^2}\right]\frac{L_{\mathrm{p}}}{L}}. \tag{43}$$

Taking the limits $L_{\mathrm{e}}^{-} \to 0$ or $L_{\mathrm{e}}^{+} \to 0$ in this expression, it can be shown that the minimum value of the damping ratio by Cowling's diffusion takes place when the prominence region is located at the magnetic tube centre ($L_{\mathrm{e}}^{-} = L_{\mathrm{e}}^{+}$).

Soler et al. (2010a) find that for $l \neq 0$ and under the thin tube and thin boundary approximations, the period and damping time by resonant absorption have the same dependence on L_{e}^{-} and L_{e}^{+}. This means that for resonant absorption the damping ratio does not depend on these quantities. Since resonant damping dominates over Cowling's diffusion, this leads to the conclusion that when considering both damping mechanisms, the damping ratio will be almost unaffected by the position of the prominence region within the fine structure.

The accuracy of the above analytical solutions can be assessed by numerically solving the general dispersion relation derived by Soler et al. (2010a). Here we only show the results obtained by Soler et al. (2010a) for the case in which the prominence thread is centred in the tube.

In the case without transverse transitional layer, $l/a = 0$, damping is only due to Cowling's diffusion. Figure 80a displays the period as a function of L_{p}/L for different values of the ionisation degree in the prominence region, whereas Fig. 80b shows the corresponding values of the damping time. As can be seen, the period increases when the length of the thread is increased and tends to the value for a homogeneous prominence cylinder when $L_{\mathrm{p}}/L \to 1$. In addition, the period is independent of the ionisation degree. On the contrary, the damping time strongly depends on the ionisation degree, and for a fixed $\tilde{\mu}_{\mathrm{p}}$ it slightly increases as L_{p}/L becomes larger. In all solutions, the analytical expressions for the period and the damping time are in agreement with the solution of the full dispersion relation for realistic, small values of L_{p}/L, i.e., $L_{\mathrm{p}}/L \leq 0.4$, whereas the approximate expressions diverge from the actual solution when the prominence region occupies most of the magnetic tube. Figure 80c displays τ_{d}/P versus L_{p}/L. The numerical solution shows little dependence on L_{p}/L, while

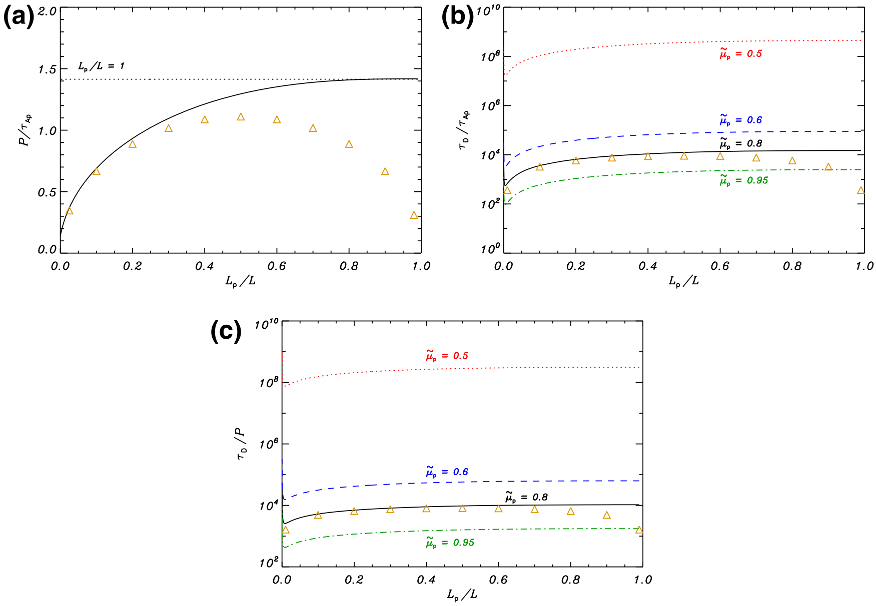

Fig. 80 Results for the thread model in Fig. 79 without transverse transitional layer and for the prominence thread located at the central part of the magnetic tube. **a** Period, P, of the fundamental kink mode in units of the internal Alfvén travel time, τ_{Ap}, as a function of L_{p}/L. The horizontal dotted line corresponds to the period of the kink mode in a homogeneous prominence cylinder. The symbols are the analytic solution (Eq. 24 in Soler et al. 2010a). **b** Damping time, τ_{d}, in units of the internal Alfvén travel time, τ_{Ap}, as a function of L_{p}/L. The different lines denote $\tilde{\mu}_{\mathrm{p}} = 0.5$ (dotted), 0.6 (dashed), 0.8 (solid) and 0.95 (dash-dotted). The symbols are the analytic approximation for $\tilde{\mu}_{\mathrm{p}} = 0.8$ (Eq. 27 in Soler et al. 2010a). **c** τ_{d}/P versus L_{p}/L. The line styles have the same meaning as in (**b**) and the symbols are the approximation given by Eq. (41). Image reproduced with permission from Soler et al. (2010a), copyright by AAS

the analytical approximation (Eq. 41) diverges from the numerical value in the limit of large L_{p}/L. Given the obtained large values of τ_{d}/P, Soler et al. (2010a) concluded that the efficiency of the damping due to Cowling's diffusion in a partially filled flux tube does not improve with respect to the longitudinally homogeneous tube case shown in Sect. 7.5.1.

Next, Soler et al. (2010a) included resonant damping. The period and the damping time of the fundamental kink mode were computed as a function of the different parameters, namely $\tilde{\mu}_{\mathrm{p}}$, l/a and L_{p}/L. Regarding the period, Soler et al. (2010a) found that both its value and its dependence on L_{p}/L are the ones plotted in Fig. 80a because the period is almost independent $\tilde{\mu}_{\mathrm{p}}$ and l/a. For a fixed ionisation degree of $\tilde{\mu}_{\mathrm{p}} = 0.8$, the damping time decreases with l/a. The approximate analytical estimate of the damping time is in good agreement with the full solution for L_{p}/L below 0.4 (see Fig. 81a). In order to assess the efficiency of resonant damping, Fig. 81b displays the corresponding values of τ_{d}/P. If we compare the damping ratios in this figure with those corresponding to Cowling's diffusion (see Fig. 80c), much smaller values of τ_{d}/P are now obtained. The damping ratio is almost independent of the length of the thread. This is because under the thin tube and thin boundary approximations,

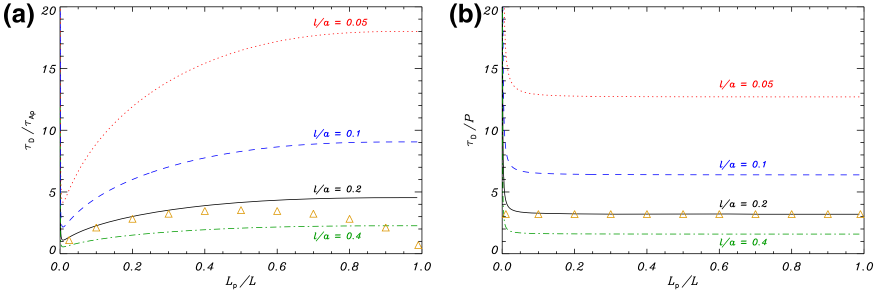

Fig. 81 Results for a thread configuration with a transverse transitional layer and for the prominence thread located at the central part of the magnetic tube. **a** τ_d in units of the internal Alfvén travel time, τ_Ap, and **b** τ_d/P as a function of L_p/L. The different lines in both panels denote $l/a = 0.05$ (dotted), 0.1 (dashed), 0.2 (solid) and 0.4 (dash-dotted). The symbols in (**a**) and (**b**) correspond to the analytic approximations with $l/a = 0.2$, Eqs. (34) and (32) in Soler et al. (2010a). Image reproduced with permission, copyright by AAS

made by Soler et al. (2010a), the dependence of the period and damping time on the length of the thread is the same. Overall, a very good agreement is obtained between the numerical result and the analytical approximation, even for large values of the length of the thread.

In summary, the dominant damping mechanism is resonant absorption, which produces damping ratios in agreement with the observations, whereas ion-neutral collisions are irrelevant for the damping. The values of the damping ratio are independent of both the prominence thread length and its position within the magnetic tube, and coincide with the values for a tube fully filled with the prominence plasma. A recent study that further analyses resonant damping of thread oscillations in two-dimensional equilibrium models can be found in Arregui et al. (2011). These authors additionally analysed the influence of the density in the evacuated part of the thread. This quantity is seen to influence periods and damping times, but has little influence on the damping rate of transverse thread oscillations. The implications of some of these results for the determination of physical properties in transversely oscillating threads are discussed in Sect. 8.

7.7 Resonant damping in flowing prominence threads

Two typical features of the observed oscillations in prominence threads are the time damping of the amplitude of transverse motions and the simultaneous presence of mass flows along the threads. The theoretical analysis of their joint effect on the amplitude of transverse thread oscillations was performed by Soler et al. (2012). By interpreting the observed oscillations as transverse MHD kink waves, damped by resonant absorption, and the observed flows as the motion of the thread material along the prominence magnetic structure, a governing equation describing the temporal and spatial evolution for the transverse displacement of the fundamental mode of the magnetic tube was solved.

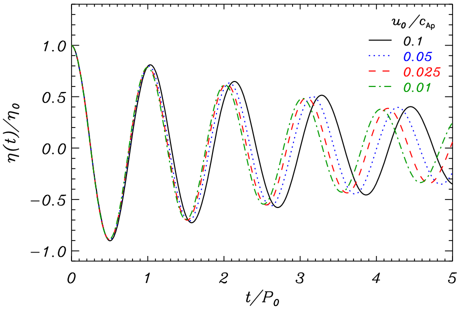

Fig. 82 Prominence thread transverse displacement as a function of time (in units of the instantaneous period at $t = 0$, P_0), for various values of the flow velocity, u_0/c_{Ap}, with $c_{\mathrm{Ap}} = v_{\mathrm{Ap}}$ the thread Alfvén speed. In all computations the transverse inhomogeneity length-scale is $l/a = 0.1$, the density contrast is $\rho_{\mathrm{p}}/\rho_{\mathrm{c}} = 200$, and the length of the thread is 0.1 times the full length of the flux tube, L. Image reproduced with permission from Soler et al. (2012), copyright by ESO

The obtained solutions show that flows and resonant damping can compete in determining the amplitude profile of the oscillations. Because of the presence of flows, the amplitude profile is found to deviate from the classic exponential profile for resonantly damped kink waves in static flux tubes. Flow introduces a progressive shift of the oscillation period, when compared to the evolution found in the static case.

Figure 82 shows an example solution for the thread displacement as a function of time for different values of the flow velocity. As can be appreciated, a progressive shift between the solutions corresponding to different flow velocities is obtained. The reason is that the instantaneous period is a function of the mass flow. When the transitional layer is very thin, so that the damping by resonant absorption is weak, the variation of the amplitude is mainly governed by the effect of the flow. In the example solutions displayed in Fig. 82, a layer 0.1 times the radius of the tube was chosen, so the amplitude is weakly affected by the flow velocity.

7.8 Damping by wave leakage

The solutions obtained for the oscillations of prominence line current models (Oord and Kuperus 1992; Schutgens 1997a, b; Oord et al. 1998) mentioned in Sect. 4.4 suggest the existence of time amplification and damping of the studied oscillations. While the amplification should be linked to a prominence destabilisation, the attenuation seems to be very efficient for many of the considered parameter values, and the ratio of the damping time to the period is between 1 and 10 (i.e., in agreement with observations). This indicates that the oscillations are efficiently damped (Fig. 83a). On the other hand, in the prominence model used by Schutgens and Tóth (1999) vertical oscillations are very efficiently attenuated for all the parameters considered and the same happens with horizontal oscillations (Fig. 83b) for coronal densities above $\simeq 5 \times 10^{-13}$ kg m^{-3}. These constraining properties of damped horizontal and vertical oscillations could be used for prominence seismology.

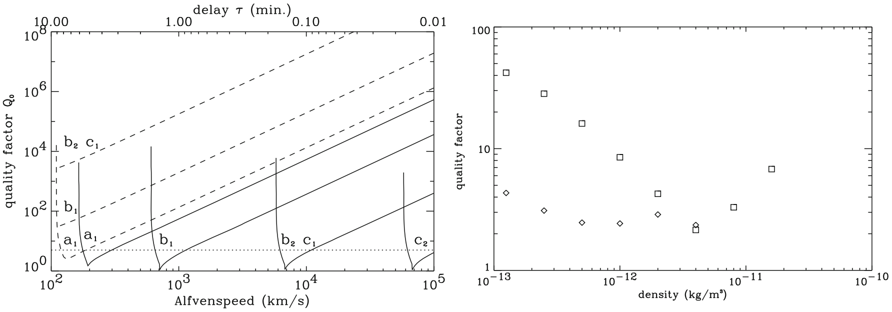

Fig. 83 Attenuation of prominence oscillations by wave leakage. **a** Quality factor ($Q_0 \equiv \pi\tau_d/P$) of stable IP (solid curves) and NP (dashed curves) prominence oscillations as a function of the coronal Alfvén speed. **b** Quality factor of the horizontally (squares) and vertically (diamonds) polarised stable oscillations versus the coronal density. IP and NP respectively stand for inverse polarity and normal polarity prominence models. Images reproduced with permission from (left) Schutgens (1997b), copyright by ESO; and (right) from Schutgens and Tóth (1999), copyright by AAS

However, the exact nature of the damping mechanism should be pointed out, and Schutgens and Tóth (1999) suggest that the damping of oscillations is due to the emission of waves by the prominence, i.e., wave leakage. The damping of horizontal motions is attributed to the emission of slow waves, whereas fast waves are invoked as the cause of the damping of vertical motions. Taking into account that the main difference between this work and those of Oord and Kuperus (1992), Schutgens (1997a, b) and Oord et al. (1998) lies essentially in the cross section of the filament, it seems that the physics involved should be the same, so wave leakage should be the mechanism responsible for the accounted damping. However, in Schutgens and Tóth (1999), the plasma-β in the prominence ranges from $\beta > 1$ in its central part to $\beta < 0.1$ at its boundary. Hence, waves emitted by the prominence into the corona propagate in a $\beta \ll 1$ environment in which magnetic field lines are closed. Under these conditions, slow modes propagate along magnetic field lines and are unable to transfer energy from the prominence into the corona and so wave leakage in the system studied by Schutgens and Tóth (1999) is only possible by fast waves. Then, it is hard to understand how the prominence oscillations can be damped by the emission of slow waves in this particular model, in which the dense, cool plasma is only allowed to emit fast waves. It must be mentioned, however, that the plasma-β in the corona increases with the distance from the filament, which implies that the emitted fast waves can transform into slow waves when they traverse the $\beta \simeq 1$ region. This effect has been explored by McLaughlin and Hood (2006) and McDougall and Hood (2007); see also references therein for similar studies.

8 Prominence seismology

Solar atmospheric seismology aims to determine physical parameters that are difficult to measure by direct means in magnetic and plasma structures. It is a remote diagnostics method that combines observations of oscillations and waves in magnetic structures, together with theoretical results from the analysis of oscillatory properties of given theoretical models. The philosophy behind this discipline is akin to that of Earth seismology, the sounding of the Earth interior using seismic waves, and helioseismology, the acoustic diagnostic of the solar interior. It was first suggested by Uchida (1970) and Roberts et al. (1984), in the coronal context, and by Tandberg-Hanssen (1995) in the prominence context. The increase in the number and quality of high resolution observations in the 1990s has lead to the rapid development of solar atmospheric seismology. In the context of coronal loop oscillations, recent applications of this technique have allowed the estimation and/or restriction of parameters such as the magnetic field strength (Nakariakov and Ofman 2001), the Alfvén speed in coronal loops (Zaqarashvili 2003; Arregui et al. 2007; Goossens et al. 2008), the transversal density structuring (Goossens et al. 2002; Verwichte et al. 2006; Arregui et al. 2015), the coronal density scale height (Andries et al. 2005; Verth et al. 2008; Arregui et al. 2013) or the estimation of the adiabatic index in the oscillating plasma (Doorsselaere et al. 2011).

The application of inversion techniques to prominence seismology is less developed. This is due to the complexity of these objects in comparison to, e.g., coronal loops. Recent advances in the theoretical modelling of large amplitude oscillations have enabled to relate observed periodicities with properties of the global magnetic field structure supporting the oscillating plasma (see, e.g., Luna et al. 2014). Also, the refinement of theoretical models that incorporate the fine structuring of prominences and the high resolution observations of small amplitude oscillations have produced an increase in prominence seismology studies. Several techniques for the inversion of physical parameters have been developed that make use of observational estimates for quantities such as phase velocities, periods, damping times and flow speeds. In general, the solution to the inverse problem cannot give a single value for all the physical parameters of interest. However, important information about unknown physical quantities can be obtained using this method. Bayesian inference methods, widely used in other areas, are now being implemented in prominence seismology. They enable to diagnose the physical conditions of interest in a probabilistic framework. The most relevant results of the MHD prominence seismology technique are here discussed.

The theoretical models described in Sect. 6 make use of different conceptual views of prominences, such as the string model, the slab model and the thread model for their fine structure. Seismology efforts in the area have followed the same pattern. We describe them in increasing intricacy order, starting with a mechanical analogue (Sect. 8.1), followed by slab models (Sect. 8.2) and ending with the seismology of fine structure oscillations (Sects. 8.3–8.6). The emerging field of Bayesian prominence seismology is discussed in Sect. 8.7, by providing examples of applications in parameter inference and model comparison.

8.1 Seismology of large amplitude prominence oscillations

Several studies have made use of the observed characteristics of large amplitude oscillations in prominences to deduce physical parameters of these objects. The classic example is the interpretation by Hyder (1966) of the winking filament phenomenon.

This author modelled the eleven winking filament events reported by Ramsey and Smith (1965) as damped harmonic oscillators and obtained estimates of the vertical magnetic field strength in the range 2–30 G and of the coronal coefficient of viscosity. Another classic determination was made by Kleczek and Kuperus (1969) using Eq. (3). Once the period of oscillation (P) is known, the length of the filament (L) has been measured and a typical density (ρ) has been assumed, the strength of the magnetic field (B) could be determined. In addition, they estimated the energy needed to induce the oscillations to be in the range 10^{19}–10^{20} J. In spite of their simplicity, these models have been used to perform prominence seismology in recent observations. For instance, Isobe and Tripathi (2006) used the Kleczek and Kuperus (1969) model to perform prominence seismology of a pre-erupting filament. Assuming typical prominence values for the density and knowing the length of the filament, a magnetic field strength of 9.8 G and an Alfvén speed of 87 km s^{-1} were determined. Transverse oscillations observed by Gilbert et al. (2008) and Gosain and Foullon (2012) were also interpreted in terms of the Kleczek and Kuperus (1969) model, and this interpretation allowed to determine values for the magnetic field of 30 and 25 G, respectively. Furthermore, using the line-of-sight velocity, Gilbert et al. (2008) determined the total maximum kinetic energy involved in the oscillations, that was of the order of 10^{19}–10^{20} J. Hyder's model has also been used by Shen et al. (2014a) to determine the radial component of the magnetic field in the observed chain of winking filaments.

Vršnak et al. (2007) reported on H_α observations of large amplitude, large scale periodical plasma motions along the axis of a filament. They plugged the wave period and the length of the filament into Eq. (6) to infer the Alfvén speed $v_{\mathrm{A}\varphi} \sim 100\,\mathrm{km\ s}^{-1}$. By further assuming that the number density of the prominence plasma is in the range 10^{10}–10^{11} cm^{-3}, the azimuthal magnetic field strength results in the range 5–15 G. Next, measuring the pitch angle, Vršnak et al. (2007) additionally determined the internal structure of the flux rope helical magnetic field, from which the axial magnetic field strength was estimated to be in the range 10–30 G. The twisted flux rope model was also invoked by Pintér et al. (2008) in their analysis of SOHO EUV observations of large amplitude transverse oscillations in a polar crown filament previously studied by Isobe and Tripathi (2006). Oscillations were present along a foot belonging to a larger prominence structure, occurred prior to the eruption of the full structure and wavelet analysis tools were used to shed light into the temporal and spatial behaviour of oscillations. The analysis of the spatial properties of the oscillations shows evidence of a global standing transverse oscillation, although some small scale oscillations within the structure cannot be discarded. Using the twisted flux rope model for the filament and based on the same scenario and analysis as Vršnak et al. (2007), the azimuthal Alfvén speed component was estimated to be $v_{\mathrm{A}\varphi} = 49$ km s^{-1} and the poloidal magnetic field strength in the range 2–10 G. In this case, the pitch angle could not be measured. By assuming a mean value of 65°, Pintér et al. (2008) estimated that the axial component of the magnetic field must be in the range 1–5 G.

From the analysis of the longitudinal oscillations of a filament observed with SDO, and assuming that gravity was the restoring force, Luna et al. (2014) used Eqs. (4) and (5) to calculate the radius of curvature of the dipped magnetic field lines, which was in the range $43-66$ Mm, and the minimum magnetic field strength at the field line dips obtaining 14 ± 8 G. The validity of this approach was tested by Luna et al. (2016b) using numerical simulations and the agreement of the numerical results with the Luna and Karpen (2012) theoretical model was excellent (see Sect. 4.3). Also, following Luna and Karpen (2012) they computed the mass accretion rate, needed to explain the observed damping, which was of the order of $(36 \pm 27) \times 10^6$ kg h^{-1} in agreement with the predictions of the thermal non-equilibrium model (Luna et al. 2012b). Finally, they calculated the energy injected to the filament by the jet triggering the oscillations which is in the range 10^{17}–10^{20} J, although this quantity is only an unknown fraction of the total energy released by the energetic event (Zhang et al. 2013). Luna et al. (2014) concluded that since the derived properties were almost uniform along the filament this was an indication of a high degree of cohesiveness along the filament channel. Following Luna and Karpen (2012), Li and Zhang (2012), Bi et al. (2014) and Zhang et al. (2017) estimated the minimum magnetic field strengths in filament threads undergoing longitudinal oscillations. These strengths were in the range 28–55 G in the first case and equal to 15 G in the second and third case. Furthermore, Zhang et al. (2017) using Eq. (4) and the determined periods (see Sect. 3.3) estimated the curvature radius of the magnetic dips supporting the filament. The results, between 70 and 134 Mm, were higher than those computed in Luna et al. (2014).

MHD seismology has also been used by several authors. For instance, in the observations made by Hershaw et al. (2011) a growth of the velocity amplitude with height was detected together with the fact that the oscillation seemed to start in phase for both legs, which led to the authors to suggest that the oscillatory behaviour was caused by a global kink mode. An approximate analytical relationship between the damping time (τ) and the period (P) such as $\tau = (1.6\pm0.2)P^{0.9\pm0.1}$ was derived for the disturbance caused by the first wave train. This analytical fit suggests a linear dependence between the damping time and the period that could be compatible with resonant absorption as the damping mechanism (Ruderman and Roberts 2002; Ofman and Aschwanden 2002; Arregui et al. 2008b). However, this interpretation must be taken with care since the use of scaling laws to discriminate between damping mechanisms is questionable, at least for resonant absorption (Arregui et al. 2008a). On the other hand, Liu et al. (2012) and Xue et al. (2014) performed prominence seismology based on transverse oscillations by assuming that these oscillations were produced by standing kink modes, then, following Nakariakov and Verwichte (2005), the magnetic field is given by,

$$B_0 = \frac{L}{P}\sqrt{2\mu_0\rho_0(1+\frac{\rho_\mathrm{e}}{\rho_0})}, \tag{44}$$

where ρ_e and ρ_0 are the densities outside and inside the prominence, respectively, L is the length of the prominence and P the oscillatory period. Assuming a typical prominence density and a value for the ratio between the coronal and prominence densities, a magnetic field strength of 17.6 G. was determined.

The main limitation of prominence diagnostics using large amplitude oscillations is the lack of a sufficiently detailed, and at the same time sophisticated, physical model to explain the observations. This degree of refinement is now being incorporated to the modelling of small amplitude oscillations in prominence fine structures at a much greater pace, and has produced some relevant results that we discuss below.

8.2 Seismology of prominence slabs

The MHD wave properties for slab models of prominences are described in Sect. 6.2. Two relevant studies have made use of some of these models to infer physical properties in prominences. Their methodology is based on the identification of observed oscillations with theoretical eigenmodes.

Régnier et al. (2001) consider the possible theoretical modes that can explain their observations of oscillations in an active region filament. The slab model with a uniform and inclined magnetic field by Joarder and Roberts (1993b) is used (see Fig. 39). The dispersion relations for Alfvén modes and magnetoacoustic modes are considered. They give the frequency of six fundamental modes: the symmetric Alfvén, slow and fast kink modes and the antisymmetric Alfvén, slow and fast sausage modes, as a function of the prominence parameters. Observations provide with estimates for the width (8000 km) and length (63,000 km) of the filament. Assumptions on other parameters, such as the temperature of the filament (8000 K) and of its environment (10^6 K), the density of the slab (10^{12} cm^{-3}), the magnetic field strength (20 G) and for the angle between the magnetic field and the long axis of the slab (25°) are made. The dispersion relations are then solved by using these parameters and the corresponding periods are obtained and classified.

Observations and Fourier analysis of Doppler velocity time series enable Régnier et al. (2001) to detect intermediate (between 5 and 20 min in this case) and long ($>$ 40 min) period oscillations. From the comparison between the observed and calculated frequencies, an identification method of the oscillation modes in the observed filament is presented. The method makes use of the fact that the frequency ratio of the fundamental even Alfvén mode to the fundamental odd Alfvén mode only depends on the ratio of the half-with of the slab to the half-length of the filament. This quantity is measurable. The same applies to the frequency ratios involving the slow kink/sausage and fast kink/sausage modes. Parametric calculations for the frequencies as a function of the magnetic field strength and the inclination angle, while keeping the slab density constant, are next performed. A diagnostic of the observed filament is obtained by looking for the parameters values that enable the matching of theoretical and observed frequencies. By following this method, the angle between the magnetic field and the long axis of the slab is estimated to be 18°. Using this value, an algebraic relation for the magnetic field strength as a function of the slab density is derived.

A more involved and ambitious diagnostic, using the Joarder and Roberts (1993b) slab model, was performed by Pouget et al. (2006). The long duration and high temporal resolution observations with CDS/SoHO enable these authors to detect and measure the entire range of periodicities theoretically expected in a filament. In particular both the short (less that 10 min) and the long ones (more than 40 min) are detected.

The detailed analysis of three filaments is presented. The seismic inversion technique closely follows that by Régnier et al. (2001), in the sense that the first step towards the diagnostic is the use of frequency ratios between fundamental even/odd (kink/sausage) modes. These ratios only depend on the ratio of the filament half-width to its half-length. Once this ratio is measured, with a given uncertainty, Pouget et al. (2006) assume that their 16-h long observation has allowed them to observe the six modes of interest, since the slowest mode is expected at a period of 5 h, for standard prominence parameters.

The inversion method first assigns a possible triplet of measured frequencies to the three odd fundamental frequencies (odd Alfvén, slow sausage and fast sausage modes). The coherence of each choice is examined against two tests. The first requires to find three corresponding even frequencies, with the condition that the even/odd frequency ratios are consistent with the measured half-width to half-length ratio. The second involves the inferred values for the density, temperature, magnetic field inclination angle and magnetic field strength to be consistent with typical values reported in the literature. For each test, if the test was negative, the full triplet was changed and the series started again. On the contrary, if the tests succeeded, Pouget et al. (2006) considered that the six fundamental modes were identified.

The three filament observations led to coherent diagnostics and a single possible set of frequencies was found for each observation. The importance of this study is its ability to simultaneously determine the values of the inclination angle, temperature and Alfvén speed for the same prominence. The drawback is that the modeling, as in Régnier et al. (2001), does not permit to capture the highly inhomogeneous nature of prominences.

8.3 Seismology of propagating transverse thread oscillations

Transverse thread oscillations observed by Lin et al. (2009) and discussed in Sect. 5.9.4 show evidence of waves propagating along individual threads. Ten of the swaying threads were chosen by Lin et al. (2009) for further investigation, and for each selected thread two or three perpendicular cuts were made in order to measure the properties of the propagating waves. Periods and amplitudes of the waves, as well as their phase velocity, were derived for each thread. Lin et al. (2009) interpreted the observed events as propagating MHD kink waves supported by the thread body. This mode is the only one producing a significant transverse displacement of the cylinder axis. In addition, it also produces short-period oscillations of the order of minutes, compatible with the observed periods (see Sect. 6.3.1).

If an infinitely long, straight, cylindrical thread model, with the tube fully filled with cool and dense material (Fig. 43), is assumed, a comparison between the observed wave properties and the theoretical prediction can be made. This enabled Lin et al. (2009) to obtain estimates for some physical parameters of interest, namely the Alfvén speed and the magnetic field strength in the studied threads. To this end, the observed phase velocity was directly associated to the kink speed

$$c_{\mathrm{k}} = \frac{\omega_{\mathrm{k}}}{k_z} = v_{\mathrm{Ap}} \left[\frac{2\zeta}{1+\zeta} \right]^{1/2}, \tag{45}$$

where Eq. (30) for the kink frequency has been used. In this expression v_{Ap} is the Alfvén speed in the prominence thread and $\zeta = \rho_{\mathrm{p}}/\rho_{\mathrm{c}}$ is the density contrast. Both quantities are unknown, hence no unique solution to Eq. (45) can be obtained from the observed period alone. In the limit of high density contrast, typical of prominence

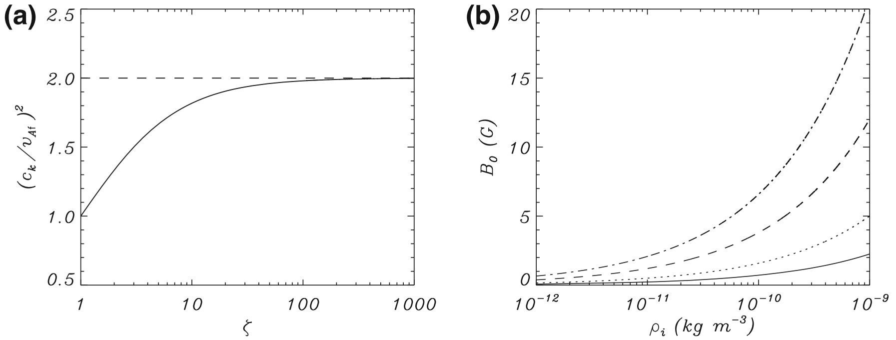

Fig. 84 **a** Ratio $c_\mathrm{k}^2/v_\mathrm{Af}^2$ (solid line) as a function of the density contrast, ζ. The dotted line corresponds to the value of the ratio $c_\mathrm{k}^2/v_\mathrm{Af}^2$ for $\zeta \to \infty$. **b** Magnetic field strength as a function of the internal density, ρ_p, corresponding to four selected threads. Image reproduced with permission from Lin et al. (2009), copyright by AAS

plasmas, the ratio $\rho_\mathrm{p}/\rho_\mathrm{c}$ is very large and the ratio $c_\mathrm{k}^2/v_\mathrm{Ap}^2$ is almost independent from it (see Fig. 84a). The kink speed can then be approximated by

$$c_\mathrm{k} \approx \sqrt{2} v_\mathrm{Ap}. \tag{46}$$

Lin et al. (2009) assumed that thread oscillations observed from the H_α sequences were the result of a propagating kink mode, which implies that the measured phase velocity, c_ph, is equal to the kink speed. Then, the thread Alfvén speed can be computed from

$$v_\mathrm{Ap} \approx \frac{c_\mathrm{ph}}{\sqrt{2}}. \tag{47}$$

The inferred values of v_Ap for the ten selected threads are displayed in Table 2 in Lin et al. (2009). The results show a strong dispersion, suggesting that the physical conditions in different threads were very different in spite of belonging to the same filament. This result clearly reflects the highly inhomogeneous nature of solar prominences. Once the Alfvén speed in each thread was determined, the magnetic field strength could be computed after a value for the thread density was assumed. For the analysed events, and considering a typical value $\rho_\mathrm{p} = 5 \times 10^{-11}$ kg m^{-3}, magnetic field strengths in the range 0.9–3.5 G were obtained (see Fig. 84b).

8.4 Seismology of damped transverse thread oscillations

A feature clearly observed by Lin et al. (2009) is that the amplitudes of the waves passing through two different cuts along a thread are notably different. Apparent changes can be due to damping of the waves in addition to noise in the data. The damping of prominence oscillations is a common feature in many observed events and damping time-scales are an additional source of information that can be used when performing parameter inference using seismology inversion techniques, once a physical model

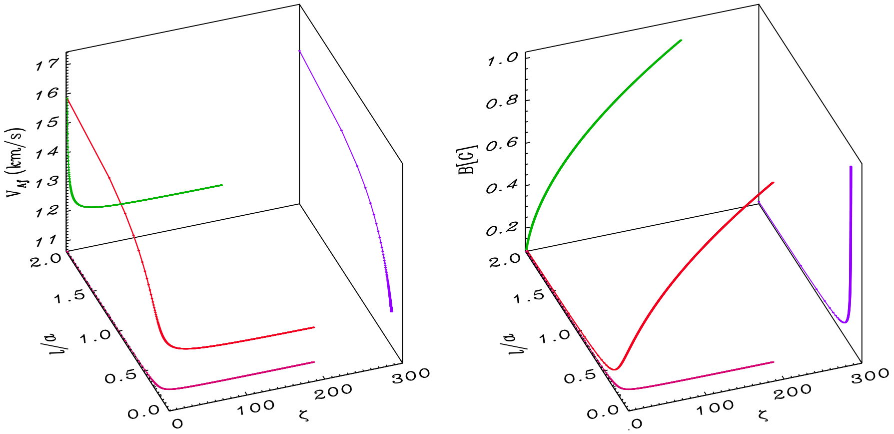

Fig. 85 Left: analytic inversion of physical parameters in the (ζ, l/a, v_{Ap}) space for a filament thread oscillation with $P = 3$ min, $\tau_{\mathrm{d}} = 9$ min and a wavelength $\lambda = 3000$ km (see, e.g., Lin et al. 2007). Right: magnetic field strength as a function of the density contrast and transverse inhomogeneity length-scale, derived from the analytic inversion for a coronal density $\rho_{\mathrm{c}} = 2.5 \times 10^{-13}$ kg m^{-3}

that provides us with an explanation is available. Among the different damping mechanisms described in Sect. 7, resonant absorption in the Alfvén continuum seems a very plausible one and has been used to perform prominence thread seismology, using the damping as an additional source of information. In the context of coronal loop seismology, the use of damping rates in combination with oscillatory periods gives information about the transverse density structuring of coronal loops (Goossens et al. 2002; Arregui et al. 2007; Goossens 2008; Goossens et al. 2008; Arregui and Asensio Ramos 2014; Arregui et al. 2015).

The model considered here is an infinitely long thread of radius a surrounded by a thin transition sheath of thickness l in which a smooth transition from the thread to the coronal density takes place (see Fig. 67). For standing kink waves, and without using the thin tube and thin boundary approximation, the normal mode period and damping ratio are functions of the relevant equilibrium parameters,

$$P = P(k_z, \zeta, l/a, v_{\mathrm{Ap}}), \qquad \frac{P}{\tau_{\mathrm{d}}} = \frac{P}{\tau_{\mathrm{d}}}(k_z, \zeta, l/a), \tag{48}$$

with v_{Ap} the prominence thread Alfvén speed. Note that in the thin tube and thin boundary approximations (Eq. 31 for P and Eq. 37 for the damping ratio), the period does not depend on l/a and the damping ratio is independent of the wavelength. This is not true in the general case (Arregui et al. 2008b). The period is a function of the longitudinal wavenumber, k_z, the transverse inhomogeneity length-scale, l/a, and the internal Alfvén speed. Similarly for the damping ratio, except for the fact that it cannot depend on any time-scale. The long wavelength approximation further eliminates the k_z dependence of the damping ratio. In the case of coronal loop oscillations, an estimate for k_z can be obtained directly from the length of the loop and the fact that the fundamental kink mode wavelength is twice this quantity. For prominence threads, the wavelength of oscillations needs to be measured. Relations (48) indicate that, if no assumption is made on any of the physical parameters of interest, there are infinite different equilibrium models that can equally well explain the observations (namely the period and damping ratio). The parameter values that define these valid equilibrium models are displayed in Fig. 85a, where the analytical algebraic expressions in the thin tube and thin boundary approximations by Goossens et al. (2008) have been used to invert the problem. It can be appreciated that, even if an infinite number of solutions is obtained, they define a rather constrained range of values for the thread Alfvén speed. Because of the insensitiveness of the damping rate with the density contrast for the typically large values of this parameter in prominence plasmas, the obtained solution curve displays an asymptotic behaviour for large values of ζ. This makes possible to obtain precise estimates for the thread Alfvén speed, $v_{\mathrm{Ap}} \simeq 12$ km s^{-1}, and the transverse inhomogeneity length scale, $l/a \simeq 0.21$. Note that these asymptotic values can directly be obtained by inverting Eqs. (31) and (37) for the period and the damping rate in the limit $\zeta \rightarrow \infty$. The computation of the magnetic field strength from the obtained seismological curve requires the assumption of a particular value for either the filament or the coronal density. The resulting curve for a typical coronal density is shown in Fig. 85b. Precise values of the magnetic field strength cannot be obtained, unless the density contrast is accurately known.

The transverse inhomogeneity length scale of an oscillating thread could also be estimated by using observations of spatial damping of propagating kink waves and theoretical results described in Sect. 7.5.2. In the context of coronal loops, Terradas et al. (2010) have shown that the ratio of the damping length to the wavelength, due to resonant damping of propagating kink waves, has the same dependence on the density contrast and transverse inhomogeneity length-scale as the ratio of the damping time to the period for standing kink waves. Similar inversion techniques to the ones explained here for the temporal damping of oscillations could be applied to the spatial damping of propagating waves.

Seismology using the period and damping time of kink oscillations has been applied to global oscillations in a solar filament observed in H_α with the National Solar Observatory GONG instrument by Pant et al. (2015). The oscillations are generated by an M1.1-class flare and produce periods of about 61–67 min with damping times of 92–117 min. Using the theory of resonant absorption and the analytical inversion scheme by Goossens et al. (2008), the study obtains constraints on the filament Alfvén speed and the transverse density inhomogeneity length-scale, for varying values of the density contrast. By further estimating the filament density using an automated Differential Emission Measure (DEM) analysis technique, estimates for the filament magnetic field strength in the range ~ 0.6–1.2 G are obtained. The analysis by Pant et al. (2015) is a nice example of the applicability of this kind of technique, although the modelling of the global filament structure as a single magnetic flux tube presents some limitations.

Going back to filament threads, the main downside of the technique just described is the use of thread models in which the full magnetic tube is filled with cool and dense plasma. The solution to the forward problem in the case of two-dimensional thread models is discussed in Sect. 7.6. The analytical and numerical results obtained by Soler et al. (2010a) using these models indicate that the length of the thread and its

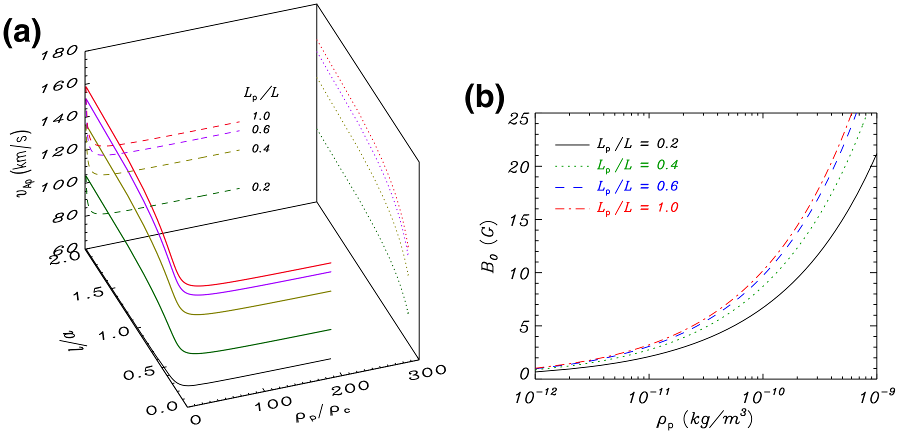

Fig. 86 Determination of **a** prominence Alfvén speed and **b** magnetic field strength from the computation of periods and damping times for standing kink oscillations in two-dimensional prominence thread models and observations of period and damping times in transverse thread oscillations. The observed period and damping time are 20 and 60 min, respectively, and $L = 10^5$ km. Image reproduced with permission from Soler et al. (2010b), copyright by ESO

position along the magnetic tube influence the period and damping time of transverse thread oscillations. On the contrary, the damping ratio is rather insensitive to these model properties.

From the inversion curve displayed in Fig. 85a, we notice that a change in the period produces a vertical shift of the solution curve, hence the period influences the inferred values for the Alfvén speed. On the other hand, the damping ratio determines the projection of the inversion curve onto the $(\zeta, l/a)$-plane. We can conclude that ignorance of the length of the thread or the length of the supporting magnetic flux tube will have a significant impact on the inferred values for the Alfvén speed (hence magnetic field strength) in the thread. On the contrary, because of the smaller sensitivity of the damping ratio to changes in the longitudinal density structuring, seismological estimates of the transverse density structuring will be less affected by our ignorance about the longitudinal density structuring of prominence threads.

An example of the inversion of physical parameters for different values of the thread length was presented by Soler et al. (2010a). When partially filled threads, i.e., with the dense part occupying a length L_p shorter than the total length of the tube L, are considered, one curve is obtained for each value of the length of the thread. The solutions to the inverse problem are shown in Fig. 86a for a set of values of L_p. Even if each curve gives an infinite number of solutions, again each of them defines a rather constrained range of values for the thread Alfvén speed. The figure shows that the ratio L_p/L is a fundamental parameter in order to perform an accurate seismology of prominence threads, since different curves produce different estimates for the prominence Alfvén speed, as anticipated above. Because of the insensitiveness of the damping ratio with respect to the length of the thread, all solution curves for different lengths of the threads produce the same projection onto the $(\zeta, l/a)$-plane. Hence, the same precise estimates of the transverse inhomogeneity length scale obtained from infinitely long thread models are valid, irrespective of the length of the thread. The computation of the magnetic field strength from the obtained seismological curve requires the assumption of a particular value for either the filament or the coronal density. The resulting curves for a typical coronal density and several values of L_p/L are shown in Fig. 86b. Here again, precise values of the magnetic field strength cannot be obtained, unless the prominence density is accurately known.

8.5 Seismology using period ratios of thread oscillations

The widespread use of the concept of period ratios as a seismological tool has been remarkable in the context of coronal loop oscillations (see Andries et al. 2009, for a review). The idea was first put forward by Andries et al. (2005) and Goossens et al. (2006) as a means to infer the coronal density scale height using multiple mode oscillations in coronal loops embedded in a vertically stratified atmosphere. In coronal loop seismology, the ratio of the fundamental mode period to twice that of its first overtone in the longitudinal direction ($P_1/2P_2$) mainly depends on the density structuring along magnetic field lines. It can therefore be used as a diagnostic tool for the coronal density scale height.

In the context of prominence seismology, a similar approach was proposed by Díaz et al. (2010) to obtain information about the density structuring along prominence threads using the piece-wise longitudinally structured thread model by Díaz et al. (2002) (see Fig. 56). These authors showed that the non-dimensional oscillatory frequencies of the fundamental kink mode and the first overtone are almost independent of the ratio of the thread diameter to its length. Thus, the dimensionless oscillatory frequency depends, basically, on the density ratio of the prominence to the coronal plasma, $\rho_\mathrm{p}/\rho_\mathrm{c}$, and the non-dimensional length of the thread, W/L,

$$\frac{\omega L}{v_\mathrm{Ap}} = f(W/L, \rho_\mathrm{p}/\rho_\mathrm{c}). \tag{49}$$

Here we follow the notation of Díaz et al. (2010), who use $2L$ and $2W$ for the length of the magnetic tube and the thread length, rather than that of Soler et al. (2010b), who denote these lengths by L and by L_p. In order to determine the dimensional frequency when comparing to observations, an additional parameter is needed, namely the Alfvén velocity in the corona or in the prominence (involving some knowledge of the magnetic field strength and density). Note, however, that the non-dimensional frequencies of the fundamental mode and its first overtone can be cast as

$$\frac{\omega_1 L}{v_\mathrm{Ap}} = f_1(W/L, \rho_\mathrm{p}/\rho_\mathrm{c}), \tag{50}$$

$$\frac{\omega_2 L}{v_\mathrm{Ap}} = f_2(W/L, \rho_\mathrm{p}/\rho_\mathrm{c}), \tag{51}$$

Fig. 87 Plot of the solution lines satisfying $P_1/2P_2 =$ constant in the parameter space. The upper line corresponds to $P_1/2P_2 = 1.25$ and the lower one to $P_1/2P_2 = 3$, with each line showing an increment in $P_1/2P_2$ of 0.25 from the previous one. Image reproduced with permission from Díaz et al. (2010), copyright by AAS

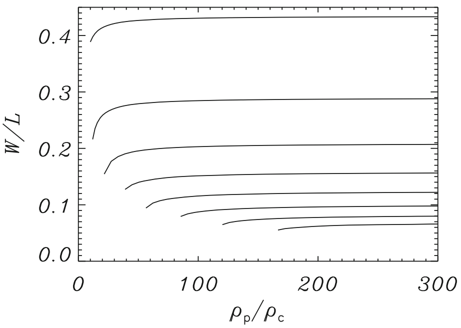

so that the dependence on the length of the tube and the thread Alfvén speed can be removed by considering the period ratio,

$$\frac{P_1}{2P_2} = F(W/L, \rho_p/\rho_c). \tag{52}$$

Equation (52) can be used for diagnostic purposes, once reliable measurements of multiple mode periods are obtained. The curves in Fig. 87 display the solution to the inverse problem in the (ρ_p/ρ_c, W/L) parameter space for several values of the period ratio. Given the period ratio from an observation, it only depends on W/L in first approximation. Once W/L has been obtained, one can estimate the value of the magnetic field length $2L$, since the thread length, $2W$, can be determined quite accurately from the observations.

The use of the period ratio technique needs the unambiguous detection of two periodicities in the same oscillating prominence thread. Díaz et al. (2010) pointed out two main difficulties in this respect. From a theoretical point of view, the overtone with period P_2 is an antisymmetric mode in the longitudinal direction, with a node in the centre of the thread and two maxima located outside it. Only for sufficiently long threads, with $W/L \sim 0.1$, the anti-nodes of the overtone are located inside the thread and could hence be measured in the part of the tube visible in, e.g., H_α. From an observational point of view, no conclusive measurement of the first overtone period has been reported so far in the literature, although there seem to be hints of its presence in some observations by, e.g., Lin et al. (2007), who reported on the presence of two periods, $P_1 = 16$ min and $P_2 = 3.6$ min in their observations of a prominence region, and where P_2 could be associated with the second overtone. Díaz et al. (2010) used the period ratio from these observations to infer the value for the length of the thread ratio $W/L = 0.12$. Although it is difficult to estimate the length of the particular thread under consideration, assuming a value of 13,000 km, as for other threads analysed by Lin et al. (2007), results in a magnetic tube length $L \sim 130{,}000$ km.

This new seismological information can be now used to obtain further information about the physical conditions in the oscillating thread. Using analytical approximations for the dimensionless frequency of the first overtone, the following expression for the prominence Alfvén speed as a function of the length of the thread is obtained,

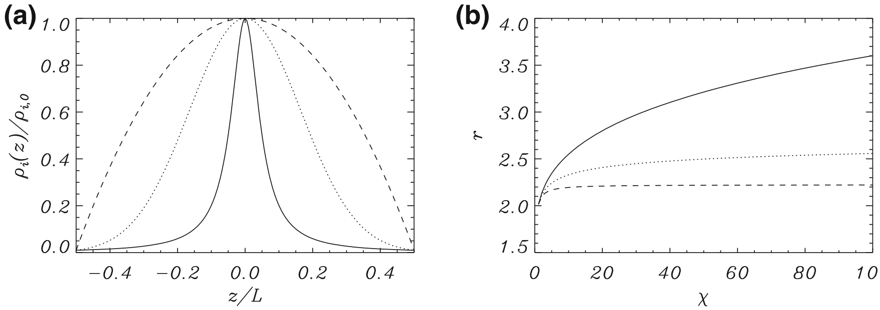

Fig. 88 **a** Spatial variation of the equilibrium mass density along the magnetic flux tube for prominence thread models with a Lorentzian profile (solid line), a Gaussian profile (dotted line) and a parabolic profile (dashed line). The ratio of centre to foot-points densities is $\chi = 100$. **b** Dependence of the numerically computed period ratio $r = P_1/P_2$ with χ for the Lorentzian profile (solid line), the Gaussian profile (dotted line) and the parabolic profile (dashed line). For these computations the tube length to radius ratio is $L/R = 100$ and the density contrast is $\zeta = 100$. P_1 and P_2 denote the periods of a homogeneous thread with $\rho_\mathrm{i} = \rho_{\mathrm{i},0}$. Image adapted from Soler et al. (2015)

$$v_\mathrm{Ap} = \frac{\pi L}{P_1}\sqrt{2\frac{W}{L}\left(1-\frac{W}{L}\right)}. \tag{53}$$

Once the length of the tube is known, an estimate for the prominence Alfvén speed can be inferred from Eq. (53). In the example shown by Díaz et al. (2010), the high density contrast limit was used to infer the value $v_\mathrm{Ap} \sim 160$ km s^{-1}.

The concept of period ratios between the fundamental mode and the first overtone of transverse thread oscillations has been used to diagnose the density structuring along prominence fine structures by Soler et al. (2015), using continuous density profiles along the magnetic field instead of piecewise density models as done by Díaz et al. (2010). In their study, Soler et al. (2015) define three alternative density models, with Lorentzian, Gaussian and parabolic profiles (see Fig. 88a). The idea is to emulate density variations in which the plasma is more or less concentrated around the central part of the tube. The Lorentzian profile is similar to the piecewise models used by, e.g., Díaz et al. (2010). In the parabolic profile the dense prominence plasma is broadly distributed along the tube. Finally, the Gaussian profile represents an intermediate situation between Lorentzian and parabolic profiles. The relevant parameter in all three models is the ratio of densities between the internal density at the central part and at the end of a flux tube of length L, namely $\chi = \rho_{\mathrm{i},0}/\rho_{\mathrm{i},L/2}$.

The period ratio of transverse thread oscillations is 2 in longitudinally homogeneous thin tubes, but differs from this value when longitudinal density inhomogeneity is introduced. By numerically solving the linear MHD wave equations for small amplitude perturbations produced by kink modes the dependence of the period ratio on the density gradient parameter χ was obtained. The results are displayed in Fig. 88b. In agreement with previous works that used simple piecewise constant density profiles, Soler et al. (2015) find that the period ratio is larger than 2 in longitudinally inhomogeneous prominence threads. When the ratio of the central density to that at the footpoints is fixed, the period ratio depends strongly on the form of the density profile along the thread. The more concentrated the dense prominence plasma near the centre of the tube, the larger the period ratio is.

The Lorentzian profile produces a significant increase of the period ratio, with a value around 3.5 when $\chi = 100$. The increase of the period ratio is small for the parabolic profile and reaches a value of about 2.2 when $\chi = 100$. The results for the Gaussian profile intermediate to those obtained using the Lorentzian and parabolic profiles and the period ratio increase is moderate, with a value around 2.5 when $\chi = 100$. Interestingly, Soler et al. (2015) find that, by considering the spatially averaged density in the thread to be same for all three profiles, i.e., comparing thread models with the same total mass, the period ratio is independent of the specific density profile that is chosen (see Fig. 4c in Soler et al. 2015).

These computations are then used by Soler et al. (2015) to perform a seismology diagnostics of the density gradient parameter and to assess, in view of the obtained results, which one among the three alternatives density models is more likely. To this end, an empirical fit was first performed to the period ratio dependence on the average density for each of the profiles. By making use of the periodicities reported by Lin et al. (2007), with a period ratio of ~ 4.4 and inverting this dependency, Soler et al. (2015) find that the parabolic profile is unable to explain this particular observation, since this model predicts a constant ratio of 2.2 for large values of χ. The inversion leads to values for the ratio of central to footpoint density of $\chi = 347$ and $\chi = 10^{48}$ for the Lorentzian and Gaussian profiles, respectively. The inferred values of χ suggest that, among the three profiles, the Lorentzian profile may provide us with the best explanation for the ratio of the two periods reported by Lin et al. (2007). A more rigorous treatment of this model comparison problem, using Bayesian techniques, is presented in Sect. 8.7.2.

8.6 Seismology of flowing and oscillating prominence threads

Mass flows in conjunction with phase speeds, oscillatory periods and damping times might constitute an additional source of information about the physical conditions of oscillating threads. The first application of prominence seismology using Hinode observations of flowing and transversely oscillating threads was presented by Terradas et al. (2008), using observations obtained in an active region filament by Okamoto et al. (2007) discussed in Sect. 5.9.4.

The observations show a number of threads that flow following a path parallel to the photosphere while they oscillate in the vertical direction. The relevance of this particular event is that the coexistence of waves and flows can be firmly established, so that there is no ambiguity about the wave or flow character of a given dynamic feature: both seem to be present in this particular event. However, other interpretations for the apparent motion in the plane of the sky could be also possible, for instance, an ionisation wave or a thermal front. Okamoto et al. (2007) analysed six threads whose relevant measured properties are displayed in Table 2.

In their seismological analysis of these oscillations Terradas et al. (2008) started by neglecting the mass flows. Then, they interpreted these events in terms of the standing kink mode of a finite-length thread in a magnetic flux tube (see Fig. 56 and Sect. 6.4).

Table 2 Summary of geometric and wave properties of horizontally flowing and vertically oscillating threads analysed by Okamoto et al. (2007)

Thread	L_{p} (km)	v_0 (km s^{-1})	P (s)	V (km s^{-1})	H (km)
1	3600	39	174 ± 25	16	18,300
2	16,000	15	240 ± 30	15	12,400
3	6700	39	230 ± 87	12	14,700
4	2200	46	180 ± 137	8	19,000
5	3500	45	135 ± 21	9	14,300
6	1700	25	250 ± 17	22	17,200

L_{p} is the thread length, v_0 its horizontal flow velocity, P the oscillatory period, V the oscillatory velocity amplitude and H the height above the photosphere

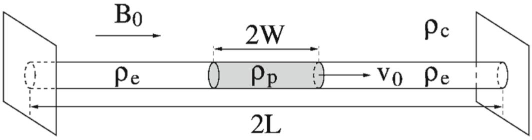

Fig. 89 Sketch of the magnetic and plasma configuration used to represent a flowing thread (shaded volume) in a thin magnetic tube. The two parallel planes at both ends of the cylinder represent the photosphere. Image reproduced with permission from Terradas et al. (2008), copyright by AAS

By using theoretical results by Díaz et al. (2002) and Dymova and Ruderman (2005) (see Sect. 6.4), Terradas et al. (2008) found that, although it is not possible to univocally determine all the physical parameters of interest, a one-to-one relation between the thread Alfvén speed and the coronal Alfvén speed could be established. This relation comes in the form of a number of curves relating the two Alfvén speeds for different values of the length of the magnetic flux tube and the density contrast between the filament and coronal plasma. Figure 90 shows these curves for the selection of 6 threads made by Okamoto et al. (2007). An interesting property of the obtained solution curves is that they display an asymptotic behaviour for large values of the density contrast, which is typical of filament to coronal plasmas, and hence a lower limit for the thread Alfvén speed can be obtained. Take for instance thread #6. Considering a magnetic flux tube length of 100 Mm, a value of 120 km s^{-1} for the thread Alfvén speed is obtained.

Terradas et al. (2008) next incorporated mass flows into their analysis (see Fig. 89). First a simple approximation was made by taking into account that the flow velocity along the cylinder, v_0, enters the linear MHD wave equations through the differential operator

$$\frac{\partial}{\partial t} + v_0 \frac{\partial}{\partial z}.$$

The terms coming from the equilibrium flow can, in a first approximation, be ignored because, as noted by Dymova and Ruderman (2005), inside the cylinder the terms with derivatives along the tube are much smaller than those with radial or azimuthal derivatives. By following this approach the problem reduces to solving a time–dependent problem with a varying density profile, $\rho(z, t)$, representing a dense part moving along the tube with the flow speed. By using the flow velocities in Table 2 and after solving the two-dimensional wave equations, Terradas et al. (2008) found that the flow velocities of thread's material, with respect to the surrounding plasma, measured by Okamoto et al. (2007) result in slightly shorter kink mode periods than the ones derived in the absence of flow. Differences are small, however, and produce period shifts between 3 and 5%. As a consequence, the curves in Fig. 90 can be considered a good approximation to the solution of the inverse problem.

A more complete approach to the problem was followed by Terradas et al. (2008), who considered the numerical solution of the non-linear, ideal, low-β MHD equations with no further approximations, that is, the thin tube approximation was not used and the flow was maintained in the equations. The numerical results confirm the previous approximate results regarding the effect of the flow on the obtained periods and, therefore, on the derived Alfvén speed values. We must note that in this case, and because of the small value of the flow speeds measured by Okamoto et al. (2007) in this particular event, there are no significant variations of the wave properties, and hence of the inferred Alfvén speeds, although larger flow velocities may have more relevant consequences on the determination of physical parameters in prominence threads.

To test the robustness of seismological estimates of the transverse inhomogeneity length scale, Soler et al. (2012) used a configuration similar to that of Fig. 79 (i.e., a finite length thread with a radial transitional density layer) that moves parallel to magnetic field lines with a constant speed. They assumed a linear density profile for the transitional layer and generated a synthetic signal representing a prominence thread transverse oscillation detected with a real instrument. To represent the limited cadence of the instrument, a temporal sampling of the signal was performed and, furthermore, a randomly generated noise was added to it. In Fig. 91a, the theoretical transverse displacement together with the synthetic signal are shown, while in Fig. 91b the wavelet power spectrum of the synthetic signal and the instantaneous period of the original data are displayed. The wavelet power spectrum recovers well the period of the original data, although the time variation of the period is not evident in the wavelet spectrum. This means that the effect of the flow on the period is undetectable when wavelet analysis is used. Figure 91c shows the joint plots of the original signal, an exponentially damped harmonic function without added noise and an exponentially damped harmonic function with noise added. A progressive phase shift between the different curves is observed because the fitted functions do not take into account the temporal variation of the period. More importantly, different damping rates for the three curves are also observed. This last feature has a direct influence on the seismological estimation of the transverse inhomogeneity length-scale, l/R (here R is used to denote the mean radius of the thread) when the fitted P and τ_D are used. In the original data, $l/R = 0.1$ was used, while $l/R = 0.13$ and $l/R = 0.16$ are obtained for the fitted signal without noise and with noise, respectively.

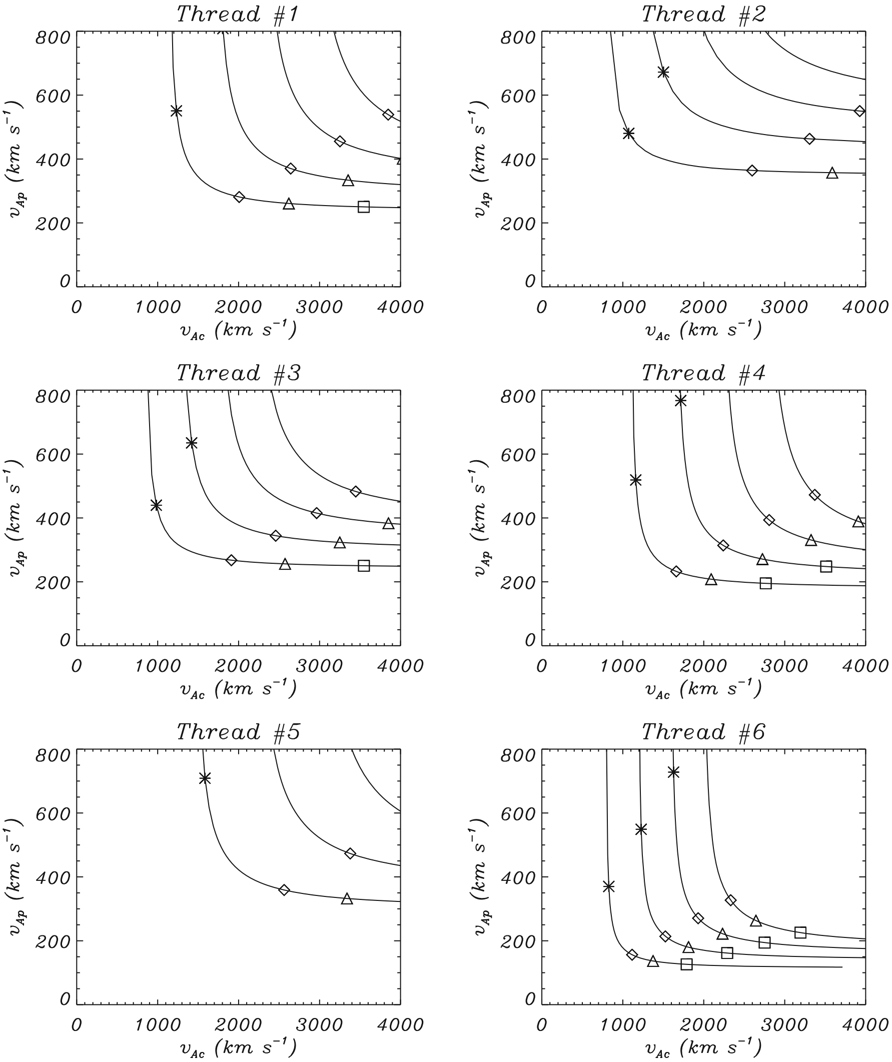

Fig. 90 Dependence of the Alfvén velocity in the thread as a function of the coronal Alfvén velocity for the six threads observed by Okamoto et al. (2007). In each panel, from bottom to top, the curves correspond to a length of magnetic field lines of 100,000, 150,000, 200,000 and 250,000 km, respectively. Asterisks, diamonds, triangles and squares correspond to density ratios of the thread to the coronal gas $\zeta \simeq 5, 50, 100, 200$. Image reproduced with permission from Terradas et al. (2008), copyright by AAS

The computations by Soler et al. (2012) have implications for seismology of prominence fine structures. The damping rate from observed transverse thread oscillations can be used to obtain information on the transverse inhomogeneity length scale of the density across the magnetic field. The commonly employed expression, however, does not take into account the possible presence of mass flows (see Sect. 8.4). With the aim of estimating the possible impact of mass flows on the seismologically inferred

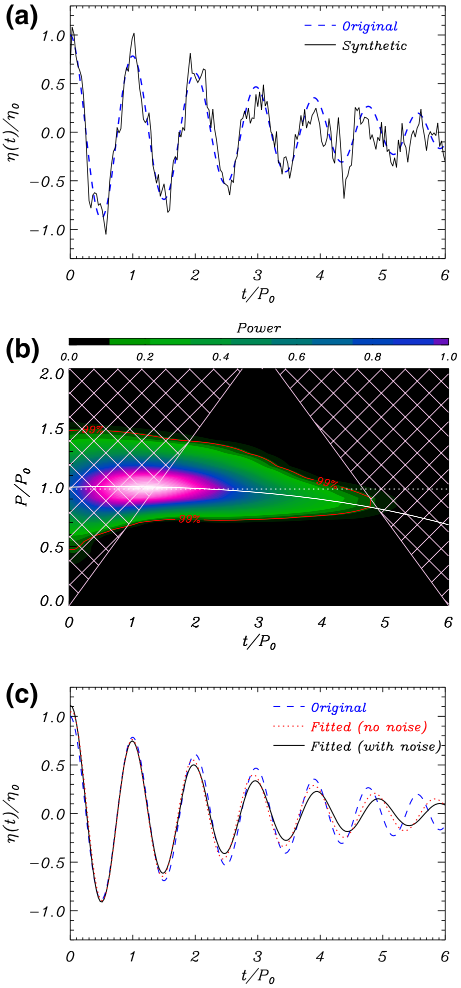

Fig. 91 **a** Original (dashed) and synthetic (solid) data used in the seismological test. **b** Wavelet power spectrum for the dimensionless period, P/P_0, corresponding to the synthetic signal displayed in (**a**). The white solid line is the original data instantaneous period, whereas the horizontal dotted line is the period obtained from the fitting method. The red solid line denotes the 99% confidence level. **c** Comparison of the original (dashed) and fitted signals with noise (solid) and without noise (dotted). In this simulation, $z_0/L = -0.05$ (position of the centre of the prominence thread with respect to the centre of the magnetic tube at $t = 0$), $L_\mathrm{p}/L = 0.1$ (length of the thread), $l/R = 0.1$ (transverse inhomogeneity length-scale), $u_0/v_\mathrm{Ap} = 0.1$ (flow velocity) and $\rho_\mathrm{p}/\rho_\mathrm{c} = 200$ (density contrast). Image reproduced with permission from Soler et al. (2012), copyright by ESO

transverse inhomogeneity length scale, Soler et al. (2012) used the created synthetic data to perform a statistical study of the inferred values for this parameter. Their results indicate that this parameter can be overestimated when the presence of flows is not considered. Figure 92 shows histograms containing 10^4 data realisations for three values of the flow speed. By visual inspection, the histograms seem to follow a Gaussian distribution. By performing the corresponding fittings, Soler et al. (2012) find that as the flow velocity increases, the mean values are shifted towards larger values of l/R. The widths of the Gaussians are however rather unaffected by the considered flow velocities. These results indicate that neglecting mass flows can have a relevant impact on the seismologically inferred values for the transverse inhomogeneity length scale.

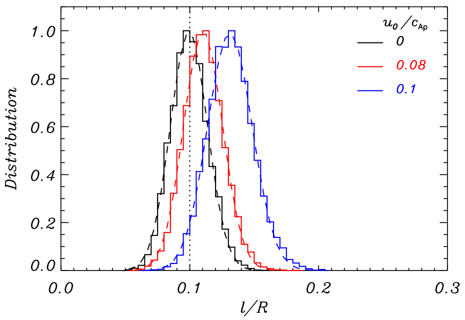

Fig. 92 Seismology of resonantly damped thread oscillations in the presence of flows. The figure shows normalised histograms for the seismologically estimated values of l/R for three values of the flow velocity. The dashed lines are the Gaussian fits and the vertical dotted line is the actual value of l/R. Image reproduced with permission from Soler et al. (2012), copyright by ESO

8.7 Bayesian prominence seismology

Solving the inversion problem to extract information about model parameters by comparison of their theoretical predictions to observed data is not straightforward. In contrast to the process of measurement of a physical quantity in a laboratory, the remote sensing of physical conditions has to be pursued without direct control of the parameters of interest and with information that is incomplete and uncertain. These difficulties, common to all areas in astrophysical research, have led to the development and application of Bayesian diagnostic methods.

The Bayesian formalism offers a self-consistent way to obtain information about unknown physical parameters and model evidence (see, e.g., Gregory 2005; Toussaint 2011). The methodology is based on Bayes' theorem for conditional probability (Bayes and Price 1763). Applied to the problem of inferring a set of parameters $\boldsymbol{\theta}$ of a theoretical model M taking into account observed data D, the theorem states that the probability of the parameters taking on given values conditional on the observed data, the posterior $p(\boldsymbol{\theta}|D)$, is a combination of how well the data are reproduced by the model parameters, the likelihood function $p(D|\boldsymbol{\theta})$, and the probability of the parameters independently of the observed data, the prior distribution $p(\boldsymbol{\theta})$. Both prior and likelihood represent probabilities that are directly assigned, whilst the posterior is computed as follows

$$p(\boldsymbol{\theta}|D, M) = \frac{p(D|\boldsymbol{\theta}, M)p(\boldsymbol{\theta}, M)}{\int p(D|\boldsymbol{\theta}, M)p(\boldsymbol{\theta}, M)d\boldsymbol{\theta}}. \tag{54}$$

The denominator in this expression is the so-called evidence, an integral of the likelihood over the prior distribution that normalises the likelihood and turns it into a probability. Once the posterior is known, problems involving parameter inference or model comparison can be solved, as shown in the two example applications that are discussed below.

8.7.1 Inference of magnetic field strength and transverse density inhomogeneity

Measuring periods and damping times of transverse thread oscillations enables to obtain information on the magnetic field strength in the threads and the transverse inhomogeneity length scale for the plasma density (see Sect. 8.4). The classic approach to the inversion problem, whose results are displayed in Fig. 85, dealt with finding the mathematical solution for the one-dimensional inversion curve in the three-dimensional parameter space by imposing the exact matching of the theoretically predicted period and damping time values with those observed.

Arregui et al. (2014) have solved the same problem in the Bayesian framework. To solve the forward problem and create the synthetic data to be compared to observations, Eqs. (31) and (37) for the period and damping rate are used. For large density contrast values, $\zeta \pm 1 \sim \zeta$ and the density contrast cannot be inferred since both period and damping time become independent of this parameter. This leads to two expressions that relate the oscillation period and damping time to the thread Alfvén speed ($v_{\rm Ap}$) and the transverse density inhomogeneity length scale (l/R, with R the mean radius of the thread),

$$P \sim \frac{\sqrt{2}}{2}\frac{\lambda}{v_{\rm Ap}} \quad \text{and} \quad \frac{\tau_{\rm d}}{P} \sim \frac{2}{\pi}\frac{R}{l}, \tag{55}$$

where the factor $2/\pi$ arises because of the assumption of a sinusoidal density profile at the non-uniform layer.

To solve the inverse problem, Arregui et al. (2014) first gather the parameters to be inferred in the vector of unknowns $\boldsymbol{\theta} = (v_{\rm Ap}, l/R)$ and the two observable quantities in $D = (P, \tau_{\rm d})$. The prior probabilities for the parameters are taken to be uniform distributions, over a given range, for each of the unknowns. A Gaussian likelihood, which incorporates uncertainties on measured period and damping time, is adopted to perform the comparison between theoretically predicted and observed wave properties. Once the full posterior is computed, using Eq. (54), the so-called marginal posterior, $p(\theta_i|D) = \int p(\theta|D) d\theta_1 \ldots d\theta_{i-1} d\theta_{i+1} \ldots d\theta_N$, provides us with the most probable values of a given parameter, θ_i, compatible with observed data D, in the form of a conditional probability distribution, $p(\theta_i|D)$.

Figure 93 shows the marginal posteriors for the Alfvén speed in the filament thread and the transverse inhomogeneity length-scale in the density, for given observed period, wavelength and damping time. Once the Alfvén speed is inferred, information on the magnetic field strength can also be obtained, provided a value for the thread density is assumed. The three posteriors provide us with a well constrained, fully consistent, solution to the inverse problem. Instead of solution curves in the parameter space of unknowns, the inference results are now given in terms of posterior probability density distributions. The magnitude of the posterior for each value of the unknown parameter is a measure of the plausibility of that particular value in explaining the observed data. The method also enables to correctly propagate the uncertainty from measured data to inferred parameters.

8.7.2 Field aligned density structure in prominence threads

The observation of multiple periodicities in transverse thread oscillations offers information on the structuring of the plasma along the magnetic field (see Sect. 8.5). Soler et al. (2015) have shown that theoretical predictions for the period ratio depend on

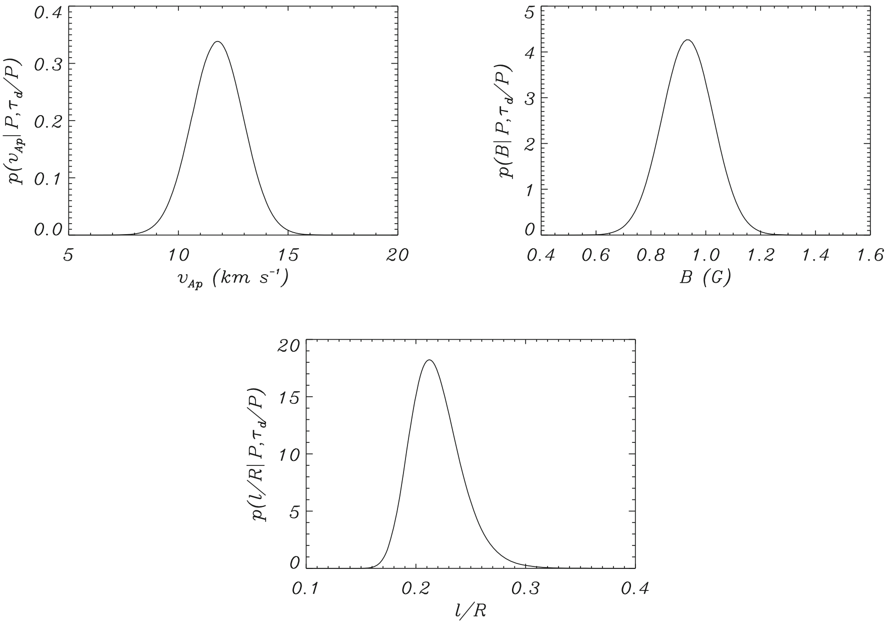

Fig. 93 Marginal posteriors for the filament Alfvén velocity (v_{Ap}), magnetic field strength (B), and transverse inhomogeneity length-scale of the plasma density (l/R) for a thread oscillation with $P = 3$ min, $\tau_{\mathrm{d}} = 9$ min and a wavelength $\lambda = 3000$ km (see, e.g., Lin et al. 2007). This inversion assumes a coronal density $\rho_{\mathrm{c}} = 2.5 \times 10^{-13}$ kg m^{-3} and 10% relative errors in the measured period, wavelength and damping time. For the inferred parameters, the median and errors and the 68% credible region are: $v_{\mathrm{Ap}} = 11.80^{+1.15}_{-1.20}$; $B = 0.93^{+0.10}_{-0.09}$; and $l/R = 0.22^{+0.03}_{-0.02}$ (adapted from Arregui et al. 2014)

the particular profile that is adopted to model field-aligned density variations. As the exact profile is unknown, this poses a problem since inference results depend on the theoretical model that has been assumed.

To quantify the relative plausibility of inferences performed using alternative models, the second level of Bayesian inference can be used, namely model comparison. When different models are presented to explain observations, a quantitative analysis can be performed to assess which one among the proposed alternatives better explains the obtained data. This is done by considering posterior ratios, which enable us to quantify how much plausible a given model is in comparison to an alternative. Consider two such hypothetical models M^{i} and M^{j}. Applying Eq. (54), the posterior ratio is given by

$$\frac{p(M^{\mathrm{i}}|D)}{p(M^{\mathrm{j}}|D)} = \frac{p(D|M^{\mathrm{i}})}{p(D|M^{\mathrm{j}})}\frac{p(M^{\mathrm{i}})}{p(M^{\mathrm{j}})} = BF^{\mathrm{ij}}\frac{p(M^{\mathrm{i}})}{p(M^{\mathrm{j}})}, \tag{56}$$

with BF^{ij} the Bayes factor. If we consider that both models are equally probable a priori, $p(M^{\mathrm{i}}) = p(M^{\mathrm{j}})$, the prior ratio is unity and the posterior ratio reduces to the Bayes factor, i.e., the ratio of marginal likelihoods for both models. The marginal likelihood, $p(D|M) = \int p(D,\theta|M)d\theta = \int p(D|\theta,M)p(\theta|M)d\theta$, provides us with

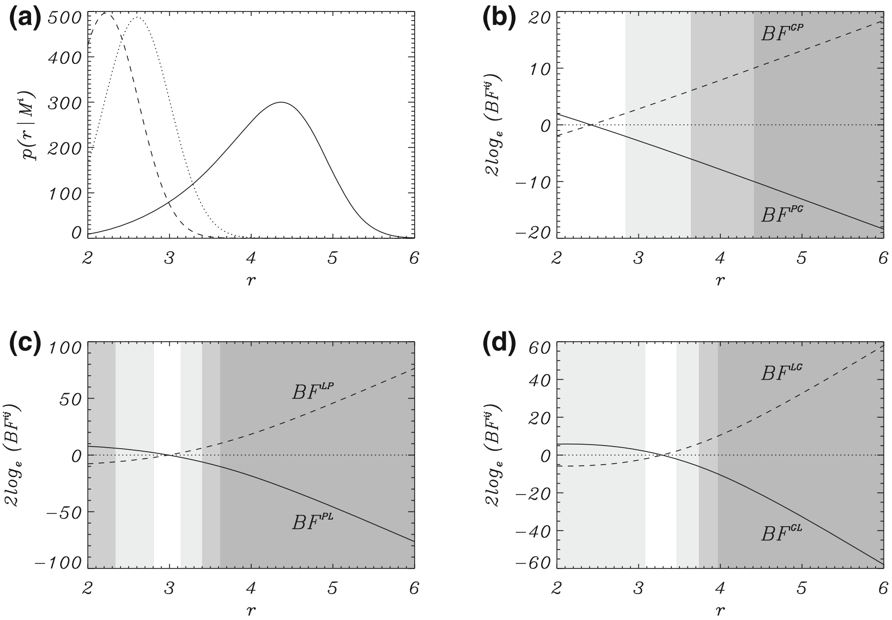

Fig. 94 **a** Marginal likelihoods for three density models considered by Arregui and Soler (2015) as a function of the observable period ratio (r): $p(r|M^{\mathrm{P}})$ as a dashed line, $p(r|M^{\mathrm{G}})$ as a dotted line and $p(r|M^{\mathrm{L}})$ as a solid line. **b**–**d** Bayes factors for the model comparisons between **b** the parabolic, M^{P}, and the Gaussian, M^{G}, density models; **c** the parabolic, M^{P}, and the Lorentzian, M^{L}, density models; and **d** the Gaussian, M^{G}, and the Lorentzian, M^{L}, density models, as a function of the period ratio. Different shades of grey limit ranges in period ratio with different levels of evidence for one model being preferred against the alternative, depending on the magnitude of the Bayes factors and following the empirical table by Kass and Raftery (1995), described in the text. White regions indicate values of period ratio for which there is minimal evidence for any of the models that are being compared. Then, different shades of grey indicate regions with positive, strong and very strong evidence, with the level of evidence being larger for darker regions. Image reproduced with permission from Arregui and Soler (2015), copyright by ESO

the probability of the observed data D, given that we have assumed a model M is true. It tells us how well the observed data are predicted by model M, with parameter set θ. These model comparison tools were applied by Arregui and Soler (2015) to study the relative performance of the field-aligned density models employed by Soler et al. (2015) to explain given period ratio data. In particular, Arregui and Soler (2015) performed marginal likelihood calculations to obtain the plausibility of each density model as a function of the observable period ratio and computed the Bayes factors to quantify the relative evidence for each model, given a period ratio observation.

Their results are displayed in Fig. 94. The three arbitrary density profiles discussed in Sect. 8.5 were considered with Lorentzian, Gaussian and parabolic shapes, denoted as M^{L}, M^{G} and M^{P}, respectively. The distribution of marginal likelihoods for each of these models, shown in Fig. 94a, indicates that the parabolic and Gaussian profiles are likely to produce period ratios in the lower half of the considered period ratios range, from 2 to 4. Beyond that, their likelihood decreases significantly. Hence, if our observed period ratio is in the range between 2 and 4, it can be difficult to obtain significant evidence for one model to be preferred over the other. The Lorentzian profile is more likely to reproduce values of the period ratio larger than those that can be reproduced by the parabolic and the Gaussian profiles. The distribution peaks at about 4.4, but is rather extended and covers almost all values of the considered range for the period ratio.

In order to make statements on the relative plausibility of one model over another, based on quantitative calculations, Bayes factors were computed. To assign levels of evidence for a given model M^i in front of the alternative M^j, based on the magnitude of the obtained Bayes factor BF^{ij}, the empirical table by Kass and Raftery (1995) was used. According to this table, values of $2\log(BF^{ij})$ in between 0 and 2 correspond to minimal evidence; values in between 2 and 6 correspond to positive evidence; values in between 6 and 10 to strong evidence; and values larger than 10 would indicate very strong evidence. The results displayed in Fig. 94b-d indicate that a Lorentzian density profile, with plasma density concentrated around the centre of the tube, seems to offer the most plausible inversion result. The model comparison results indicate that the evidence points to the Gaussian and parabolic profiles for period ratios in between 2 and 3, while the Lorentzian profile is preferred for higher period ratio values. This model comparison technique could be used to obtain information on the plasma structure along threads, provided period ratio measurements become widely available.

The two examples discussed in this section show that Bayesian analysis techniques exhibit great promise for prominence seismology. They enable us to quantify the grade of belief on unknown parameters taking on given values and to compare, in a quantitative way, the relative performance of alternative physical models in explaining observed data.

9 Open issues

Solar prominences are among the most complicated structures in the solar corona. A full understanding of their formation, magnetic structure and disappearance has not been reached yet, and a lot of physical effects remain to be included in prominence models. For this reason, theoretical models set up to interpret small amplitude oscillations are still poor. High-resolution observations of filaments suggest that they are made of threads whose thickness is at the the limit of the available spatial resolution. Then, one may wonder whether future improvements of the spatial resolution will provide with thinner and thinner threads or, on the contrary, there is a lower limit for thickness and we will be able to determine it in the future. The presence of these long and thin threads together with the place where they are anchored and the presence of flows along them suggest that they are thin flux tubes filled with continuous or discontinuous cool material.

This cool material is probably subject to cooling, heating, ionisation, recombination, motions, etc., which, altogether, makes very difficult a proper theoretical treatment. For instance, in the case of the considered thermal mechanisms, up to now only optically thin radiation has been taken into account, while the inclusion of optically thick effects would probably be more realistic; the prominence heating mechanisms taken usually into account are tentative and “ad hoc”, while true prominence heating processes are still deeply unknown. An important step ahead would be to consistently couple radiative transfer with magnetohydrodynamic waves as a mean to establish a relationship between velocity, density, magnetic field and temperature perturbations, and the observed signatures of oscillations like spectral line shift, width and intensity. On the other hand, oscillations have also been studied by producing small perturbations in a background equilibrium with stationary physical properties. However, the stationary assumption is not realistic and the effects produced by a non-stationary background on MHD waves should be studied. Ballester et al. (2016) have made a first step in this direction by studying the effect of the temporal variation of the prominence temperature, produced by an imbalance between heating and cooling processes, on slow MHD waves excited in a plasma with prominence physical properties. However, this issue needs to be explored using more realistic models for prominence configuration as well as for processes that modify in time, or in space, prominence physical properties.

Partial ionisation is another topic of interest for prominence oscillations since, apart from influencing the behaviour of magnetohydrodynamic waves, it poses an important problem for prominence equilibrium models since cross-field diffusion of neutral atoms can give place to flows and drain prominence material. Furthermore, time or space variations of temperature, density, etc. could substantially affect some of the parameters involved in the dissipative terms of the induction equation.

Another issue which still remains a mystery is the triggering mechanism of small amplitude oscillations. In the case of large amplitude oscillations, observations provide with information about the exciting mechanism, but the available observations of small amplitude oscillations show no signature of their exciting mechanism. Are these oscillations of chromospheric or photospheric origin? Are they generated inside prominence magnetic structures by small reconnection events? Are they produced by weak external disturbances coming from far away in the solar atmosphere? Indirect evidence about this topic is given by Hillier et al. (2013), who found that the velocity power spectrum of transverse oscillations in a quiescent prominence is consistent with the power spectrum of horizontal motions of photospheric magnetic elements.

The presence of flows adds another ingredient to be taken into account in the study of prominence oscillations and, up to now, we can only obtain one or two-dimensional information about the flow behaviour. It would be of great interest to collect information about the three-dimensional structure of flows and, probably, in the near future we could acquire this information by means of IRIS (http://iris.lmsal.com/).

The physical changing conditions of prominence plasmas suggest that for an in-depth theoretical study of prominence oscillations more complex models together with numerical simulations are needed. Therefore, and as a step ahead, in the next future numerical studies of the time evolution of magnetohydrodynamic waves in partially ionised flowing inhomogeneous prominence plasmas, subject to different physical processes such as ionisation, recombination, etc., should be undertaken. However, a full three-dimensional dynamical prominence model involving magnetic equilibrium, radiative transfer, etc., whose oscillatory behaviour could be studied seems to be still far away in the future.

Acknowledgements The authors acknowledge the financial support received from the MINECO and FEDER funds under Grants Nos. AYA2014-54485-P and AYA2014-55456-P. They also thank R. Soler for producing some of the figures of this review.

Appendix: List of symbols

Speeds	
v_{A}	Alfvén speed
v_{Ai}	Internal (prominence) Alfvén speed
v_{Ae}	External (coronal) Alfvén speed
v_{Ap}	Prominence Alfvén speed
v_{A0}	Prominence Alfvén speed
v_{Ac}	Coronal Alfvén speed
v_{Af}	Filament Alfvén speed
c_{s}	Sound speed
c_{sp}	Prominence sound speed
c_{s0}	Prominence sound speed
c_{sc}	Coronal sound speed
c_{f}	Fast speed
c_{T}	Cusp speed
c_{Tp}	Cusp speed in the thread
c_{str}	Natural wave speed in string models
c_{pro}	Prominence wave speed in string models
c_{cor}	Coronal wave speed in string models
c_{ph}	Phase velocity
v_{g}	Group velocity
c_{k}	Kink speed
Diffusivity coefficients	
η ($\tilde{\eta}$)	Ohmic diffusion (dimensionless form)
η_{A}	Ambipolar diffusion
η_{C} ($\tilde{\eta}_{\mathrm{C}}$)	Cowling's diffusion (dimensionless form)
η_{H} ($\tilde{\eta}_{\mathrm{H}}$)	Hall's diffusion (dimensionless form)
$\tilde{\eta}_{\mathrm{Cc,p}}$	Dimensionless coronal, prominence Cowling's diffusion
Densities	
ρ_{p} (ρ_0, ρ_{i})	Prominence (internal) density
ρ_{c} (ρ_{e})	Coronal (external) density
ρ_{f}	Filament density

References

Anderson GF (1967) Transient flare-associated phenomena in the solar atmosphere. PhD thesis, University of Colorado at Boulder, Boulder, CO

Andries J, Arregui I, Goossens M (2005) Determination of the coronal density stratification from the observation of harmonic coronal loop oscillations. Astrophys J Lett 624:L57–L60. https://doi.org/10.1086/430347

Andries J, Arregui I, Goossens M (2009) The influence of longitudinal density variation in coronal loops on the eigenfunctions of kink-oscillation overtones. Astron Astrophys 497:265–272. https://doi.org/10.1051/0004-6361/200811481

Antolin P, Okamoto TJ, De Pontieu B, Uitenbroek H, Van Doorsselaere T, Yokoyama T (2015) Resonant absorption of transverse oscillations and associated heating in a solar prominence. II. Numerical aspects. Astrophys J 809:72. https://doi.org/10.1088/0004-637X/809/1/72. arXiv:1506.09108

Anzer U (2009) Global prominence oscillations. Astron Astrophys 497:521–524. https://doi.org/10.1051/0004-6361/200811107

Anzer U, Heinzel P (2005) On the nature of dark extreme ultraviolet structures seen by SOHO/EIT and TRACE. Astrophys J 622:714–721. https://doi.org/10.1086/427817

Arregui I, Asensio Ramos A (2014) Determination of the cross-field density structuring in coronal waveguides using the damping of transverse waves. Astron Astrophys 565:A78. https://doi.org/10.1051/0004-6361/201423536. arXiv:1404.0584

Arregui I, Ballester JL (2011) Damping mechanisms for oscillations in solar prominences. Space Sci Rev 158:169–204. https://doi.org/10.1007/s11214-010-9648-9. arXiv:1002.3489

Arregui I, Soler R (2015) Model comparison for the density structure along solar prominence threads. Astron Astrophys 578:A130. https://doi.org/10.1051/0004-6361/201525720. arXiv:1505.03448

Arregui I, Andries J, Van Doorsselaere T, Goossens M, Poedts S (2007) MHD coronal seismology using the period and damping of resonantly damped quasi-mode kink oscillations. Astron Astrophys 463:333–338. https://doi.org/10.1051/0004-6361:20065863

Arregui I, Terradas J, Oliver R, Ballester JL (2007) Resonantly damped surface and body MHD waves in a solar coronal slab with oblique propagation. Solar Phys 246:213–230. https://doi.org/10.1007/s11207-007-9041-3. arXiv:0708.3783

Arregui I, Ballester JL, Goossens M (2008a) On the scaling of the damping time for resonantly damped oscillations in coronal loops. Astrophys J Lett 676:L77–L80. https://doi.org/10.1086/587098. arXiv:0802.1143

Arregui I, Terradas J, Oliver R, Ballester JL (2008b) Damping of fast magnetohydrodynamic oscillations in quiescent filament threads. Astrophys J Lett 682:L141–L144. https://doi.org/10.1086/591081

Arregui I, Soler R, Ballester JL, Wright AN (2011) Magnetohydrodynamic kink waves in two-dimensional non-uniform prominence threads. Astron Astrophys 533:A60. https://doi.org/10.1051/0004-6361/201117477. arXiv:1011.5175

Arregui I, Asensio Ramos A, Díaz AJ (2013) Bayesian analysis of multiple harmonic oscillations in the solar corona. Astrophys J Lett 765:L23 arXiv:1302.3393

Arregui I, Ramos AA, Díaz AJ (2014) The promise of Bayesian analysis for prominence seismology. In: Schmieder B, Malherbe JM, Wu ST (eds) Nature of prominences and their role in space weather, Cambridge University Press, Cambridge, IAU Symposium, vol 300, pp 393–394. https://doi.org/10.1017/S1743921313011241

Arregui I, Soler R, Asensio Ramos A (2015) Model comparison for the density structure across solar coronal waveguides. Astrophys J 811:104. https://doi.org/10.1088/0004-637X/811/2/104 axXiv:1509.02340

Asai A, Ishii TT, Isobe H, Kitai R, Ichimoto K, UeNo S, Nagata S, Morita S, Nishida K, Shiota D, Oi A, Akioka M, Shibata K (2012) First simultaneous observation of an Hα Moreton wave, EUV wave, and filament/prominence oscillations. Astrophys J Lett 745:L18. https://doi.org/10.1088/2041-8205/745/2/L18. arXiv:1112.5915

Aschwanden MJ, Fletcher L, Schrijver CJ, Alexander D (1999) Coronal loop oscillations observed with the transition region and coronal explorer. Astrophys J 520:880–894. https://doi.org/10.1086/307502

Bakhareva NM, Zaitsev VV, Khodachenko ML (1992) Dynamic regimes of prominence evolution. Solar Phys 139:299–314. https://doi.org/10.1007/BF00159156

Ballai I (2003) On dissipative effects in solar prominences. Astron Astrophys 410:L17–L19. https://doi.org/10.1051/0004-6361:20031401

Ballester JL (2010) The damping of small-amplitude oscillations in quiescent prominences. Adv Space Res 46:364–376. https://doi.org/10.1016/j.asr.2009.09.015

Ballester JL, Priest ER (1989) Model for the fibril structure of solar prominences. Astron Astrophys 225:213–221

Ballester JL, Carbonell M, Soler R, Terradas J (2016) Prominence oscillations: effect of a time-dependent background temperature. Astron Astrophys 591:A109. https://doi.org/10.1051/0004-6361/201527953

Balthasar H, Wiehr E (1994) Temporal and spatial variation of physical parameters in a quiescent prominence. Astron Astrophys 286:639–644

Balthasar H, Knoelker M, Wiehr E, Stellmacher G (1986) Evidence for quasi-periodic Doppler motions in solar prominences. Astron Astrophys 163:343–346

Balthasar H, Wiehr E, Schleicher H, Wohl H (1993) Doppler oscillations in solar prominences simultaneously observed with two telescopes. discovery of a 30 s oscillation. Astron Astrophys 277:635–638

Barceló S, Carbonell M, Ballester JL (2011) Time damping of non-adiabatic magnetohydrodynamic waves in a partially ionised prominence medium: effect of a background flow. Astron Astrophys 525:A60. https://doi.org/10.1051/0004-6361/201015499

Bashkirtsev VS, Mashnich GP (1984) Oscillatory processes in prominences. Solar Phys 91:93–101. https://doi.org/10.1007/BF00213616

Bashkirtsev VS, Mashnich GP (1993) Some regularities of velocity oscillations in prominences. Astron Astrophys 279:610–614

Bashkirtsev VS, Kobanov NI, Mashnich GP (1983) The observations of 80-min oscillations in the quiescent prominences. Solar Phys 82:443–445. https://doi.org/10.1007/BF00145584

Bayes M, Price M (1763) An essay towards Solving a Problem in the Doctrine of Chances. By the Late Rev. Mr. Bayes, F. R. S. Communicated by Mr. Price, in a Letter to John Canton, A. M. F. R. S. Philos Trans R Soc Lond 53:370–418. https://doi.org/10.1098/rstl.1763.0053

Berger TE, Shine RA, Slater GL, Tarbell TD, Title AM, Okamoto TJ, Ichimoto K, Katsukawa Y, Suematsu Y, Tsuneta S, Lites BW, Shimizu T (2008) Hinode SOT observations of solar quiescent prominence dynamics. Astrophys J Lett 676:L89–L92. https://doi.org/10.1086/587171

Bernstein IB, Frieman EA, Kruskal MD, Kulsrud RM (1958) An energy principle for hydromagnetic stability problems. Proc R Soc Lond Ser A 244:17–40. https://doi.org/10.1098/rspa.1958.0023

Bi Y, Jiang Y, Yang J, Hong J, Li H, Yang D, Yang B (2014) Solar filament material oscillations and drainage before eruption. Astrophys J 790:100. https://doi.org/10.1088/0004-637X/790/2/100

Blanco S, Bocchialini K, Costa A, Domenech G, Rovira M, Vial JC (1999) Multiresolution wavelet analysis of SUMER/SOHO observations in a solar prominence. Solar Phys 186:281–290. https://doi.org/10.1023/A:1005185523486

Bocchialini K, Baudin F, Koutchmy S, Pouget G, Solomon J (2011) Oscillatory motions observed in eruptive filaments. Astron Astrophys 533:A96. https://doi.org/10.1051/0004-6361/201016342. arXiv:1107.0596

Bommier V, Leroy JL (1998) Global pattern of the magnetic field vector above neutral lines from 1974 to 1982: Pic-du-Midi observations of prominences. In: Webb DF, Schmieder B, Rust DM (eds) New perspectives on solar prominences, Astronomical Society of the Pacific, San Francisco, ASP Conference Series, vol 150, pp 434–438

Bommier V, Landi Degl'Innocenti E, Leroy JL, Sahal-Bréchot S (1994) Complete determination of the magnetic field vector and of the electron density in 14 prominences from linear polarization measurements in the HeI D_3 and Hα lines. Solar Phys 154:231–260. https://doi.org/10.1007/BF00681098

Cally PS (1986) Leaky and non-leaky oscillations in magnetic flux tubes. Solar Phys 103:277–298. https://doi.org/10.1007/BF00147830

Carbonell M, Oliver R, Ballester JL (2004) Time damping of linear non-adiabatic magnetohydrodynamic waves in an unbounded plasma with solar coronal properties. Astron Astrophys 415:739–750. https://doi.org/10.1051/0004-6361:20034630

Carbonell M, Terradas J, Oliver R, Ballester JL (2006) Spatial damping of linear non-adiabatic magnetoacoustic waves in a prominence medium. Astron Astrophys 460:573–581. https://doi.org/10.1051/0004-6361:20065528

Carbonell M, Oliver R, Ballester JL (2009) Time damping of non-adiabatic MHD slow and thermal waves in a prominence medium: effect of a background flow. New Astron 14:277–284. https://doi.org/10.1016/j.newast.2008.09.001

Carbonell M, Forteza P, Oliver R, Ballester JL (2010) The spatial damping of magnetohydrodynamic waves in a flowing partially ionised prominence plasma. Astron Astrophys 515:A80. https://doi.org/10.1051/0004-6361/200913024. arXiv:1001.4962

Chen PF, Innes DE, Solanki SK (2008) SOHO/SUMER observations of prominence oscillation before eruption. Astron Astrophys 484:487–493. https://doi.org/10.1051/0004-6361:200809544. arXiv:0802.1961

Chin R, Verwichte E, Rowlands G, Nakariakov VM (2010) Self-organization of magnetoacoustic waves in a thermally unstable environment. Phys Plasmas 17:032107. https://doi.org/10.1063/1.3314721

Chitta LP, van Ballegooijen AA, Rouppe van der Voort L, DeLuca EE, Kariyappa R (2012) Dynamics of the solar magnetic bright points derived from their horizontal motions. Astrophys J 752:48. https://doi.org/10.1088/0004-637X/752/1/48. arXiv:1204.4362

de Jager C (1959) Structure and dynamics of the solar atmosphere. In: Flügge S (ed) Astrophysik 3: Das Sonnensystem, Handbuch der Physik, vol 52. Springer, Berlin, p 80

De Pontieu B, Martens PCH, Hudson HS (2001) Chromospheric damping of Alfvén waves. Astrophys J 558:859–871. https://doi.org/10.1086/322408

Díaz AJ, Roberts B (2006) Fast magnetohydrodynamic oscillations in a fibril prominence model. Solar Phys 236:111–126. https://doi.org/10.1007/s11207-006-0137-y

Díaz AJ, Oliver R, Erdélyi R, Ballester JL (2001) Fast MHD oscillations in prominence fine structures. Astron Astrophys 379:1083–1097. https://doi.org/10.1051/0004-6361:20011351

Díaz AJ, Oliver R, Ballester JL (2002) Fast magnetohydrodynamic oscillations in cylindrical prominence fibrils. Astrophys J 580:550–565. https://doi.org/10.1086/343039

Díaz AJ, Oliver R, Ballester JL (2003) Fast MHD oscillations of a 3-dimensional prominence fibril. Astron Astrophys 402:781–789. https://doi.org/10.1051/0004-6361:20030285

Díaz AJ, Oliver R, Ballester JL (2005) Fast magnetohydrodynamic oscillations in a multifibril Cartesian prominence model. Astron Astrophys 440:1167–1175. https://doi.org/10.1051/0004-6361:20052759

Díaz AJ, Oliver R, Ballester JL (2010) Prominence thread seismology using the $P_1/2P_2$ ratio. Astrophys J 725:1742–1748. https://doi.org/10.1088/0004-637X/725/2/1742

Dungey JW (1953) A family of solutions of the magneto-hydrostatic problem in a conducting atmosphere in a gravitational field. Mon Not R Astron Soc 113:180–187. https://doi.org/10.1093/mnras/113.2.180

Dymova MV, Ruderman MS (2005) Non-axisymmetric oscillations of thin prominence fibrils. Solar Phys 229:79–94. https://doi.org/10.1007/s11207-005-5002-x

Edwin PM, Roberts B (1983) Wave propagation in a magnetic cylinder. Solar Phys 88:179–191. https://doi.org/10.1007/BF00196186

Engvold O (1981) The small scale velocity field of a quiescent prominence. Solar Phys 70:315–324. https://doi.org/10.1007/BF00151336

Engvold O (1998) Observations of filament structure and dynamics. In: Webb DF, Schmieder B, Rust DM (eds) New perspectives on solar prominences, Astronomical Society of the Pacific, San Francisco, ASP Conference Series, vol 150, pp 23–31

Engvold O (2008) Observational aspects of prominence oscillations. In: Erdélyi R, Mendoza-Briceño CA (eds) Waves and oscillations in the solar atmosphere: heating and magneto-seismology. Cambridge University Press, Cambridge, IAU Symposia, vol 247, pp 152–157. https://doi.org/10.1017/S1743921308014816

Eto S, Isobe H, Narukage N, Asai A, Morimoto T, Thompson B, Yashiro S, Wang T, Kitai R, Kurokawa H, Shibata K (2002) Relation between a Moreton wave and an EIT wave observed on 1997 November 4. Publ Astron Soc Jpn 54:481–491. https://doi.org/10.1093/pasj/54.3.481

Field GB (1965) Thermal instability. Astrophys J 142:531–567. https://doi.org/10.1086/148317

Forteza P, Oliver R, Ballester JL, Khodachenko ML (2007) Damping of oscillations by ion-neutral collisions in a prominence plasma. Astron Astrophys 461:731–739. https://doi.org/10.1051/0004-6361:20065900

Forteza P, Oliver R, Ballester JL (2008) Time damping of non-adiabatic MHD waves in an unbounded partially ionised prominence plasma. Astron Astrophys 492:223–231. https://doi.org/10.1051/0004-6361:200810370

Foullon C, Verwichte E, Nakariakov VM (2004) Detection of ultra-long-period oscillations in an EUV filament. Astron Astrophys 427:L5–L8. https://doi.org/10.1051/0004-6361:200400083

Foullon C, Verwichte E, Nakariakov VM (2009) Ultra-long-period oscillations in EUV filaments near to eruption: two-wavelength correlation and seismology. Astrophys J 700:1658–1665. https://doi.org/10.1088/0004-637X/700/2/1658

Galindo Trejo J (1987) Stability analysis of two-dimensional models of quiescent prominences. Solar Phys 108:265–313

Galindo Trejo J (1989a) Influence of a non-uniform axial magnetic field on the instability of a quiescent prominence overlying a solar bipolar region. Rev Mex Astron Astrof 17:47–58

Galindo Trejo J (1989b) MHD stability of a filament immersed in a solar bipolar magnetic region. Geophys Astrophys Fluid Dyn 47:69–91. https://doi.org/10.1080/03091928908221817

Galindo Trejo J (1998) Hydromagnetic stability analysis of a solar prominence suspended in an external horizontal magnetic field. Astron Nachr 319:391–408. https://doi.org/10.1002/asna.2123190608

Galindo Trejo J (2006) MHD stabiblity of a solar prominence embedded in an external vertical magnetic field. Rev Mex Astron Astrof 42:89–98

Gilbert HR, Daou AG, Young D, Tripathi D, Alexander D (2008) The filament-Moreton wave interaction of 2006 December 6. Astrophys J 685:629–645. https://doi.org/10.1086/590545

Goossens M (2003) An introduction to plasma astrophysics and magnetohydrodynamics. Astrophysics and Space Science Library, vol 294. Kluwer, Dordrecht. https://doi.org/10.1007/978-94-007-1076-4

Goossens M (2008) Seismology of kink oscillations in coronal loops: two decades of resonant damping. In: Erdélyi R, Mendoza-Briceño CA (eds) Waves and oscillations in the solar atmosphere: heating and magneto-seismology. Cambridge University Press, Cambridge, IAU Symposium, vol 247, pp 228–242. https://doi.org/10.1017/S1743921308014920

Goossens M, Hollweg JV, Sakurai T (1992) Resonant behaviour of MHD waves on magnetic flux tubes. III. Effect of equilibrium flow. Solar Phys 138:233–255. https://doi.org/10.1007/BF00151914

Goossens M, Ruderman MS, Hollweg JV (1995) Dissipative MHD solutions for resonant Alfvén waves in 1-dimensional magnetic flux tubes. Solar Phys 157:75–102. https://doi.org/10.1007/BF00680610

Goossens M, Andries J, Aschwanden MJ (2002) Coronal loop oscillations: an interpretation in terms of resonant absorption of quasi-mode kink oscillations. Astron Astrophys 394:L39–L42. https://doi.org/10.1051/0004-6361:20021378

Goossens M, Andries J, Arregui I (2006) Damping of magnetohydrodynamic waves by resonant absorption in the solar atmosphere. Philos Trans R Soc Lond Ser A 364:433–446. https://doi.org/10.1098/rsta.2005.1708

Goossens M, Arregui I, Ballester JL, Wang TJ (2008) Analytic approximate seismology of transversely oscillating coronal loops. Astron Astrophys 484:851–857. https://doi.org/10.1051/0004-6361:200809728

Goossens M, Terradas J, Andries J, Arregui I, Ballester JL (2009) On the nature of kink MHD waves in magnetic flux tubes. Astron Astrophys 503:213–223. https://doi.org/10.1051/0004-6361/200912399. arXiv:0905.0425

Goossens M, Erdélyi R, Ruderman MS (2010) Resonant MHD waves in the solar atmosphere. Space Sci Rev. https://doi.org/10.1007/s11214-010-9702-7

Gosain S, Foullon C (2012) Dual trigger of transverse oscillations in a prominence by EUV fast and slow coronal waves: SDO/AIA and STEREO/EUVI observations. Astrophys J 761:103. https://doi.org/10.1088/0004-637X/761/2/103. arXiv:1210.6690

Gouttebroze P, Labrosse N (2009) Radiative transfer in cylindrical threads with incident radiation. VI. A hydrogen plus helium system. Astron Astrophys 503:663–671. https://doi.org/10.1051/0004-6361/200811483. arXiv:0905.3466

Gregory PC (2005) Bayesian logical data analysis for the physical sciences: a comparative approach with ‘Mathematica’ support. Cambridge University Press, Cambridge

Harvey JW (1969) Magnetic fields associated with solar active-region prominences. PhD thesis, University of Colorado at Boulder, Boulder, CO

Heinzel P (1995) Multilevel NLTE radiative transfer in isolated atmospheric structures: implementation of the MALI-technique. Astron Astrophys 299:563

Heinzel P, Anzer U (2006) On the fine structure of solar filaments. Astrophys J Lett 643:L65–L68. https://doi.org/10.1086/504980

Heinzel P, Zapiór M, Oliver R, Ballester JL (2014) Synthetic hydrogen spectra of prominence oscillations. Astron Astrophys 562:A103. https://doi.org/10.1051/0004-6361/201322346. arXiv:1401.2131

Hershaw J, Foullon C, Nakariakov VM, Verwichte E (2011) Damped large amplitude transverse oscillations in an EUV solar filament, triggered by large-scale transient coronal waves. Astron Astrophys 531:A53. https://doi.org/10.1051/0004-6361/201116750

Hillier A, Morton RJ, Erdélyi R (2013) A statistical study of transverse oscillations in a quiescent prominence. Astrophys J Lett 779:L16. https://doi.org/10.1088/2041-8205/779/2/L16. arXiv:1310.8009

Hollweg JV, Yang G (1988) Resonance absorption of compressible magnetohydrodynamic waves at thin ‘surfaces’. J Geophys Res 93:5423–5436. https://doi.org/10.1029/JA093iA06p05423

Hyder CL (1966) Winking filaments and prominence and coronal magnetic fields. Z Astrophys 63:78–84

Ionson JA (1978) Resonant absorption of Alfvénic surface waves and the heating of solar coronal loops. Astrophys J 226:650–673. https://doi.org/10.1086/156648

Isobe H, Tripathi D (2006) Large amplitude oscillation of a polar crown filament in the pre-eruption phase. Astron Astrophys 449:L17–L20. https://doi.org/10.1051/0004-6361:20064942. arXiv:astro-ph/0602432

Isobe H, Tripathi D, Asai A, Jain R (2007) Large-amplitude oscillation of an erupting filament as seen in EUV, Hα, and microwave observations. Solar Phys 246:89–99. https://doi.org/10.1007/s11207-007-9091-6. arXiv:0711.3952

James SP, Erdélyi R, De Pontieu B (2003) Can ion-neutral damping help to form spicules? Astron Astrophys 406:715–724. https://doi.org/10.1051/0004-6361:20030685

Jing J, Lee J, Spirock TJ, Xu Y, Wang H, Choe GS (2003) Periodic motion along a solar filament initiated by a subflare. Astrophys J Lett 584:L103–L106. https://doi.org/10.1086/373886

Jing J, Lee J, Spirock TJ, Wang H (2006) Periodic motion along solar filaments. Solar Phys 236:97–109. https://doi.org/10.1007/s11207-006-0126-1

Joarder PS, Roberts B (1992a) The modes of oscillation of a prominence. I. The slab with longitudinal magnetic field. Astron Astrophys 256:264–272

Joarder PS, Roberts B (1992b) The modes of oscillation of a prominence. II. The slab with transverse magnetic field. Astron Astrophys 261:625–632

Joarder PS, Roberts B (1993a) The modes of oscillation of a Menzel prominence. Astron Astrophys 273:642–646

Joarder PS, Roberts B (1993b) The modes of oscillation of a prominence. III. The slab in a skewed magnetic field. Astron Astrophys 277:225–234

Joarder PS, Nakariakov VM, Roberts B (1997) Oscillations in prominence fine-structures. Solar Phys 173:81–101. https://doi.org/10.1023/A:1004917710650

Joshi AD, Hanaoka Y, Suematsu Y, Morita S, Yurchyshyn V, Cho KS (2016) Pre-eruption oscillations in thin and long features in a quiescent filament. Astrophys J 833:243. https://doi.org/10.3847/1538-4357/833/2/243. arXiv:1612.04917

Kass RE, Raftery AE (1995) Bayes factors. J Am Stat Assoc 90:773. https://doi.org/10.1080/01621459.1995.10476572

Khodachenko ML, Arber TD, Rucker HO, Hanslmeier A (2004) Collisional and viscous damping of MHD waves in partially ionized plasmas of the solar atmosphere. Astron Astrophys 422:1073–1084. https://doi.org/10.1051/0004-6361:20034207

Kippenhahn R, Schlüter A (1957) Eine Theorie der solaren Filamente. Z Astrophys 43:36–62

Kleczek J, Kuperus M (1969) Oscillatory phenomena in quiescent prominences. Solar Phys 6:72–79. https://doi.org/10.1007/BF00146797

Kolotkov DY, Nisticò G, Nakariakov VM (2016) Transverse oscillations and stability of prominences in a magnetic field dip. Astron Astrophys 590:A120. https://doi.org/10.1051/0004-6361/201628501

Kuperus M, Raadu MA (1974) The support of prominences formed in neutral sheets. Astron Astrophys 31:189–193

Kuperus M, Tandberg-Hanssen E (1967) The nature of quiescent solar prominences. Solar Phys 2:39–48. https://doi.org/10.1007/BF00155891

Labrosse N, Heinzel P, Vial JC, Kucera T, Parenti S, Gunár S, Schmieder B, Kilper G (2010) Physics of solar prominences: I—spectral diagnostics and non-LTE modelling. Space Sci Rev 151:243–332. https://doi.org/10.1007/s11214-010-9630-6. arXiv:1001.1620

Landman DA, Edberg SJ, Laney CD (1977) Measurements of Hβ, He D_3, and Ca^+ λ8542 line emission in quiescent prominences. Astrophys J 218:888–897. https://doi.org/10.1086/155744

Leake JE, Arber TD, Khodachenko ML (2005) Collisional dissipation of Alfvén waves in a partially ionised solar chromosphere. Astron Astrophys 442:1091–1098. https://doi.org/10.1051/0004-6361:20053427. arXiv:astro-ph/0510265

Lerche I, Low BC (1980) On the equilibrium of a cylindrical plasma supported horizontally by magnetic fields in uniform gravity. Solar Phys 67:229–243. https://doi.org/10.1007/BF00149804

Leroy JL (1980) Mass balance and magnetic structure in quiescent prominences. In: Moriyama F, Henoux JC (eds) Proceedings of the Japan–France seminar on solar physics, Nihon Gakujutsu Shinkokai and CNRS, Tokyo, p 155

Leroy JL (1988) Observations of prominence magnetic field. In: Ballester JL, Priest ER (eds) Dynamics and structure of solar prominences, Universitat de les Illes Balears, Palma de Mallorca, Conferències i comunicacions, vol 5, pp 33–40

Leroy JL (1989) Observation of prominence magnetic fields. In: Priest ER (ed) Dynamics and structure of quiescent solar prominences, Astrophysics and Space Science Library, vol 150. Kluwer, Dordrecht, pp 77–113

Li L, Zhang J (2013) The evolution of barbs of a polar crown filament observed by SDO. Solar Phys 282:147–174. https://doi.org/10.1007/s11207-012-0122-6

Li T, Zhang J (2012) SDO/AIA observations of large-amplitude longitudinal oscillations in a solar filament. Astrophys J Lett 760:L10. https://doi.org/10.1088/2041-8205/760/1/L10. arXiv:1210.5110

Lin Y (2005) Magnetic field topology inferred from studies of fine threads in solar filaments. PhD thesis, University of Oslo, Oslo

Lin Y (2011) Filament thread-like structures and their small-amplitude oscillations. Space Sci Rev 158:237–266. https://doi.org/10.1007/s11214-010-9672-9

Lin Y, Engvold OR, Wiik JE (2003) Counterstreaming in a large polar crown filament. Solar Phys 216:109–120. https://doi.org/10.1023/A:1026150809598

Lin Y, Engvold O, Rouppe van der Voort LHM, Wiik JE, Berger TE (2005) Thin threads of solar filaments. Solar Phys 226:239–254. https://doi.org/10.1007/s11207-005-6876-3

Lin Y, Engvold O, Rouppe van der Voort LHM, van Noort MJ (2007) Evidence of traveling waves in filament threads. Solar Phys 246:65–72. https://doi.org/10.1007/s11207-007-0402-8

Lin Y, Martin SF, Engvold O (2008) Filament substructures and their interrelation. In: Howe R, Komm RW, Balasubramaniam KS, Petrie GJD (eds) Subsurface and atmospheric influences on solar activity, ASP Conference Series, vol 383. Astronomical Society of the Pacific, San Francisco, pp 235–242

Lin Y, Soler R, Engvold O, Ballester JL, Langangen Ø, Oliver R, Rouppe van der Voort LHM (2009) Swaying threads of a solar filament. Astrophys J 704:870–876. https://doi.org/10.1088/0004-637X/704/1/870

Liu W, Ofman L, Nitta NV, Aschwanden MJ, Schrijver CJ, Title AM, Tarbell TD (2012) Quasi-periodic fast-mode wave trains within a global EUV wave and sequential transverse oscillations detected by SDO/AIA. Astrophys J 753:52. https://doi.org/10.1088/0004-637X/753/1/52. arXiv:1204.5470

Low BC (1981) The field and plasma configuration of a filament overlying a solar bipolar magnetic region. Astrophys J 246:538–548. https://doi.org/10.1086/158954

Luna M, Karpen J (2012) Large-amplitude longitudinal oscillations in a solar filament. Astrophys J Lett 750:L1. https://doi.org/10.1088/2041-8205/750/1/L1. arXiv:1203.5027

Luna M, Terradas J, Oliver R, Ballester JL (2008) Transverse oscillations of two coronal loops. Astrophys J 676:717–727. https://doi.org/10.1086/528367. arXiv:0707.0758

Luna M, Díaz AJ, Karpen J (2012a) The effects of magnetic-field geometry on longitudinal oscillations of solar prominences. Astrophys J 757:98. https://doi.org/10.1088/0004-637X/757/1/98. arXiv:1207.6358

Luna M, Karpen JT, DeVore CR (2012b) Formation and evolution of a multi-threaded solar prominence. Astrophys J 746:30. https://doi.org/10.1088/0004-637X/746/1/30. arXiv:1201.3559

Luna M, Knizhnik K, Muglach K, Karpen J, Gilbert H, Kucera TA, Uritsky V (2014) Observations and implications of large-amplitude longitudinal oscillations in a solar filament. Astrophys J 785:79. https://doi.org/10.1088/0004-637X/785/1/79. arXiv:1403.0381

Luna M, Díaz AJ, Oliver R, Terradas J, Karpen J (2016a) The effects of magnetic-field geometry on longitudinal oscillations of solar prominences: cross-sectional area variation for thin tubes. Astron Astrophys 593:A64. https://doi.org/10.1051/0004-6361/201628845. arXiv:1607.02996

Luna M, Terradas J, Khomenko E, Collados M, de Vicente A (2016b) On the robustness of the pendulum model for large-amplitude longitudinal oscillations in prominences. Astrophys J 817:157. https://doi.org/10.3847/0004-637X/817/2/157. arXiv:1512.05125

Mackay DH, Karpen JT, Ballester JL, Schmieder B, Aulanier G (2010) Physics of solar prominences: II—magnetic structure and dynamics. Space Sci Rev 151:333–399. https://doi.org/10.1007/s11214-010-9628-0. arXiv:1001.1635

Malherbe JM, Schmieder B, Mein P (1981) Dynamics in the filaments. I. Oscillations in a quiescent filament. Astron Astrophys 102:124–128

Malherbe JM, Schmieder B, Mein P, Tandberg-Hanssen E (1987) Dynamics of solar filaments. V. Oscillations in the Hα and 1548 Å C iv lines. Astron Astrophys 172:316–322

Malville JM, Schindler M (1981) Oscillations of a loop prominence preceding a limb flare. Solar Phys 70:115–128. https://doi.org/10.1007/BF00154395

Martin SF, Lin Y, Engvold O (2008) A method of resolving the 180-degree ambiguity by employing the chirality of solar features. Solar Phys 250:31–51. https://doi.org/10.1007/s11207-008-9194-8

Mashnich GP, Bashkirtsev VS (1990) Observations of Doppler velocity oscillations of mass motion in a quiescent prominence during three consecutive days. Astron Astrophys 235:428–430

Mashnich GP, Bashkirtsev VS (1999) Latitudinal variations of line-of-sight velocity oscillations in the photosphere, chromosphere and prominences. Solar Phys 185:35–40. https://doi.org/10.1023/A:1005166214261

Mashnich GP, Bashkirtsev VS, Khlystova AI (2009a) Spatial distribution of oscillations in filaments. Geomagn Aeron 49:891–897. https://doi.org/10.1134/S0016793209070111

Mashnich GP, Bashkirtsev VS, Khlystova AI (2009b) Velocity structure and variations in the region of quiet solar filaments. Astron Lett 35:253–260. https://doi.org/10.1134/S1063773709040057

Mashnich GP, Bashkirtsev VS, Khlystova AI (2012) Small-amplitude oscillations in solar filaments. Astron Rep 56:241–249. https://doi.org/10.1134/S1063772912030055

Matsumoto T, Kitai R (2010) Temporal power spectra of the horizontal velocity of the solar photosphere. Astrophys J Lett 716:L19–L22. https://doi.org/10.1088/2041-8205/716/1/L19. arXiv:1004.5173

McDougall AMD, Hood AW (2007) A new look at mode conversion in a stratified isothermal atmosphere. Solar Phys 246:259–271. https://doi.org/10.1007/s11207-007-0393-5. arXiv:0707.0830

McLaughlin JA, Hood AW (2006) MHD mode coupling in the neighbourhood of a 2D null point. Astron Astrophys 459:641–649. https://doi.org/10.1051/0004-6361:20065558. arXiv:0712.2402

Menzel DH (1951) Solar electromagnetism. In: The dynamics of ionised media, UCL, London. http://discovery.ucl.ac.uk/14698/

Molowny-Horas R, Oliver R, Ballester JL, Baudin F (1997) Observations of Doppler oscillations in a solar prominence. Solar Phys 172:181–188. https://doi.org/10.1023/A:1004922809950

Molowny-Horas R, Baudin F, Oliver R, Ballester JL (1998) He I 10830 Å Doppler oscillations in a solar filament. In: Donahue RA, Bookbinder JA (eds) Cool stars, stellar systems, and the sun, Astronomical Society of the Pacific, San Francisco, ASP Conference Series, vol 154, pp 650–657

Molowny-Horas R, Wiehr E, Balthasar H, Oliver R, Ballester JL (1999) Prominence Doppler oscillations. In: Antalová A, Balthasar H, Kučera A (eds) JOSO annual report 1998, Astronomical Institute of Slovak Academy of Sciences, Tatranská Lomnica, Slovakia, pp 126–127. http://www.joso-info.org/JOSO_PROJEKT/annual/annual90.htm

Moreton GE, Ramsey HE (1960) Recent observations of dynamical phenomena associated with solar flares. Publ Astron Soc Pac 72:357–358. https://doi.org/10.1086/127549

Murawski K (1993) Cross-talk in solar coronal loops. Acta Astron 43:161–176

Nakariakov VM, Ofman L (2001) Determination of the coronal magnetic field by coronal loop oscillations. Astron Astrophys 372:L53–L56. https://doi.org/10.1051/0004-6361:20010607

Nakariakov VM, Verwichte E (2005) Coronal waves and oscillations. Living Rev Sol Phys 2:lrsp-2005-3. https://doi.org/10.12942/lrsp-2005-3

Nakariakov VM, Ofman L, DeLuca EE, Roberts B, Davila JM (1999) TRACE observations of damped coronal loop oscillations: implications for coronal heating. Science 285:862–864. https://doi.org/10.1126/science.285.5429.862

Ning Z, Cao W, Goode PR (2009a) Behavior of the spines in a quiescent prominence observed by Hinode/SOT. Astrophys J 707:1124–1130. https://doi.org/10.1088/0004-637X/707/2/1124

Ning Z, Cao W, Okamoto TJ, Ichimoto K, Qu ZQ (2009b) Small-scale oscillations in a quiescent prominence observed by HINODE/SOT: prominence oscillations. Astron Astrophys 499:595–600. https://doi.org/10.1051/0004-6361/200810853

Ofman L, Aschwanden MJ (2002) Damping time scaling of coronal loop oscillations deduced from transition region and coronal explorer observations. Astrophys J Lett 576:L153–L156. https://doi.org/10.1086/343886

Ofman L, Knizhnik K, Kucera T, Schmieder B (2015) Nonlinear MHD waves in a prominence foot. Astrophys J 813:124. https://doi.org/10.1088/0004-637X/813/2/124. arXiv:1509.07911

Okamoto TJ, Nakai H, Keiyama A, Narukage N, UeNo S, Kitai R, Kurokawa H, Shibata K (2004) Filament oscillations and Moreton waves associated with EIT waves. Astrophys J 608:1124–1132. https://doi.org/10.1086/420838

Okamoto TJ, Tsuneta S, Berger TE, Ichimoto K, Katsukawa Y, Lites BW, Nagata S, Shibata K, Shimizu T, Shine RA, Suematsu Y, Tarbell TD, Title AM (2007) Coronal transverse magnetohydrodynamic waves in a solar prominence. Science 318:1577–1580. https://doi.org/10.1126/science.1145447

Okamoto TJ, Antolin P, De Pontieu B, Uitenbroek H, Van Doorsselaere T, Yokoyama T (2015) Resonant absorption of transverse oscillations and associated heating in a solar prominence. I. Observational aspects. Astrophys J 809:71. https://doi.org/10.1088/0004-637X/809/1/71. arXiv:1506.08965

Oliver R (1999) Prominence oscillations: observations and theory. In: Wilson A et al (eds) Magnetic fields and solar processes, ESA Special Publication, vol 448. ESA, Noordwijk, p 425

Oliver R (2009) Prominence seismology using small amplitude oscillations. Space Sci Rev 149:175–197. https://doi.org/10.1007/s11214-009-9527-4

Oliver R, Ballester JL (1995) Magnetohydrodynamic waves in a bounded inhomogeneous medium with prominence–corona properties. Astrophys J 448:444–458. https://doi.org/10.1086/175975

Oliver R, Ballester JL (1996) The influence of the temperature profile on the magnetohydrodynamic modes of a prominence-corona system. Astrophys J 456:393–398. https://doi.org/10.1086/176661

Oliver R, Ballester JL (2002) Oscillations in quiescent solar prominences observations and theory (invited review). Solar Phys 206:45–67. https://doi.org/10.1023/A:1014915428440

Oliver R, Ballester JL, Hood AW, Priest ER (1992) Magnetohydrodynamic waves in a solar prominence. Astrophys J 400:369–379. https://doi.org/10.1086/172003

Oliver R, Ballester JL, Hood AW, Priest ER (1993) Oscillations of a quiescent solar prominence embedded in a hot corona. Astrophys J 409:809–821. https://doi.org/10.1086/172711

van den Oord GHJ, Kuperus M (1992) The effect of retardation on the stability of current filaments. Solar Phys 142:113–129. https://doi.org/10.1007/BF00156636

van den Oord GHJ, Schutgens NAJ, Kuperus M (1998) The effect of delays on filament oscillations and stability. Astron Astrophys 339:225–238

Osherovich VA (1985) Solar prominence model based on eigenvalue solutions. I. Isolated filaments and their properties under the influence of external horizontal magnetic field. Astrophys J 297:314–323. https://doi.org/10.1086/163530

Osherovich VA (1989) Solar prominence model based on eigenvalue solutions. II. Filaments in the vertical magnetic fields. Astrophys J 336:1041–1049. https://doi.org/10.1086/167073

Pandey BP, Wardle M (2008) Hall magnetohydrodynamics of partially ionized plasmas. Mon Not R Astron Soc 385:2269–2278. https://doi.org/10.1111/j.1365-2966.2008.12998.x. arXiv:0707.2688

Pant V, Srivastava AK, Banerjee D, Goossens M, Chen PF, Joshi NC, Zhou YH (2015) MHD seismology of a loop-like filament tube by observed kink waves. Res Astron Astrophys 15:1713. https://doi.org/10.1088/1674-4527/15/10/008. arXiv:1503.02281

Patsourakos S, Vial JC (2002) SOHO contribution to prominence science. Solar Phys 208:253–281. https://doi.org/10.1023/A:1020510120772

Pintér B, Jain R, Tripathi D, Isobe H (2008) Prominence seismology: wavelet analysis of filament oscillations. Astrophys J 680:1560–1568. https://doi.org/10.1086/588273

Poland A, Anzer U (1971) Energy balance in cool quiescent prominences. Solar Phys 19:401–413. https://doi.org/10.1007/BF00146067

Pouget G (2007) Analyse des protubérances solaires observées à partir de la sonde solaire SOHO et du télescope Sacramento Peak: Oscillations, diagnostic, instabilités. PhD thesis, Université de Paris-Sud, Paris

Pouget G, Bocchialini K, Solomon J (2006) Oscillations in a solar filament: first observation of long periods in the He I 584.33 Å line, modelling and diagnostic. Astron Astrophys 450:1189–1198. https://doi.org/10.1051/0004-6361:20053886

Ramsey H, Smith SF (1965) Flare-initiated filament oscillations. Astron J 70:688. https://doi.org/10.1086/109569

Ramsey HE, Smith SF (1966) Flare-initiated filament oscillations. Astron J 71:197–199. https://doi.org/10.1086/109903

Régnier S, Solomon J, Vial JC (2001) Oscillations in an active region filament: observations and comparison with MHD waves. Astron Astrophys 376:292–301. https://doi.org/10.1051/0004-6361:20010972

Rempel M, Schmitt D, Glatzel W (1999) Stability of a flux tube model for prominences. Astron Astrophys 343:615–623

Roberts B (1991) Waves in the solar atmosphere. Geophys Astrophys Fluid Dyn 62:83–100. https://doi.org/10.1080/03091929108229127

Roberts B, Joarder PS (1994) Oscillations in quiescent prominences. In: Belvedere G, Rodono M, Simnett GM (eds) Advances in solar physics. Lecture Notes in Physics, vol 432. Springer, Berlin, pp 173–178. https://doi.org/10.1007/3-540-58041-7_215

Roberts B, Edwin PM, Benz AO (1984) On coronal oscillations. Astrophys J 279:857–865. https://doi.org/10.1086/161956

Robertson D, Ruderman MS (2011) Resonantly damped oscillations of two coronal loops. Astron Astrophys 525:A4. https://doi.org/10.1051/0004-6361/201015525

Ruderman MS, Luna M (2016) Damping of prominence longitudinal oscillations due to mass accretion. Astron Astrophys 591:A131. https://doi.org/10.1051/0004-6361/201628713. arXiv:1605.03376

Ruderman MS, Roberts B (2002) The damping of coronal loop oscillations. Astrophys J 577:475–486. https://doi.org/10.1086/342130

Sakai J, Colin A, Priest E (1987) Dynamical model of prominence formation and oscillation. Solar Phys 114:253–271. https://doi.org/10.1007/BF00167345

Schmieder B, Kucera TA, Knizhnik K, Luna M, Lopez-Ariste A, Toot D (2013) Propagating waves transverse to the magnetic field in a solar prominence. Astrophys J 777:108. https://doi.org/10.1088/0004-637X/777/2/108. arXiv:1309.1568

Schutgens NAJ (1997a) Prominence oscillations and stability: communicating the distant photospheric boundary. Astron Astrophys 323:969–985

Schutgens NAJ (1997b) Vertical prominence oscillations and stability: a comparison of the influence of the distant photosphere in inverse polarity and normal polarity prominence models. Astron Astrophys 325:352–359

Schutgens NAJ, Tóth G (1999) Numerical simulation of prominence oscillations. Astron Astrophys 345:1038–1048 arXiv:astro-ph/9903128

Shen Y, Ichimoto K, Ishii TT, Tian Z, Zhao R, Shibata K (2014a) A chain of winking (oscillating) filaments triggered by an invisible extreme-ultraviolet wave. Astrophys J 786:151. https://doi.org/10.1088/0004-637X/786/2/151. arXiv:1403.7705

Shen Y, Liu YD, Chen PF, Ichimoto K (2014b) Simultaneous transverse oscillations of a prominence and a filament and longitudinal oscillation of another filament induced by a single shock wave. Astrophys J 795:130. https://doi.org/10.1088/0004-637X/795/2/130. arXiv:1409.1304

Soler R, Goossens M (2011) Kink oscillations of flowing threads in solar prominences. Astron Astrophys 531:A167. https://doi.org/10.1051/0004-6361/201116536. arXiv:1106.3937

Soler R, Oliver R, Ballester JL (2007) The effect of the solar corona on the attenuation of small-amplitude prominence oscillations. I. Longitudinal magnetic field. Astron Astrophys 471:1023–1033. https://doi.org/10.1051/0004-6361:20077633. arXiv:0704.1566

Soler R, Oliver R, Ballester JL (2008) Nonadiabatic magnetohydrodynamic waves in a cylindrical prominence thread with mass flow. Astrophys J 684:725–735. https://doi.org/10.1086/590244. arXiv:0803.2600

Soler R, Oliver R, Ballester JL (2009a) Attenuation of small-amplitude oscillations in a prominence corona model with a transverse magnetic field. New Astron 14:238–248. https://doi.org/10.1016/j.newast.2008.08.008. arXiv:0801.3744

Soler R, Oliver R, Ballester JL (2009b) Magnetohydrodynamic waves in a partially ionized filament thread. Astrophys J 699:1553–1562. https://doi.org/10.1088/0004-637X/699/2/1553. arXiv:0904.3013

Soler R, Oliver R, Ballester JL (2009c) Propagation of nonadiabatic magnetoacoustic waves in a threaded prominence with mass flows. Astrophys J 693:1601–1609. https://doi.org/10.1088/0004-637X/693/2/1601. arXiv:0809.4765

Soler R, Oliver R, Ballester JL (2009d) Resonantly damped kink magnetohydrodynamic waves in a partially ionized filament thread. Astrophys J 707:662–670. https://doi.org/10.1088/0004-637X/707/1/662. arXiv:0909.3599

Soler R, Oliver R, Ballester JL, Goossens M (2009e) Damping of filament thread oscillations: effect of the slow continuum. Astrophys J Lett 695:L166–L170. https://doi.org/10.1088/0004-637X/695/2/L166. arXiv:0902.0572

Soler R, Arregui I, Oliver R, Ballester JL (2010a) Seismology of standing kink oscillations of solar prominence fine structures. Astrophys J 722:1778–1792. https://doi.org/10.1088/0004-637X/722/2/1778. arXiv:1007.1959

Soler R, Oliver R, Ballester JL (2010b) Time damping of non-adiabatic magnetohydrodynamic waves in a partially ionized prominence plasma: effect of helium. Astron Astrophys 512:A28. https://doi.org/10.1051/0004-6361/200913478. arXiv:0910.2883

Soler R, Oliver R, Ballester JL (2011) Spatial damping of propagating kink waves in prominence threads. Astrophys J 726:102. https://doi.org/10.1088/0004-637X/726/2/102. arXiv:1009.4871

Soler R, Ruderman MS, Goossens M (2012) Damped kink oscillations of flowing prominence threads. Astron Astrophys 546:A82. https://doi.org/10.1051/0004-6361/201220111. arXiv:1209.3382

Soler R, Goossens M, Ballester JL (2015) Prominence seismology using the period ratio of transverse thread oscillations. Astron Astrophys 575:A123. https://doi.org/10.1051/0004-6361/201424205. arXiv:1501.05238

Spruit HC (1982) Propagation speeds and acoustic damping of waves in magnetic flux tubes. Solar Phys 75:3–17. https://doi.org/10.1007/BF00153456

Suematsu Y, Yoshinaga R, Terao N, Tsubaki T (1990) Oscillatory and transient features detected simultaneously in the Ca ii K and Hβ line spectra of a quiescent prominence. Publ Astron Soc Jpn 42:187–203

Suetterlin P, Wiehr E, Bianda M, Kueveler G (1997) Problems in measuring prominence oscillations. Astron Astrophys 321:921–926

Takahashi T, Asai A, Shibata K (2015) Prominence activation by coronal fast mode shock. Astrophys J 801:37. https://doi.org/10.1088/0004-637X/801/1/37. arXiv:1501.01592

Tandberg-Hanssen E (1995) The nature of solar prominences, Astrophysics and Space Science Library, vol 199. Kluwer, Dordrecht. https://doi.org/10.1007/978-94-017-3396-0

Terradas J, Oliver R, Ballester JL (2001) Radiative damping of quiescent prominence oscillations. Astron Astrophys 378:635–652. https://doi.org/10.1051/0004-6361:20011148

Terradas J, Molowny-Horas R, Wiehr E, Balthasar H, Oliver R, Ballester JL (2002) Two-dimensional distribution of oscillations in a quiescent solar prominence. Astron Astrophys 393:637–647. https://doi.org/10.1051/0004-6361:20020967

Terradas J, Carbonell M, Oliver R, Ballester JL (2005) Time damping of linear non-adiabatic magnetoacoustic waves in a slab-like quiescent prominence. Astron Astrophys 434:741–749. https://doi.org/10.1051/0004-6361:20041984

Terradas J, Arregui I, Oliver R, Ballester JL (2008) Transverse oscillations of flowing prominence threads observed with Hinode. Astrophys J Lett 678:L153–L156. https://doi.org/10.1086/588728

Terradas J, Arregui I, Oliver R, Ballester JL, Andries J, Goossens M (2008) Resonant absorption in complicated plasma configurations: applications to multistranded coronal loop oscillations. Astrophys J 679:1611–1620. https://doi.org/10.1086/586733. arXiv:0802.0591

Terradas J, Goossens M, Verth G (2010) Selective spatial damping of propagating kink waves due to resonant absorption. Astron Astrophys 524:A23. https://doi.org/10.1051/0004-6361/201014845. arXiv:1004.4468

Terradas J, Soler R, Díaz AJ, Oliver R, Ballester JL (2013) Magnetohydrodynamic waves in two-dimensional prominences embedded in coronal arcades. Astrophys J 778:49. https://doi.org/10.1088/0004-637X/778/1/49. arXiv:1309.4934

Terradas J, Soler R, Luna M, Oliver R, Ballester JL, Wright AN (2016) Solar prominences embedded in flux ropes: morphological features and dynamics from 3D MHD simulations. Astrophys J 820:125. https://doi.org/10.3847/0004-637X/820/2/125. arXiv:1512.07096

Thompson WT, Schmieder B (1991) Oscillations in Hα filaments: center-to-limb study. Astron Astrophys 243:501–511

Titov VS, Démoulin P (1999) Basic topology of twisted magnetic configurations in solar flares. Astron Astrophys 351:707–720

Tripathi D, Isobe H, Jain R (2009) Large amplitude oscillations in prominences. Space Sci Rev 149:283–298. https://doi.org/10.1007/s11214-009-9583-9. arXiv:0910.4059

Tsubaki T, Takeuchi A (1986) Periodic oscillations found in the velocity field of a quiescent prominence. Solar Phys 104:313–320. https://doi.org/10.1007/BF00159084

Tsubaki T, Ohnishi Y, Suematsu Y (1987) Short-period oscillations found in a quiescent prominence. Publ Astron Soc Jpn 39:179–188

Tsubaki T, Toyoda M, Suematsu Y, Gamboa GAR (1988) New evidence for oscillatory motions in a quiescent prominence. Publ Astron Soc Jpn 40:121–126

Uchida Y (1970) Diagnosis of coronal magnetic structure by flare-associated hydromagnetic disturbances. Publ Astron Soc Jpn 22:341–364

Van Doorsselaere T, Nakariakov VM, Verwichte E (2008a) Detection of waves in the solar corona: Kink or Alfvén? Astrophys J Lett 676:L73–L75. https://doi.org/10.1086/587029

Van Doorsselaere T, Ruderman MS, Robertson D (2008b) Transverse oscillations of two parallel coronal loops. Astron Astrophys 485:849–857. https://doi.org/10.1051/0004-6361:200809841

Van Doorsselaere T, Wardle N, Del Zanna G, Jansari K, Verwichte E, Nakariakov VM (2011) The first measurement of the adiabatic index in the solar corona using time-dependent spectroscopy of Hinode/EIS observations. Astrophys J Lett 727:L32. https://doi.org/10.1088/2041-8205/727/2/L32

Verth G, Erdélyi R, Jess DB (2008) Refined magnetoseismological technique for the solar corona. Astrophys J Lett 687:L45–L48. https://doi.org/10.1086/593184

Verwichte E, Nakariakov VM, Ofman L, Deluca EE (2004) Characteristics of transverse oscillations in a coronal loop arcade. Solar Phys 223:77–94. https://doi.org/10.1007/s11207-004-0807-6

Verwichte E, Foullon C, Nakariakov VM (2006) Seismology of curved coronal loops with vertically polarised transverse oscillations. Astron Astrophys 452:615–622. https://doi.org/10.1051/0004-6361:20054437

von Toussaint U (2011) Bayesian inference in physics. Rev Mod Phys 83:943–999. https://doi.org/10.1103/RevModPhys.83.943

Vršnak B, Veronig AM, Thalmann JK, Žic T (2007) Large amplitude oscillatory motion along a solar filament. Astron Astrophys 471:295–299. https://doi.org/10.1051/0004-6361:20077668. arXiv:0707.1752

Vršnak B (1993) Classification of prominence oscillations. Hvar Obs Bull 17:23

Wiehr E, Balthasar H, Stellmacher G (1984) Oscillations of the Hα emission in solar prominences. Solar Phys 94:285–288. https://doi.org/10.1007/BF00151318

Wiehr E, Balthasar H, Stellmacher G (1989) Doppler velocity oscillations in quiescent prominences. Hvar Obs Bull 13:131–135

Xia C, Chen PF, Keppens R, van Marle AJ (2011) Formation of solar filaments by steady and non-steady chromospheric heating. Astrophys J 737:27. https://doi.org/10.1088/0004-637X/737/1/27. arXiv:1106.0094

Xue ZK, Yan XL, Qu ZQ, Zhao L (2014) Transverse oscillation of a filament triggered by an extreme ultraviolet wave. In: Nagendra KN, Stenflo JO, Qu Q, Samooprna M (eds) Solar polarization 7, Astronomical Society of the Pacific, San Francisco, ASP conference series, vol 489, p 53

Yi Z, Engvold O (1991) Vertical velocities and oscillations in quiescent filaments. Solar Phys 134:275–286. https://doi.org/10.1007/BF00152648

Yi Z, Engvold O, Keil SL (1991) Structure and oscillations in quiescent filaments from observations in He I λ 10830 Å. Solar Phys 132:63–80. https://doi.org/10.1007/BF00159130

Zapiór M, Kotrč P, Rudawy P, Oliver R (2015) Simultaneous observations of solar prominence oscillations using two remote telescopes. Solar Phys 290:1647–1659. https://doi.org/10.1007/s11207-015-0696-x

Zapiór M, Oliver R, Ballester JL, Heinzel P (2016) Synthetic hydrogen spectra of oscillating prominence slabs immersed in the solar corona. Astrophys J 827:131. https://doi.org/10.3847/0004-637X/827/2/131

Zaqarashvili TV (2003) Observation of coronal loop torsional oscillation. Astron Astrophys 399:L15–L18. https://doi.org/10.1051/0004-6361:20030084. arXiv:astro-ph/0301316

Zhang QM, Chen PF, Xia C, Keppens R (2012) Observations and simulations of longitudinal oscillations of an active region prominence. Astron Astrophys 542:A52. https://doi.org/10.1051/0004-6361/201218786. arXiv:1204.3787

Zhang QM, Chen PF, Xia C, Keppens R, Ji HS (2013) Parametric survey of longitudinal prominence oscillation simulations. Astron Astrophys 554:A124. https://doi.org/10.1051/0004-6361/201220705. arXiv:1304.3798

Zhang QM, Li T, Zheng RS, Su YN, Ji HS (2017) Large-amplitude longitudinal oscillations in a solar filament. Astrophys J 842:27. https://doi.org/10.3847/1538-4357/aa73d2. arXiv:1705.04820

Zhou YH, Zhang LY, Ouyang Y, Chen PF, Fang C (2017) Solar filament longitudinal oscillations along a magnetic field tube with two dips. Astrophys J 839:9. https://doi.org/10.3847/1538-4357/aa67de. arXiv:1703.06560

Zirker JB, Engvold O, Martin SF (1998) Counter-streaming gas flows in solar prominences as evidence for vertical magnetic fields. Nature 396:440–441. https://doi.org/10.1038/24798